UNIVERSITÀ DEGLI STUDI DI NAPOLI
PARTHENOPE

University of Study of Naples "Parthenope"

Department of Science and Technology

PhD Program in Environmental Phenomena and Risks

XXXVIII Cycle

Multi-sensor analysis of hailstorms in the Mediterranean Region

Academic Year 2024/2025

Author:

Federico Vermi

Supervisor(s):

Prof. Giorgio Budillon, Supervisor

Dr. Vincenzo Capozzi, Co-Supervisor

Dr. Sante Laviola, Co-Supervisor

PhD Program Coordinator:

Prof. Antonio Occhiuzzi

Table of Contents

Summary Abstract

Hailstorms are among the most impactful manifestations of thunderstorm development and evolution and represent a major meteorological risk in the Mediterranean region, where they cause significant socio-economic losses. Despite their relevance, hail events are still not accurately and comprehensively captured due to their local-scale extent, the lack of appropriate observing systems and the limited availability of high-resolution modelling studies. In the context of climate warming and the expected increase in frequency and intensity of extreme weather events across Europe, improving the detection and understanding of hailstorms has become crucial.

This PhD research presents a multi-sensor analysis of hailstorms in the Mediterranean Basin, integrating satellite, lightning and radar data to investigate their formation, development and detection. The first part of the work focuses on the "Multi-sensor Approach for Satellite Hail Advection" (MASHA) Method, a satellite-based technique that exploits the physical interaction between ice hydrometeors (ice crystals, graupel and hailstones) and microwave and infrared electromagnetic waves to estimate hail probability (HP) every five minutes over a wide Mediterranean domain. Strengths and limitations of the MASHA Method were assessed, highlighting issues related to the calibration of the MWCC-H algorithm and to the misinterpretation of overshooting top (OT) structures in severe hailstorms. To overcome these limitations, two complementary approaches were explored. First, a neural network-based method relying on a ResNet-50 Convolutional Neural Network (CNN) was trained using infrared satellite images to recognize hailstorms. Preliminary results demonstrated promising performance in distinguishing hail-producing storms from ordinary thunderstorms, opening new perspectives for satellite-based monitoring. Second, lightning activity was investigated as a proxy for hail detection. A new hail probability (NHP), combining MASHA-derived HP and lightning-based indicators, significantly improved hail report classification and reduced underestimation, particularly for deep OT hailstorms producing large and very large hailstones. Further exploratory analyses examined the relationship between lightning variables and hail occurrence through the development of an innovative mathematical approach for lightning jump (LJ) detection. Results showed that LJ indicators, lead time (LT) and jump intensity are strongly associated with hail occurrence and severity, with a positive correlation between lightning jump intensity and maximum hail size. The comparison between the LJ method and a radar-based hail detection algorithm demonstrated comparable performance, while their combination maximized detection capability.

Overall, this research highlights the potential of a multi-sensor framework for improving hailstorm identification and monitoring in the Mediterranean region, emphasizing the role of satellite and lightning data for real-time applications and nowcasting systems, and providing new insights into the relationship between electrification processes and hail severity.

Chapter 1 Introduction

Among the different types of precipitation associated with atmospheric phenomena, hail is considered one of the most impactful manifestations of a thunderstorm's development and evolution. Hailstorms are dangerous and costly phenomena that represent an important meteorological risk in the Mediterranean region and can cause considerable damage to buildings, crops, and cars, resulting in large economic and insured losses. Hail-bearing thunderstorms are usually highly organized convective systems in terms of multicells, mesoscale convective systems (MCS), or supercells. Hailstorms are not accurately and comprehensively captured due to the local-scale extent of hail-affected areas and a lack of appropriate observing systems in most regions, which hinder the study of hail climatologies and the production of statistical analyses about the frequency of hail phenomena (Punge and Kunz, 2016). In the framework of climate warming (Luo, 2007), studying topics like low-level moisture and convective instability, microphysical processes and vertical wind shear becomes crucial for understanding hail formation and properties. In addition, the lack of hail observations and high-resolution modelling studies, and gaps in the understanding of physical processes, contribute to the current high uncertainty around the effects of climate change on hailstorms worldwide (Raupach et al., 2021). Even if recently the increase in popularity of "apps" on mobile smartphone is simplifying the way to share photos, pictures and reports of precipitation related phenomena (Allen et al., 2020), hail observations usually underestimate both the number of hail events occurred and maximum hail size produced by the storms, due to considerable geographical differences in terms of population density. This is the reason why future studies should focus on furthering process understanding and improving proxy relationships and, at the same time, during last years many works have been carried out in the Mediterranean basin trying to improve our knowledge about hail phenomena. In fact, it is highly likely that in the coming decades extreme weather events (such as strong wind gusts, severe thunderstorms, lightning, and especially large hail) will become increasingly frequent across Europe (Rädler et al., 2019). Consequently, hail is expected not only to remain a defining feature of Europe's climate in the years ahead, but also to intensify in both frequency and hailstone size (Piani et al., 2005; Kunz et al., 2009; Berthet et al., 2011). Using the Global Precipitation Measurement (GPM) Constellation (Hou et al., 2014), Laviola et al., (2022a) analyzed the hailstorms that occurred from 1999 to 2021 finding that hail events are increasing in the Mediterranean regions since 2010. Merino et al., (2013) and Merino et al., (2014) characterized the hailstorms in Southwestern Europe through the definition of a synoptic environment favorable to convection, the establishment of mesoscale configurations on hailstorm days, and an analysis of prediction parameters for the presence of hail. Nisi et al., (2016) studied the spatial and temporal distribution of hailstorms in the Alpine region through a high resolution radar-based analysis, while Nisi et al., (2020) highlighted the importance of nowcasting systems suggesting that the increase of lightning rate (referred to as lightning jump) may be used as additional data for hailstorm nowcasting. Moreover, the occurrence of severe hailstorms producing giant hailstones with size higher than 10 cm in some Mediterranean

regions like Spain (García-Ortega, et al., 2007; Farnell et al., 2023; Martín et al., 2024), Italy (Marra et al., 2017; Tiesi et al., 2022; Ricchi et al., 2023;) and Greece (Papavasileiou et al., 2022) is progressively focusing attention on these extreme phenomena which can endanger human life.

Within thunderstorm clouds, a wide variety of hydrometeors can be found, including graupel (irregular ice pellets with diameters generally smaller than 5 mm) and hail, which can be defined as a type of precipitation in the form of balls or irregular lumps of ice with diameters generally in the range 5–50 mm, generally showing a spheroidal, conical, or irregular shape, and which can be either transparent or partly or completely opaque (Heymsfield et al., 2018). Although both graupel and hail require strong updrafts to be sustained aloft and to grow, they represent two distinct forms of precipitation. Before examining how these hydrometeors form and evolve, it is essential to highlight two fundamental ingredients that make such processes possible. First, ice-nucleating particles such as sea salt aerosols, dust, smog, and microorganisms (Michaud et al., 2014) must be present in clouds: around them, hailstones can develop and grow in size (Rosinski and Kerrigan, 1969). A recent study on two hailstones collected in central Argentina determined that particles ranged in diameter from 1 to 256 μm, with the largest particles consistently found in the hailstone embryos. Agglomerated mineral and organic particles dominated the elemental composition in both the embryo and outer layers, with the largest agglomerated particle (256 μm) being an organic-rich particle in the embryo of the larger hailstone (Bernal Ayala et al., 2025). In general, varying the concentration of cloud condensation nuclei and the shape of the cloud droplet size distribution has a significant impact on hail accumulated at the ground and on the size of the hailstones (Noppel et al., 2010) and their mean diameter increases with greater cloud condensation nuclei concentrations (Yang et al., 2011). Also, the ice accretion is entirely dependent on the continous deposition of large amounts of supercooled water droplets that can be defined as liquid droplets that remain unfrozen even at temperatures below 0 °C (Knight and Knight, 2001) and, according to existing studies, the latter may persist down to about –38 °C (Allen et al., 2020), even if growth takes place primarily between –10 and –25°C (Foote, 1984). When the updraft ranges up to several tens of meters per second, frozen hydrometeors can remain suspended for extended periods, allowing hailstones to grow to considerable sizes. The width of the updraft is found to be an important factor in limiting hail growth in the storm as well as melting during fall-out is also significant and can finally reduce the size of the hailstones when detected at the ground (Foote, 1984). Hail formation is the outcome of a development process that may last up to 30 minutes, during which the presence of alternate layers of cloudy and clear ice is attributed to transitions between dry and wet growth (Browning et al., 1963). In such storms, the interplay between strong updrafts and downdrafts allows ice particles to be repeatedly transported upward and downward until they become too heavy to remain suspended. Under colder conditions with limited water availability (downdraft regions), dry deposition occurs: supercooled droplets freeze rapidly on the hailstone surface, trapping numerous air bubbles within the new ice layer and producing a characteristically opaque appearance. Conversely, in warmer regions with abundant supercooled droplets (updraft zones), wet deposition dominates: droplets freeze more slowly, leading to the formation of transparent ice layers (Rasmussen and Heymsfield, 1987; Allen et al., 2020). The outcome of this alternating process is hailstones with highly variable shapes (spheroidal, conical, etc.), typically displaying concentric layering as

described in Figure 1 (Allen et al., 2020). Considering the terminal velocity of a hydrometeor, that can be defined as the speed at which its downward acceleration due to gravity balances the upward acceleration due to the drag of the air, in general hailstones have terminal velocities of about 10 m · s^{-1} but large hydrometeors may reach 50 m · s^{-1} (Knight and Knight, 2001).

Figure 1. Pictures of hailstones showing alternating opaque and transparent ice layers (adapted from Allen et al., 2020).

Exploiting different data sources mainly involving satellite, lightning and radar data, this research project aims to improve our knowledge about the hailstorms and their detection in the Mediterranean region, analyzing how they form, develop and dissipate. Starting from the "Multi-sensor Approach for Satellite Hail Advection" (MASHA) Method (Laviola et al., 2022b), a satellite hail tool developed to monitor the evolution of the hailstorms in the whole Mediterranean basin in quasi real-time, strenghts and limitations linked to this method were assessed. After evaluating the performance of MASHA Method and highlighting the main critical issues, new potential approaches were explored in order to improve the detection of the hailstorms:

- neural network methods: in this framework, we carried out a preliminary study based on a specific type of neural networks (Convolutional Neural Networks (CNNs); O'Shea and Nash, 2015) that are primarily used to solve difficult image-driven pattern recognition tasks. In our case, the CNNs training involved infrared (IR) satellite-images in order to recognize hailstorms only using geostationary satellite data. Results are still preliminary but very interesting and open new perspectives about the satellite monitoring of the hailstorms;

- proxy data such as lightning activity characterizing the hailstorms. The need to investigate relationships between hailstorms and other proxies like lightning activity were highlighted in many previous studies (e.g. Raupach et al., 2021). In this work, we focused on some patterns linked to lightning data (e.g. total lightning, lightning jumps, intra-cloud and cloud-to-ground trends and lead time) that could help to detect the hailstorms in real-time and giving out some useful information about their potential severity (especially in terms of maximum hail size) and the areas mainly affected by their passing. These results open the perspective to be exploited not only in this research field, but also for nowcasting systems operating in real-time.

This thesis is organized as follows. In Chapter 2, after introducing the MASHA Method, the main strengths and limitations of this tool are discussed. In the last part of this Section, to overcome some problems related to the latter, a preliminary study exploiting a new neural network-based approach is presented. In Section 3, the electrification of thunderstorms is treated, explaining the main reasons why lightning activity has been chosen as a proxy for the hailstorms. In the second part of this chapter, the Italian Lightning Network LAMPINET is described and lightning trends are studied on the Italian Peninsula, also comparing them with the main thunderstorm climatologies proposed. In Chapter 4, two preliminary studies carried out using the Lightning Network LAMPINET and the European Lightning Network LINET are presented, investigating the potential relationship between some lightning variables and the occurrence of hailstorms and introducing a new methodology for the lightning jump computation. Exploiting the total lightning, in Section 5, some tests are performed to evaluate the potential improvement of MASHA Method while in Chapter 6, the outcomes related to lightning variables obtained thanks to the new mathematical approach are compared with hail proxies given by the "Campania Region Meteorological Radar Network" (CARMEN; Capozzi et al., 2022) hail detection tool, which is based on radar data. Finally, the main conclusions of this research project are resumed in Section 7.

Chapter 2 The Multi-sensor Approach for Satellite Hail Advection ("MASHA") Method

2.1 Introduction to the MASHA Method

During the last 20 years, the detection of the hailstorms using passive microwave satellites has been explored in depth and some methodologies for estimating hail occurrence were developed. Ferraro et al. (2020) state that the identification of hailfall from passive microwave sensors is based on the detection of scattering signatures associated with large ice particles at various microwave observation frequencies, depending upon the sensor being used. The larger the ice size and ice volume within a satellite footprint (FOV), the greater the brightness temperature (TB) depression will be. Microwave sounders, although typically with larger FOV sizes, have an added advantage at 150 and 183 GHz channels, showing a higher sensitivity to water vapor variations at different altitudes in the atmosphere. Thus, TB depressions at the highest peaking channels (e.g., 183 ± 1 GHz) are indicative of strong cloud updrafts associated with hail. Cecil (2009) confirmed that extremely low TBs are often accompanied by large hail at the surface. The three frequencies examined (85, 37, and 19 GHz) all showed an increasing likelihood of hail reports with decreasing TB. In addition, Cecil and Blankenship (2012) produced an 8-year global climatology of large hail-bearing storms estimated from satellite measurements using Advanced Microwave Scanning Radiometer for Earth Observing System (AMSR-E). Ferraro et al. (2015) developed a prototype Advanced Microwave Sounding Unit (AMSU-A and -B) based hail detection algorithm using a collocated satellite and surface hail reports over the continental US for a 10-year period (2000–2009): final comparisons with the surface observations confirmed that the algorithm detected approximately 40% of hail occurrences. A novel probability-based method for hail detection is the "MicroWave Convective Cloud method for Hail Detection" (hereafter, MWCC-H) algorithm introduced by Laviola et al. (2020a), originally conceived for AMSU-B/Microwave Humidity Sounder (MHS), and subsequently extended to all sensors of the Global Precipitation Measurement (GPM) constellation (polar satellites) operating within the 150–170 GHz frequency range (the Advanced Technology Microwave Sounder (ATMS), the Special Sensor Microwave Imager/Sounder (SSMIS), and the GPM Microwave Imager GMI; Laviola et al., 2020b). The MWCC-H method is based on the inverse proportionality between the upwelling radiation and hail cross-sections. The frequencies at 150 and 190 GHz are the most sensitive to the presence of hail being subject to a modification of their radiation field as a function of hail diameter. In addition, the difference between these two frequencies is demonstrated to be very sensitive to the growth of ice aggregates particularly when hail size is the order of centimeters (Laviola et al., 2020a). Therefore, the equation modeling the hail detection is a modified sigmoidal function as follows:

$$f(x,y) = 1 - \frac{1}{1+ e^{-(x-y)}} \quad (1)$$

where x and y are the TBs at 150 and 190 GHz, respectively. To prevent unrealistic probability growth (overshooting), a dynamic carrying capacity K (Meyer and Ausubel, 1999) is introduced, similarly to population models:

$$K(x) = \frac{\alpha}{x} \tag{2}$$

where α = 104 K (the absolute minimum found in the training dataset) and x is the TB at 150 GHz, that is the fastest frequency at reaching saturation conditions. The carrying capacity K is a dimensionless variable and its concept derives from biological species, acting as a regulator of the maximum population the environment can sustain. If applied to hailstorms, the growth of the hail sizes increases the scattering and the population load: thus, when K becomes equal to 1, the model saturates and the computation is stopped. By combining Equations (1) and (2), a compact expression is derived that links hail probability directly to TB at 150 GHz:

$$H\big(K(x)\big) = 0.9844\ \ln K(x)) + 0.9072 \tag{3}$$

This function summarizes the expected probability response as TB decreases. Finally, the MWCC-H method converts the TB detected by polar satellites into a hail probability range moving from 0 (clear sky conditions) to 1 (hail is observed): higher values highlight an increased probability of large hail and severe phenomena. Thanks to Equation (3), it is possible to plot in Figure 2 the hail probability as a function of TB signal at 150 GHz (hereafter, TB150) arriving to microwave radiometers (Laviola et al., 2020a).

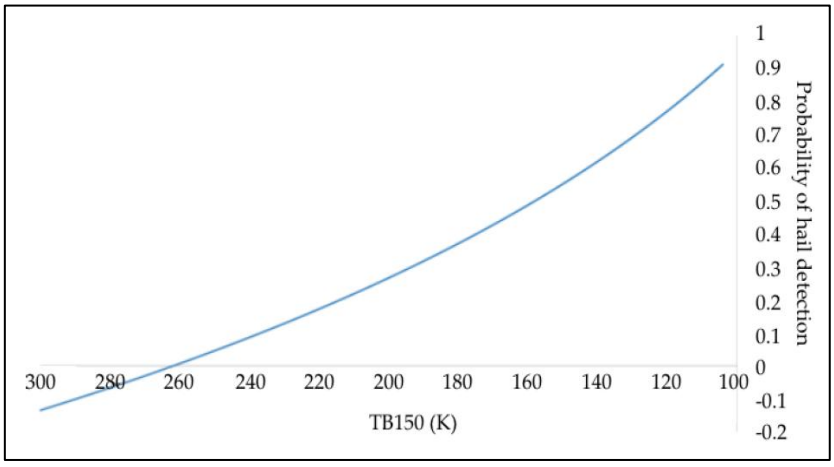

Figure 2. Distribution of hail probabilities as a function of TB150 for AMSU-B/MHS (adapted from Laviola et al., 2020a).

The resulting blue curve in Fig. 2 depicts a decreasing exponential function, which describes the hail probability (hereafter, HP) trend found for AMSU-B/MHS sensor. The MWCC-H algorithm saturates when TB150 approaches the critical value of 103.70 K, i.e., the absolute minimum found in the training dataset: for lower TB150 values, the corresponding HP will be equal to 1.00. The HP range is associated with five hail classes depending on the mean diameter of hail and potential damage produced by the hailstorms, as shown in Table 1.

Table 1. Five hail probability classes defined by the MWCC-H method. Each of them is associated with a HP range, mean diameter of the hailstones and potential damage produced.

	No Hail	Hail Potential	Hail Initiation	Large Hail	Super Hail
Interval	$0.00 \leq P < 0.20$	$0.20 \leq P < 0.36$	$0.36 \leq P < 0.45$	$0.45 \leq P < 0.60$	$0.60 \leq P \leq 1.00$
Diameter	/	< mm	0-2 cm	2-10 cm	> 10 cm
Damage	/	/	Negligible	Important	Severe

As can be noted from Table 1, up to a value of 0.20, the MWCC-H method is unable to distinguish the presence of frozen hydrometeors. For hail probability values between 0.20 and 0.36, graupel and ice crystals are generally observed within the cloud, but no damage is produced at ground. When the hail probability ranges from 0.36 to 0.60, hydrometeor sizes increase, leading to the formation of aggregates that may reach the surface, evolving from graupel to hailstones with diameters of several centimeters and damage that progressively increases in severity. In the range between 0.60 and 1.00, the "Super Hail" category is identified: in this class, the diameter of the hailstones may exceed 10 cm, and the associated surface damage is typically severe. An example of the MWCC-H method final output is depicted in Figure 3, in which two hail probability maps are obtained thanks to the scan performed by the GMI radiometer on 25 July 2023 at 06:43 UTC (Fig. 3a) and by the NPP sensor on board ATMS on 04 September 2021 at 01:15 UTC (Fig. 3b).

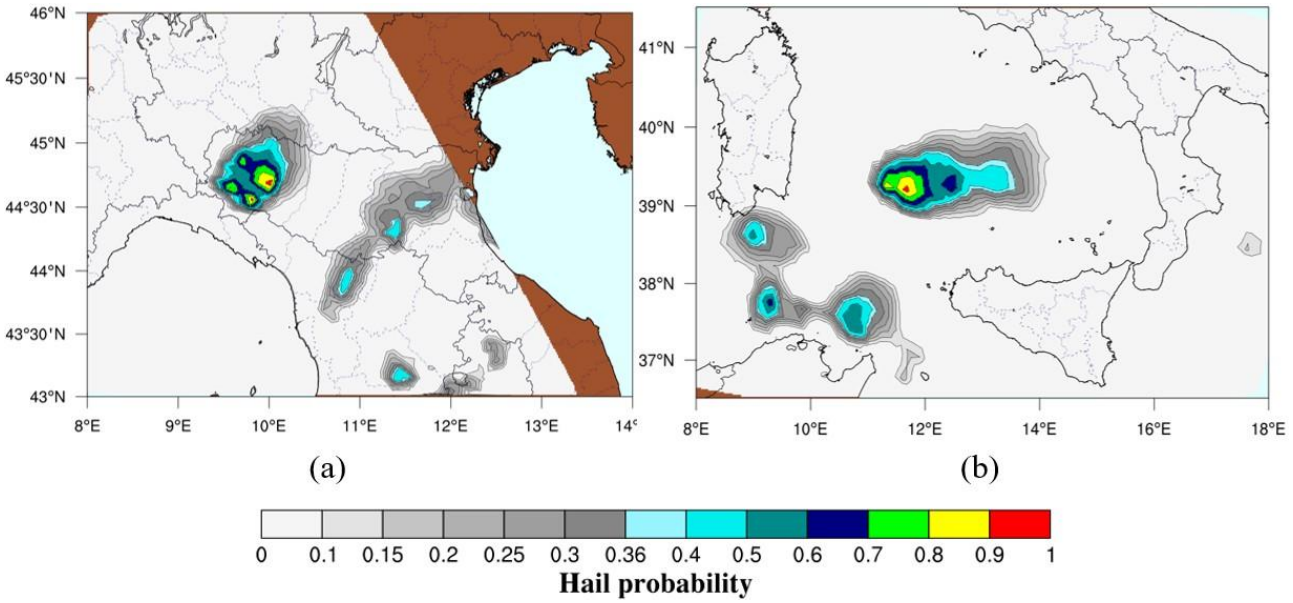

Figure 3. Hail probability maps obtained by using the MWCC-H method. The GMI radiometer (a) and the NPP sensor on board ATMS (b) scanned some portions of the Italian Peninsula identifying strong developing hailstorms on 25 July 2023 at 06:43 UTC (a) and on 04 September 2021 at 01:15 UTC (b).

As can be seen from Fig. 3a-b, the MWCC-H enhances areas characterized by severe evolving hailstorms reaching hail probability values until the Super Hail category. In Fig. 3a, some areas in northeastern Italy and

along the Adriatic Sea are not covered by the passing of the GMI radiometer (in this case land is brown colored while sea surface is light blue colored): it means that those areas were not scanned by the sensor and, consequently, information about potential developing hailstorms are not available. However, even if the MWCC-H method was extended to all microwave radiometers operative in a high frequency range between 150 and 170 GHz, the main drawback is related to the temporal frequency with which a region is scanned by one of these sensors. Indeed, on average, we can assume that if we focus on a specific region, the latter will be scanned about 30-35 times per day in an irregular way. It means that the same area could not be covered even for two or three consecutive hours depending on case by case, resulting in a too much long temporal window for which the hailstorms are not monitored. In this framework and for overcoming these problems, the MASHA Method (Laviola et al., 2022b) was developed. The main idea was to exploit satellite data coming from Meteosat-9 (MSG-2), Meteosat-10 (MSG-3) and Meteosat-11 (MSG-4), all of them belonging to the Meteosat Second Generation (MSG) program: positioned at an altitude of approximately 36.000 km above the equator, they operate in geostationary orbits, also defined as geosynchronous. The satellites observed area extends from the equator to roughly 70° latitude, since observations at higher latitudes are considerably distorted. The radiometer onboard the MSG satellites is the Spinning Enhanced Visible and InfraRed Imager (SEVIRI), equipped with twelve channels: four in the visible spectrum and eight in the infrared. SEVIRI provides full-disk imagery every fifteen minutes, and imagery over Europe every five minutes through the Meteosat Rapid Scan Service (MSG-RSS). Each scan line comprises 2500 pixels, with a spatial resolution of 4.8 km in the infrared channels (Levizzani et al., 2001). Two of the eight infrared channels were selected and employed as the primary source of information to identify hail during time intervals when hail probability data from microwave sensors were unavailable. The first is a window channel centered at a wavelength of 10.8 μm. At this wavelength, the Earth's surface can be observed under clear-sky conditions, while in the presence of thick clouds, only the cloud-top TB can be measured. The second channel employed is centered at 6.2 μm, located within the water vapor absorption band. In this case, most of the detected radiation originates from the mid-to-upper troposphere, and surface features cannot be identified. Indeed, the weighting function of the 6.2 μm channel shows a radiance peak at an altitude of approximately 8 km, whereas the weighting function of the 10.8 μm channel reaches its maximum at the Earth's surface (Santurette and Georgiev, 2005; Figure 4). Unfortunately, the infrared radiation cannot provide information about the internal structure of convective clouds because, in this case, the TB signal comes from the cloud top, but here the main advantage is that infrared satellite data are available every five minutes, thanks to the MSG-RSS mode. Therefore, the main idea behind the MASHA Method is to exploit the 10.8 μm channel to propagate in time the information provided by the MWCC-H algorithm while the difference between the 6.2 μm channel and the 10.8 μm channel allows us to calculate the overshooting index (that will be discussed in Section 2.3.2). In this framework, the proposed hybrid technique aims to establish correlations, through pairings based on selected statistical relationships, between TBs measured by geostationary satellites (hereafter, IR-TB), which provide excellent spatiotemporal coverage, and hail probability estimates derived from microwave sensors TBs (hereafter, MW-TB), whose information is comparatively sparse in both space and time (Torricella et al., 2007).

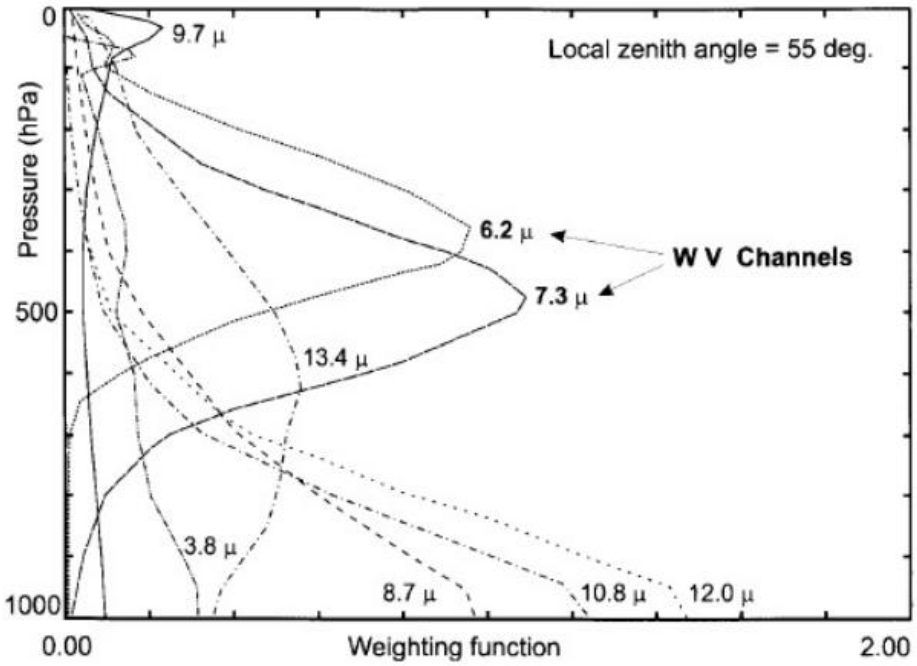

Figure 4. Weighting functions measured for eight infrared channels detected by SEVIRI radiometer (adapted from Santurette and Georgiev, 2005).

So, the MWCC-H method acts as a calibrator for the IR-TB, which in turn, propagate the hail probability information until a new scan performed by a polar satellite upgrades the statistical relationship between the MW-TB and IR-TB. Therefore, the three key-points of the MASHA Method can be resumed as follows:

1) production of coincidence files: data provided by GPM and MSG-RSS are combined. Only those characterized by a similar geolocation (≤ 10 km) and time of acquisition (≤ 15 minutes) are considered to apply the MWCC-H algorithm;
2) histogram-matching: for each box (having a 0.5° × 0.5° size) belonging to the spatial domain considered (from 27.50°N to 50.00°N and from -20.0° E to 31.0°E), a relationship between MW-TB (GPM) and IR-TB is determined;
3) geolocation: MSG-RSS data and histograms represent the new input for producing hail maps every 5 minutes all over our domain: an example of this final output is proposed in Figure 5, in which severe hailstorms are developing in northwestern Italy (Fig. 5a) and in the Tyrrhenian Sea (Fig. 5b), both reaching HP values belonging to the Super Hail Category.

The MASHA algorithm logical flux of information is schematized in Figure 6. Further technical details about the MASHA Method can be found in Vermi (2022).

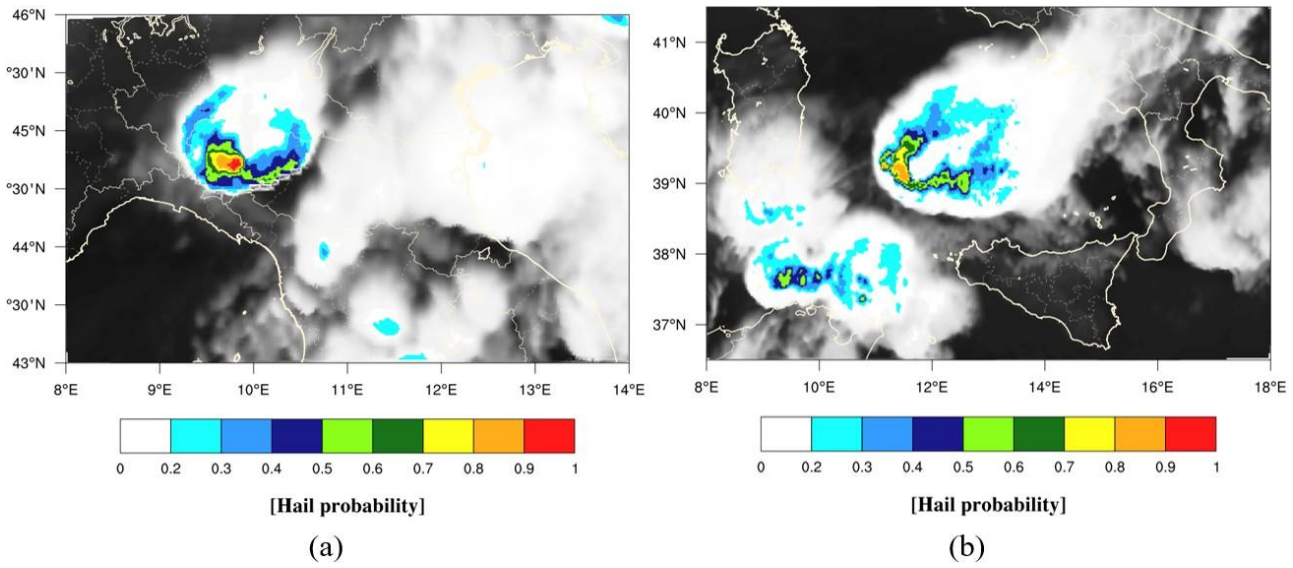

Figure 5. MASHA Method final output, after MWCC-H algorithm calibration provided in Fig. 3. Hail probability maps based on IR-TB are shown for 25 July 2023 at 06:50 UTC (a) and for 04 September 2021 at 01:15 UTC (b).

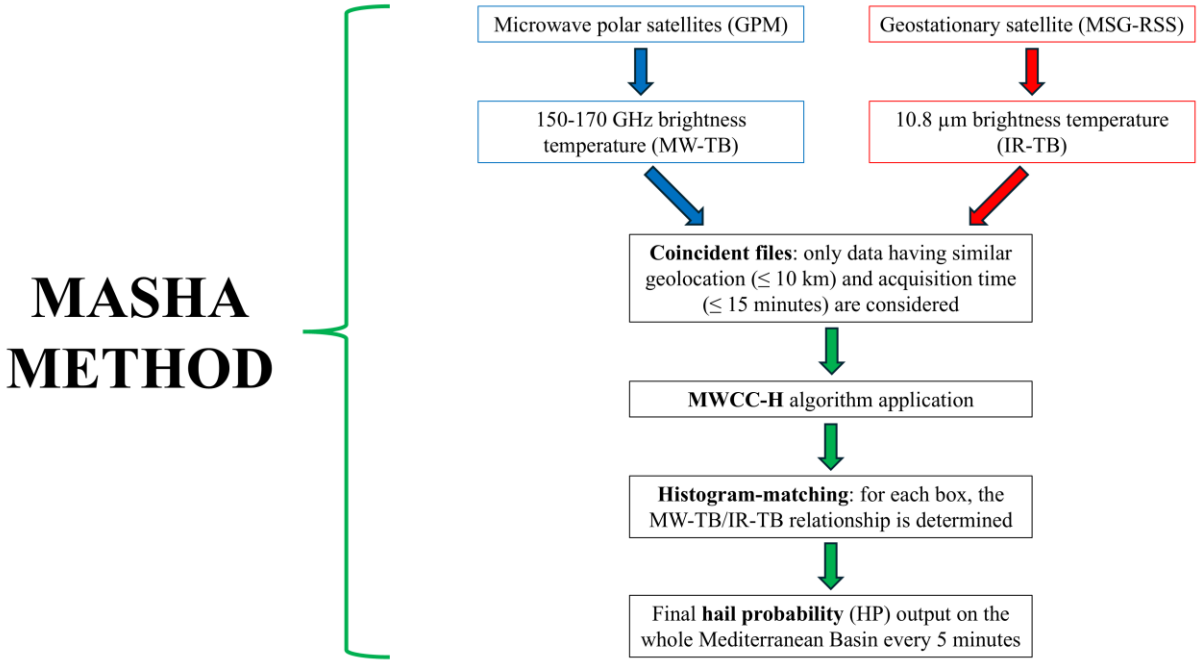

Figure 6. The data flow architecture behind the MASHA Method.

2.2 MASHA Method strengths

In this paragraph, we highlight some of the most important results obtained by exploiting the MASHA Method for the identification and monitoring of the hailstorms:

- HP is computed through the MWCC-H method, a validated algorithm operating in passive microwaves;

- the resulting relationship between MW-TB and IR-TB gives hail indications even when the information provided by polar satellites is not available. In addition, as soon as a new scan from polar satellites is provided in the same area, the calibration operated by the MWCC-H method is immediately updated, exploiting the new microwave sensor overpass;
- the final product is a comprehensive high-space-and-time resolution (5-minute, 6 × 6 km² regular grid) hail probability map, tracking and monitoring hailstorms over the whole Mediterranean Basin area, which can allow us to observe evolving hailstorms on both inlands and sea areas.

In the next two sub-sections, we will explore the main strengths related to the onset of the MASHA Method in quasi real-time.

2.2.1 MASHA Method satellite monitoring of the Mediterranean Basin

Exploiting a spatial domain that goes in latitude from the northern sector of the Sahara Desert (27.50°N) to Central Europe (50.0°N) and in longitude from Atlantic Ocean (-20.0°E) to the west side of the Black Sea (31.0°E), the MASHA Method is able to monitor the hailstorms evolution along almost the entire Mediterranean Basin (except from the southeasterly side), every 5 minutes. Usually, having hail-bearing storms a local-scale extension, hail phenomena as well as damage produced can differ a lot even in the same region or district, making it difficult to understand physical processes. In addition, the lack of observation systems complicates the estimation of hail frequencies and the production of hail climatology maps (Punge and Kunz, 2016). In this sub-section, we will analyze the atmospheric conditions that characterized the European territory from 10 June 2025 to 16 June 2025 focusing on the hailstorms activity, thanks to the HP maps provided by the MASHA Method. Together with them, we will also consider 500 hPa geopotential and sea level pressure reanalysis maps obtained by the NCEP Climate Forecast System Reanalysis (CFSR; Saha et al., 2010; https://www.wetterzentrale.de/de/reanalysis.php?model=cfsr), having a spatial resolution of 0.5°, and hail reports provided by the European Severe Storm Laboratory's European Severe Weather Database (hereafter ESWD, Dotzek et al., 2009; https://eswd.eu/) which is the first european database containing many different severe weather observations, including large hail reports (maximum hail diameter ≥ 2.0 cm). In ESWD, for each hail observation, date, time, latitude, longitude, maximum hail size (cm), pictures, newspaper articles or post by social media are provided. In the framework of our analysis, we will use only hail reports belonging to the two highest quality levels: QC1 ("report confirmed by reliable source") and QC2 ("scientific case study"). During last years, this reliable dataset lead to many studies about hailstorm characteristics, hail frequency and large hail climatology in Europe (Punge et al., 2014; Pilorz, 2015; Punge and Kunz, 2016; Istrate et al., 2017; Kunz et al., 2020; Fluck et al., 2021; Wilhelm et al., 2021; Battaglioli et al., 2023a-b; Hulton and Schultz, 2024; Kahraman et al., 2024).

The analysis of the meteorological situation which characterized the Mediterranean Basin and the European territory can start considering the 500 hPa geopotential and sea level pressure reanalysis map for the 10 June 2025, at 18:00 UTC (Figure 7).

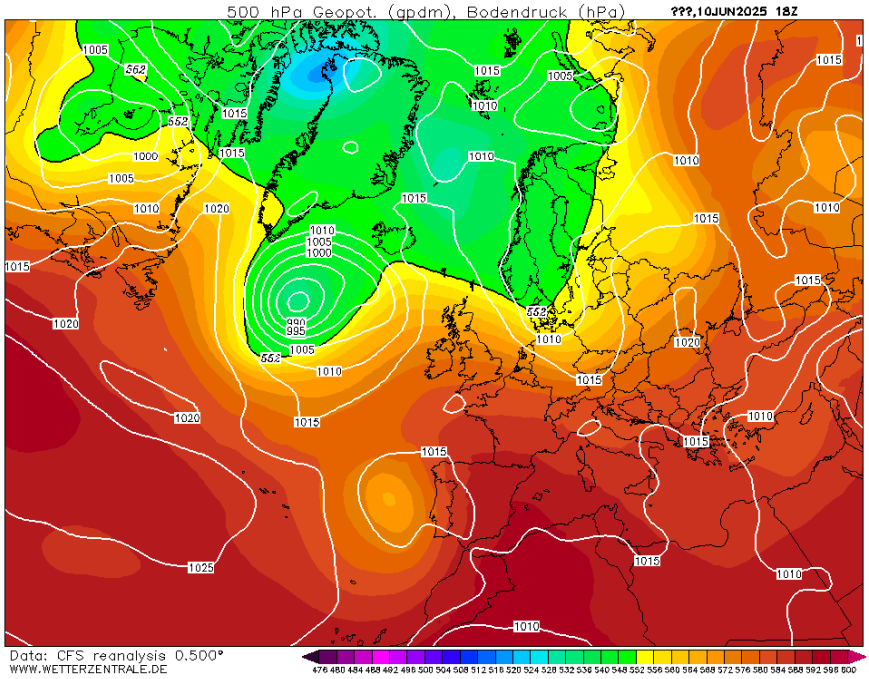

Figure 7. 500 hPa geopotential and sea level pressure reanalysis map on 10 June 2025, at 18:00 UTC (https://www.wetterzentrale.de/de/reanalysis.php?model=cfsr).

If we focus on the Mediterranean region, atmospheric conditions are stable, thanks to the presence of the subtropical high pressure on a great part of this area. However, on the western side, an upper-level low is approaching the Portuguese coastline. Some hours later, the eastern movement of the low-pressure system caused the development of many convective cells on the Iberian Peninsula and some of them were classified by the MASHA Method as hail-bearing storms (i.e. when HP exceeds 0.36, the critical value above which Hail Initiation class is reached, see Table 1). In Figure 8, the HP map produced for 10 June 2025 at 22:00 UTC (for brevity we don't show the entire hailstorm evolution) indicates the presence of evolving hailstorms in the extreme northwestern sector of Portugal, with a maximum HP ranging from 0.50 to 0.59 (light green color in Fig. 8). According to Table 1, these HP values belong to the Hail class, for which the expected hail diameter is between 2 and 10 cm and important damage can be observed during the passing of the hailstorm. After analyzing the ESWD hail reports (green triangles) map (Figure 9a) obtained between 21:30 UTC and 22:30 UTC, we counted 12 hail observations in the corresponding high HP area highlighted by the MASHA Method. Pictures referring to these hail reports are attached to Fig. 9b-c, in which some of the hailstones produced by the examined hailstorm were collected at ground.

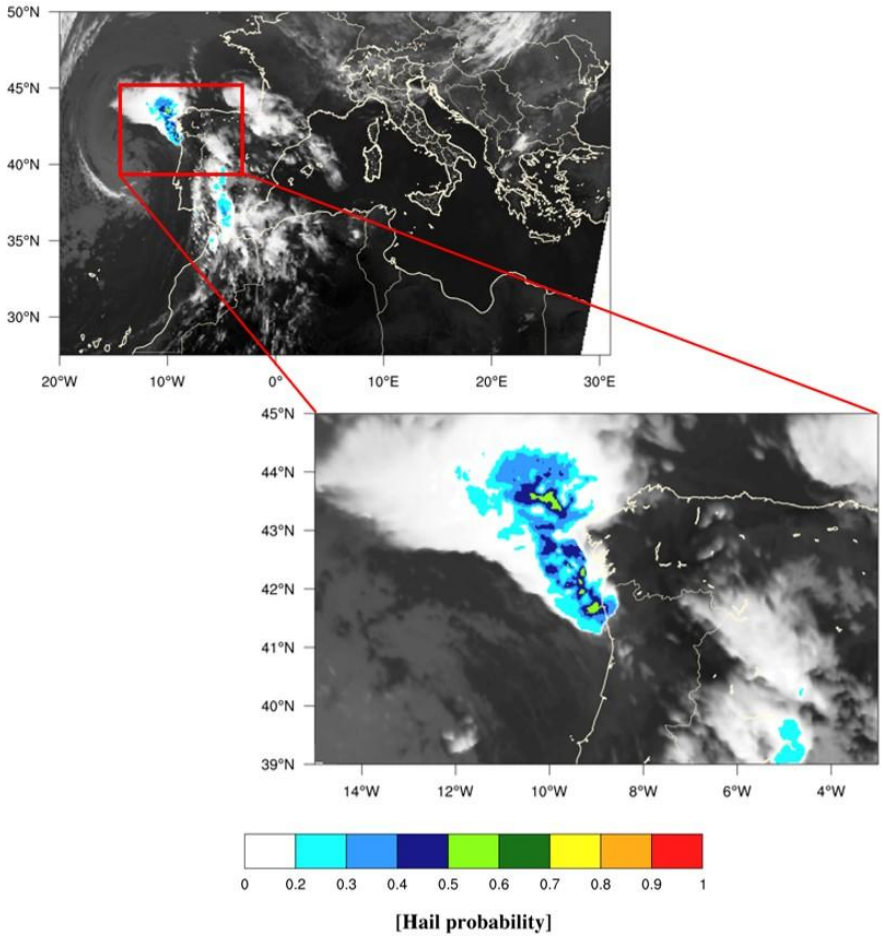

Figure 8. MASHA Method HP map for 10 June 2025, at 22:00 UTC. The zoomed area refers to the northwestern sector of the Iberian Peninsula.

(a) (b) (c)

Figure 9. ESWD hail reports (green triangles) map (a) provided on 10 June 2025 from 21:30 UTC to 22:30 UTC. In (b-c), pictures of hailstones collected are shown (https://eswd.eu/).

Among the hailstones reported, the maximum hail size was equal to 7 cm (Fig. 9b): these dimensions are in accordance with the calibration provided by the MWCC-H method, which predicted maxima HP values in the

Hail class, where the estimation of hail size is between 2 and 10 cm. Going on with the investigation, in Figure 10 we provide the 500 hPa geopotential and sea level pressure reanalysis map for the 13 June 2025, at 18:00 UTC: from the latter, it can be noted that a subtropical ridge is interesting the central part of the Mediterranean basin whereas a low-pressure system is located on the west side of the British Islands and France, evolving easterly in the following hours.

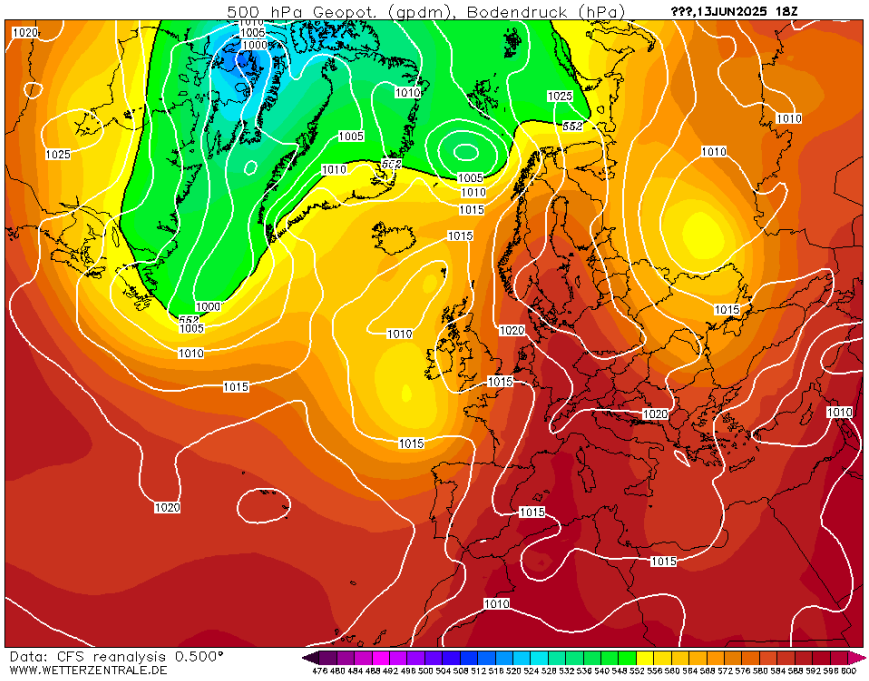

Figure 10. 500 hPa geopotential and sea level pressure reanalysis map on 13 June 2025, at 18:00 UTC (https://www.wetterzentrale.de/de/reanalysis.php?model=cfsr).

This movement brought to the development of several thunderstorms during the afternoon of 13 June 2025 along the Iberian Peninsula, the western sector of France and the British Islands. In particular, the MASHA Method detected many hailstorms evolving from northeastern Spain to northern France: in Figure 11, the HP map is provided for 13 June 2025 at 20:00 UTC. As can be noticed from the zoomed image, two strong hailstorms are identified in northwestern and southwestern sectors of France: for both, HP maxima computed thanks to the MWCC-H calibration oscillate between 0.60 and 0.70, meaning that atmospheric conditions could be favourable to produce even hailstones of maximum size higher than 10 cm (i.e. Super Hail class). In this case, the comparison with the ESWD hail reports map (Figure 12a) showed that more than 200 hail observations were recorded in ESWD database on 13 June 2025 between 14:00 UTC and 21:00 UTC, indicating the very strong hailstorm activity that affected the French territory on that day. In this case, during the hail-falling, hailstones until 9 cm in diameter were detected, confirming the presence of hail-prone atmospheric conditions and of severe hailstorms. In Fig. 12b, pictures of hailstones collected in Bordeaux (southwestern France) were attached to the hail report.

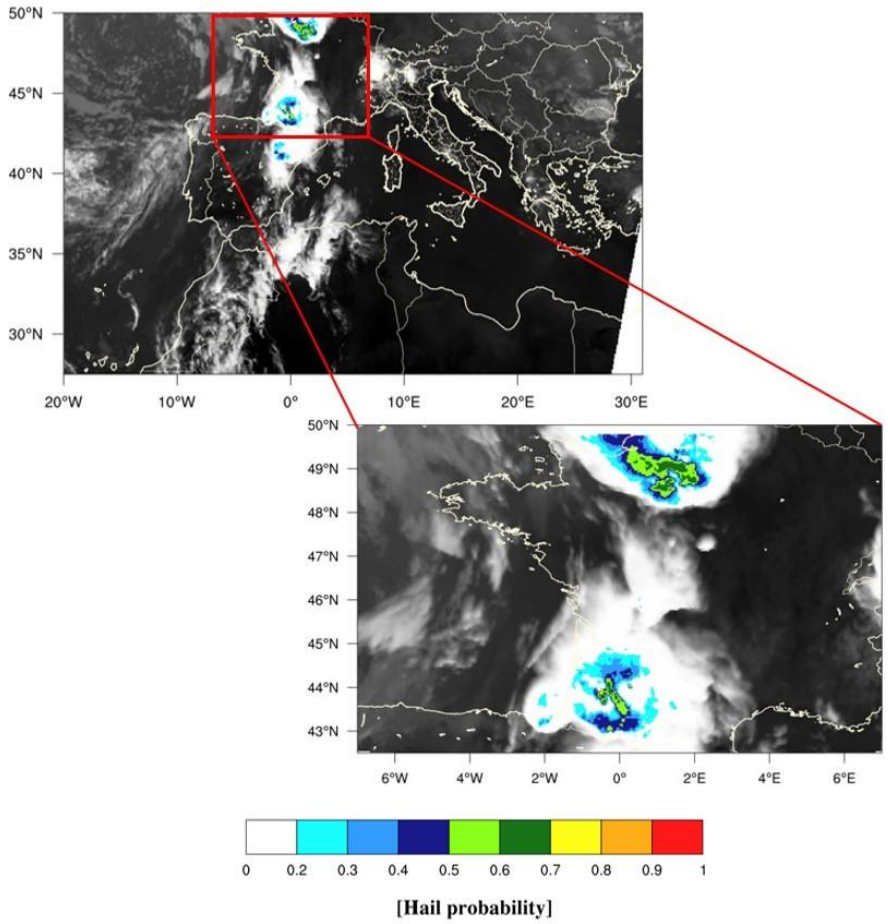

Figure 11. MASHA Method HP map calculated on 13 June 2025, at 20:00 UTC. The zoomed area refers to the French territory.

(a) (b)

Figure 12. ESWD hail reports map (a) for 13 June 2025 from 14:00 UTC to 21:00 UTC (a). In this case, more than 200 hail observations (green triangles) were recorded in France. In (b), hailstones collected in Bordeaux (southwestern France), having a maximum hail size of 9 cm (https://eswd.eu/).

The last case study we analyzed, occurred on 16 June 2025 on the Italian Peninsula: in Figure 13, the 500 hPa geopotential and sea level pressure reanalysis map at 12:00 UTC is provided. The evolving atmospheric

conditions lead to a new reinforcement of the Azores anticyclone in Western Europe, bringing to general stable weather conditions in these areas. On the other hand, a trough positioned along the northern Adriatic Sea, caused the incoming of cooler air currents from Northern Europe, creating an ideal weather situation for the development of strong storm systems.

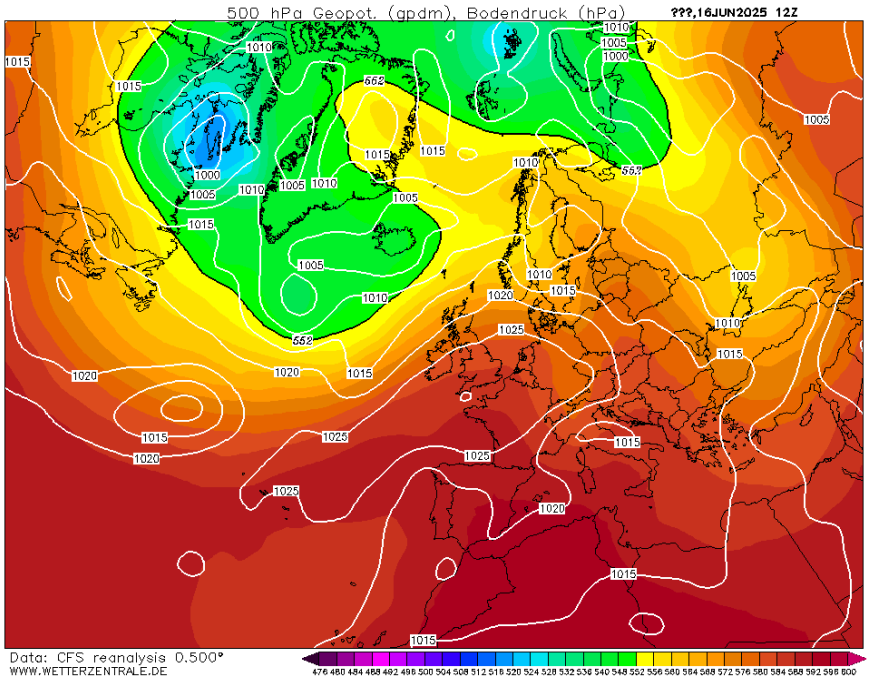

Figure 13. 500 hPa geopotential and sea level pressure reanalysis map on 16 June 2025, at 12:00 UTC (https://www.wetterzentrale.de/de/reanalysis.php?model=cfsr).

From the late morning of 16 June, storm activity was very intense in northeastern Italy and along the Southern Apennine Mountain chain, where many thunderstorms were classified as hailstorms by the MASHA Method. In Figure 14, the corresponding HP map referring to 16 June at 13:25 UTC is provided: the latter depicts many hailstorms especially affecting the Emilia-Romagna region and Northern Apennines areas. Focusing on the zoomed HP map, we can notice that HP maximum values exceed 0.80, meaning that severe hailstorms are developing in the Po Valley. Hail-bearing storms are also identified in correspondence of Southern Apennines, reaching typical HP values belonging to the Hail class. In Figure 15a, the green triangles representing hail reports confirm the presence of two main areas in which hailstorms developed corresponding to northeastern Italy and Southern Apennines. On those zones, from 11:00 UTC to 18:00 UTC, 48 hail observations were recorded, leading to a maximum hail size of 6.5 cm detected in Emilia-Romagna region and of 6 cm in Southern Italy. Again, the comparison between HP values and the distribution of hail reports highlights the good reconstruction operated by the MASHA Method for these case studies characterized by very large hail occurrence. For northeastern Italy, the maximum hail size is slightly lower than expected, but it should be highlighted that these hailstorms had a duration of many hours. So, it can't be excluded that hailstones, even with higher dimensions, affected some rural areas where hail reports are usually underestimated due to the low population density.

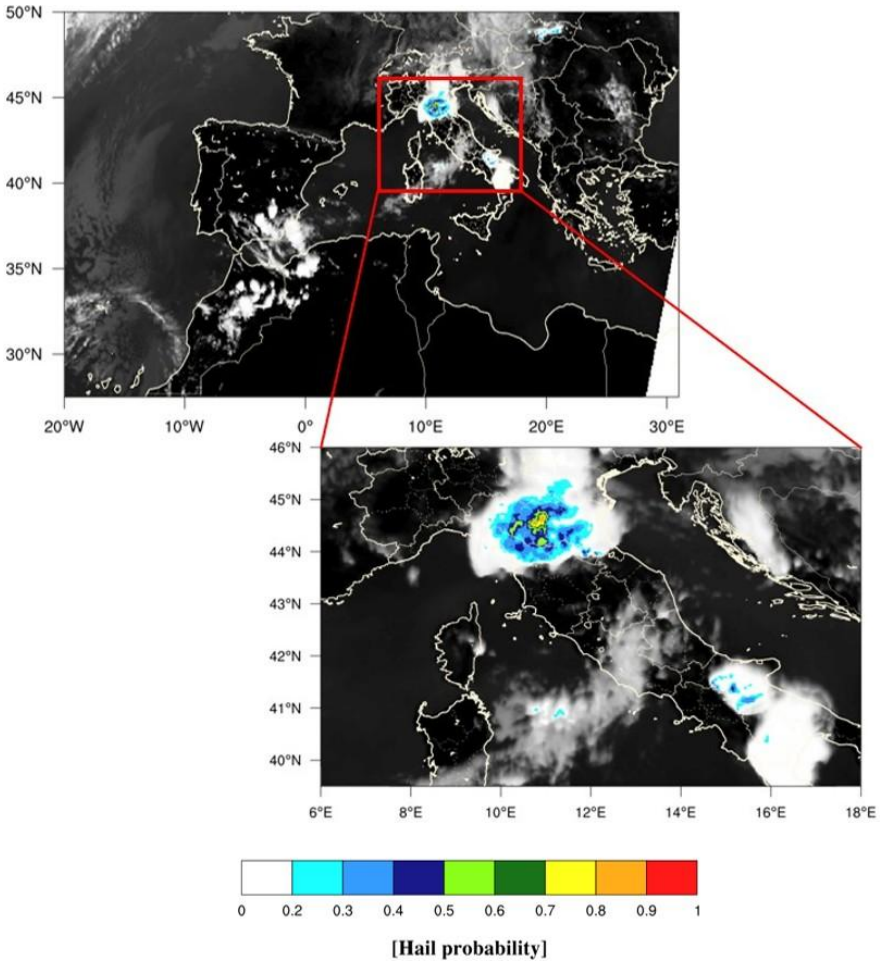

Figure 14. MASHA Method HP map calculated on 16 June 2025, at 13:25 UTC. The zoomed picture highlights hailstorms developing on the Italian Peninsula.

(a) (b) (c)

Figure 15. ESWD hail reports map (a) for 16 June 2025 from 11:00 UTC to 18:00 UTC (a), in which 48 hail observations (green triangles) were recorded along the Italian Peninsula. In (b-c), pictures of hailstones collected in Emilia-Romagna region are provided, having a maximum hail size of 6.5 cm (https://eswd.eu/).

This brief analysis about hailstorms developed during the period from 10 June to 16 June 2025 in some areas of the Mediterranean Basin and on European territory exhibited some key-advantages regarding the satellite

detection of the hailstorms, showing that the MASHA Method can propagate the hail information provided by the MWCC-H Method every 5 minutes, covering the Mediterranean region with a good spatial resolution (i.e. 6×6 km^2 regular-grid). In addition, the MASHA Method can operate in quasi real-time, potentially becoming a very important tool for nowcasting and early warning systems.

Nevertheless, these HP final outputs can be exploited for carrying out some studies about hail patterns characterizing different areas of the Mediterranean basin, with the final aim of producing a complete satellite hail climatology for this region. For instance, considering the MASHA Method run performed from 01 June to 16 June 2025, we analyzed HP data obtained for a smaller domain representing Northern Italy going from 43.75°N to 47.00°N and from 6.60°E to 13.75°E, i.e. the inner part of the red box described in Figure 16. After defining the Northern Italy domain, considering the MSG-RSS native spatial resolution of about 4.8 km and the resulting output provided every 5 minutes, we selected the maximum HP pixel inside this region to understand which days were characterized by severe hailstorms. This choice limits the information about the spatial extension of storm systems but, on the other hand, highlights the most severe hail phenomena potentially developing and affecting the above-mentioned areas. So, the maximum HP pixel selection allows us to build the red curve represented in Figure 17a, showing the maximum HP trend from 01 to 16 June for Northern Italy domain. In this panel, maximum hail probability is depicted as a function of time while four light blue, blue, gold and purple-colored horizontal lines represent the point at which Hail Potential, Hail Initiation, Hail and Super Hail classes begin, respectively. In the first five days, HP maxima oscillated between Hail Potential and Large Hail classes, reaching very rarely the latter. These trends were mainly related to afternoon orographic convection (HP maxima peaks are often in the middle of the day) especially in the Alpine region, which caused the development of not very impacting storms.

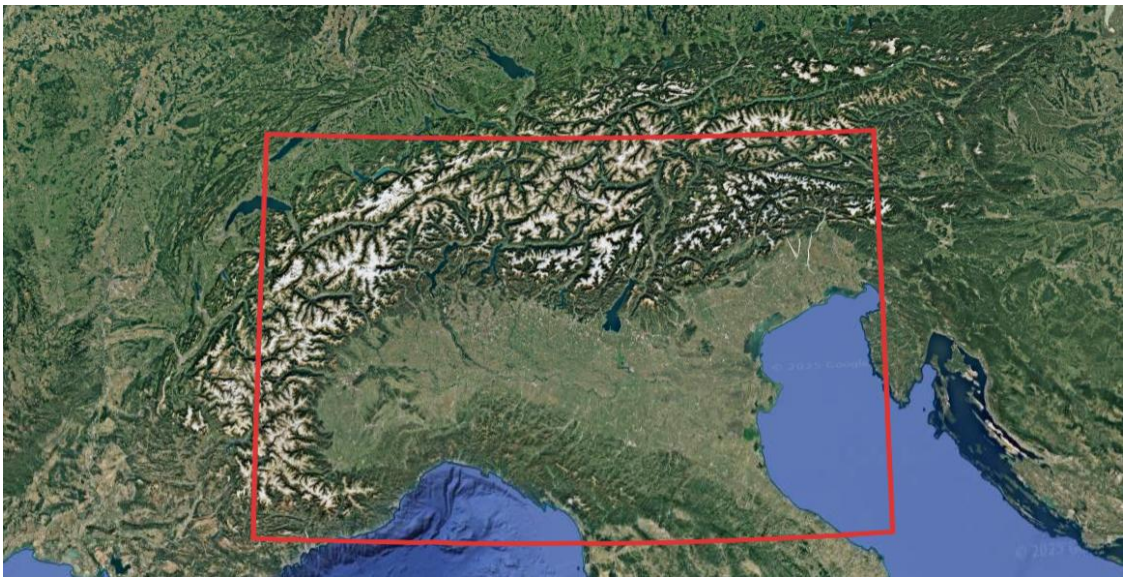

Figure 16. The red box surrounds the Northern Italy domain ranging from 43.75°N to 47.00°N and from 6.60°E to 13.75°E (Images credit: © Google Earth, Data Sio, NOAA, U.S. Navy, NGA, GEBCO).

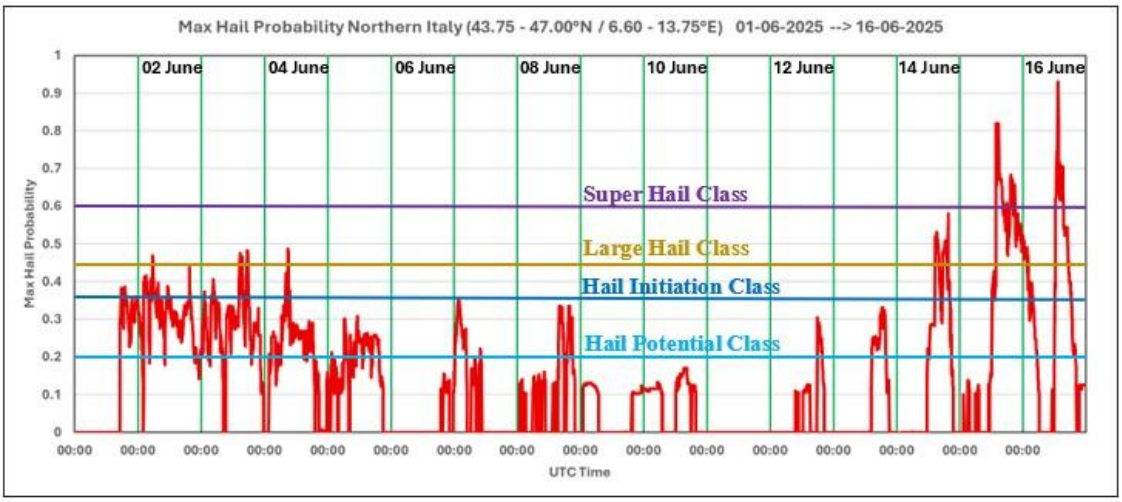

(a)

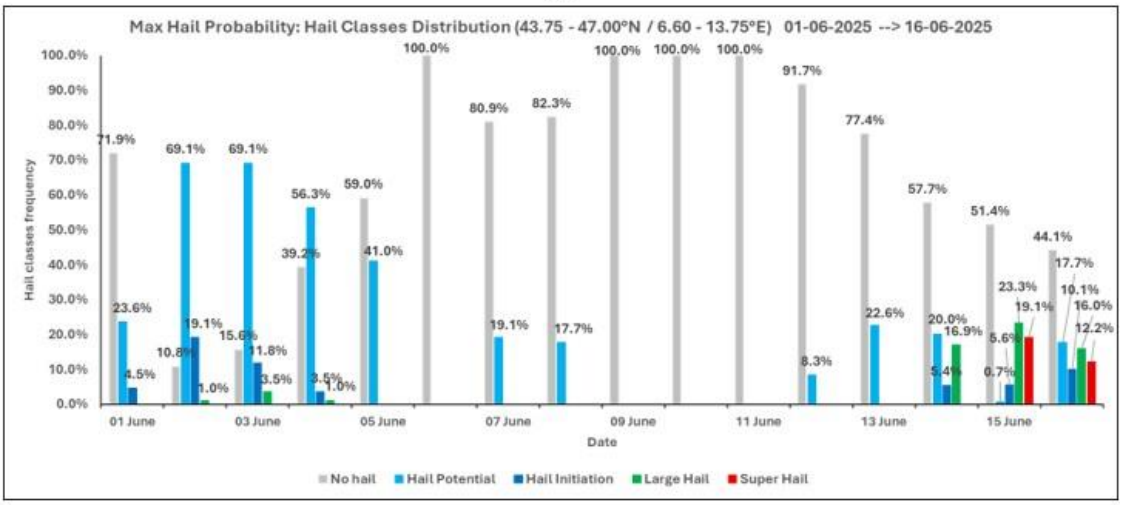

(b)

Figure 17. Maximum HP trend (red curve) from 01 to 16 June 2025 in Northern Italy (a) and distribution of maximum HP pixel depending on five hail categories (b).

From 06 to 13 June, the reinforcement of the subtropical high pressure increased the stability of the atmospheric conditions, leading to a general decrease in HP maxima, which in some days didn't even reach the Hail Potential threshold class. Finally, starting from 14 June, the progressive approach to Northern Italy of a low-pressure system gradually brought to the rise of HP maxima, which reached their peak and Super Hail category on 15 and 16 June. In Fig. 17b, we provide the distribution of the maximum HP in the five different classes from 01 to 16 June, in terms of frequency of the pixel. Labeling the frequency of maximum HP pixel above each column, this graph highlights the distribution of HP maxima as a function of the five hail categories: as said above, on some days (i.e. 06-09-10-11 June) the No Hail class reaches a frequency of 100%, whereas during 15 and 16 June even the Super Hail category appears (red bars).

2.2.2 Monitoring hailstorms in the Mediterranean Sea

Another MASHA Method key-advantage is represented by the satellite monitoring of hail-bearing storms in the Mediterranean Sea, where for instance other hail tools such as radar-based ones, cannot provide reliable hail information far from the coastline. In this sub-section, we will briefly show how the MASHA Method can contribute following the evolution of "medicanes" (from *Medi*terranean hurri*canes*), that is one of the most impactful atmospheric phenomena in the Mediterranean Basin. Medicanes are "Mediterranean tropical-like cyclones", warm-core cyclones that occasionally put in danger the islands and coastal regions. Despite large geographical differences between the Mediterranean Sea and the tropical oceans, their genesis mechanisms, based on the thermodynamical disequilibrium between the sea and the atmosphere, are similar (Tous and Romero, 2013). Owing to their potential destructiveness on the islands and continental coastal zones, medicane risk assessment is of paramount importance (Romero and Emanuel, 2013). Cavicchia et al. (2014) stated that medicanes occur with a very low frequency (about 1.6 per year over the whole Mediterranean basin) and that they are formed mostly in the western Mediterranean and in the region extending between the Ionian Sea and the North-African coast. The formation of medicanes exhibits a peculiar seasonal cycle, characterized by a peak at the beginning of winter season. However, the year-to-year variability is strong, but no significant trend is found in the last 60 years. In addition, Cavicchia et al. (2014) found that the triggering of medicanes is characterized by the presence of cold temperature anomalies in the high troposphere that increase the atmospheric instability. A low wind shear, high moisture content, and high low-level vorticity are all factors that favor the development of medicanes (Miglietta et al., 2025).

In Figure 18a-h, MASHA Method HP maps (one per day) are proposed for the Daniel medicane evolution, which lasted for six days (from 04 to 09 September 2023) in the Mediterranean Sea, before crossing northern Libya and then decaying over Egypt between 10 and 11 September 2023. Hewson et al. (2024) studied the trajectories of Daniel medicane stating that during Daniel development as a discrete cyclone, extreme rainfall/flooding over Bulgaria, Turkey and Greece occurred while flood devastation over Libya was much more directly related to Daniel's passage. Results obtained by MASHA Method confirm this medicane evolution in terms of HP: from 04 September (Fig. 18a, 20:40 UTC) the hailstorm activity mainly involved Greece, Turkey and Bulgaria, in which the following day (e.g. Fig. 18b, 05 September at 22:55 UTC) HP values reached the Super Hail category. On 06 September, the HP pattern partially decreased in intensity, but hailstorms continued affecting the same areas, even including Southern Italy (e.g. Fig. 18c, 16:45 UTC) where thunderstorms were less severe, until the first part of the next day. From 07 September afternoon (e.g. Fig. 18d, 17:20 UTC), hailstorms associated with Daniel medicane fully developed on the sea surface, again reaching HP values belonging to Super Hail class in more than one storm system. The hailstorms activity went on the Mediterranean Sea for the next two days, in which the intensity of the hailstorms was more related to Large Hail class (Fig. 18e, 08 September at 17:50 UTC and Fig. 18f, 09 September at 14:40 UTC).

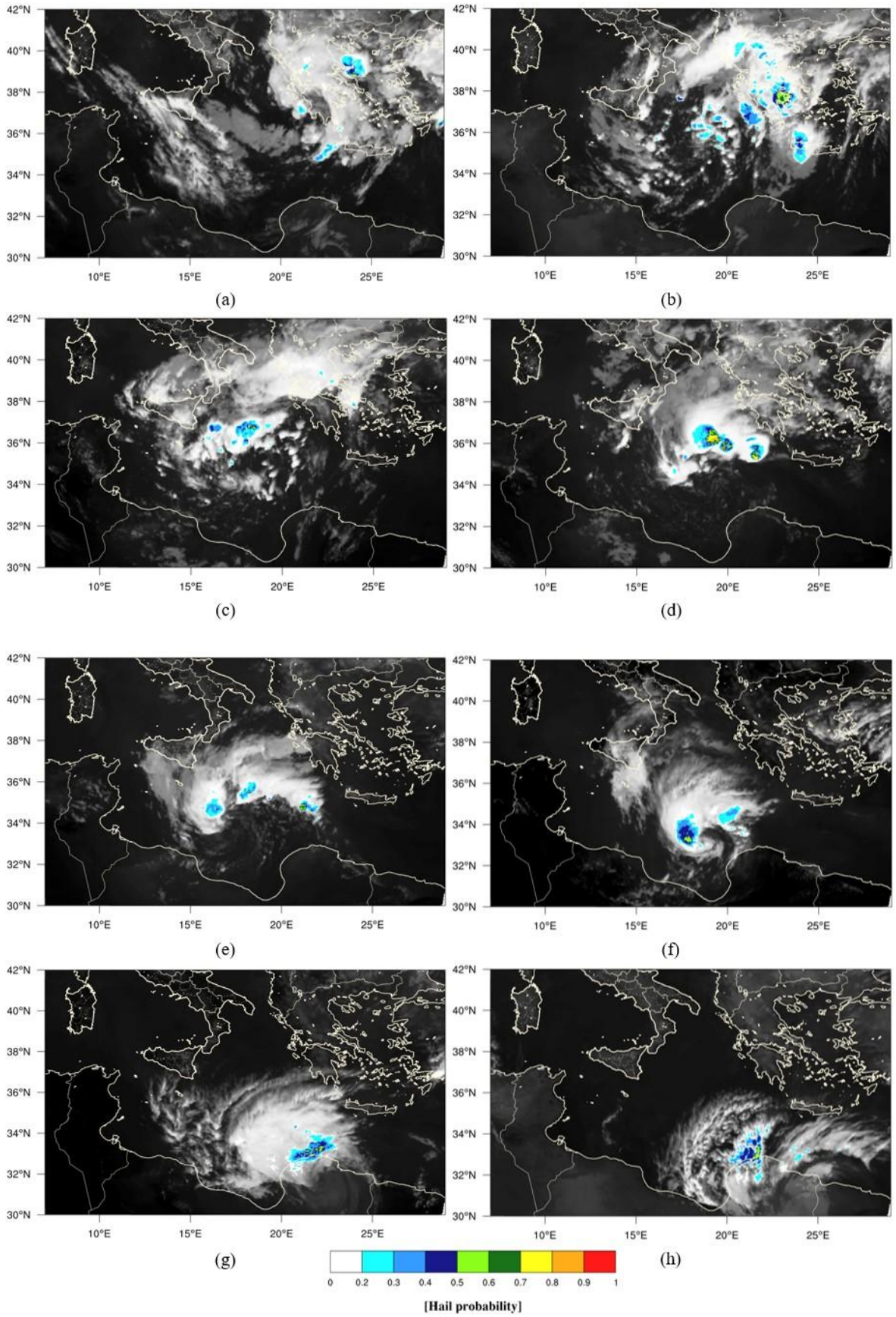

Figure 18. MASHA Method HP maps for Daniel medicane from 04 to 11 September 2023 (one per day, a-h) at 20:40 UTC (a), 22:55 UTC (b), 16:45 UTC (c), 17:20 UTC (d), 17:50 UTC (e), 14:40 UTC (f), 16:20 UTC (g) and 04:55 UTC (h), respectively.

Starting from the 10 September first hours, storm activity originally affected the Libyan coastline (Fig. 18g, 16:20 UTC) and, from 10 September evening, even Libyan inland areas until the first part of the following day (Fig. 18h, 04:55 UTC). Finally, Daniel dissipated over Egypt during the second part of 11 September. Being the great part of storm activity on the Mediterranean Sea, we don't have reports available about potential hail phenomena occurred in that area. Therefore, to analyze the hailstorms that happened from 04 to 11 September, we applied the same analysis explained in Section 2.2.1, based on the maximum HP pixel in a spatial domain going in latitude from 30.00°N to 42.00°N and in longitude from 10.00°E to 26.00°E (Figure 19).

Figure 19. The red box surrounds the Daniel medicane area of interest between 04 to 11 September 2023, ranging from 30.00°N to 42.00°N and from 10.00°E to 26.00°E (Images credit: © Google Earth, Data Sio, NOAA, U.S. Navy, NGA, GEBCO).

In Figure 20a, we show the maximum HP trend (red curve) for the period of time examined. From this panel, it emerges that a very high hailstorm activity was associated with the Daniel medicane: considering the maximum HP pixel, we can notice that No Hail class was never interested by HP maxima if we exclude the first part of 04 September and the second part of 11 September 2023. Something similar can be said about the Hail Potential class, which was mainly involved only during the 04 September. So, as a first approximation, we can state that the HP maxima were always above 0.36, meaning that HP values ranged from Hail Initiation to Super Hail class for 7 consecutive days. In particular, on 05 September and again from 07 to 08 September, maximum HP values remained in the Super Hail Category for several consecutive hours, highlighting extreme weather conditions affecting some areas of the examined study area. In Fig. 20b, the frequency of HP maxima has been computed considering two different groups: the first one (blue columns) includes the sum of the

frequency of No Hail, Hail Potential and Hail Initiation classes while red columns represent the sum of Large Hail and Super Hail categories.

(a)

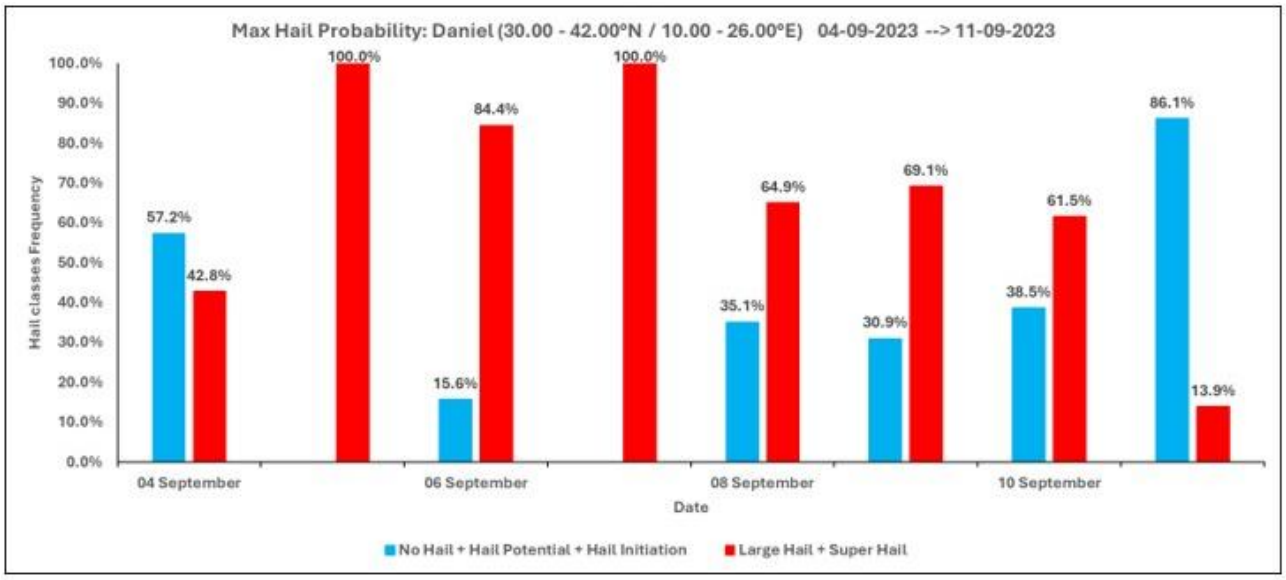

(b)

Figure 20. Maximum HP trend (red curve) related to the Daniel medicane from 04 to 11 September 2023 (a) and distribution of maximum HP pixel depending on less (No Hail, Hail Potential and Hail Initiation) or more severe (Large Hail and Super Hail) hail categories (b).

This plot highlights impressive results we found related to hailstorms development linked to Daniel medicane: indeed, for most of the days going from 05 to 10 September, Large and Super Hail dominated in terms of maximum HP pixel and it was even more clear between 05 and 07 September. From this plot, only during 04 and 11 September hail phenomena were more related to the three less severe categories. This brief analysis shows preliminary but very interesting results about the development of hailstorms in medicanes. Considering

the lack of previous works on this topic in literature, the MASHA Method opens new perspectives about the study of hail phenomena associated with medicanes and a new way to track these dangerous weather events in the Mediterranean Sea, where other hail detection tools cannot monitor the potential occurrence of hailstorms.

2.3 MASHA Method limitations

After giving an overview of the MASHA Method strengths related to the detection of hailstorms in Mediterranean Basin, in this paragraph we introduce the two most important limitations linked to the HP computation in the MASHA Method final output:

1) when recent GPM-overpasses are not available, MASHA Method makes use of an "old" GPM-calibration provided by the MWCC-H algorithm: depending on that case by case, it can lead to a general underestimation of the final HP;
2) overshooting area: for deep convective storm systems characterized by overshooting top, the cloud top of this region is warmer than the surrounding areas. Consequently, the hail probability computed is lower than expected.

In the next two sub-sections, we will discuss these two main drawbacks that contribute to decrease the HP estimation, affecting the final result computed by the MASHA Method.

2.3.1 MASHA Method space-time limited calibration

The first problem related to the underestimation of HP regards the space-time frequency of polar satellites overpasses. As already mentioned in Section 2.1, microwave sensors are the best for detecting hailstorms, thanks to the interaction that occurs between ice crystals, graupel and hailstones and microwave electromagnetic waves. However, these sensors are limited in space and time because every scan covers only some portions of sea/land and time frequency is irregular and depends on the polar orbit performed by each sensor. For these reasons, the extension of the MWCC-H algorithm to all sensors of the GPM constellation operating within the 150–170 GHz frequency range improved the identification of the hailstorms but, even in this way, some areas can remain uncovered for some hours. In Figure 21a-c, we show what can happen when the MWCC-H algorithm doesn't provide an updated calibration to the MASHA Method in a determined region. In Fig. 21a (top right) and Fig. 21c (bottom right), we propose the MASHA Method HP output computed on 02 August 2024 at 16:40 UTC (a) and 16:45 UTC (c), respectively. In the central part on the left (Fig. 21b), the MWCC-H HP output obtained by the F17 sensor (SSMIS) scan between the 16:40 UTC and 16:45 UTC is shown. As a result, for the areas depicted in Fig. 21a-c, the MWCC-H algorithm provides a new HP calibration thanks to the F17 sensor overpass. Starting from this situation, it is interesting to analyze what happens in two areas highlighted by the red (northwestern Italy) and orange (Slovenian territory) boxes: in the latter, some thunderstorms have been classified as hailstorms by the MASHA Method, as visible in Fig. 21a.

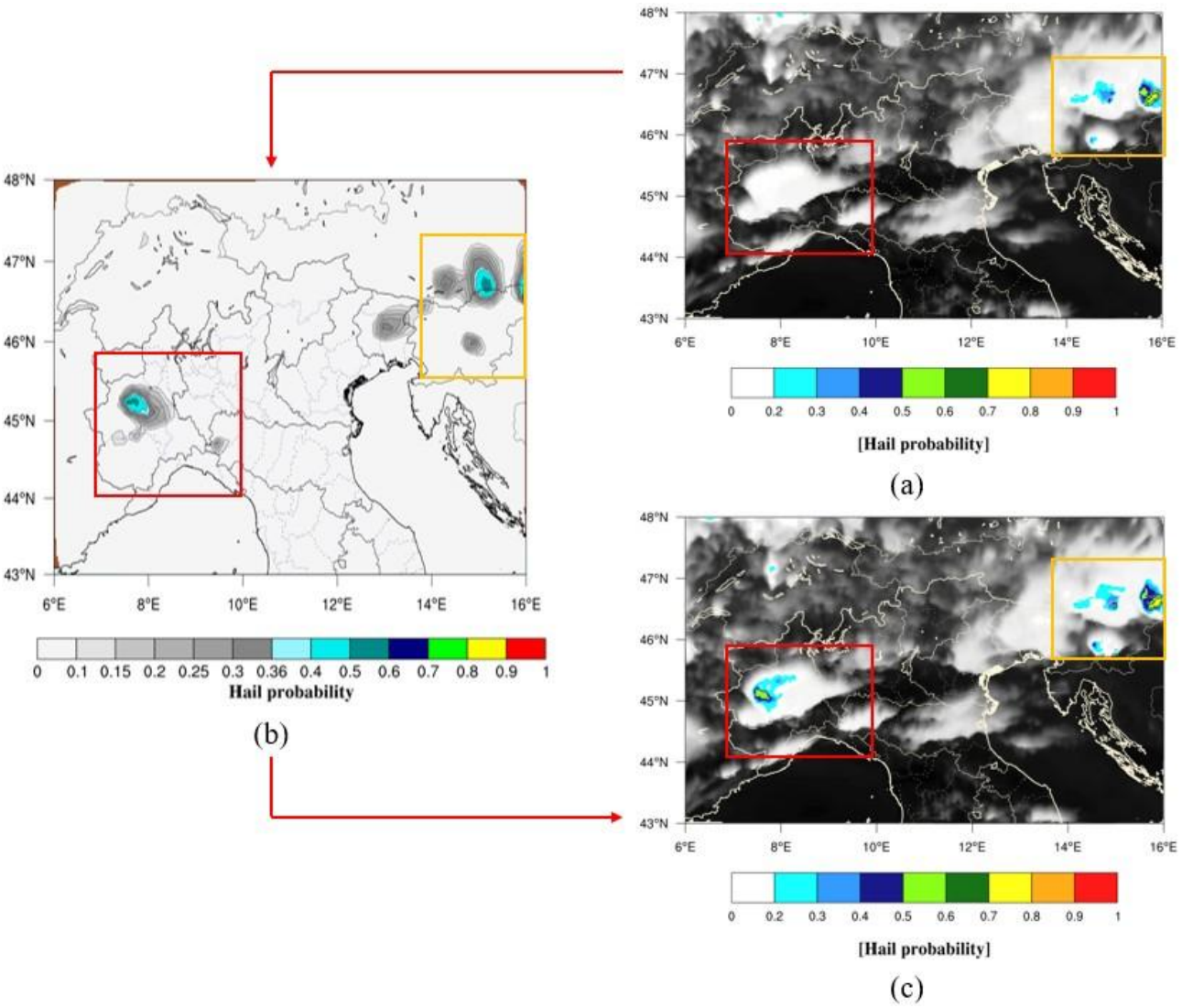

Figure 21. MASHA Method HP output for 02 August 2024 at 16:40 UTC (a) and at 16:45 UTC (c) and MWCC-H algorithm output computed thanks to the F17 (SSMIS) sensor overpass.

After the F17 sensor calibration has been assimilated (between 16:40 UTC and 16:45 UTC) into the MASHA Method, the first new HP output is represented in Fig. 21c, where it can be seen that hailstorm patterns have been slightly modified according to the new MWCC-H algorithm calibration, but the difference in terms of HP values is minimal if compared to the previous five-minute HP map (Fig. 21a). It means that, in this region, the MASHA Method was already well calibrated and hailstorm pattern modifications passing from Fig. 21a to Fig. 21c had low impact in terms of HP range. Now, if we move to the red box in northwestern Italy, we can observe that the situation is quite different: indeed, in Fig. 21a, we can notice that storms having low IR-TB (indicated by white pixels) are not flagged by significant HP values, meaning that the MASHA Method is assigning the No Hail class to these thunderstorms, with maximum HP below 0.20. However, five minutes later, HP values sharply increase reaching a maximum value equal to 0.56 (light green color in red box in Fig. 21c), according to MWCC-H calibration computed thanks to the F17 sensor overpass between 16:40 UTC and 16:45 UTC in northwestern Italy. This wide variation of the hailstorm pattern is not due to a fast change in the

severity of the storm, but it completely depends on the polar satellite passage, indicating that potential developing hailstorms occurred in last minutes or hours (depending on when the last polar sensor passed in that area) were not correctly detected. To check the potential underestimation of HP in the red box, we looked for any hail reports recorded in ESWD in the previous hours. Given that the MASHA Method didn't classify hailstorms in the previous hours in the red box, from the ESWD hail reports map we found one hail report (green triangle in Figure 22a) recorded in Turin (Piemonte region) on 02 August at 15:45 UTC (± 5 minutes), with hailstones having maximum size of 7 cm (Fig. 22b). This report confirmed that the MASHA Method underestimated the HP pattern in northwestern Italy for some hours, during which even large hail was detected, due to the lack of recent calibrations provided by the MWCC-H algorithm.

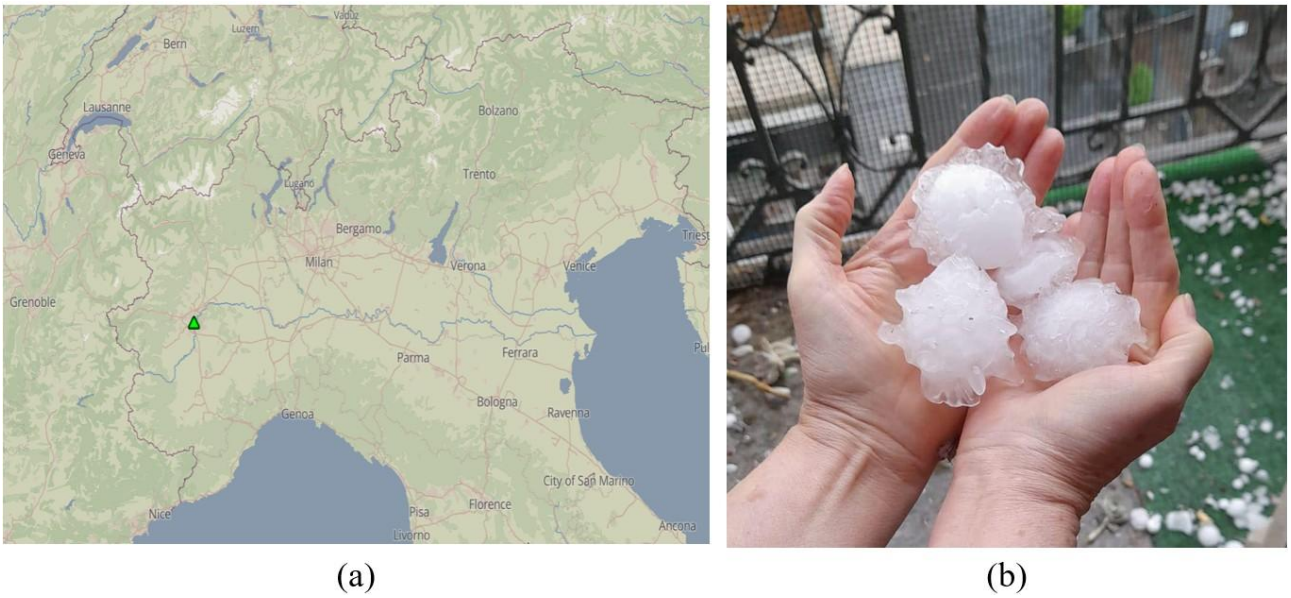

Figure 22. ESWD hail reports map for 02 August 2024 from 14:00 UTC to 16:30 UTC (a). In (b), pictures of hailstones collected in Turin (Piemonte region) are provided, having a maximum size of 7 cm (https://eswd.eu/).

This first limitation is strongly related to the spatial and temporal frequency of polar satellite overpasses, which can cause an important underestimation of the HP pattern computed by the MASHA Method. This problem cannot be directly solved, depending on the orbit performed by these satellites themselves. Thus, to overcome this limitation, during this PhD research project, a new neural network-based method was developed for recognizing geostationary satellite IR-images. This study and preliminary results of this new technique will be discussed in Section 2.4.

2.3.2 Underestimation of HP in hailstorm overshooting top regions

The second problem regarding the underestimation of HP is linked to a particular structure known as "overshooting top", that is usually observed in deep convective hailstorms. An overshooting convective cloud

top is defined by the American Meteorological Society's Glossary of Meteorology (Glickman, 2000) as "a domelike protrusion above a cumulonimbus anvil, representing the intrusion of an updraft through its equilibrium level". Overshooting tops (hereafter, OTs) indicate the presence of a deep convective storm with an updraft of sufficient strength to penetrate through the tropopause and into the lower stratosphere (Bedka et al., 2010). Deep convective clouds with OT were detected in MSG-SEVIRI data, using methods based on the infrared window (10.8 μm) channel and absorption channels of water vapor (WV, 6.2 μm), ozone (O_3, 9.7 μm) and carbon dioxide (CO_2, 13.4 μm) in the form of TB differences (e.g. Mikuš and Mahović, 2013; Jurković et al., 2015) leading to the overshooting index (hereafter, OI) computation. Into the MASHA Method, OI is expressed in K and is computed as the difference between the TB at 6.2 μm (hereafter, $TB_{6.2}$) channel and TB at 10.8 μm (hereafter, $TB_{10.8}$) channel in the following way:

$$OI = TB_{6.2} - TB_{10.8} \tag{4}$$

Since the troposphere cools with increasing altitude, Equation (4) shows that under ordinary conditions the $TB_{10.8}$ is much higher than $TB_{6.2}$ (see Fig. 4 in Section 2.1) and therefore the OI is strongly negative, often with values lower than –50 K. In the presence of clouds with varying vertical development, $TB_{10.8}$ corresponds to radiation emitted from the cloud top instead of from the earth's surface. In the water vapor band, the detected radiation originates from moisture located above the cloud top. Consequently, as the cloud top rises further into the upper troposphere, the radiation reaching the satellite decreases more rapidly in the window channel than in the water vapor channel, and the OI, while remaining negative, approaches zero. However, the most relevant aspect of this behavior occurs in the lower stratosphere. Here, the temperature profile inverts, with temperature increasing with height. When the updraft is particularly intense, water vapor is forced upward into the lower stratosphere by the overshooting top. In this specific case, the water vapor emits at higher temperatures than those observed in the window channel, and the OI may become positive, thus identifying the region where the overshooting top is located (Bedka et al., 2010). In conclusion, an OI value greater than zero can be considered indicative of deep convective systems and the presence of one or more overshooting tops, representing a potential proxy for hail detection (Bedka et al., 2010; Mikuš and Mahović, 2013; Punge et al., 2017; Giordani et al., 2024). Even if OI can represent an important proxy for hail detection, on the other hand it can affect the MASHA Method correct classification of the hailstorms through the HP computation. Indeed, after each MWCC-H algorithm calibration, the MASHA Method propagates in time the hail information thanks to the relationship between MW-TB and IR-TB, in which the lowest IR-TBs are coupled with the highest HP values obtained by the MWCC-H algorithm. However, in the OT region the temperature grows with altitude, but the MASHA Method does not correctly interpret this phenomenon. As a result, for severe hailstorms that arrive in stratosphere, the cloud top of this region is warmer than the surrounding areas and, consequently, the final HP is lower.

For better understanding what happens during the MASHA Method HP allocation in presence of OT regions, in Figure 23a-c we propose the atmospheric situation occurred on 24 July 2023 at 19:05 UTC in Northern Italy,

when three severe hailstorms were crossing the pre-Alpine area, moving eastward. In Fig. 23a (top left) and Fig. 23c (bottom center), $TB_{10.8}$ (ranging from 190 K to 226 K) and OI (ranging from -1.5 K to 10.0 K) maps are provided: for both, not colored portions are associated with areas having $TB_{10.8}$ > 226 K and OI < -1.5 K, respectively. In Fig. 23b (top right), HP map computed by MASHA Method is depicted: from the latter, it is possible to notice three severe hailstorms characterized by HP values between Large and Super Hail categories, all showing a central part (i.e. the OT region rounded by a red circle or ellipse) in which HP is much lower and almost always in the No Hail class.

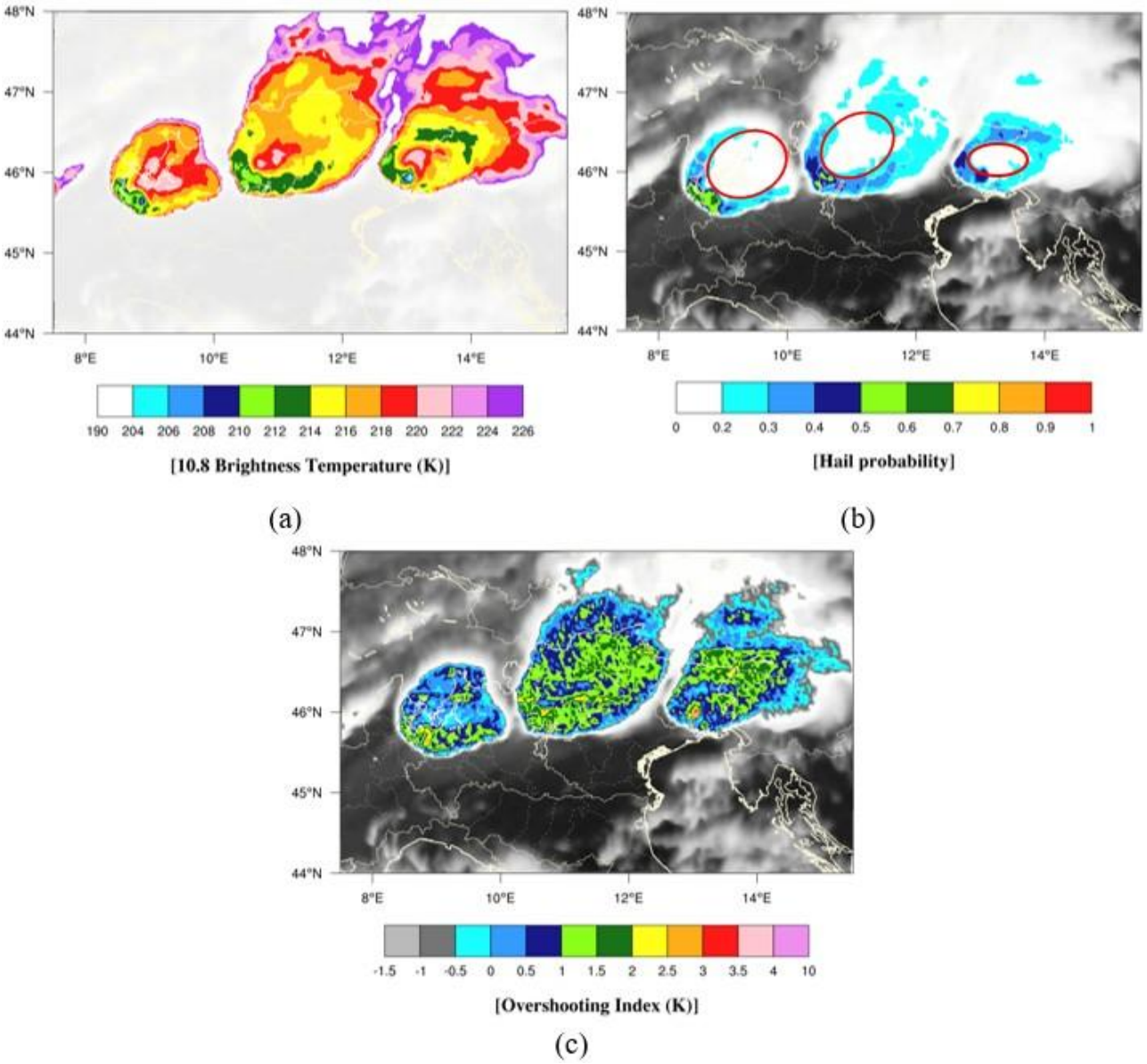

Figure 23. $TB_{10.8}$ (a, top left), HP (b, top right) and OI (c, bottom central) maps for 24 July 2023 at 19:05 UTC in pre-Alpine region are provided. In (b), red circles or ellipses surround the OT region.

The reason why it happens can be found in Fig. 23a: here, in the middle of the hailstorms, we see the formation of a pink colored warmer area ($TB_{10.8}$ reaches 220 - 222 K), in correspondence of OT. This region is rounded

in almost all directions by lower $TB_{10.8}$ values, easily reaching 214 K - 216 K (yellow zones), but occasionally decreasing even below 210 K (blue and light blue areas). Therefore, the development of an OT structure can drastically reduce the HP predicted by the MASHA Method in a wrong way, not being directly linked to the decreasing of the cloud top altitude. In the same way, the OI computation defines boundaries of these storm systems (Fig. 23c), but the OI ranging from -0.5 K to 4.0 K covers a much wider portion of area, without showing a clear relationship with the above-mentioned warmer zones located in correspondence of OT region. This example highlights how the resolution of the HP underestimation in OT regions is tricky and cannot be limited to the OI computation. However, Jurković et al., (2015) stated that the spatial distribution of lightning generally coincides with the spatial distribution of the detected OT. In addition, they found that lightning activity showed a similar temporal distribution, with an increase in lightning activity evident at or close to the time of the OT detections. Mikuš and Mahović (2013) stated that in most of analyzed cases, sharp increase of lightning activity and larger values of the electric current are evident at the time of the OT detections and the total number of lightning strikes sharply increases with the beginning of the hail-shower. Furthermore, Wapler (2018) confirmed that lightning density of thunderstorms with overshooting tops is much larger when compared to thunderstorms without OTs. These findings testify an important relationship between lightning activity and OT detection both in spatial and intensity terms and encouraged us to better explore the role of lightning activity in hailstorms during this PhD research project. The main idea was trying to understand if lightning strikes could represent an opportunity to improve the detection of the hailstorms and the HP pattern computed by the MASHA Method. Starting from Chapter 3, we will discuss in detail this topic and the potential connections with hailstorms and their severity.

2.4 Overcoming space-time limitations related to MWCC-H algorithm: using a ResNet-50 model to improve the detection of the hailstorms in the Mediterranean region

In this Section, we introduce a new neural network-based approach for recognizing developing hailstorms from satellite IR-images, to fill the spatial and temporal gaps that occur between two polar satellite overpasses. The following study has been carried out during the three-months period spent abroad at University of Cologne, as planned by the PhD program.

2.4.1 Introduction

Hailstorms represent an important meteorological risk in the Mediterranean region and their detection and classification is crucial for understanding severe weather patterns and improving early warning systems. Starting from the MASHA Method, conceived for the real-time detection and advection of hail clouds (Laviola et al. 2022b), the latter was applied using deep learning models to avoid some problems related to the

calibration of the algorithm and for extending the tracking of the hailstorms even outside the Mediterranean region. Indeed, the whole GPM constellation (polar satellites) acts as a calibrator through the MWCC-H Method (Laviola et al. 2020a; Laviola et al. 2020b) to recognize the hailstorms in the Mediterranean basin. The resulting relationship between MWCC-H and the MSG-RSS gives hail indications even when the information provided by polar satellites is not available. The final product is a comprehensive high-space and time resolution (5-min, 6x6 km² regular grid) hail map extremely useful to track the evolution of hail clouds in order to better anticipate the hazard and associated impacts. Hail maps are produced using a hail probability range that moves from 0 to 1: higher values signal an increased probability of large hail and severe phenomena.

In this project, we explore the use of a ResNet-50 deep learning model to classify hailstorms based on satellite IR-images, exploiting a binary classification approach ("YES Hail" vs "NO Hail" class). The final goal of this work is to extend this configuration to a deep learning model able to recognize and monitor the hailstorms, being independent from polar satellite overpasses (whose observations are not regular in time and space), thanks to the neural network training performed on a large dataset.

2.4.2 Data and Methods

2.4.2.1 Data sources

This study exploits two main types of satellite data:

- polar orbiting satellites (e.g. GPM constellation): equipped with passive microwave radiometers operating in the 150–170 GHz range. These are used to compute hail probability through the MWCC-H algorithm, which converts microwave brightness temperature values into a continuous hail probability score (HP), ranging from 0 (clear sky) to 1 (high probability of severe hail);
- geostationary satellites (MSG-2, MSG-3): provide continuous IR imagery (10.8 μm channel) every 5 minutes through the Rapid Scanning Service (RSS).

However, the 10.8-IR channel gives out information only about the cloud top height: for this reason, we need to build a new dataset labeling IR-images with microwave sensors. The MWCC-H algorithm defines five hail classes that, in this project, have been remapped into a binary classification (Table 2):

- "NO Hail" class: $0.00 \leq HP < 0.36$;
- "YES Hail" class: $0.36 \leq HP \leq 1.00$.

Table 2. Five hail classes are defined by the MWCC-H algorithm in which hail probability (P) goes from 0 to 1. For each hail class, the potential diameter of the hailstones is reported. In this project, native hail classes have been reorganized into a binary classification: "NO Hail" contains the hail probability ranging between 0 and 0.36 while "YES Hail" class goes from 0.36 to 1.00.

	No Hail	Hail Potential	Hail Initiation	Large Hail	Super Hail
Interval	$0.00 \leq P < 0.20$	$0.20 \leq P < 0.36$	$0.36 \leq P < 0.45$	$0.45 \leq P < 0.60$	$0.60 \leq P \leq 1.00$
Diameter	/	< mm	0-2 cm	2-10 cm	> 10 cm
Classification	**NO Hail**	**NO Hail**	**YES Hail**	**YES Hail**	**YES Hail**

2.4.2.2 Machine learning approach

The calibration provided by the MWCC-H algorithm is the critical point in the MASHA Method and, when it is not available, it can result in a strong underestimation of the evolving convective systems and hail patterns. For these reasons, the main goal of this project is to extend this technique to a machine learning approach, trying to overcome difficulties such as the spatial and temporal coincidences between polar and geostationary satellites and the consequent underestimation of the hail probability. This aim complies with the machine learning concepts, in which statistical algorithms can learn the main features of a given dataset to generalize unseen data (LeCun et al., 2015). In particular, a classification consisting of a supervised approach has been performed, where the training of the model involves input objects and output values that are human-made labels (in this case “NO Hail” and “YES Hail” classes). Convolutional Neural Networks (CNNs) are primarily used to solve difficult image-driven pattern recognition tasks (O'Shea and Nash, 2015) and consist of an input layer, hidden layers and an output layer. The input is a tensor with shape described in Equation (5):

$$\text{(input height) x (input width) x (input channels) x (number of inputs)} \quad (5)$$

In addition, CNNs preserve spatial structure assuming that input are images and learn features via filter (kernel) optimization. The passing of the filter leads to a double advantadge:

1) strongly reducing the number of weights that must be learned (e.g. in Figure 24 from 32×32 to 5×5), decreasing model training time and cost;
2) making feature search insensitive to feature location in the image.

Considering these strengths, it was decided to use a ResNet-50 model: it is a 50-layer CNN, a mid-sized variant between simpler (e.g. ResNet-18) and more complex (ResNet-101) networks. It belongs to the ResNet (Residual Networks) family designed to tackle the degradation problem, a performance worsening of training and test error as networks become deeper (He et al., 2016; Figure 25). In particular, the ResNet family introduces the residual block with skip connections to ease the training of very deep networks. A residual block is defined as:

$$y = F(x) + x \tag{6}$$

where F(x) is the output of a few convolutional layers and x is the original input as described in Equation (6).

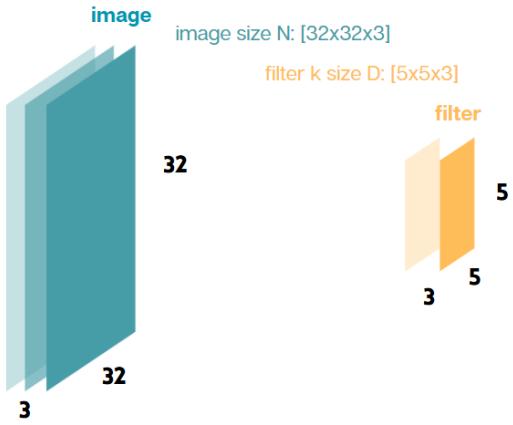

Figure 24. Example of an image size N [32x32x3] and a filter size D [5x5x3] in a CNN.

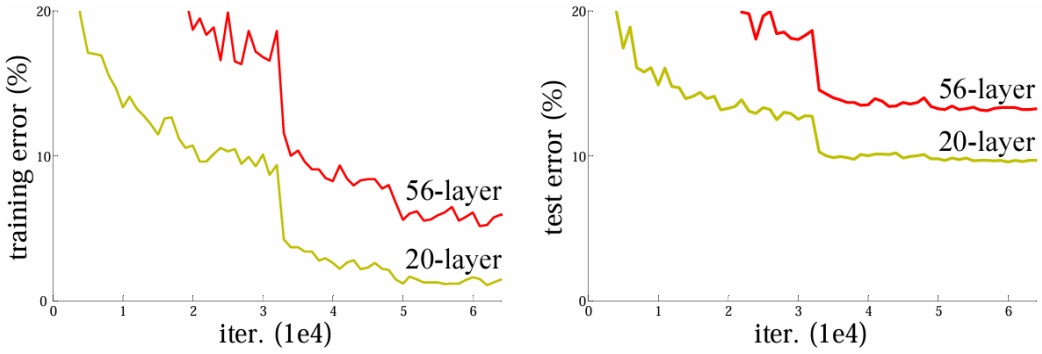

Figure 25. The so-called degradation problem: deeper networks (red line) show higher training error (on the left) and higher test error (on the right; He et al., 2016).

2.4.2.3 Dataset preparation

The dataset comprises 12 820 IR-images collected in 11 years (from 2013 to 2023) during the semester going from April to September. The 10.8 μm IR-images were labeled using MWCC-H outputs and formatted into 128×128-pixel crops, having a 7×7-pixel size filter. Spatial structure (height, width) is preserved while the temporal dimension is not considered. The pre-processing of the dataset involved the two following steps:

1) apply a cloud mask to correct parallax and remove ground signal;
2) remove invalid data (e.g. not a number (hereafter, NaNs), placeholders).

After this procedure, 11 292 IR-images remained for the running of the ResNet-50 model:

- 10 703 IR-images (87,07% of the dataset) labelled by “NO Hail” class;
- 1 589 IR-images (12,93% of the dataset) labelled by “YES Hail” class.

As expected, it results in a very unbalanced dataset in which the “NO Hail” class has a frequency of almost 9/10 events. For evaluating how the ResNet-50 model is learning and getting better over time, two common metrics were used: accuracy and loss. Accuracy is measured in percentages (%) and is defined as the ratio between the number of correct predictions and the total number of IR-images. For example, if a model correctly predicts 90 out of 100 samples, accuracy is equal to 90%. On the other hand, the loss curve computes the error between its predicted output and the true output. Lower loss generally indicates better performance, and it is used during the training to update the model (usually via backpropagation and optimization). It’s important to note that the accuracy computation depends also on the unbalanced dataset we are dealing with. Indeed, if the model deliberately assigned to the whole dataset the “NO Hail” class, accuracy would result equal to 87,07%. This value is very high and must be taken into account during the results evaluation.

Before running the model, the dataset has been split into three independent sections:

- 80% of IR-images: training dataset;
- 10% of IR-images: validation dataset;
- 10% of IR-images: test dataset.

2.4.3 Preliminary results and discussion

2.4.3.1 Training and validation dataset

In this Section, we will show preliminary results about the ResNet-50 model after two runs in which we changed only the number of epochs, rising from 20 (Figure 26a, on the left) to 50 (Figure 26b, on the right). Other parameters have been maintained fixed. The blue curves refer to the training dataset while the oranges to the validation one. Symmetrically, the accuracy is displaced in the upper panels while the loss is described in the lower ones. Starting from Fig. 26a, it can be noticed that accuracy and loss improve as the training progresses, reaching 91.8% and 0.188 at the 20^{th} epoch, respectively. Even considering the validation dataset, best values appear in the second part of the training process, from the 11^{th} to the 20^{th} epoch. So, we decided to extend the number of epochs to 50 in order to explore potential further improvements of the model. In Fig. 26b, comparing the trend between training and validation accuracy, the two curves start separating, especially from the 25^{th} epoch. The same occurs when loss curves are considered. Indeed, even if the training dataset curves keep improving, this is not true for the validation metrics. This behaviour is known as the overfitting problem and typically occurs when the model learns training data too well, memorizing them and including noise and irrelevant details. In addition, the neural network doesn’t learn general patterns which are much more useful for the classification task in the test dataset. Probably, in this case, overfitting appears because our dataset is small if compared to the complexity of the model (ResNet-50 can manage millions of data while here we are training the model with about 10 000 IR-images).

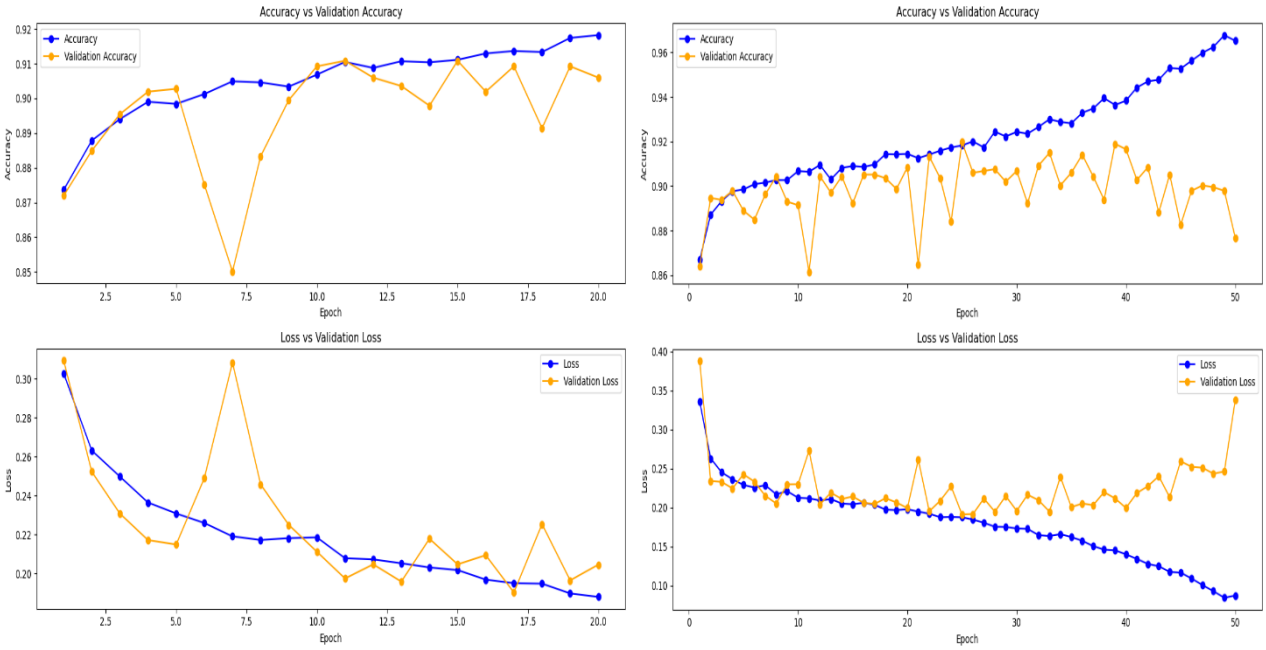

Figure 26. ResNet-50 run after 20 (a) and 50 (b) epochs. Blue curves represent training dataset accuracy and loss whereas oranges describe the same metrics for the validation one.

Possible solutions are:

- increase the starting satellite dataset (e.g. involving more years, extending the geographic domain, etc.);
- apply data augmentation techniques;
- try networks with a lower number of deep layers (e.g. ResNet-18 or ResNet-34) to generalize better patterns and avoid training too many parameters.

2.4.3.2 Test dataset

After the training process, the ResNet-50 model has been tested on a new independent dataset containing 1224 IR-images. The MWCC-H algorithm split them into:

- 1077 IR-images (≈ 88% of the dataset) labelled by "NO Hail" class;
- 147 IR-images (≈ 12% of the dataset) labelled by "YES Hail" class.

For checking the model performance, both configurations at 20 and 50 epochs were tested on the same dataset. Main results are shown using confusion matrices in Table 3. Since we are dealing with a very unbalanced dataset, these results have been normalized with respect to the total amount of "NO Hail" IR-images (orange columns) and "YES Hail" IR-images (green columns) to ease the understanding of Table 3. If we look at the 20-epoch configuration, true negatives (97.8%) strongly outweigh false positives (2.2%) meaning that the neural network recognizes very well "NO Hail" IR-images, misclassifying only the 2.2% of them.

Table 3. Confusion matrices for test dataset after 20 and 50-epoch training.

20 epochs				50 epochs			
Confusion Matrix		Observed		Confusion Matrix		Observed	
		YES	NO			YES	NO
Predicted	YES	46.9%	2.2%	Predicted	YES	81.6%	9.7%
	NO	53.1%	97.8%		NO	18.4%	90.3%

However, if we focus on the "YES Hail" class, results show that false negatives are equal to 53.1% indicating that for the ResNet-50 model is hard to recognize the hailstorms, missing more than 1/2 hail events. Moving to the 50-epoch configuration, these outcomes are quite different, especially considering the "YES Hail" set of IR-images. Indeed, here true positives (81.6%) have significantly increased, showing an important improvement regarding the hailstorms' detection. On the other hand, "NO Hail" results got a bit worse, but here false positives are contained below 10% (more detailed explanations even including native MWCC-H algorithm classes are provided in the next paragraph). Another interesting point is that accuracy decreases from 91.6% (20 epochs) to 89.3% (50 epochs). This range suggests that the model had a better performance after 20-epoch training. Nevertheless, it should be noted that this metric may be unreliable in presence of unbalanced datasets. In fact, accuracy is defined as the sum of true positives and true negatives divided by the total number of IR-images (1224) in the dataset. In this case, even if false alarms grow from 2.2% to 9.7%, at the same time missed events greatly reduce from 53.1% to 18.4%. But the accuracy decreasing can be explained considering absolute values moving from 20 to 50-epoch configuration:

- False alarms rise from 24 to 104 IR-images;
- Missed drop from 78 to 27 IR-images.

The consequent balance reveals that there are 29 IR-images misclassified more, after the 50-epoch training, explaining the accuracy decline.

2.4.3.3 Test dataset: results comparison with the MWCC-H algorithm

In this paragraph, the five hail classes identified by the MWCC-H algorithm (See Table 1 in Section 2.1) are introduced to better understand the main results obtained with the test dataset at 20 and 50 epochs. In Figure 27, we depict the unbalancing of the dataset looking at the distribution of the case studies in the five hail classes. Considering the total number of IR-images (1224), it emerges that not only the "NO Hail" category (No Hail + Hail Potential classes) has a rate of about 88%, but also that the "No Hail" class (hail probability ranging between 0.00 and 0.20) alone counts 783/1224 IR-images, representing more than half (64%) of the

dataset. This type of distribution highlights the dataset imbalance even further, making the hailstorms' recognition more difficult.

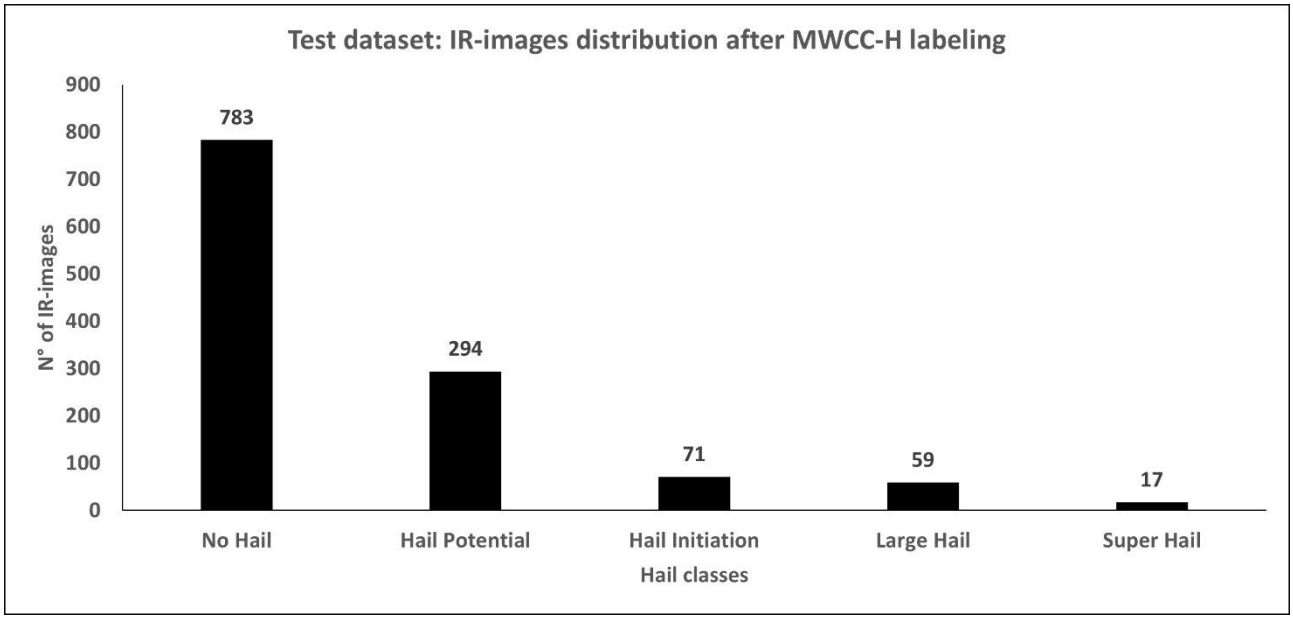

Figure 27. IR-images distribution in test dataset related to the five hail classes identified by the MWCC-H algorithm.

In the same way, it is possible to deepen the main outcomes of test dataset. For 20 and 50-epoch configuration, well-classified IR-images in absolute values (Table 4) and percentages (Table 4 and Figure 28) are reported. Considering the 20-epoch training (Table 4a and Fig. 28a), the five hail classes distribution is quite asymmetrical, with the "NO Hail" Category showing the higher percentages: in particular, the "No Hail" class reaches the 99.9% of well-classified IR-images (only 1/783 IR-images misclassified). Moving to the right, we find the "Hail Potential" and "Hail Initiation" classes, divided by the purple dashed line separating the two hail categories. Results involving these two classes are opposite: "Hail Potential" exhibits a very high value (92.2%) whereas "Hail Initiation" obtains the worst result (32.4%). These two classes are the closest to the hail probability threshold value (equal to 0.36), so it is reasonable to think that contain some case studies in which features are very similar and it is more difficult to recognize potential hailstorms. Here, it is clear that the model is preferring to be conservative dealing with the binary classification, assigning in most cases, the "NO HAIL" label: it turns out that only a few patterns are recognized as hailstorms, missing a great part of the hail events. When hailstorms develop and intensify, they achieve the "Large Hail" or "Super Hail" class: results related to them are gradually improving with respect to the "Hail Initiation" class (57.6% and 70.6%, respectively) probably because here IR-images cloud patterns take on more distinctive features. However, results remain unbalanced when compared with the "NO Hail" Category. Now, if we move to the 50-epoch configuration (Table 4b and Fig. 28b), we can immediately notice that all "YES Hail" classes have improved at the expense of the "NO Hail" category, especially considering the "Hail Potential" class. After the 50-epoch

training, the hail classes distribution becomes more symmetrical with respect to the hail probability threshold value.

Table 4. For each hail class, well-classified IR-images after 20 (a) and 50-epoch (b) training have been reported.

	20-epochs configuration				
	NO Hail Category		YES Hail Category		
	No Hail	Hail Potential	Hail Initiation	Large Hail	Super Hail
Well-classified IR-images (%)	782/783 (99.9%)	271/294 (92.2%)	23/71 (32.4%)	34/59 (57.6%)	12/17 (70.6%)

(a)

	50-epochs configuration				
	NO Hail Category		YES Hail Category		
	No Hail	Hail Potential	Hail Initiation	Large Hail	Super Hail
Well-classified IR-images (%)	769/783 (98.2%)	204/294 (69.4%)	51/71 (71.8%)	53/59 (89.8%)	16/17 (94.1%)

(b)

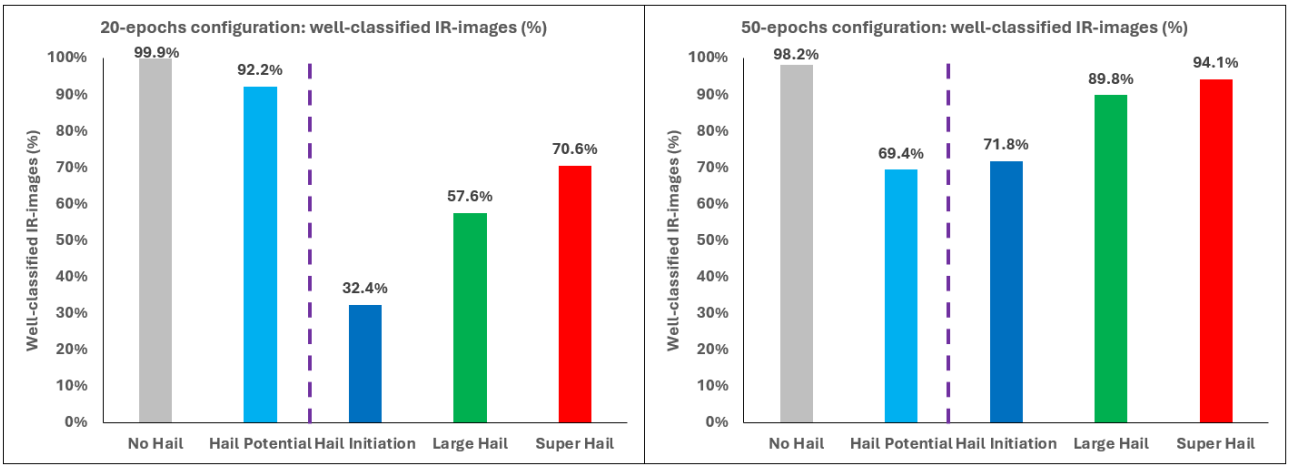

(a) (b)

Figure 28. As in Table 4, well-classified IR-images are depicted using bars. The purple dashed line separates the two hail categories.

Indeed, results related to the "Hail Potential" and "Hail Initiation" classes (69.4% and 71.8%, respectively) are much more similar and balanced showing a network more able to identify hailstorms at the cost of more false alarms appearing in the "Hail Potential" class (from 7.8% to 30.6%). Moreover, all classes far from the hail probability critical value exhibit very interesting values:

- 98.2% for "No Hail" class (showing a minor decrease if compared to the 20-epoch training);
- 89.8% for "Large Hail" class which strongly improves from the previous 57.6%;

- 94.1% for “Super Hail” class with only 1/17 IR-images misclassified.

Since we are treating a binary classification, these outcomes confirmed our expectations to have higher uncertainty focused around the hail probability threshold value and better results in hail classes further away, in which IR-images cloud patterns should be easier to recognize. In addition, the 50-epoch training generally improves hailstorms identification performance.

2.4.3.4 Test dataset: 50-epoch configuration IR-images

In this Section, we show some IR-images belonging to both hail classes, giving a brief qualitative description. Figure 29 and Figure 30 depict some well (Fig. 29a-b and Fig. 30a-b) and misclassified (Fig. 29c-d and Fig. 30c-d) IR-images for the “NO Hail” and “YES Hail” classes, using results found after the 50-epoch training, respectively. Fig. 29 represents the “NO Hail” class: here, well classified IR-images (Fig. 29a-b) have many dark pixels, showing low contrast and cloud patterns poorly organized. On the other hand, wide and cold patterns like in Fig. 29c-d induce the model to recognize hailstorms even when they are not hail-producing. Moving to the “YES Hail” class, correctly classified events (Fig. 30a-b) report high contrast between deep convective systems (white pixels) and clear sky conditions (dark pixels). In addition, hailstorms exhibit an extended and well-defined structure. In misclassified IR-images (Fig. 30c-d), cloud patterns show a worse organization and lower contrast. Moreover, deep convective systems have usually a lower spatial extension.

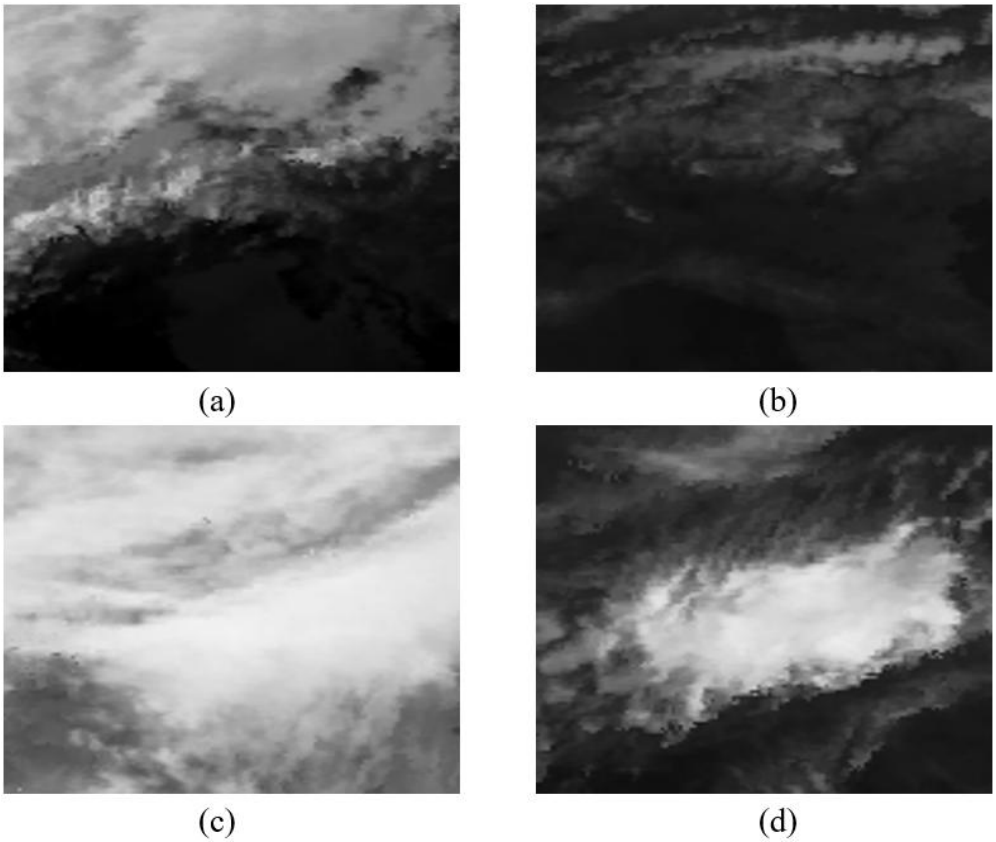

Figure 29. “NO Hail” class IR-images well classified (a-b) and misclassified (c-d).

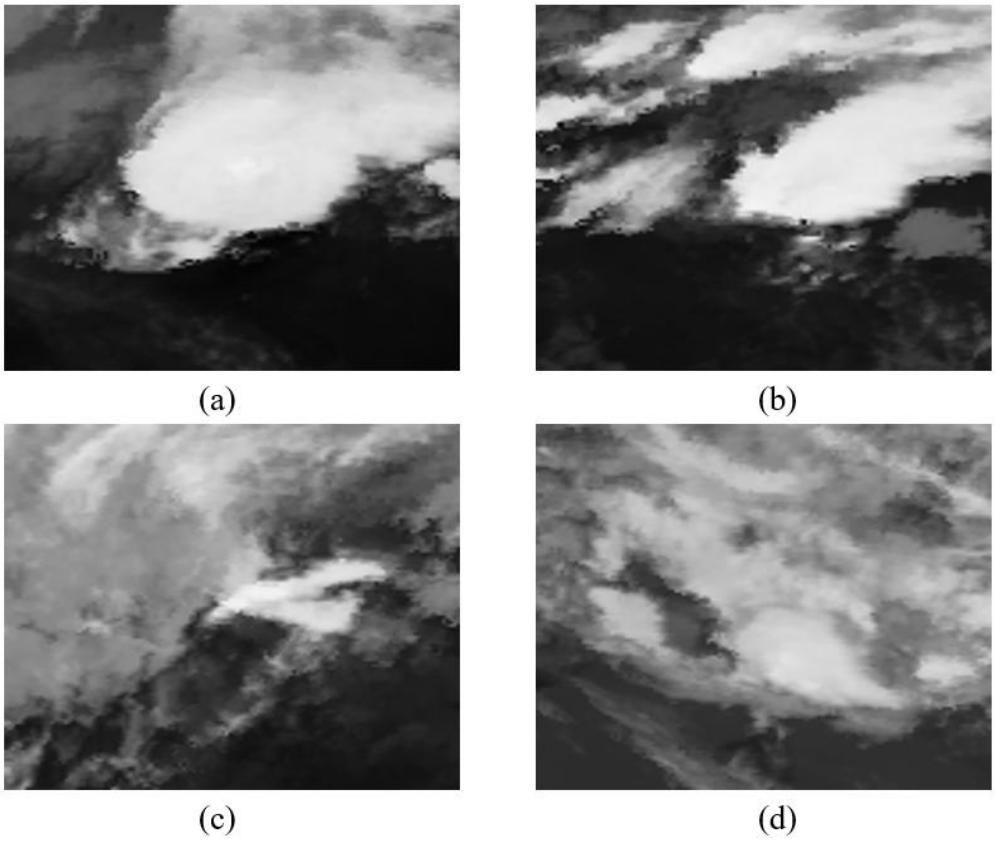

Figure 30. "YES Hail" class IR-images well classified (a-b) and misclassified (c-d).

2.4.4 Conclusions and future perspectives

This preliminary study shows promising results in using deep learning for hailstorm classification from satellite data. A ResNet-50 model has been developed to identify hailstorms using satellite IR-images labelled by the MWCC-H algorithm. In this project, a binary classification splitting IR-images in "NO Hail" and "YES Hail" classes, where hail probability equal to 0.36 is the threshold value, has been proposed. The training dataset counts about 10 000 IR-images in which no-hail events predominate, reaching about 87% of the dataset. Main results are summarized as it follows:

- accuracy is not a very good metric to evaluate the model performance because we are dealing with unbalanced datasets;
- after 25 epochs, overfitting appears limiting generalization;
- more balanced and diverse datasets are required for robust model performance.

Considering the test dataset, the 50-epoch configuration is more suitable for identifying hailstorms. Here:

- true negatives are 90.3%, even if false alarms rise to 9.7%;
- missed events strongly decrease from 53.1% to 18.4%;

- the model is affected by a symmetrical decline around the hail probability threshold value, showing better performance for “No Hail”, “Large Hail” and “Super Hail” classes. On the other hand, for the 20-epoch configuration, final results are unbalanced in favour of “No Hail” labeling, giving out many missed hail events even in “Large Hail” and “Super Hail” classes;
- white pixels, high contrast and well-defined convective systems help the model in the final recognition. Only small poorly organized patterns are misclassified.

These preliminary outcomes open the way to new interesting perspectives:

1) alternative architectures: test shallower ResNet variants (e.g., ResNet-18, ResNet-34) to improve generalization;
2) use of MTG satellite: leverage the 10.5 μm channel with higher temporal/spatial resolution for better labeling;
3) multivariate approaches: integrate lightning data (e.g. LAMPINET and EUCLID networks or MTG Lightning Imager) to enhance feature richness (Figure 31).

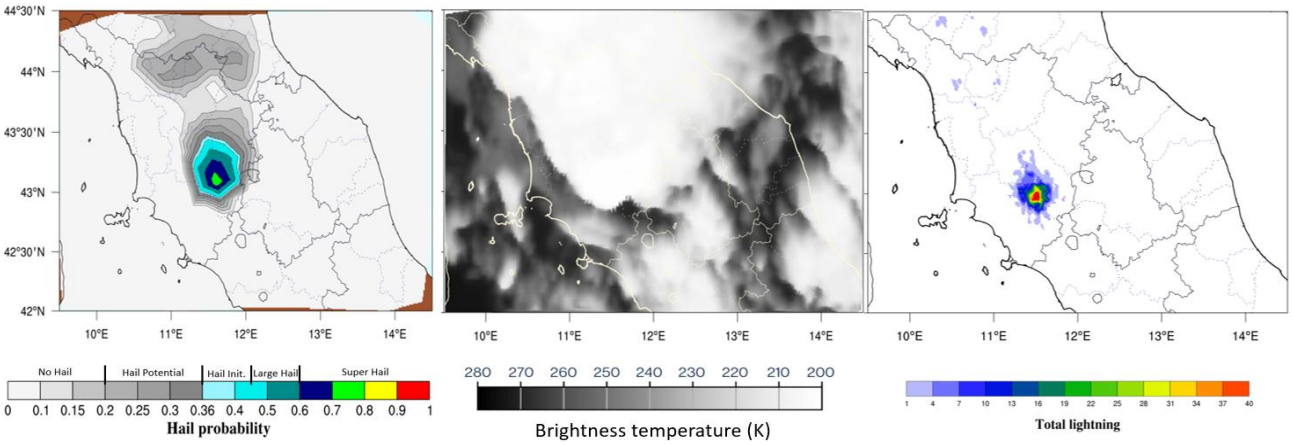

Figure 31. An example of a potential multivariate approach integrating MWCC-H algorithm (on the left), IR-image (in the middle) and lightning map (on the right).

Chapter 3 Lightning activity in thunderstorms

3.1 Introduction about lightning strikes

Lightning is one of the most spectacular natural phenomena and can be defined as a violent atmospheric electrical discharge that may originate, in most cases, within a cloud (intracloud, IC), between two clouds (cloud-to-cloud, CC), between a cloud and the ground (cloud-to-ground, CG), or, more rarely, between a cloud and the surrounding air (cloud-to-air, CA), (Uman, 2012). According to the type of strokes, in Figure 32, a general schematization of lightning activity and the location of main centers of positive and negative charge occurring in thunderstorms is provided. Generally, IC, CC and CA flashes are counted in the IC group, to better discriminate among strikes falling to the ground (CG) and flashes only affecting atmosphere (IC). Christian et al., (2003) state that, every second, there are approximately from 40 to 50 lightning flashes (IC and CG combined) in total around the planet, with an average land/ocean ratio of about 10:1. In addition, a dominant Northern Hemisphere summer peak occurs in the annual cycle. Although CG lightning accounts for only about 20 - 25% of all discharges detected on a global scale, having typical discharge current intensities ranging from several tens of kiloamperes to values exceeding 150 kA, it represents the greatest hazard to social, sporting, and economic activities such as power companies, civil aviation, wind farms, high tech industries, forestry managers, and the public in general (Rakov, 2013a; Rakov, 2021; Rosati, 2023).

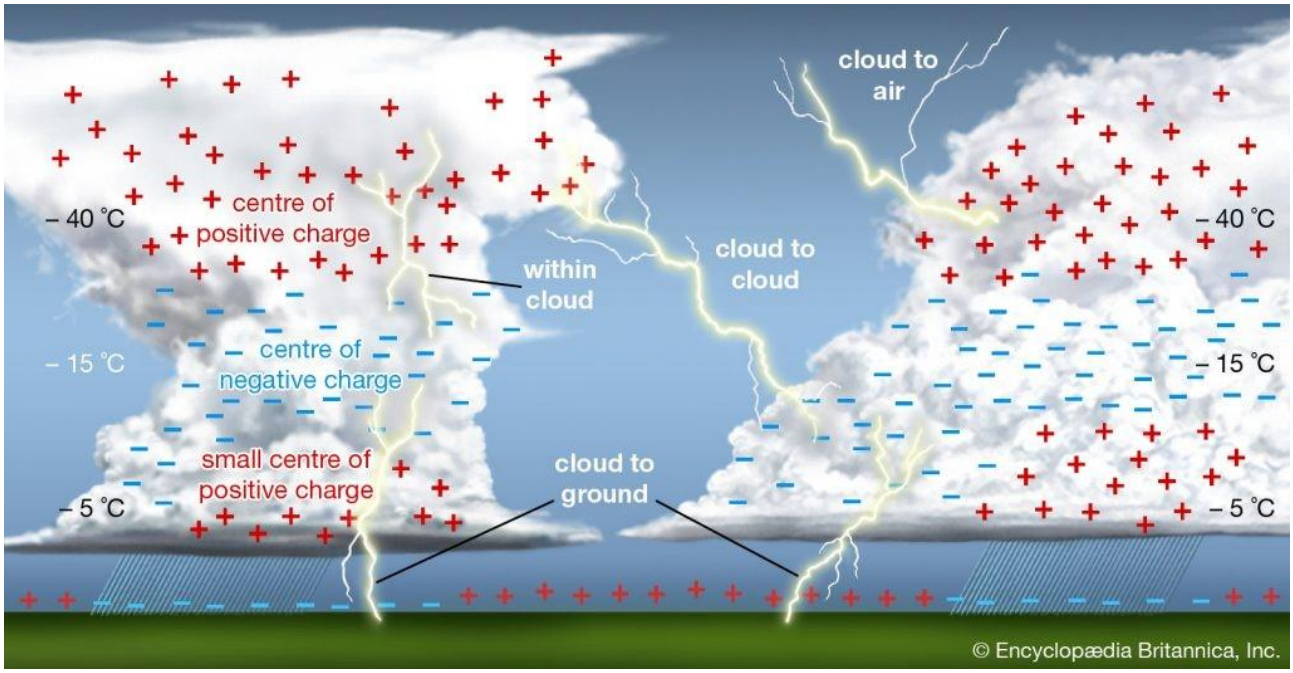

Figure 32. General classification of lightning strikes originating from thunderstorm clouds. IC and CG discharges constitute 75-80% and 20-25% of global lightning activity, respectively (adapted from © Encyclopaedia Britannica, Inc).

Cooray et al. (2007) report that thousands of people are killed every year by lightning bolts, while tens of thousands suffer injuries to respiratory, cardiovascular and nervous system, eyes, ears and of psychological type. Also, lightning strikes can locally ignite tens of fires on the same day as a storm passes through, causing

major problems for fire crews and fire management (Price, 2013). For these reasons, monitoring atmospheric electrical activity plays a fundamental role in the early detection of convective phenomena and in mitigating the risks associated with them.

3.2 Electrification of clouds

Most of the electrical energy of a thunderstorm is thought to be released in the form of lightning. A modest thunderstorm produces a few flashes per minute while large thunderstorms may produce lightning at rates in excess of 100 flashes per minute (Williams, 1988). Lightning activity in convective clouds depends both on the microphysics and dynamics of the clouds. Indeed, as stated by Williams et al. (1991), the electrification process in thunderstorms is related to the existence of hydrometeors in different phases and sizes interacting with each other through collisions, freezing, melting, coalescence, and breakup. In the thunderstorm, there is a layer where we can find liquid water (supercooled), ice crystals, snow, hail, and graupel (soft hail) all existing together. At temperatures higher than 0 °C, all ice will start melting and turn to water drops whereas at temperatures below -40 °C, all hydrometeors will be frozen solid. However, water can exist in liquid form at temperatures below 0 °C and above -40 °C, called supercooled water (e.g. Price, 2013). In this region, the electrification process is more likely, especially between -5°C and -20°C (e.g. Rosati, 2023). It has been shown in laboratory studies that collisions between all these particles (especially ice crystals and graupel), in this mixed-phase region of clouds, is key for the charge transfer between cloud particles (Reynolds, 1953; Takahashi, 1978; Saunders et al., 1991) and it is consistent with large-scale observations of thundercloud electrical structure (Williams et al., 1989). The separation between lighter and heavier particles is determined by the updraft which triggers the convection process. Electrically active storms have updrafts reaching up to 50 m/s that enhance the collisions between different-sized particles. Increased collisions result in increased charge transfer between particles, leading to rapid charge buildup in clouds. Price (2013) explains that charge transfer between particles is not a sufficient condition to produce lightning. Indeed, to build up large-scale electric fields in convective clouds, we need to separate the positively charged particles from the negatively charged particles in the cloud. If all particles in clouds randomly got either positively or negatively charged, we would have a cloud filled with charged particles, but with no net electric field on the large scale (kilometers). However, it turns out that the smaller ice crystals in clouds, in general, acquire a net positive charge due to all the collisions, while the larger graupel acquire a net negative charge (Saunders et al., 2006) as shown in Figure 33a-b, on the right (Rosati, 2023). Due to their different sizes (and terminal velocities), the smaller positive crystals are carried aloft to the top of the cloud by the updrafts, while the larger negative hailstones drift downwards to the base of the cloud. In fact, during a thunderstorm, particles can collide until $5 \cdot 10^3$ times per km^3 (Rosati, 2023), producing an increasing potential difference between the cloud top (positively charged) and cloud base (negatively charged), with electric fields approaching the breakdown electric field in air. When we pass that threshold, the system must be rebalanced through the passing of

electrical current (Fig. 33, on the left) within the cloud (IC lightning) or between the cloud base and the ground (CG lightning). Finally, we can hear the thunder.

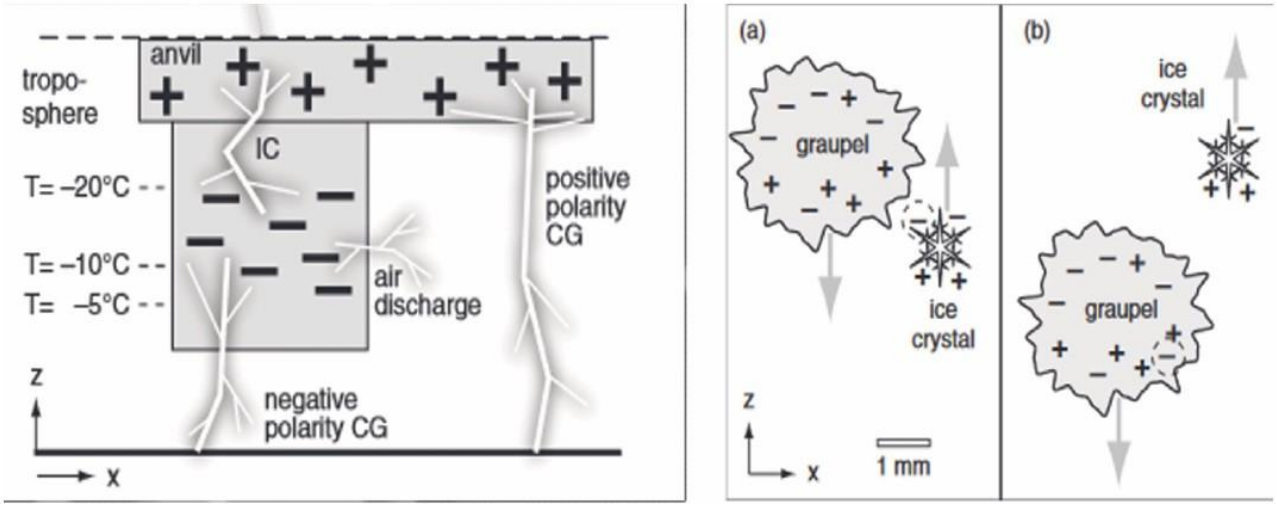

Figure 33. IC and CG lightning balancing the charge distribution in thunderstorm clouds and between the cloud and the ground (on the left) and mechanism of cloud electrification (on the right) in which graupel and ice crystals collide (a) carrying negative charge to lower levels and positive charge to upper levels of the thunderstorm (b) (adapted from Rosati, 2023).

About 90 % of global CG lightning is accounted for by negative (negative charge is effectively transported to the ground) downward (the initial process begins in the cloud and develops in the downward direction) lightning. Other types of CG lightning include positive downward, negative upward, and positive upward discharges. There are also bipolar lightning discharges sequentially transferring to ground both positive and negative charges during the same flash (Uman, 2012; Rakov, 2013a; Rakov, 2021). The basic elements of the negative downward lightning discharge are termed component strokes or just strokes. There are two major processes comprising a lightning stroke, the leader and the return stroke, which have been described in detail by Rakov (2013a) as it follows. The initial (first stroke) leader is preceded by an in-cloud process called the preliminary breakdown. The leader creates a conducting path between the negative cloud charge source region and ground and distributes negative charge from the cloud source region along this path, and the return stroke traverses that path moving from ground toward the cloud charge source region and neutralizes the negative-leader charge. Thus, both leader and return-stroke processes serve to effectively transport negative charge from the cloud to ground. The leader initiating the first return stroke differs from the leaders initiating subsequent strokes (all strokes other than first are denominated subsequent strokes). In particular, the first-stroke leader appears optically to be an intermittent process, hence the term stepped leader, while the tip of a subsequent-stroke leader appears to move continuously, appearing on streak photographs as a downward-moving “dart”, hence the term dart leader. The apparent difference between the two types of leaders is related to the fact that the stepped leader develops in virgin air, while the dart leader follows the “pre-conditioned” path of the preceding stroke or strokes. Sometimes a subsequent leader exhibits stepping while propagating along a previously formed channel; it is referred to as dart-stepped leader. When the descending stepped leader attaches

to the ground, the first return stroke begins. The first return-stroke current measured at ground typically rises to an initial peak of about 30 kA in some microseconds and decays to half-peak value in some tens of microseconds. The return stroke effectively lowers to ground the several coulombs of charge originally deposited on the stepped-leader channel including all the branches. When the first return stroke, including any associated continuing current and in-cloud discharge activity ceases, the flash may end. In this case, the lightning is called a single-stroke flash. However, more often the residual first-stroke channel is traversed by one or more dart-leader/return-stroke sequences. Once the bottom of the dart-leader channel is connected to the ground, the second (or any subsequent) return-stroke wave is launched upward, which again serves to neutralize the leader charge. The subsequent return-stroke current at ground typically rises to a peak value of 10–15 kA in less than a microsecond and decays to half-peak value in a few tens of microseconds. The high-current return-stroke wave rapidly heats the channel to a peak temperature near or above 30 000 °K and creates a channel pressure of 10 atm or more, resulting in channel expansion, intense optical radiation, and an outward propagating shock wave that eventually becomes the thunder (sound wave) we hear at a distance (Rakov, 2013a). The key-points of this mechanism are depicted in Figure 34 (Rosati, 2023): on the left (Fig. 34a), the stepped leader is approaching the ground through many single steps having an approximated length of 50 meters and a duration of 1 μs until a positive discharge coming from the ground (called "streamer") rejoins the stepped leader. When the cloud-ground path is open, we can see the first visible return stroke (Fig. 34b). Depending on the charge in cloud, usually the open path is exploited by other subsequent return-strokes, each of them taking the name of "dart leader" (Fig. 34c).

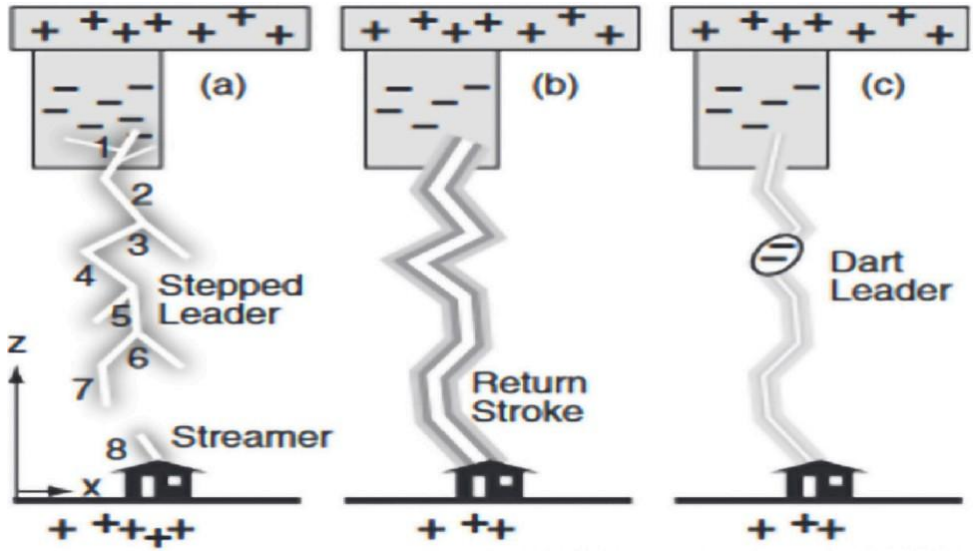

Figure 34. CG mechanism representation: the stepped leader reaches the ground joining the streamer (a) while the return stroke (b) and every subsequent dart leader (c) have the net effect of transporting the negative charge to the ground (adapted from Rosati, 2023).

Thunderstorm cells often follow a regular cycle of birth, development, maturity, decay, and dissipation as represented in Figure 35 (Price, 2013). This cycle can take around 1 h, with new thunderstorm cells forming

on the cold outflow boundary of previous cells. From the birth of the convective cloud to its dissipation, the cloud is electrified at different levels, while we only see the lightning activity during the developing, mature, and decaying stage. The lightning activity itself follows a specific pattern, with the IC lightning normally appearing first (during developing stage), followed by the CG lightning starting during the mature stage (Williams et al., 1989). Both types of lightning can occur during the decaying stage. In addition to the lightning changes, the mature stage can be associated with heavy rainfall, hail, and tornadoes, while the dissipating stage is known to be associated with downdrafts, microbursts and wind shear (Price, 2013).

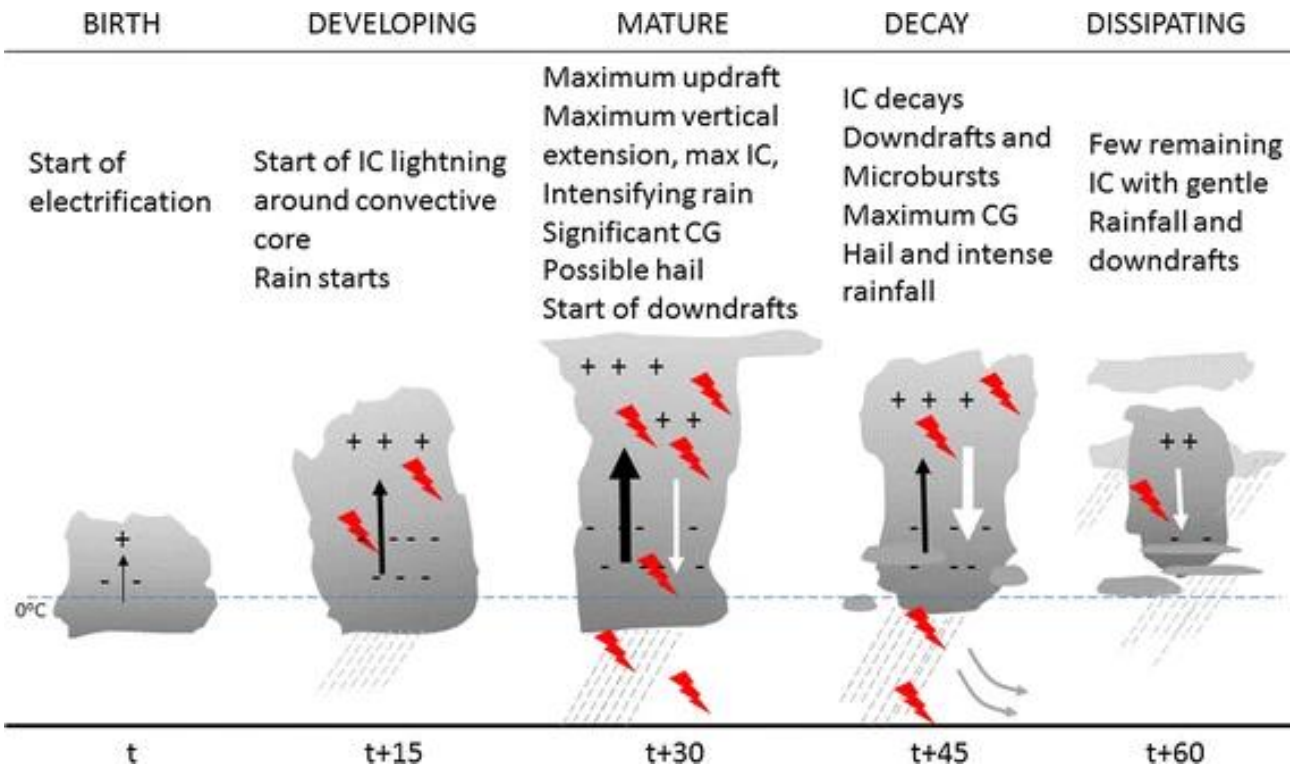

Figure 35. The various stages of development and decay of a thunderstorm cell and the associated lightning and possible severe weather related to each stage. Updrafts (black arrows) and downdrafts (white arrows) are shown relative to their intensity. IC and CG lightning are represented in red either in cloud or below cloud base. The approximate time (minutes) between each stage is shown below (adapted from Price, 2013).

3.3 The global electrical circuit

The distribution of lightning around the globe is not random, following the general circulation patterns of the atmosphere, mainly driven by solar heating and by the presence of continents and oceans. During each 24-hour period, three lightning activity maxima corresponding to the three tropical thunderstorm regions, each of them peaking in the late afternoon, are found in Southeast Asia (09 UTC), Africa (14 UTC) and South America (20 UTC), (Price, 2006). In addition, water vapor and particularly the release of latent heat during condensation and freezing, plays a vital role in thunderstorm development. Since the saturation water vapor concentrations increase ~7 % for every one degree increase in temperature (Clausius - Clapeyron relationship), the tropical atmosphere has an order of magnitude more water vapor than the polar atmospheres (Price, 2013). Given all

the above, Christian et al. (2003) state that the annual average global flash rate, which includes both IC and CG lightning, is 44 flashes per second, with an estimated uncertainty that does not exceed ± 5 flashes per second. Moreover, they found that lightning activity around the globe is mainly focused on the tropics and approximately 78% of all lightning occurs between 30°S and 30°N latitudes. The global annual cycle is dominated by land contributions in the Northern Hemisphere summer and peaks more than a month after the Northern Hemisphere summer solstice. Continental, island and coastal regions contribute 88% of the global total production. These findings confirmed that lightning activity is a continuous (but variable) process happening between the Earth's surface and atmosphere. Starting from the beginning of XXth century, some prior studies tried to estimate the average global flash rate (e.g. 100 flashes per second estimated by Brooks (1925)) in order to understand the contribution of thunderstorm activity to the maintenance of the global electric circuit (e.g. Williams, 2009). In this framework, some works and projects tried to ascertain whether thunderstorms supply negative electricity to the earth at the rate required to maintain the general negative electrification (negative surface charge) which is almost invariably observed during fair weather (e.g. Gish and Wait, 1950). In Figure 36 (Cooray, 2015), a general schematization of the global electrical circuit is provided.

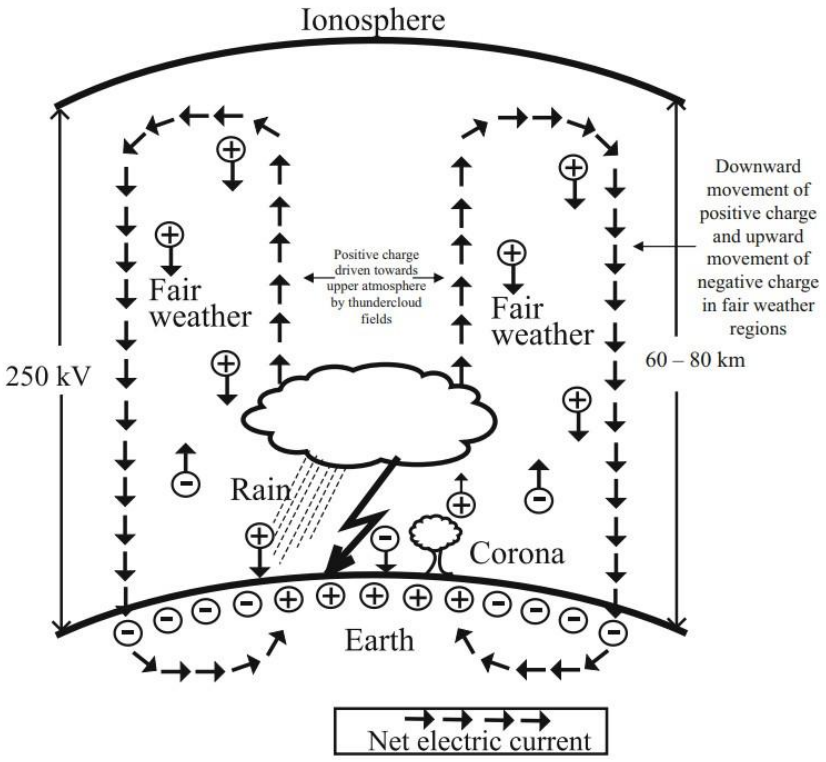

Figure 36. Thunderstorms act as a battery to keep the Earth charged negatively and the atmosphere charged positively. Atmospheric electrical currents flow downward in fair weather and upward in thunderstorms. Thunderstorms deliver charge to the earth by lightning, rain and corona discharges (adapted from Cooray, 2015; adapted from Uman, 2001).

It shows that the fair-weather electric field is in some way connected to the distribution of global thunderstorms (the total number of thunderclouds active at any given moment may vary from approximately 1500 to 2000). If we consider a thunderstorm located above the Earth, it is bounded by two conducting regions, the surface of

the Earth and the ionosphere. The electric field above the thundercloud, which is dominated by the upper positive charge center of the thundercloud, drives positive charges toward the ionosphere. On the other hand, the electric field below the thundercloud is dominated by the electric field generated by the negative charge center, and it drives negative charges toward Earth. Moreover, the majority of lightning flashes bring down a negative charge to Earth. Thus, a thunderstorm acts in a way so as to supply Earth with a net negative charge. This negative charge gives rise to the fair-weather electric field, which completes the current circuit by generating a current that transports negative charges toward the ionosphere or viceversa. It is easy to show that if all thunderstorm activity were to cease, the global electric circuit currents, fields, and charges would decay and disappear within 10 minutes (Bering et al., 1998). Hence, the constant charge on the Earth (500 000 Coulombs), the fair-weather fields and currents are maintained by the never-ending thunderstorm activity around the globe (Price, 2006).

3.4 The Italian Air Force Lightning Detection Network "LAMPINET"

In this paragraph, we will introduce the lightning detection network that we mainly used for studying the connections between lightning strikes and the hailstorms. This is the Italian Air Force Lightning Detection Network "LAMPINET", which was built up in 2003 by the Meteorological Service of the National Air Force. The most of the following information related to LAMPINET can be found in Biron (2009) and Rosati (2023). LAMPINET network consists of 15 sensors uniformly distribuited on the Italian national territory as shown in Figure 37 (Rosati, 2023). Lightning strikes are usually detected and located exploiting the radio wave emission in three main bands (e.g. Magurno and Levizzani, 2012; Rakov, 2013b):

- Very High Frequency (VHF): from 30 to 300 MHz;
- Low Frequency (LF): from 30 to 300 kHz;
- Very Low Frequency (VLF): from 3 to 30 kHz.

Both IC and CG discharges emit energy over a wide range of frequencies described in Figure 38 (Cummins et al., 2000). During breakdown and ionization processes (mostly from leaders and streamers), there are strong emissions in the VHF, the range in which IC flashes mainly emit. When high currents occur in previously ionized channels (mostly from return strokes and the active stage of cloud flashes), the most powerful emissions occur in the LF and VLF ranges. Thus, in the VLF and LF, CG strokes completely dominate the VLF and LF radiation fields produced by lightning because of their channel length and large currents (Cummins et al., 2000). Thus, the frequency range choice is crucial depending on which type of discharges we are going to measure. Indeed, VHF sensors will detect the signal only if it is emitted in a range of few kilometers, whereas LF and VLF pulses can propagate for tens or hundreds of kilometers, thanks to the reflection occurring between the Earth's surface and ionosphere (see Fig. 38). The latter allows to build up a lightning detection network with a relative low number of sensors, located even at hundreds of kilometers from

each other. This is the main reason why LAMPINET consts of 15 sensors located throughout the Italian Peninsula, operating in a frequency range of 1-350 kHz (LF).

Figure 37. The distribution along the Italian Peninsula of 15 LAMPINET sensors (adapted from Rosati, 2023).

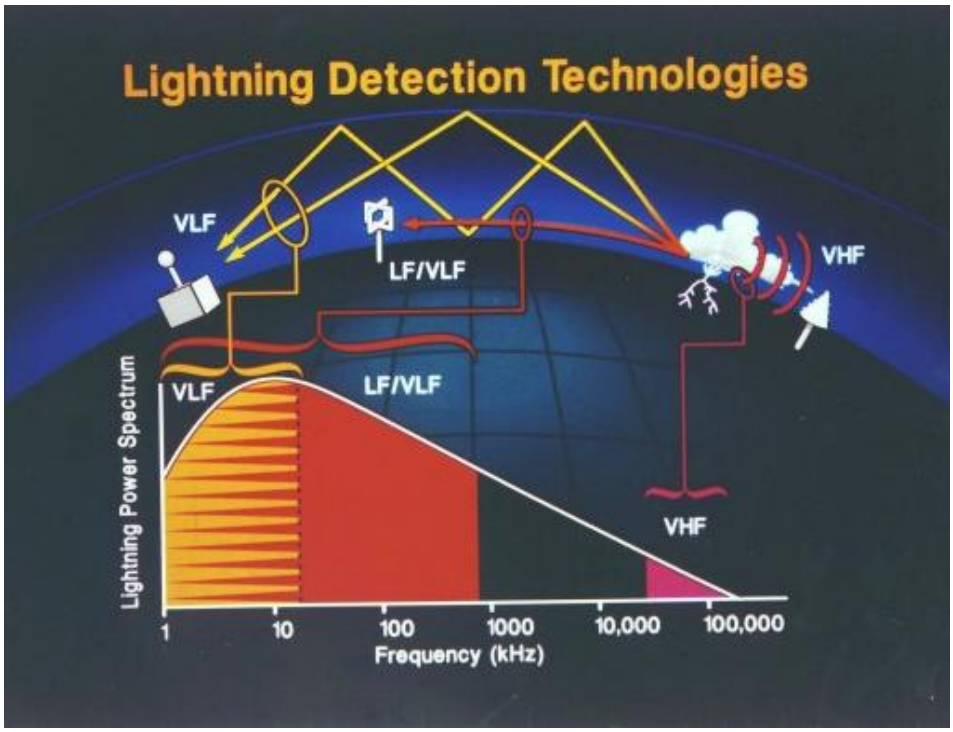

Figure 38. Relationship between frequency and lightning detection method (adapted from Cummins et al., 2000; adapted from Malan, 1963).

This feature makes LAMPINET a very good network for detecting CG discharges, with a detection efficiency (hereafter, DE) that reaches 90% for normalized currents higher than 50 kA, and a location accuracy of 500 m in the central areas of Italian Peninsula; larger errors are expected in the border areas and beyond the network. On the other hand, for IC pulses, the DE decreases to 20-30%. After discussing the main radio wave band (1-350 kHz) used by LAMPINET network, we describe how the network obtains the geolocation of each discharge. In this case, LAMPINET exploits two different techniques: Magnetic Direction Finding (MDF) and Time-of-Arrival (TOA). MDF consists of two vertical and orthogonal loops (Figure 39a) with planes-oriented North-South (NS) and West-East (WE), each measuring the magnetic field from a given vertical radiator, which can be used to obtain the direction to the source. This is the case because the output voltage of a given loop, by Faraday's law, is proportional to the cosine of the angle between the magnetic field vector and the normal vector to the plane of the loop. For a vertical radiator, the magnetic field lines are circles coaxial with respect to the source. Hence, for example, the loop whose plane is oriented NS receives a maximum signal if the source is north or south of the antenna, while the orthogonal EW loop receives no signal. In general, the ratio of the two signals from the loops is proportional to the tangent of the angle between north and the source as viewed from the antenna (Rakov, 2013b). For properly measuring the discharge geolocation, at least two sensors are needed. The TOA technique is based on the radio signal produced by a lightning strike, computing the time of arrival to each sensor that detected the stroke. It follows that every sensor of the LAMPINET network must be perfectly sinchronized in time. In this case, discharge locations are determined via the measured differences between signal arrival times at the stations. Even if three sensors are enough to geolocate the discharge thanks to the intersection of three hyperbolas (Figure 39b; Rosati, 2023), only four sensors ensure the uniqueness of the solution.

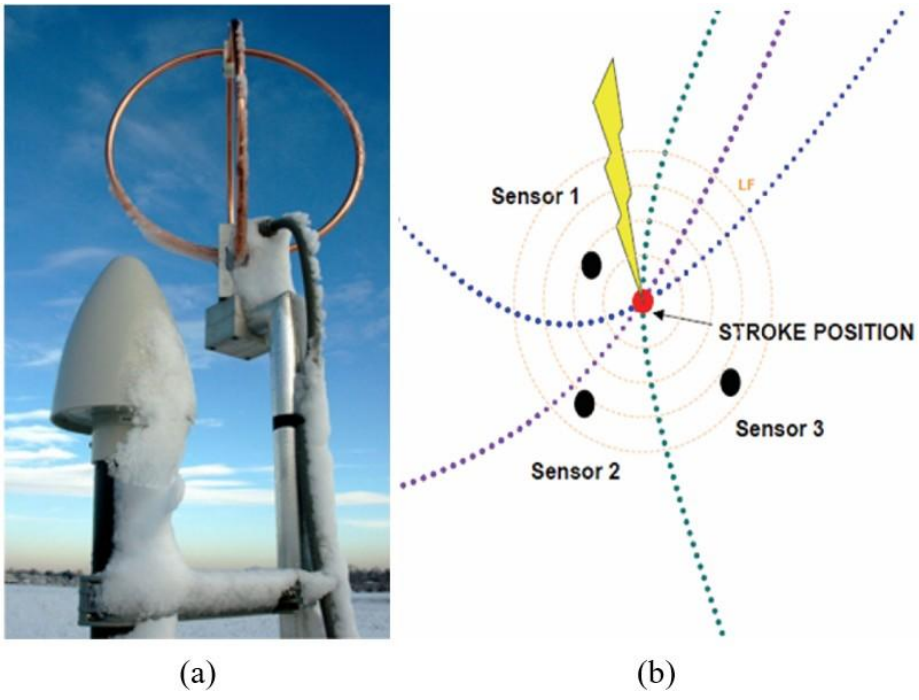

Figure 39. Sensor with two orthogonal loops for applying the MDF technique (a; adapted from Magurno and Levizzani, 2012) and schematization of the discharge geolocation exploiting the TOA technique (b; adapted from Rosati, 2023).

The combination of MDF and TOA is performed thanks to the Improved Accuracy Using Combined Technique (IMPACT) technology (Cummins et al., 1998), giving out a more robust system and an improved DE with respect to separately use MDF and TOA. Currently, LAMPINET network consists of 12 IMPACT ESP sensors and 3 last generation sensors LS7002, having a geolocation accuracy of about 500 m and a temporal resolution of 1 second. After introducing the main techniques performed by the LAMPINET network for the discharge detection, in Figure 40 we show an example of lightning data final output, in which the whole set of information is provided.

```
2025-06-16 15:35:00  45.190   13.280    -3.1 kA  C
2025-06-16 15:35:00  45.192   13.372    -4.6 kA  C
2025-06-16 15:35:00  43.995   12.792   +40.0 kA  G
2025-06-16 15:35:00  42.898   13.460    -6.8 kA  C
2025-06-16 15:35:00  43.506   12.130    +7.9 kA  C
2025-06-16 15:35:00  43.511   12.127    +5.4 kA  G
2025-06-16 15:35:00  43.506   12.136   +12.9 kA  C
2025-06-16 15:35:00  44.133   12.445    +5.7 kA  C
2025-06-16 15:35:00  44.134   12.443    +5.6 kA  C
2025-06-16 15:35:00  44.134   12.441    +4.5 kA  C
2025-06-16 15:35:01  43.842   11.727    +3.2 kA  C
2025-06-16 15:35:01  41.619   14.600    -6.3 kA  C
2025-06-16 15:35:01  44.142   12.431    +9.5 kA  G
2025-06-16 15:35:01  45.212   12.771    +3.7 kA  G
2025-06-16 15:35:01  45.228   12.761    +4.7 kA  C
2025-06-16 15:35:01  45.206   12.733    +5.2 kA  C
2025-06-16 15:35:01  45.219   12.765    +5.0 kA  C
2025-06-16 15:35:01  45.223   12.763    +5.4 kA  C
2025-06-16 15:35:01  45.253   12.630    +2.9 kA  G
2025-06-16 15:35:02  39.167   16.341    +6.4 kA  C
2025-06-16 15:35:02  44.284   12.913    +5.7 kA  C
```

Figure 40. For each lightning strike, LAMPINET network provides information about date, UTC time, latitude, longitude, current intensities and type.

For each discharge detected, from left to right we can read: date (year – month – day), UTC time (hour : minute : second), latitude, longitude, positive or negative current intensity (kA) and type of lightning strike (C = IC and G = CG). As can be noticed in Fig. 37, the distribution of the 15 sensors along the Italian Peninsula leads to the detection of discharges occurring at the same time (for instance, many strikes happen in the same second at 15:35:00 UTC, see Fig. 40) and being spaced by hundreds of kilometers from each other.

3.5 Lightning activity from 2015 to 2023 in Italy: a LAMPINET overview

Before trying to study the potential relationship between lightning strikes and hailstorms, in this section we analyzed the lightning activity detected by the LAMPINET network along the Italian Peninsula and surrounding areas, using a 9-year timeseries going from 1st January 2015 to 31st December 2023, which covers most of the case studies that will be presented in next chapters. This general characterization of lightning activity can be considered the first step for understanding the links among lightning discharges, seasonality and thunderstorm activity. For performing this investigation, it was defined a study area ranging in latitude

from 36.00°N to 48.00°N and in longitude from 6.00°E to 19.00°E (red box in Figure 41), also taking into account the distribution of LAMPINET sensors shown in Fig. 37 (Section 3.4). The same study area was used by Petracca et al. (2024) to produce a 13-year long strokes statistical analysis over the Central Mediterranean area, exploiting the Lightning Detection Network (LINET; Betz et al., 2009).

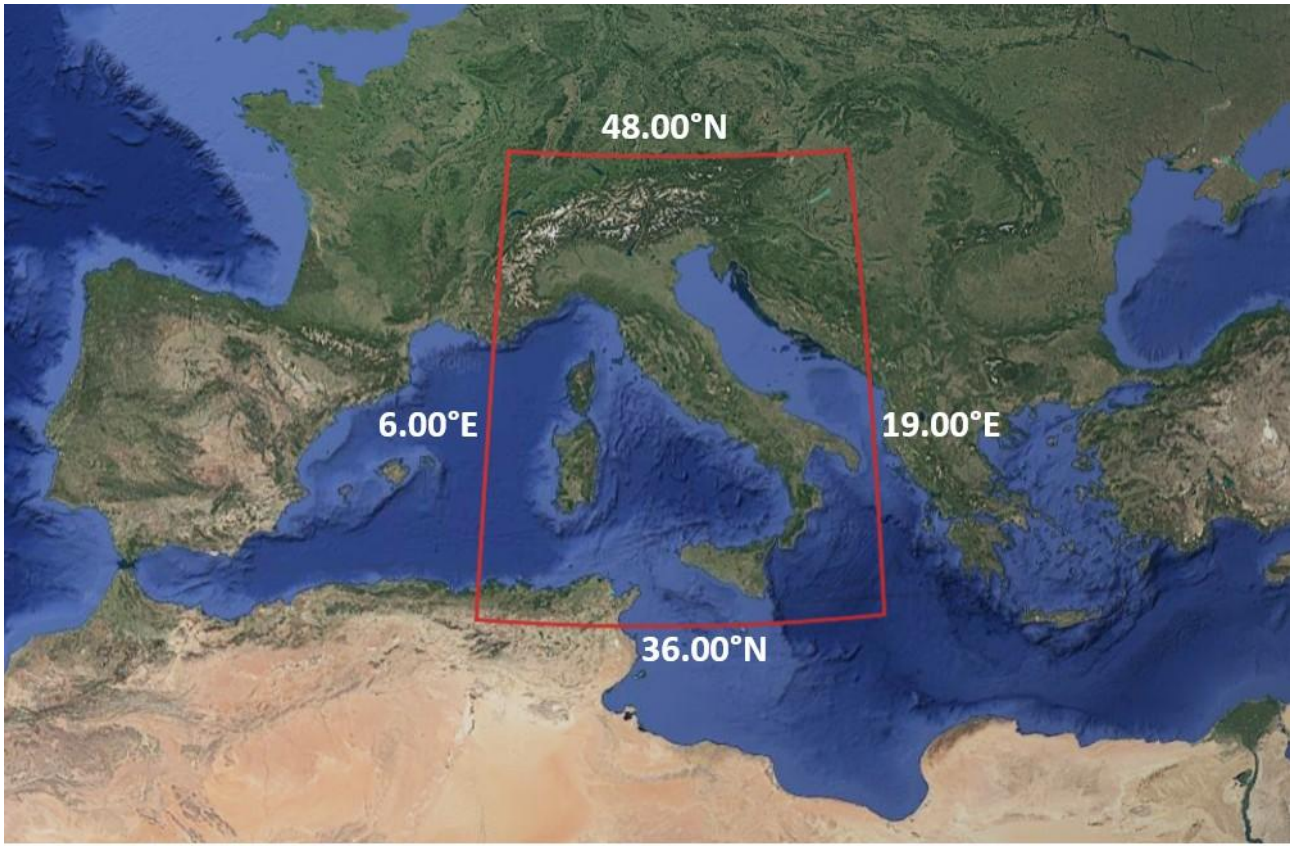

Figure 41. The red box surrounds the Italian Peninsula ranging in latitude from 36.00°N to 48.00°N and in longitude from 6.00°E to 19.00°E (Images credit: © Google Earth, Data Sio, NOAA, U.S. Navy, NGA, GEBCO).

The lightning activity examination on the Italian territory starts counting the number of discharges detected by LAMPINET every year, from 2015 to 2023. This first result is shown in Figure 42a, in which it can be noted that the number of strikes detected ranges from the minimum of 3.7 million in 2017 to a maximum of 7.9 million in 2018. However, no significative trends are found considering this time series. In Fig. 42b, the same result is plot as a function of each month of the year, while the red vertical line indicates the beginning of a new year. This second graph lets us understand the importance of seasonality with respect to lightning activity. Indeed, for each year considered, the peak of lightning activity is always detected from June to October whereas the minimum number of strikes is mainly found during the winter season, ranging from January to March. This seasonal trend can be well correlated to the thunderstorm activity that happens in the central area of Mediterranean Basin: van Delden (2001) states that, during the warm season (April to October) in western Europe, thunderstorms are more numerous in the vicinity of the Alps and that further South, the Mediterranean sea is an important source of warm moist air at low levels, especially in the second half of the summer season. Galanaki et al. (2018) confirm that thunderstorm occurrence is more frequent in summer, overland, while

winter and autumn thunderstorms are less frequent, but their majority takes place over the sea. In addition, Taszarek et al. (2019) show that thunderstorm activity peaks during summertime with a rapid increase in April and a decrease in October in Northern Italy whereas thunderstorms are more frequent from September to December, with a secondary peak in late spring, in Central and Southern Italy. Considering this time series, it can be noted that August 2018 was characterized by a much stronger lightning activity than usual, with more than 3 million strikes detected. This result is confirmed by Petracca et al. (2024), who found that August 2018 holds the absolute record among all the months analyzed from 2010 to 2022, with almost 9 million strokes.

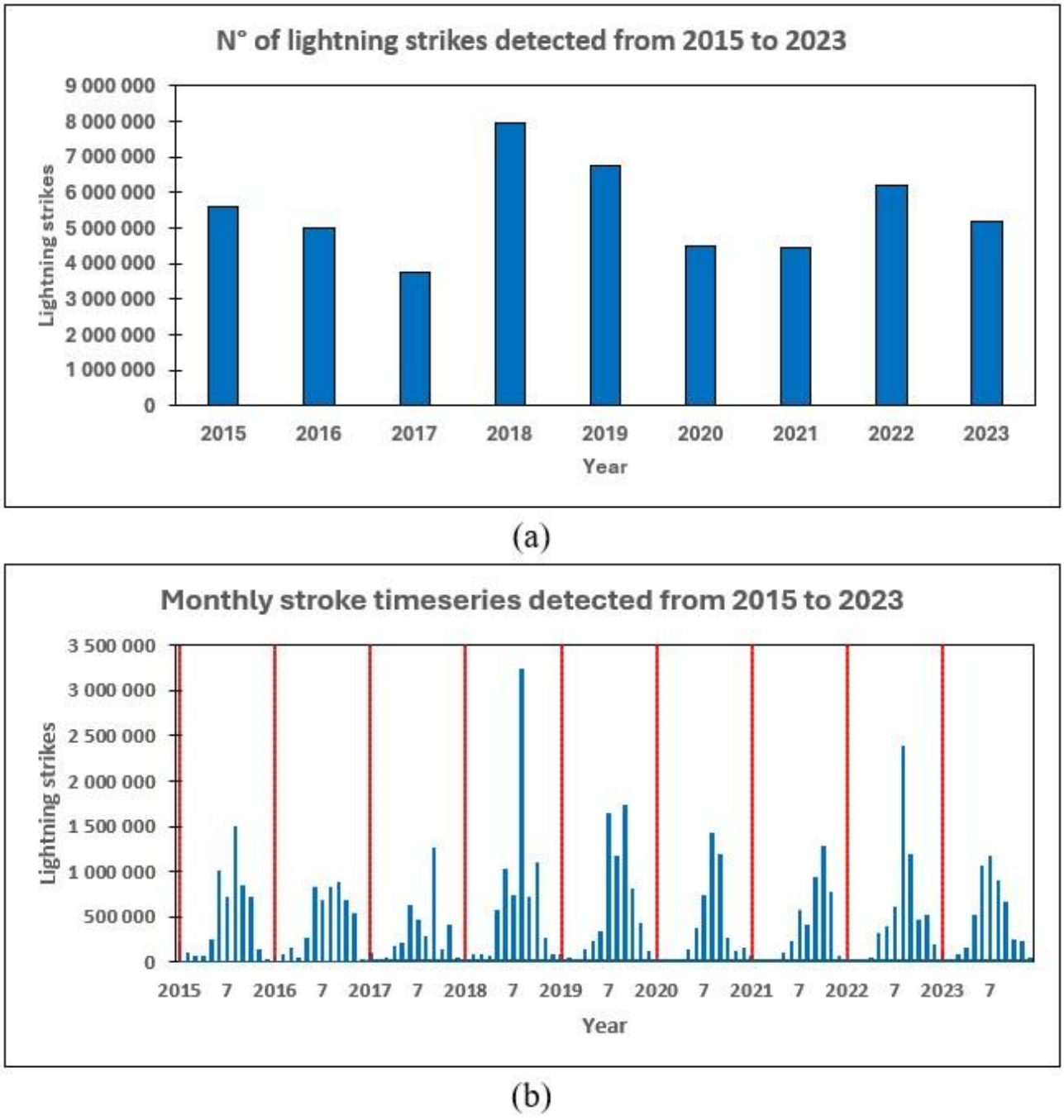

Figure 42. From 2015 to 2023, lightning discharges detected in the study area every year (a) and month (b).

The strong difference in the number of discharges measured by LINET network (3 times higher) mainly depends on the greater sensitivity of the latter, which can measure strokes with current intensities well below 1 kA. After introducing the amount of lightning discharges, we focused on the type of strikes detected by LAMPINET network in the 9-year time series. In Figure 43a, the red line represents the IC/CG ratio computed every year from 2015 to 2023 while in Fig. 43b it is shown the frequency of positive (yellow line) and negative (green line) CG current intensities.

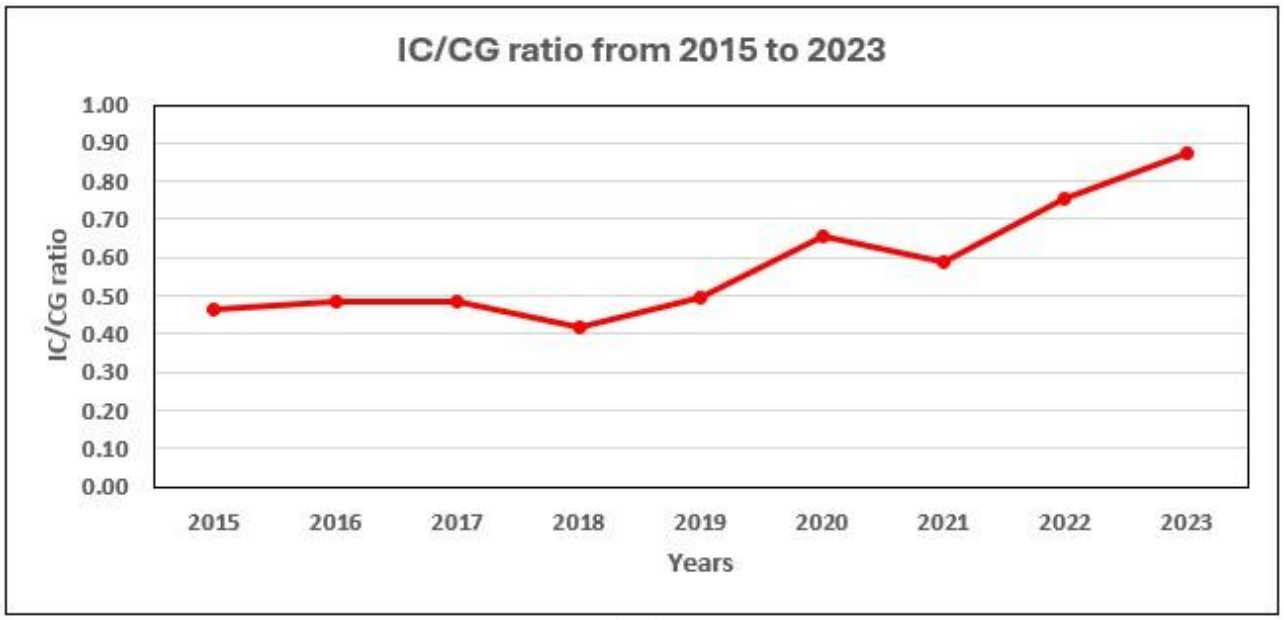

(a)

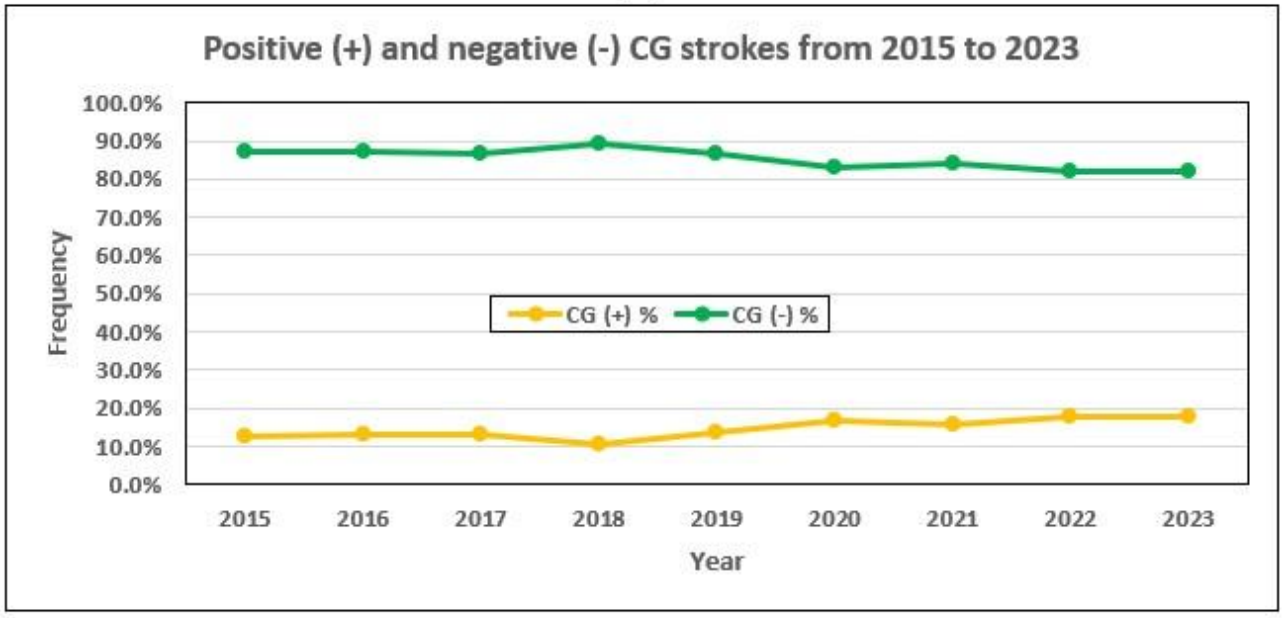

(b)

Figure 43. From 2015 to 2023, IC/CG ratio (a) and positive and negative CG strokes (b) trends are represented.

As can be seen from Fig. 43a, the IC/CG ratio oscillates between 0.42 and 0.49 in the first five years of the series, while starting from 2020, this ratio progressively increases reaching 0.87 in 2023. Previous studies state that IC/CG ratio is usually between 2.64 and 2.94 but showing anomalies ranging from 1.1 - 1.2 to 8 - 9 (Boccippio et al., 2001). Furthermore, it has been found that the IC/CG ratio abruptly increases in severe hailstorms, often reaching values from 20 to 100 (Carey and Rutledge, 1998; Montanyà et al., 2007;) and more rarely until 400 (Montanyà et al., 2009). Comparing these previous findings with the IC/CG ratio computed for LAMPINET network, it emerges that this ratio is lower than expected. Main reasons are probably linked to a poorer sensitivity to low current intensities (which mainly disadvantages IC flashes) of this network and to a DE which favors CG strokes (90%) with respect to IC flashes (20-30%). Despite that, it is true that in last four years (from 2020 to 2023), the IC/CG ratio is increasing on average, probably indicating a gradual improvement even involving the IC discharges detection. Moving to Fig. 43b, positive and negative CG strokes are characterized by a frequency of detection always between 10.7-18.0% and 82.0-89.3%, respectively. These results are in accordance with previous studies made on this topic (e.g. Uman, 2012; Rakov, 2013a), confirming a DE more reliable for CG strokes, even when the sign of current intensity is considered.

The lightning activity monthly trend (Fig. 42b) on the Italian Peninsula and surrounding areas has been better explored in the following analysis, in which the study area introduced in Fig. 41 has been split into three different boxes, named “Northern Italy” (Figure 44, blue box), “Central Italy” (Fig. 44, green box) and “Southern Italy (Fig. 44, yellow box)”.

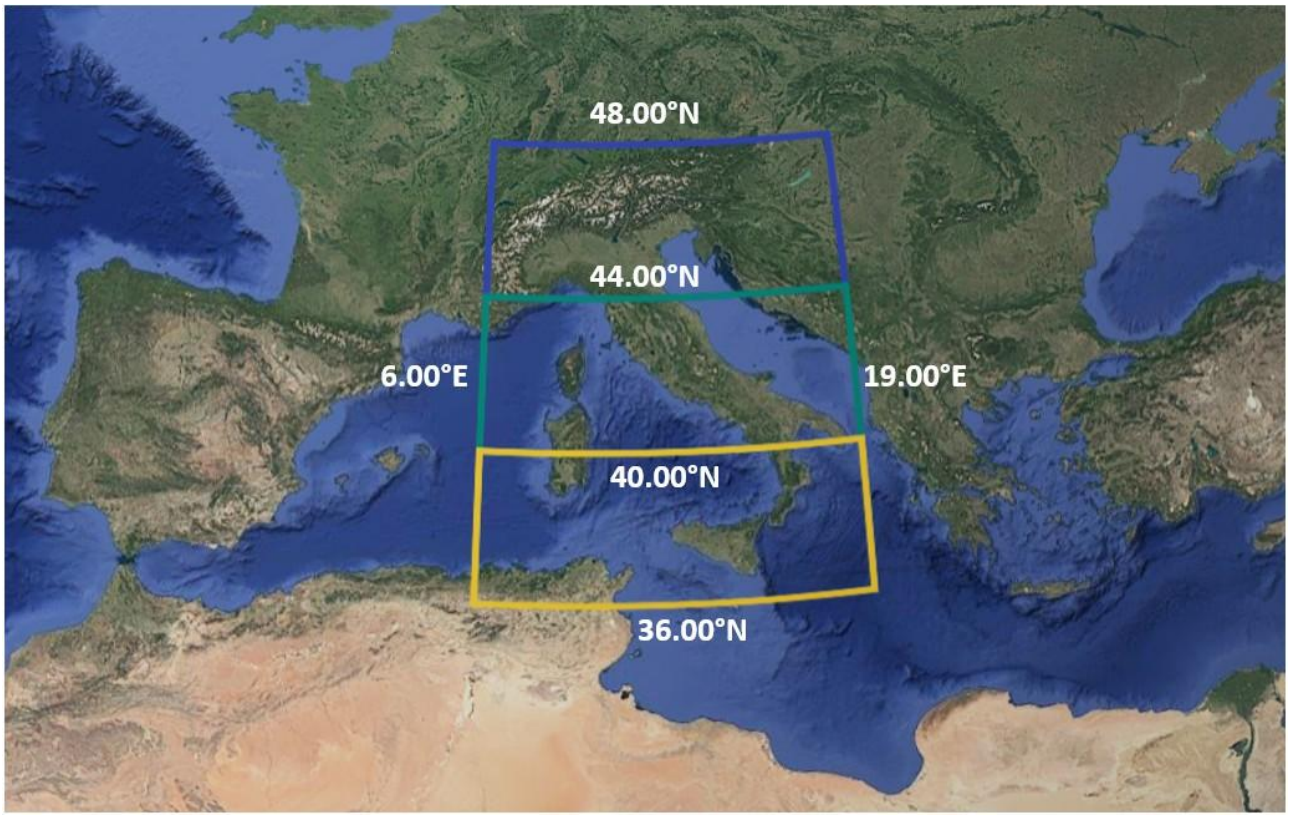

Figure 44. Three boxes surround the Italian Peninsula ranging in longitude from 6.00°E to 19.00°E and in latitude from 44.00°N to 48.00°N (Northern Italy, blue), 40.00°N to 44.00°N (Central Italy, green) and 36.00°N to 40.00°N (Southern Italy) (Images credit: © Google Earth, Data Sio, NOAA, U.S. Navy, NGA, GEBCO).

These boxes range in longitude from 6.00°E to 19.00°E and in latitude from 44.00°N to 48.00°N, from 40.00°N to 44.00°N and from 36.00°N to 40.00°N, respectively. In this way, lightning strikes counted during the 9-year time series have been distributed in three sub-regions, according to the three above-mentioned boxes. In Figure 45, for each month, the aggregated number of lightning strikes from 2015 to 2023 has been plotted for Northern Italy (blue bars), Central Italy (green bars) and Southern Italy (yellow bars). In this 9-year period, the total number of discharges detected by LAMPINET is about equal to 15.7 million in Northern Italy, 19.0 million in Central Italy and 14.7 million in Southern Italy. As highlighted in Fig. 45, even if the highest number of discharges has been counted in Central Italy, the distribution of lightning strikes among the three sub-regions is quite different and can be approximatively divided in two main time periods. The first one is the five-month time window going from December to April, which doesn't show many fluctuations in the lightning activity pattern: in this case, Central and Southern Italy have very similar results and the only important difference regards the stronger collapse of lightning activity in Northern Italy, with the exception of the month of April. On the other hand, most strokes are counted in the whole study area from May to November, but here the different latitude range plays a crucial role in the geographical distribution of strokes. Looking at Fig. 45, starting from May, Northern Italy experiences a strong increase in lightning activity until reaching the peak in July: after that, the number of discharges slightly decreases in August before strongly dropping during September and October.

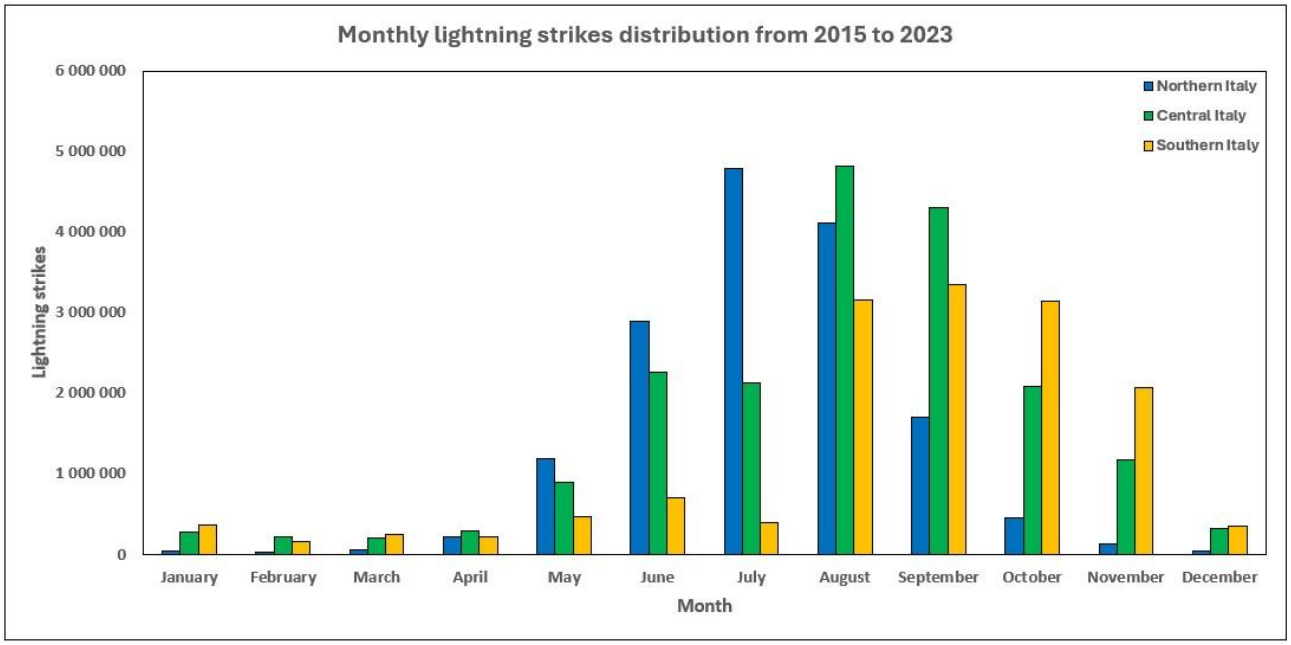

Figure 45. For each month, the aggregated number of lightning strikes detected from 2015 to 2023 is depicted.

In Central Italy, the rise of lightning activity is similar to Northern Italy among May and June, but in July the number of discharges remains nearly constant. In this region, the lightning peak occurs in August, one month later with respect to Northern Italy, with a strong lightning activity that even maintains in September. The strokes decay is observed among October and November, reaching a final plateau in December. For Southern

Italy, going from May to July, the lightning trend is very similar to Central Italy, but discharges counted are much lower (even in this case a secondary peak occurs in June). For this region, the lightning peak is wider, involving three consecutive months (August, September and October) in which more than 3 million strikes are detected. In this case, lightning activity is still high in November (which represents the 4th month in terms of strikes number for Southern Italy), before permanently dropping during December. All these trends and results are in accordance with thunderstorm activity in the Mediterranean Basin described by Taszarek et al. (2019). This general characterization has been deepened taking into account the yearly variability for the eight more active months of the year. Thus, in Figure 46, the number of strikes detected has been plotted every year going from 2015 to 2023 and each panel represents one month moving from April (Fig. 46a) to November (Fig. 46h). The yearly analysis begins from April, in which lightning strikes are generally very low and reduced to few tens of thousands in all regions. During May (Fig. 46b), lightning activity increases especially in Northern Italy, which is the dominant region except for the years 2020 and 2023. This trend also repeats in June (Fig. 46c) and July (Fig. 46d), which is the most active month for Northern Italy. Indeed, the latter always shows the maximum number of strokes measured in the whole study area during June and July, apart from June 2023. In this framework, it is also interesting notice the mirror behavior of lightning activity along the Italian Peninsula, with Southern Italy that is always characterized by the minimum result. The lightning trend modifies in August (Fig. 46e), both in terms of number of discharges and regions involved. The strong annual variability is testified by an alternance of years like 2017 and 2021 in which strikes are very low in all sectors and years such as 2018, 2020 and 2022, which contain the first four months with the highest number of discharges in the 9-year time series (1.4 million in Southern Italy in 2018, 1.2 million in Central Italy in 2018, 1.1 million in Central Italy in 2022 and almost 1 million in Northern Italy in 2020).

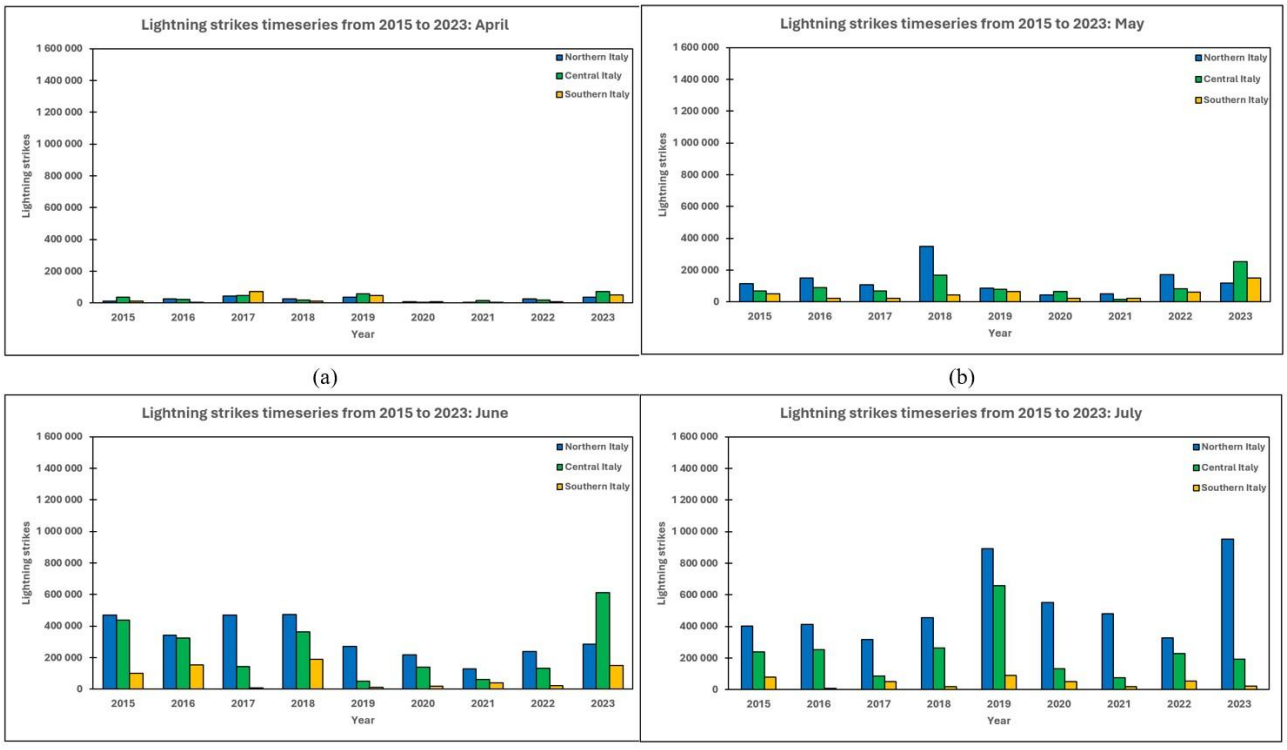

(a) (b)

(c) (d)

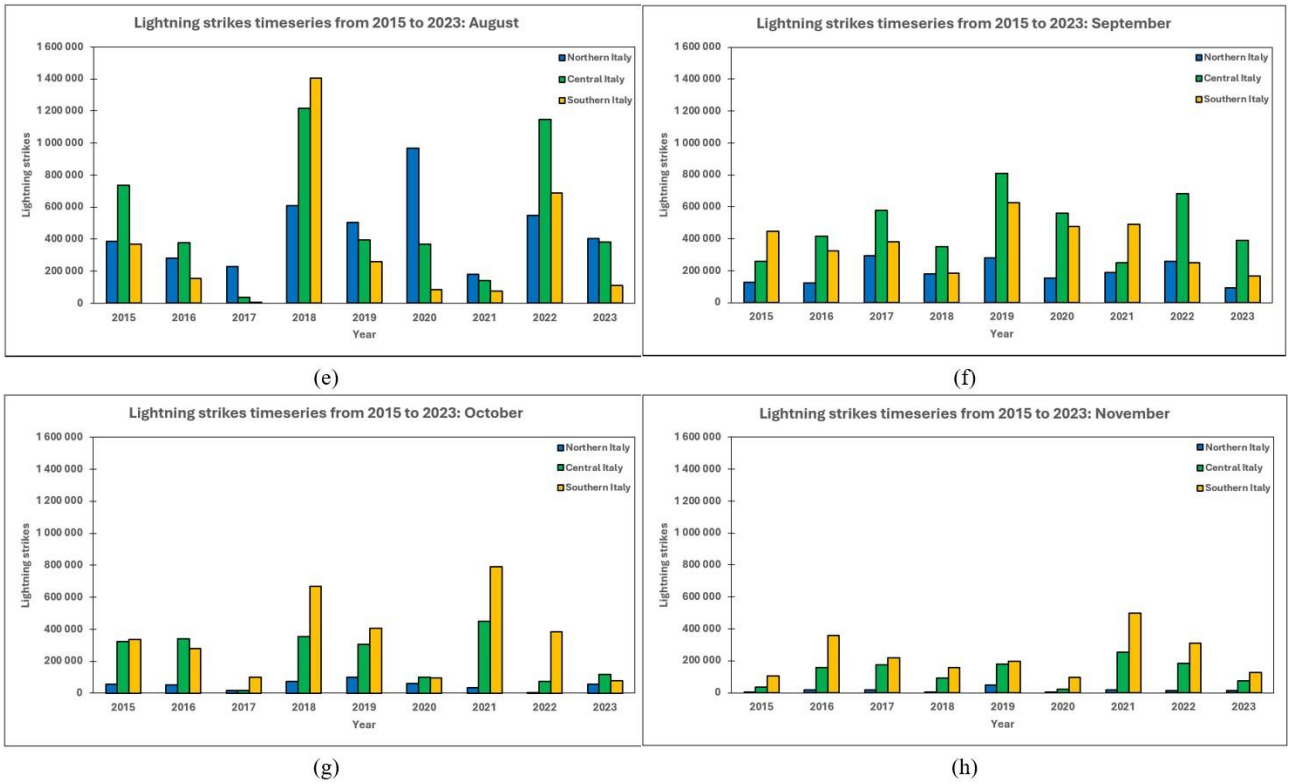

Figure 46. For every year, from April (a) to November (h), the lightning strikes trend is shown in Northern, Central and Southern Italy.

In addition, the lightning activity predominance in Northern Italy starts decreasing, with the maximum number of strikes reached in Central Italy in 2015, 2016 and 2022 and in Southern Italy in 2018. The lightning activity mirror behavior starts reversing in September (Fig. 46f) and goes on in October (Fig. 46g) and November (Fig. 46h): in these three months, the minimum number of strikes always occurs in Northern Italy, with the only exception of September 2022. Regarding Central and Southern Italy, it can be seen a gradual predominance inversion moving from September (Fig. 46f), in which Central Italy peaks for both cumulated discharges (Fig. 45) and years leaded (apart from 2015 and 2021), to November (Fig. 46h), in which lightning activity in Southern Italy is always prevailing. From this analysis, it emerges that August is the month characterized by the highest variability both in terms of number of strikes and regions involved. For better visualizing the main lightning activity patterns, the August lightning maps on the Italian Peninsula for the whole 9-year period, from 2015 (Fig. 47a) to 2023 (Fig. 47i), are provided in Figure 47. These figures were produced by remapping strokes on a 6×6 km^2 regular grid, giving out for each grid cell the total number of strikes detected in one month, i.e. the total lightning (hereafter, TL). As previously discussed, August 2017 (Fig. 47c) and August 2021 (Fig. 47g) show the lowest lightning activity trend: for both years, weak TL peaks are found in Northeastern Italy whereas in remaining areas TL is very shallow, especially in 2017. August 2015 (Fig. 47a), 2016 (Fig. 47b), 2019 (Fig. 47e), 2020 (Fig. 47f) and 2023 (Fig. 47i) are characterized by an intermediate lightning activity and by a wider distribution of TL peaks: in particular, they are found in the inlands of Northern and Central Italy, and along the Ligurian and Adriatic Sea.

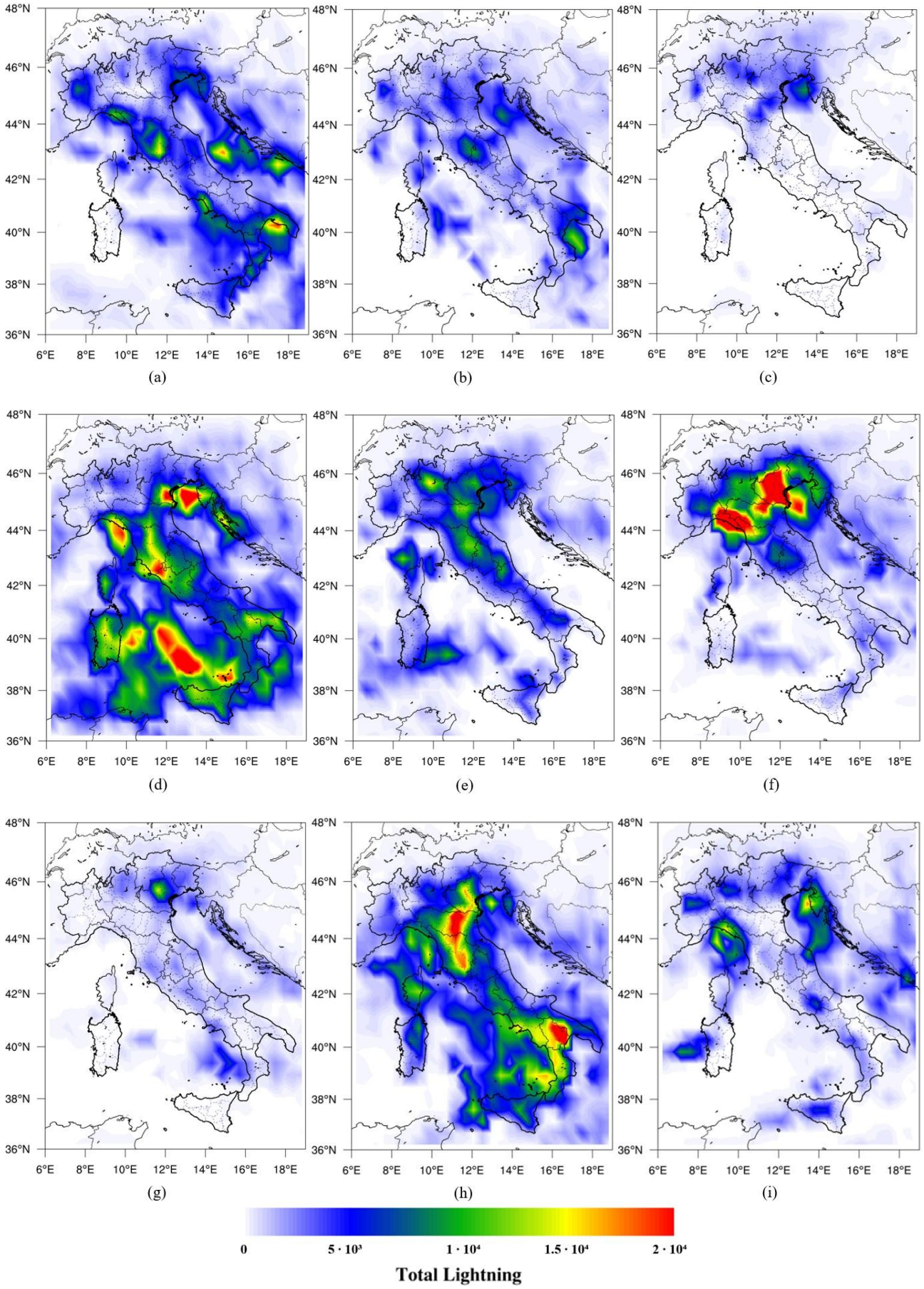

Figure 47. For the whole study area, August lightning activity maps from 2015 (a) to 2023 (i).

A particular case is represented by August 2020 (Fig. 47f), in which discharges are almost all focused on Northern Italy, with clear TL peaks going from Eastern Liguria to Po Valley and Northern Adriatic Sea. However, the strongest lightning activity has been detected during August 2018 (Fig. 47d) and, secondly, in August 2022 (Fig. 47h). In 2018, strong TL peaks occurred throughout the Italian Peninsula, with the absolute record of strokes detected that belongs to Southern Italy, mainly driven by an intense and extended pattern observed in the Southern Tyrrhenian Sea. Other areas having high TL were Northern Adriatic Sea, Eastern Liguria and Central Italy Tyrrhenian regions. Finally, Central Italy exhibited the strongest lightning activity for August 2022 (Fig. 47h), in which two main TL peaks happened in Tuscany and in Basilicata regions.

Chapter 4 Preliminary investigations about the relationship between hailstorms and lightning activity

After having introduced general aspects of hailstorms and lightning activity, in this chapter two first exploratory studies are proposed to better investigate the relationship between the formation and evolution of the hailstorms and lightning activity occurring in the storm systems. In the first one (Section 4.1), thunderstorms producing very large hail, lightning activity associated with them and hail reports recorded in the ESWD (https://eswd.eu/) have been analyzed (Vermi et al., 2025). In this work, the maximum size of the hailstones was compared with some lightning strikes related variables, such as the total lightning, lightning jump and lead time.

In the second part of this chapter (Section 4.2), a similar analysis has been performed for 16 hailstorms that occurred in Campania Region (Southern Italy), exploiting lightning data provided by the European Lightning Network "LINET". In this case, results were comparable to those found for LAMPINET dataset but in addition, other interesting outcomes emerged, being associated with the type (IC or CG) of strokes detected by the LINET network during the hailstorms development.

4.1 Lightning jump as precursor of very large hail occurrence: first evidence in the Italian territory

4.1.1 Introduction

In the previous chapter, we introduced the main mechanisms and processes related to the electrification of clouds, showing that lightning strikes can be considered a very good proxy for thunderstorm activity, as confirmed by the comparison between the climatology of thunderstorms and lightning trends found on the Italian Peninsula. In addition, in Section 3.2, we saw that the electrification process occurring in thunder clouds is mainly due to the presence of ice crystals and graupel, which can lead to the production of hailstones having large size, also depending on the intensity of the updraft. In the past, many studies tried to classify the intensity of the hailstorms (in terms of heavy rain, flash floods, large hail, wind gusts and tornadoes) starting from the total lightning detected during the development of thunderstorms. For instance, Williams et al. (1999) investigated the maximum total flash rate in storms occurred in Florida from 1996 to 1998, classifying them between non-severe and severe (large hail above 1.9 cm, wind gusts exceeding 50 knots or tornado occurrence) events. As depicted in Figure 48, the authors found that severe storms (red bars) were always characterized by a lightning rate of at least 60 flashes per minute, with some case studies exceeding 300 flashes per minute.

However, this threshold is only valid for severe thunderstorms because non-severe ones are found even above this lightning rate.

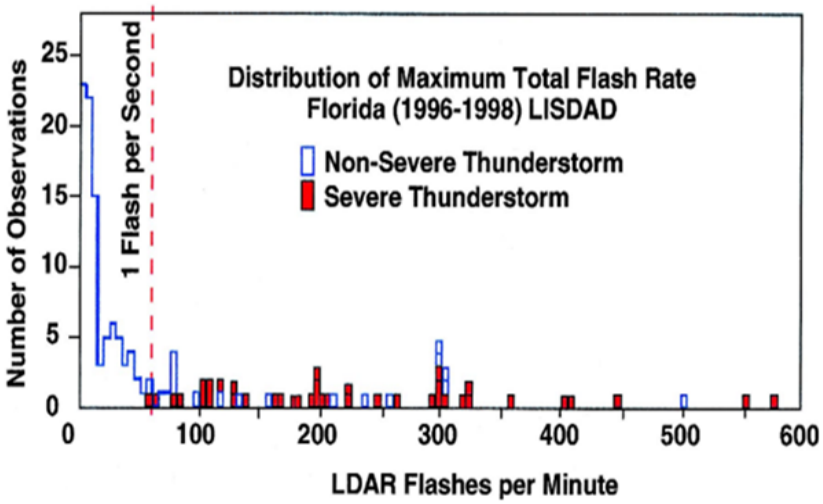

Figure 48. Lightning rate per minute (from 0 to 600) as a function of number of thunderstorms analyzed. Severe phenomena (red bars) only occur when the lightning rate is above 1 flash per second (adapted from Williams et al. 1999).

Many other works suggest that the increase of lightning rate may indicate the occurrence of more severe hailstorms and the upcoming falling of hailstones on the ground (Changnon, 1992; Saunders, 1993; Montanyà et al., 2007; Montanyà et al., 2009; Yao et al., 2013; Jurković et al., 2015; Tian et al., 2019). Starting from the total number of lightning strikes (TL), Schultz et al. (2011) examined 711 thunderstorms in four regions of the United States and found that the TL is the best information to recognize the most intense storms, while Feng et al. (2007) determined that there is a good correlation between ice water content and TL during the hailstorms. The rapid increases in total lightning activity (intracloud + cloud-to-ground) have been termed lightning jumps (LJ) by Williams et al. (1999). Some studies have developed and tested different LJ algorithms, trying to investigate the relationship between LJ and severe weather phenomena occurred at the ground (Schultz et al., 2009; Gatlin and Goodman, 2010). In particular, Schultz et al. (2009) proposed six LJ algorithm configurations, evaluating their performance in terms of probability of detection (POD), false-alarm rate (FAR), critical success index (CSI) and Heidke skill scores (HSS). In addition, they found that LJ usually occurs tens of minutes before hail ground observations, reporting average lead times of about 23 minutes. Gatlin and Goodman (2010) developed a total lightning algorithm that exploits the link between rapid increases in the total flash rate, updraft intensification and severe weather, thanks to the LJ identification. Some of these methods were reused in order to nowcast hail (Tian et al., 2022), establish a relationship with heavy rain episodes (Farnell and Rigo, 2020) or modify them expanding the period of time in which a LJ is considered (Chronis et al., 2015). Farnell et al. (2017) tested 48 cases of severe weather (hail, tornadoes and strong winds) in Catalonia, using a modified LJ algorithm proposed by Schultz et al. (2009). The authors reported that the percentage of success was close to 75% while the false alarms are equal to 10%. LJ were detected between 90 minutes before and 30 minutes after the severe weather observation, but in most of the analyzed case studies

the lead time ranged from 15 to 45 minutes. Wapler (2017) confirmed similar results, showing that lightning density is much higher in hailstorms with respect to ordinary thunderstorms. In addition, a LJ occurred in more than 75% of cases well before the observation of hail, with lead times that are tipically between 0 and 45 minutes.

In this work, an analysis of 10 hailstorms occurred in the Italian Peninsula is presented. The main goal of this study is to examine the features of lightning activity that characterize the most important and harmful hailstorms, especially considering the stages in which strokes intensificate and very large hail is detected. In addition, a new method for investigating the relationship between LJ and very large hail (≥ 5 cm) occurrence has been proposed. Indeed, in the past, several works developed different LJ algorithms to infer the formation and evolution of severe thunderstorms or the worsening of atmospheric weather conditions. However, in this work, we consider only large hail as the main atmospheric phenomenon to be investigated. Taking into account that this type of analysis was never carried out on the Italian Peninsula and the time required to the hail formation process, we decided to introduce a new formulation useful to understand what are the stages in which lightning activity strongly increases and how this trend can be potentially related to large hail observations. This work is organized as follows: Section 4.1.2 describes the information provided by hail reports and lightning data and introduces a new method to detect LJ. In Section 4.1.3, the main results regarding lightning activity, LJ detection and lead times are reported, while the conclusions of this study are summarized in Section 4.1.4.

4.1.2 Data and Methodology

To investigate the relationship between hail and lightning strikes, 10 case studies (Table 5) have been selected using hail reports recorded in the European Severe Storm Laboratory's European Severe Weather Database (ESWD) (Dotzek et al., 2009; Hulton and Schultz, 2024): five occurred in Northern Italy, two in Central Italy and three in Southern Italy. Sometimes, especially considering the maximum hail diameter, these measures can be approximate so it has been decided to select only events in which at least 5 observations with hailstones having a diameter of at least 5 cm were reported. This criterion leads to a double advantage because minimizes the risk of considering minor phenomena emphasized by erroneous measurements, focusing on the most dangerous and harmful hailstorms which produced very large hail. At the same time, it allows to monitor the trajectory of the hailstorms thanks to the high number of hail reports. However, ground observations depend on many factors such as popoulation density, orography and human activities so it is possible that similar or even larger hailstones have affected the same or the nearby areas. Lightning measurements are provided by the National Lightning Network LAMPINET managed by the Meteorological Service of the Italian National Air Force. LAMPINET data used in this work are available for the entire national territory on both inlands and coastal areas from 2015 to 2022. Data sources have a punctual geolocation and for each stroke time, latitude, longitude, type (intracloud or cloud-to-ground), polarity and electric field value are reported. For each case

study, Table 5 provides information about time of occurrence (day-month-year), region or area affected by the hailstorm and hail maximum diameter detected.

Table 5. Date, location, maximum hail diameter (cm) and identification code of the analyzed hailstorms. The information regarding the maximum hail diameter has been retrieved from ESWD (https://eswd.eu/, last access on 09/01/2025).

Date	Italian region or area	Maximum hail diameter (cm)	Identification code
05/09/2015	Campania	12	G
10/07/2019	Abruzzo	14	C
10/07/2019	Puglia	10	F
08/07/2021	Lombardia	11	B
08/07/2021	Veneto	6	D
26/07/2021	Emilia-Romagna	6	A
07/07/2022	Emilia-Romagna	9	J
18/08/2022	Liguria	7	I
18/08/2022	Central Italy	11	E
19/08/2022	Puglia	10	H

It should be noted that in Table 5 each hail event is labelled with an identification code, which will be employed in the next manuscript sections to univocally indicate a specific case study. Data processing starts with the organization of each stroke measurement in 10-minute files for studying the entire life cycle of the hailstorms. After that, lightning strikes are counted using a regular grid to find out the TL in each grid cell in the previous 10 minutes. Two examples of this first elaboration (case studies D on the left and I on the right) are shown in Figure 49a-b, using 10-minutes TL maps which are very useful for comparing the trajectories of the hailstorms with the hail reports that are represented with red filled dots. The second part consists in identifying the storm system and performing a series of statistical analysis regarding TL, LJ occurrence and lead times. In order to avoid computational errors and the incorporation of strokes not directly connected to the investigated storm, for every 10-minute step, a rectangular box (shown in dark red in Fig. 49a-b) has been centered around the maximum TL grid cell, following the thunderstorm evolution until the dissipative stage. The box dimensions are variable and adaptable considering that the extension of the hailstorms modifies every minute and also it varies case by case. Indeed, the analysis of lightning activity allows us to understand if clouds are electrified and in which steps of the hailstorm life cycle the growth of the lightning rate is more important. As stated in Section 4.1.1, many works conducted over the past several years have determined that TL is the best variable for studying the relationship between lightning activity and severe atmospheric conditions. Moreover, another important element of these previous works is the so-called LJ which appears in many of the developing severe thunderstorms. Basing our study on these existing concepts, here we deal with a sensitive topic that has never been explored on the Italian Peninsula. Moreover, in this work we solely focus on the relationship between ground hail observations (whose temporal resolution generally moves from 5 to 10 minutes) and the evolution

of lightning activity (TL, LJ and lead time computation) for understanding what are the links between lightning strikes and the hail formation process. In addition, LAMPINET sensors operate in a frequency range between 1 and 350 kHz (e.g. in Chronis et al. (2015) the lightning detection networks cover a wide frequency range, spanning from 1 Hz to 12 MHz) reaching a detection efficiency of about 90% for cloud-to-ground strokes, while the detection efficiency for intracloud flashes decreases to 30% (Biron, 2009). For these reasons, considering the exploratory approach of this study, we have decided to apply a general relaxation of the threshold values used in previous works. In particular, the best choice for our analysis is a 10-minute window which takes into account the temporal uncertainty of the hail measurements, mantaining a threshold value equal or higher than 10 lightning strikes every 10 minutes to assess a potential LJ detection.

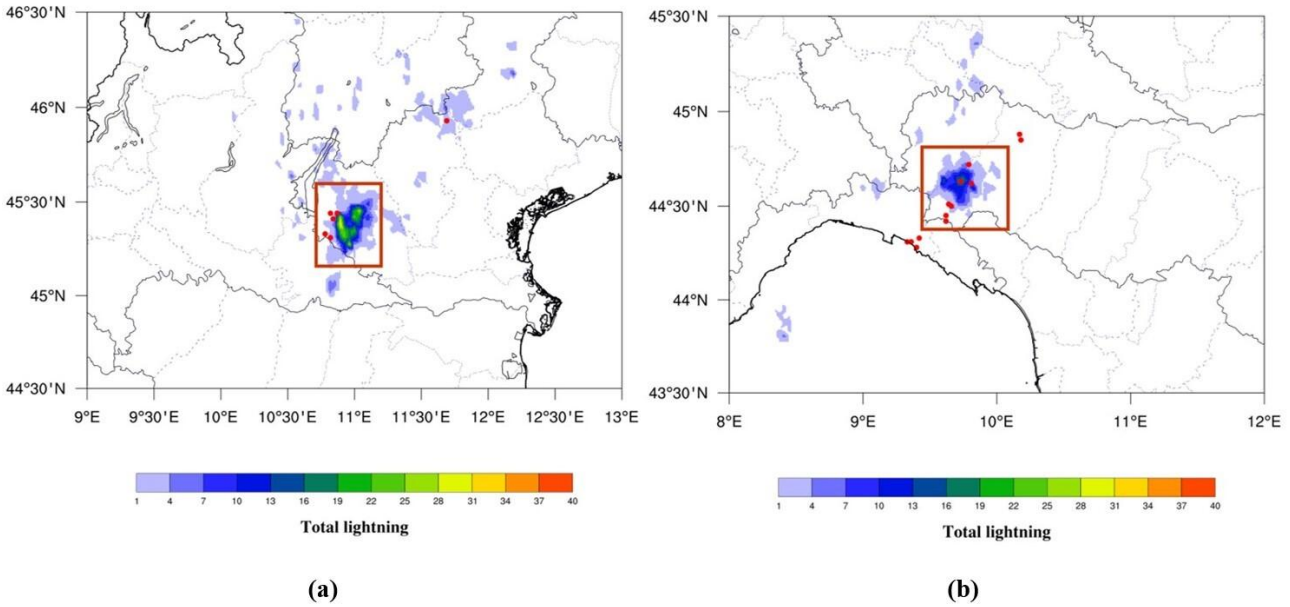

Figure 49. 10-minute total lightning maps for the hailstorms that affected the Veneto region (**a**, identification code **D**) on 08 July 2021 (17:50 UTC) and the Liguria and Emilia-Romagna regions (**b**, identification code **I**) on 18 August 2022 (05:40 UTC). Hailstones measured for event D and event I reached dimensions of 6 and 7 cm in diameter, respectively. For both case studies, red filled dots represent hail reports recorded during the whole hailstorm evolution (Source: ESWD). For each 10-minute temporal window, the rectangular box depicted in dark red surrounds the area in which lightning strikes have been counted.

Consequently, to evaluate the trend of lightning activity, we have introduced a new mathematical approach that is constituted by the three following equations:

$$LJ_{20} = \frac{TL_t}{TL_{t-20}} \quad (7a) \qquad LJ_{30} = \frac{TL_t}{TL_{t-30}} \quad (7b) \qquad LJ_{40} = \frac{TL_t}{TL_{t-40}} \quad (7c)$$

The Equations (7a – 7b – 7c) calculate the LJ as the ratio between the total lightning at time t (TL_t) and the total lightning recorded 20, 30 or 40 minutes before the observation at time t (TL_{t-20}, TL_{t-30} and TL_{t-40}), respectively. To compute the LJ, only thunderstorms producing at least 10 lightning strikes every 10 minutes have been considered: below this value, the number of strokes is not significant enough to describe the LJ phenomenon. Usually, the lightning rate rises very fast, so a time step from 20 to 40 minutes has been selected.

Finally, the lead time is calculated as the time difference between the first hail report recorded in the ESWD and the LJ detection.

4.1.3 Results and Discussion

In this Section, the results about connections between lightning activity and very large hail occurrence are presented. Analyzing the TL, an abrupt increase in the number of strokes (almost always up to several hundred) is usually observed in the developing stage of these hailstorms. This trend is evident in most case studies (e.g. Figure 50a-b, hail cases D and I respectively) and it could be used to infer the possible formation of hailstones in hail clouds before they reach the ground. On the other hand, there are some exceptions in which TL starts rising slowly and a strong increase is detected only after many hail observations have been reported (case studies F and J, see the supplementary material in Appendix A). If the entire hailstorm life cycle is investigated, it emerges that the growth of the lightning rate can start with an approximate linear (Fig. 50a, red arrow) or exponential trend (Fig. 50b, red arrows) (linear and exponential fit and related hypothesis tests are provided in the supplementary material for hail events D and I, see Appendix A).

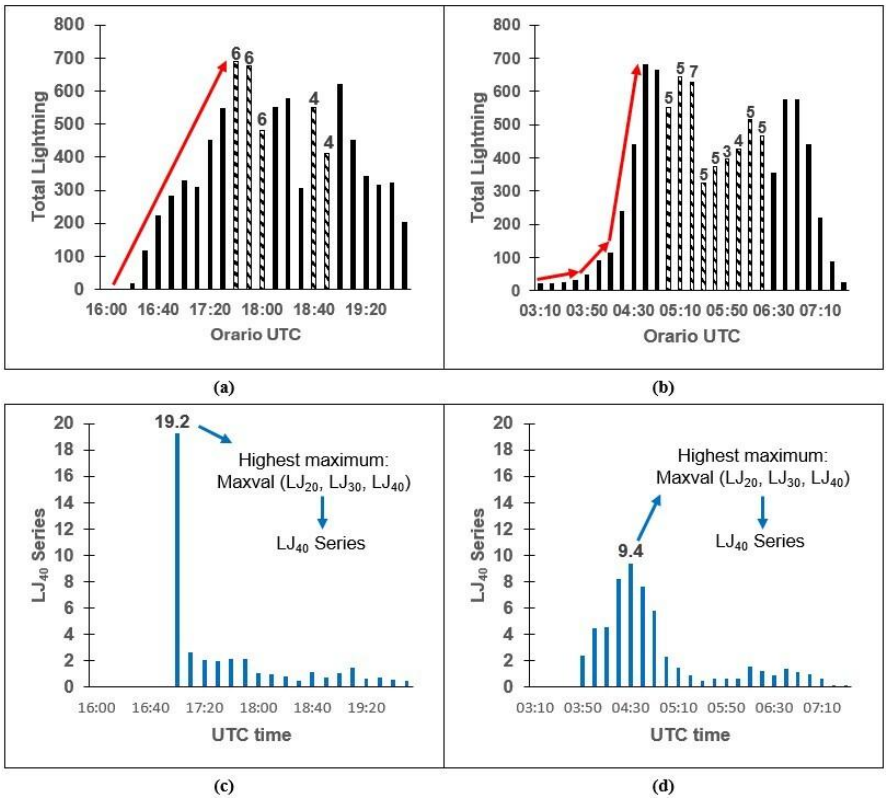

Figure 50. Ten minutes TL and LJ_{40} time series for the case studies D (on the left) and I (on the right). The red arrows indicate the approximate linear (**a**) and exponential (**b**) TL trend. The dashed columns (**a-b**) highlight the 10-minute steps in which at least one ground hail observation has been recorded: the corresponding label above each column shows the maximum hail diameter detected for that 10-minute temporal window. For both events, the LJ_{40} series contains the highest maximum computed for each hailstorm: 19.2 (**c**) and 9.4 (**d**).

Then, after the maximum is reached, this trend interrupts and the lightning activity becomes irregular. In Fig. 50a-b, the dashed columns represent 10-minute intervals in which at least one ESWD hail observation has been recorded while the label above the column indicates the maximum hail diameter detected for the same 10-minute temporal window. So, when TL is compared to the ground hail measurements it can be noticed that an increase of TL does not always result in the formation of larger hailstones. Even more, sometimes it occurs that for one or more consecutive 10-minute steps characterized by a TL like the previous one there are no hail observations in the ESWD database (analogue results have been found for the other case studies, shown in the supplementary material in Appendix A). This trend could be partially explained by a lack of ground hail measurements but also considering the complex evolution mechanism of these hailstorms. From a spatial point of view, it can happen that the area in which lightning activity is very strong is not the same where the largest hailstones reach the ground. This situation is very common and is due to the vertical structure of the hailstorms and many atmospheric features such as updraft and downdraft that contribute to the hail formation in convective clouds and the development of strong horizontal wind gusts. As a result, in some hail events, there are areas where the lightning activity is much lower, but the size of the hailstones is similar or even larger than that is affecting zones with higher flashes number. For these reasons, the LJ and lead time computation could introduce further improvements in the recognition and characterization of the hailstorms. LJ has been calculated using the Equations (7a-7b-7c): each of them leads to the computation of the temporal series at 20 (LJ_{20}), 30 (LJ_{30}) and 40 (LJ_{40}) minutes, respectively. Subsequently, the maximum value of each LJ series (at 20, 30 and 40 minutes) is selected. Finally, the highest value among the three LJ series maxima has been selected to retain information that best synthesizes the magnitude of the lightning activity increase. Usually, a single very important maximum is observed when the TL growth can be approximated with a linear trend (Fig. 50c, case study D). On the other hand, when the trend is more like an exponential (Fig. 50d, case study I), it is interesting notice that the increase of lightning activity is subdivided in many 10-minute steps which reach similar values (for the event I, 9.4 is the highest maximum of the LJ_{40} series) typically occurring, consecutively, around the highest maximum found. So, in the latter case, the LJ phenomenon must be explained also considering this behaviour, which points out that the strong increase of TL involves more than one 10-minute step. The Equations 7b and 7c, in which a time difference of 30 and 40 minutes is considered between two TL observations, respectively, allow us to find the highest maximum for almost all the case studies with respect to the Equation 7a, with frequencies that reach 60% (6/10) for the LJ_{40} series and 30% (3/10) for the LJ_{30} series (Table 6). Nevertheless, it may be possible to consider even larger temporal windows (e.g. 50 minutes or longer) but this hypothetical increase doesn't ensure to obtain better results and, simultaneously, it would bring to a worsening of lead times computed, as it will be discussed at the end of this Section. On the other hand, the use of the LJ_{10} series would improve the lead time calculation but, at the same time, the highest maximum found would be constantly lower with respect to the LJ_{20}, LJ_{30} and LJ_{40} series, so it would represent only partially the increase of lightning activity that characterizes the hailstorms analyzed. Considering the analysis performed on the selected very large hail events, Figure 51 shows that for all case studies the LJ rapidly grows from 4.5 to 35.5 times, according to the LJ series chosen for each event investigated.

Table 6. Number of instances in which a determined LJ series (computed using Equations 7a-7b-7c) captures the maximum LJ for the hailstorms investigated.

Series	Frequency of the highest maximum	Case study
LJ_{40} Series	6/10	B-D-E-F-H-I
LJ_{30} Series	3/10	A-C-G
LJ_{20} Series	1/10	J

Very high LJ values found for many of the investigated hailstorms can be interpreted, from a physical point of view, as a proxy of the rapid increase and growth of ice crystals, graupel and hailstones in those evolving storm systems. So, the analysis regarding lightning strikes and large hail benefits from the LJ introduction because it helps to understand the evolution of the whole storm system, even if, taking into account only the highest maximum, the hail size does not increase with the LJ values represented in Fig. 51.

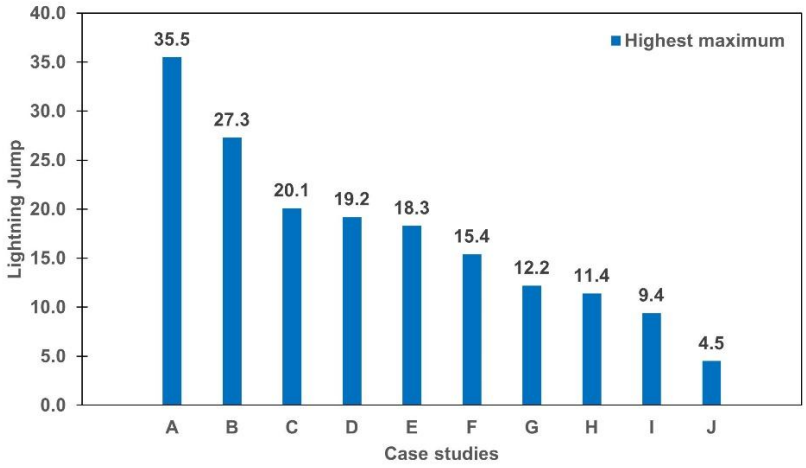

Figure 51. Highest (blue bars) maximum observed for each hailstorm analyzed. LJ values move from 35.5 (case study A) to 4.5 times (case study J)

In fact, if we consider lightning activity and the areas affected by the hailstones, there is not always overlap between them and the largest hailstones can be detected some kilometers away from the location of the highest number of flashes: for this reason, the findings of this analysis suggest that, when the LJ occurs, all the region ahead of the hailstorm should be marked with the same hail risk. These preliminary results demonstrate that for all the events considered, an increase of lightning activity has always been recorded, even if it is highly variable, depending on case by case. However, this dataset should be enriched as well as being compared with non-producing hail events, in order to strengthen these preliminary achievements. Another important outcome is obtained by the lead time (LT) introduction, which is defined as the difference (in minutes) between the time of the first hail report and the time of LJ detection. Consequently, LT will be positive when LJ anticipates the

first ground hail observation, while, in the opposite case, LT will be negative. LJ is in advance of the first hail observation in 5/10 events analyzed, reporting lead times from 10 to 60 minutes. For the case studies A and B, LJ values match with the first ground hail measurement, considering a tolerance of ± 10 minutes, which corresponds with the TL temporal window. For the remaining three hail events, the comparison between the first hail report and the highest maximum shows that LJ value is detected with a delay of more than 10 minutes. These results are summarized in Table 7.

Table 7. Case studies are classified in three categories, depending on the lead time (LT) calculation. In 5/10 hail events, LJ is detected in advance ($LT > 10$ minutes), in 2/10 case studies LJ is coincident ($10 \leq LT \leq -10$ minutes) and in 3/10 events LJ is in late ($LT < -10$ minutes).

	Advance (LT > 10 minutes)	**Coincident (**$10 \leq$ LT ≤ -10 minutes)	**Late** (LT < -10 minutes)
Case study	C – D – E – G - I	A - B	F – H – J

Probably, for the event G, LT could be even higher than 60 minutes, but in this case the hailstorm formed in the Tyrrhenian Sea where the hail reports are not available. Indeed, hail and lightning activity are also not synchronized in time because, in many of these case studies, hail falls to the ground when TL is just decreasing and the LJ has been detected with some advance. For these reasons, the LJ recognition could contribute to complete the information given by the TL and it could be used as an important element to predict very large hail in advance, following the trajectories and the evolution of these hailstorms.

4.1.4 Conclusions

In this work, ten hailstorms producing very large hail and strong lightning activity have been explored. Starting from the TL indicator, this study proposes to better investigate if additional features related to the lightning activity can be useful to infer the formation and evolution of the hailstorms. Ten hail cases, occurred over the Italian Peninsula, were selected from the European Severe Weather Database and only very large hail events (≥ 5 cm in diameter) were considered while lightning measurements were provided by the National Lightning Network LAMPINET. The most important results are:

- TL describes the different steps that characterize the evolution of the hailstorms, showing different types of behaviour from the initial stage to the dissipative one. In the first evolutionary steps, an abrupt increase in TL is usually observed, leading to a lightning rate that, in a few case studies, can be approximated with a linear or exponential trend. However, an increase of TL does not always result in the formation of larger hailstones and also ground hail measurements can be found when TL is definitely decreasing. These preliminary findings can be partially due to a lack of hail observations but need to be additionally explored;
- LJ is detected in 9/10 events using the 30 and 40-minute temporal windows: the latter seem to be a good compromise to find LJ occurrence and, at the same time, they don't overly affect the lead times

computation. Considering the whole dataset, the LJ is always detected ranging from 4.5 to 35.5 times. At the current step of this work, these values don't show a clear relationship with the maximum hail diameter detected, but further analyses should be performed on the entire group of LJ values representing the LJ series;

- In 7/10 events, LT ranges from 10 to 60 minutes (5/10 case studies) or coincides with hail reports (2/10 case studies). For the remaining hail events (3/10) LJ is observed at least 10 minutes after the first hailstones have reached the ground: the latter could be due to the limits of the computational approach which involves the use of only the highest LJ value.

Taking into account the most important results of this preliminary study conducted on 10 hailstorms occurred in Italy, the next step is to enrich this dataset with other case studies as well as exploring further features of lightning activity to strengthen these conclusions and possible future applications. It also involves the comparison between hailstorms and no producing hail events in order to check TL, LJ detection and LT behaviour in different atmospheric conditions to improve these preliminary findings. Moreover, the new mathematical approach that we presented in this work suggests considering LJ algorithms of previous works to evaluate strengths or possible differences in final results. This approach could be useful to algorithms that try to identify hailstorms in real time such as the "Multi-sensor Approach for Satellite Hail Advection" (MASHA) that is based on satellite data (Laviola et al. 2022; Laviola et al. 2020a; b) or the "Campania Region Meteorological Radar Network Project" (CARMEN) which exploits radar data (Capozzi et al. 2022).

4.2 Analysis of storm systems occurred in Campania Region through the European Lightning Network "LINET"

4.2.1 Introduction

In this paragraph, the relationship between hailstorms and strokes has been explored using the European Lightning Network "LINET" (Betz et al., 2009) for 16 hailstorms occurred in Campania Region (Southern Italy) and surrounding areas from 2012 to 2015. LINET is a spatially extended network in Europe, made by sensors operating in VLF/LF band. The maximum density of these antennas is in Central Europe, where the DE reaches 90% for CG pulses whereas is generally lower for IC flashes. Unlike results found in Vermi et al. (2025), for which no crucial information was found in the examination of the IC and CG flashes, the analysis on LINET dataset showed new interesting trends about the type of strokes characterizing these hailstorms. Indeed, some previous studies stated that a rapid increase of the IC/CG ratio can be measured during the hail-producing phase of the storms, variably moving from 20 (Carey and Rutledge, 1998; Montanyà et al., 2007) to 400 (Montanyà et al., 2009). In the meantime, the rise of positive CG flash rate might indicate the occurrence of the hail-falling while, in the termination stage, positive CG flash rate decreases gradually (Liu et al., 2009).

However, from a spatial point of view, the incidence of CG flashes inside hail areas is negligible because IC and CG patterns have usually different locations (Changnon, 1992).

4.2.2 Data and Methodology

As for LAMPINET, even in LINET dataset data sources have a punctual geolocation and for each stroke time, latitude, longitude, type (IC or CG) and current has been provided. In the same way, hail ground observations are based on measurements made by volunteers or found in newspaper articles and pictures posted on social media. However, the main difference regards the information provided by the hail reports because, in this case, the latter is unique and is given in binary mode (HAIL YES or HAIL NO): hence, for both positive and negative events, the database provides only one point at a fixed latitude, longitude and time in which hail has been detected or not, but no further detail regarding the size of the hailstones is granted. The only exception is the hail event that occurred on 05 September 2015 in the Gulf of Naples, for which lightning data from both LAMPINET and LINET datasets and hail reports provided by ESWD are available. For this reason, the hailstorm trajectories are less accurate in geographical terms and the maximum hail diameter, when the signal is positive, is not known. Integrating the LINET dataset with the hail reports, it follows that 16 case studies can be analyzed to study the main features of the hailstorms split into 11 positive (HAIL YES) hail events and 5 negative (HAIL NO) ones. In some days, which presented particularly favorable atmospheric conditions, even more than one hailstorm was investigated. As for LAMPINET dataset, in Table 8 each hail event has been labelled with an identification code. The approach used to investigate the LINET dataset is the same applied for LAMPINET, so flashes have been counted every 10 minutes and remapped on a regular grid and only 10-minute timeslots with 10 or more lightning strikes were considered to compute the LJ as described by the Equations (7a-7b-7c). The only change regards the addition of the type of flashes in the following analysis. For most of the thunderstorms following a typical behaviour, the lightning activity starts with IC flashes as a result of the ice crystals growth in clouds. After that, CG strokes are detected when the main core of the convective cell descends to lower altitudes (Montanyà et al., 2007) in the mature stage. Taking in consideration these ordinary steps, in this work the percentage of IC and CG with respect to the total lightning (TL) is calculated as it follows:

$$IC\% = \frac{IC}{TL} \times 100 \quad (8a) \qquad CG\% = \frac{CG}{TL} \times 100 \quad (8b)$$

In Equations (8a-8b), the IC% and CG% are computed in order to assess if the hail formation and falling to the ground can be inferred by the IC or CG trend, especially for those events in which TL was very low and LJ hadn't very good performances. After computing the hailstorm CG% average every 10 minutes, depending on the duration of the hailstorm examined, for the positive cases the CG% average has been computed from the initial to the dissipative stage whereas for the negative ones the CG% average has been calculated from the initial stage to the time of the observation. Indeed, after that, there is no information about the hailstorm

evolution, especially if hail has formed and reached the ground in a later stage. Moreover, the CG% computation involves the whole storm spatial extension; therefore, it can't be excluded that small size hailstones have created and fallen in the nearby areas.

Table 8. Case studies analyzed using LINET dataset: for each storm system date, identification code and positive or negative hail signal have been reported.

Campania Region case studies (2012-2015)		
Date	Identification Code	Hail detection
12/10/2012	A	NO
27/10/2012 (a)	B1	NO
27/10/2012 (b)	B2	NO
23/01/2013	C	YES
16/12/2014 (a)	D1	YES
16/12/2014 (b)	D2	YES
18/01/2015	E	YES
01/02/2015	F	YES
03/02/2015	G	YES
07/06/2015 (a)	H1	YES
07/06/2015 (b)	H2	YES
08/06/2015	I	YES
09/06/2015	L	YES
10/06/2015 (a)	M1	NO
10/06/2015 (b)	M2	NO
05/09/2015	N	YES

4.2.3 Results and Discussion

In this paragraph, results obtained by computing the LJ temporal series, lead times and potential IC or CG trends are discussed. First of all, having lightning data from both LAMPINET and LINET datasets, it was decided to analyze the TL trend for the strong hailstorm occurred on 05 September 2015 in the Gulf of Naples which produced hailstones of size even higher than 10 cm (https://eswd.eu/). This comparison was very useful to understand if these lightning networks could be interchangeably used depending on the availability of data and, at the same time, to evaluate in which way lightning data could differ. In Figure 52, the 10-minute TL trend from 06:00 UTC to 11:50 UTC has been depicted using vertical grey bars for LINET and black ones for LAMPINET. Dashed columns from 09:30 UTC to 10:30 UTC point out the timeslots in which hailstones were collected in coastal areas, while the corresponding above label indicates the maximum size of the hailstones reported (12 cm in diameter).

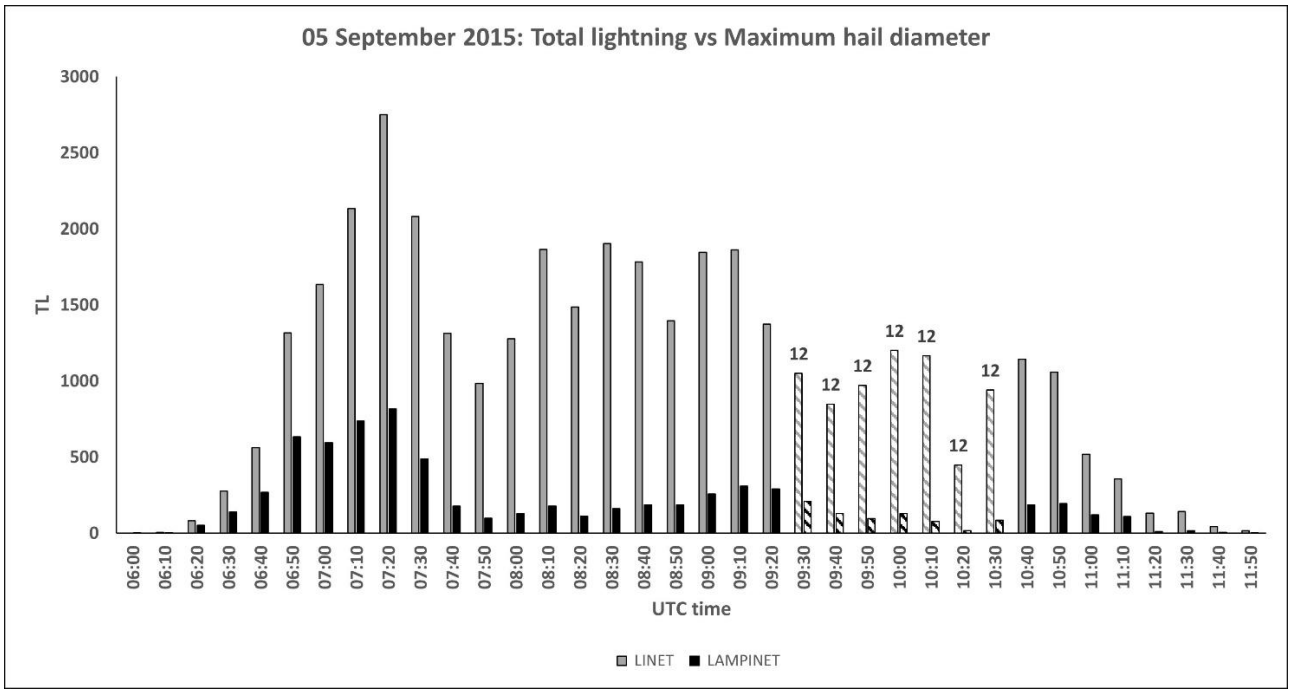

Figure 52. 10-minute TL trend for the case study happened on 05 September 2015 in the Gulf of Naples from 06:00 UTC to 11:50 UTC. Grey bars indicate TL obtained using LINET dataset while black bars show the number of strokes counted exploiting LAMPINET network. The dashed columns highlight the 10-minute steps in which at least one ground hail observation has been recorded: the corresponding label above each column shows the maximum hail diameter detected for that 10-minute temporal window.

TL shown in Fig. 52 highlights a systematic difference characterizing the two lightning detection networks: indeed, strokes measured by LINET in different time windows are always many more with respect to LAMPINET, with a ratio TL (LINET) / TL (LAMPINET) that usually ranges from 5 to 10, even if occasionally the latter can be even exceeded. Given these clear differences in TL, from Fig. 52 we can appreciate a similar trend found for both networks: in fact, the lightning activity peak has been recorded in the same timeslot (07:20 UTC), with 2750 flashes measured for LINET and 817 for LAMPINET. After that, TL starts dropping reaching a minimum, even in this case measured by both networks, at 07:50 UTC (985 strikes detected by LINET, 99 by LAMPINET). Subsequently, TL increases again reaching a secondary maximum between 08:10 UTC and 09:10 UTC for LINET and around 09:10 UTC for LAMPINET. Approaching the time window in which hailstones are falling into coastal areas (from 09:30 UTC to 10:30 UTC), lightning networks agree again showing TL is decreasing with respect to the previous hours. Even considering the initial and final steps of this hailstorm, LINET and LAMPINET are in accordance with the timeslots, maintaining the bias regarding the number of flashes detected. This first analysis on TL gave light to similar TL trends but also to strong differences in the detection efficiency that characterizes the two lightning networks and, although technical distinctions among LINET and LAMPINET instrumentation are known, it makes impossible to use them in an interchangeably way especially if, like in this case, the TL information is exploited to compute lightning jumps and IC% or CG% trends.

After this first examination, the Equations (7a-7b-7c) were applied to 16 case studies that occurred in Campania Region using the LINET dataset. Unlike hail events analyzed in Vermi et al. (2025), in which only storm systems producing very large hail (maximum hail diameter ≥ 5 cm) were considered, these case studies are more heterogeneous and have been split into 11 hailstorms (HAIL YES, for which hail size is not known) and 5 (HAIL NO) ordinary thunderstorms. However, even if this dataset involves more case studies and storms show clear different features regarding hail phenomena, the highest maximum is mainly found using LJ_{30} and LJ_{40} temporal series as reported in Table 9.

Table 9. Number of instances in which a determined LJ series (computed using Equations. 7a-7b-7c) captures the highest maximum for the hailstorm investigated.

Series	Frequency of the highest maximum	Case study
LJ_{40} Series	6/16	B2-C-E-I-L-N
LJ_{30} Series	8/16	A-B1-D1-D2-G-H1-H2-M2
LJ_{20} Series	2/16	F-M1

Indeed, as observed in Vermi et al. (2025), we can notice that the LJ_{20} series identifies the highest maximum only in 2/16 (12.5%) case studies confirming that probably, even considering different atmospheric dynamics, the lightning activity peak generally needs more time to be reached. This is the main reason why, on average, LJ_{30} and LJ_{40} detect the highest maximum in nearly all case studies, even if here the LJ_{30} series (50% of events) outperforms LJ_{40} (37.5%). In Figure 53a-b, the highest maximum computed for both hail-bearing thunderstorms (Fig. 53a, blue bars) and no-hail producing storms (Fig. 53b, orange bars) has been reported. Considering hail events depicted in Fig. 53a, it emerges that the distribution of highest maxima is extremely variable, moving from 1.7 (case study F) to 20.6 (case study D1). In addition, the lack of information on the maximum hail size doesn't allow us to make any speculation regarding the connection between the intensity of hail phenomena and the highest maximum found in LJ series. However, from Fig. 53a, we can notice that for hail events E, C, G and F the highest maximum is much lower than the other ones (summing up results obtained in Fig. 53a and in Fig. 51 it emerges that lightning activity jumps at least by 9 times for 16/21 hail cases). One possible explanation related to these values derives from the low TL that is usually measured during the winter season: indeed, cases E, C, G and F happened between January and February when the size of the hailstones is usually quite small and the different atmospheric conditions involve a milder lightning activity as discussed in Section 3.5 and by Petracca et al. (2024). It could mean that, in the cold season (here the diameter of the hailstones can only be hypothesized) these phenomena could be more difficult to identify since they are characterized by a general reduction of TL. On the other hand, if we analyze results obtained from negative case studies in which hail was not signaled (Fig. 53b), it follows that, in most cases, LJ values are lower than homologous LINET "HAIL YES" events or hailstorms producing very large hail examined in Vermi et al. (2025).

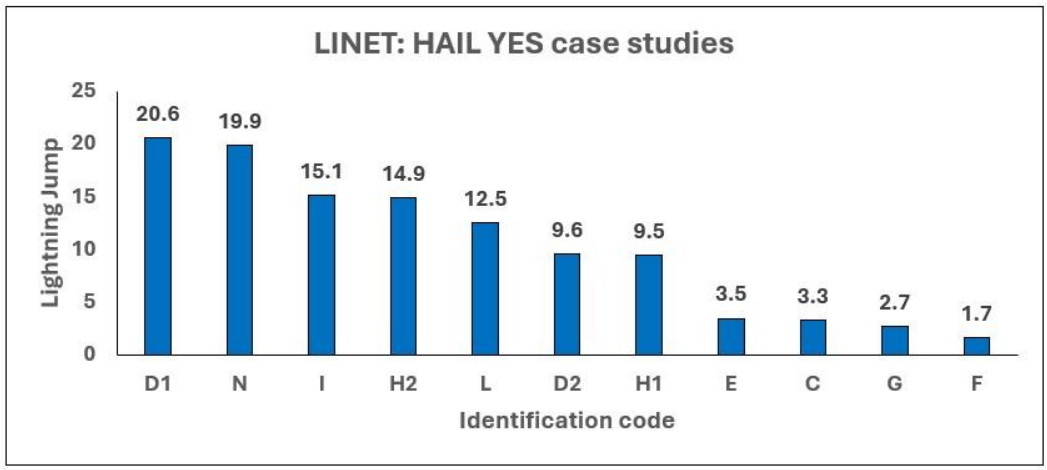

(a)

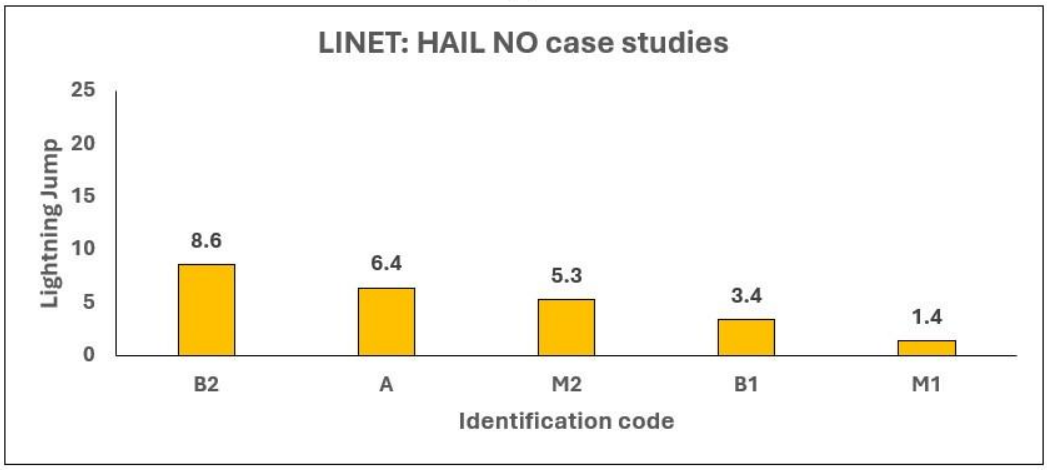

(b)

Figure 53. Highest maximum observed for "HAIL YES" case studies (a, blue bars) and "HAIL NO" ones (b, orange bars).

Although these preliminary results show an important increase of lightning activity characterizing the storm systems, at this stage of the work the information provided by the highest maximum can't be used alone to univocally discriminate between hailstorms and thunderstorms that are not producing hailstones, having found hail events which show very low LJ values (case studies J in Vermi et al. (2025) and E, C, G and F using LINET dataset). The computation of the highest maxima makes it possible to calculate the lead time (LT), which is defined as the difference (in minutes) between the time of the hail observation and the time of LJ detection. In Table 10, for each "HAIL YES" case study, the time of ground hail observation and LJ detection are reported. Main results show that, in 9/11 hail events, LT is in advance with respect to the time of hail report, in case study F, LT is coincident (LT = 0 minutes) and in case E it is in late by 30 minutes. As found in many previous studies, this brief analysis regarding LT stresses that, when the LJ is detected, in most cases it is in advance with respect to hail reports. This is a very important outcome, even from an operative point of view, letting real-time weather forecasters interpret the LJ detection as a signal for potential falling of the hailstones in the next tens of minutes.

Table 10. For each case study, time of hail report, LJ detection and LT are provided. Positive lead times mean that LJ advances the hail ground observation. For "HAIL NO" events LT can't be computed.

Campania Region case studies (2012-2015)			
Identification Code	Time of hail report (UTC)	Time of LJ detection (UTC)	Lead time (minutes)
A	NO	07:50	/
B1	NO	10:40	/
B2	NO	14:30	/
C	13:30	12:10	80
D1	08:55	07:50	65
D2	12:40	12:30	10
E	07:30	08:00	-30
F	15:50	15:50	0
G	18:55	18:00	55
H1	14:30	13:50	40
H2	15:10	14:30	40
I	15:00	13:50	70
L	13:50	13:00	50
M1	NO	14:10	/
M2	NO	15:30	/
N	09:30	07:00	150

The last investigation regards the type of flashes detected by the LINET network that characterize these storms. Every 10 minutes, IC% and CG% were computed using the Equations (8a-8b) to assess if the flash type can add useful information to recognize hail events, especially those in which the LJ method hadn't very good performances. Results of the CG% average calculation for positive (red bars) and negative (blue bars) hail events are represented in Figure 54. In this graph, on average, CG% is higher for hailstorms whereas it is always below 15% for no hail-bearing thunderstorms. Moreover, if we focus on the above-mentioned winter cases which resulted in very low jumps, it is clear that for hail events C, E and G CG% average oscillates between 16% and 20% while for the case F it reaches 43%, which is the highest CG% average found for this dataset. Unlike the LJ method, these results highlight that CG% average is not strictly dependent on the TL (which for winter cases is very low) and could improve the classification of the hail risk adding new information useful to understand the hailstorm features. Despite that, the cases D1 and D2 which presented stronger maxima (20.6 and 9.6, respectively) and a higher TL (especially D1) are characterized by a CG% average equal to 11% and 8%, respectively. Considering that the hail signal is unique in terms of spatial and temporal position, it has been decided to calculate the CG% average much more related to the ground observation which refers to a temporal round equal to ± 5 or 10 minutes, depending on the minute in which the hail information was reported. It allows us to be much more accurate and faithful to the hail remark, to understand if something more related to the hail-falling could be inferred. In Figure 55, the same plot proposed in Fig. 54 has been reconsidered, but here the ± 5/10 minute-CG% average round the hail signal has been introduced using yellow bars.

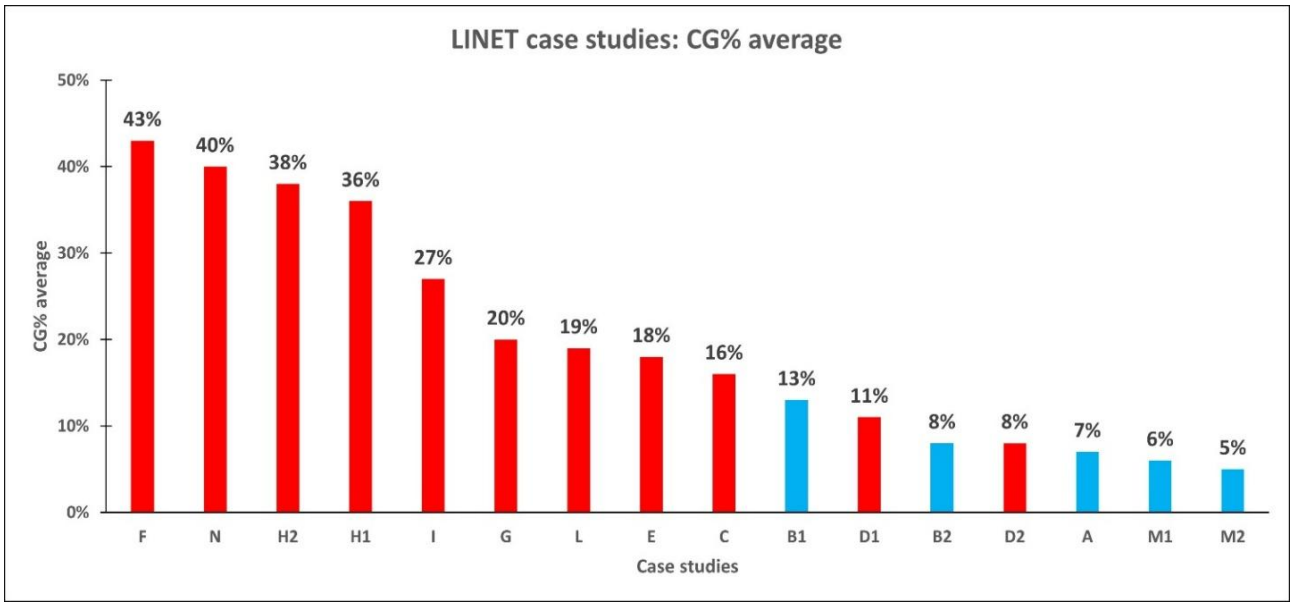

Figure 54. CG% average for positive (HAIL YES, red bars) and negative (NO HAIL, blue bars) hail events.

It is immediately clear that, for almost all positive case studies, CG% average increases or remains similar, apart from the hail event F in which it partially decreases. The two cold season case studies D1 and D2 show an important rise passing from 11% to 33% and from 8% to 19%, respectively. Fig. 55 points out that, for positive cases, CG% average goes from 19% to 65%. The latter is a very significant value that was reached when an intense hailstorm affected the city of Naples with hailstones until 12 cm in diameter. Indeed, case N is surely the most severe of the LINET dataset and it suggests that these features seem to progressively highlight as the hailstorms get stronger and more severe.

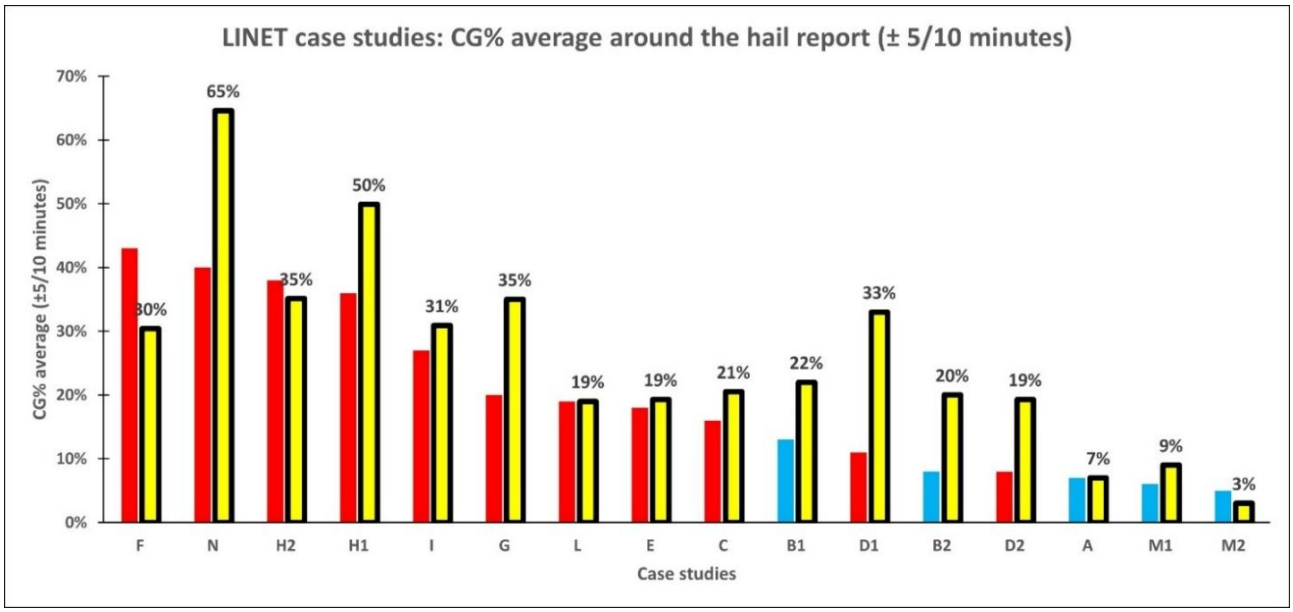

Figure 55. Like in Fig. 54, the ±5/10 minute-CG% average round the hail signal has been added with yellow bars for all case studies.

Finally, if we take into account the negative events A, M1 and M2, they characterize for a CG% average definitely lower, always below 10%, confirming again that for less deep thunderstorms, the percentage of CG strokes measured typically decreases. However, these results about IC and CG trends are in contrast with findings reported by some previous studies (e.g. Carey and Rutledge, 1998; Montanyà et al., 2007; Montanyà et al., 2009) which state that the IC/CG ratio measured during the hailstorms sharply increases in a typical range between 20 and 400, while in less severe thunderstorms the IC flashes are less prevailing, showing a lower IC/CG ratio. In this work, the ± 5/10 minute-CG% average round the hail signal ranges from 19% to 65% for the hailstorms (indicating an IC/CG ratio oscillating between 0.54 and 4.3) and from 3% to 22% for no hail-bearing storms (IC/CG ratio among 3.5 and 32.5). So, results emerging from our analysis, not only are in contrast with previous studies, but the IC/CG ratio seems to decrease as storms become more intense and severe, in the opposite way with respect to what was found in previous works. In light of this anomalous trend, here we discuss some possible explanations. First, it has to be considered that DE for these sensors is about 90% for CG strokes, but it widely drops for IC flashes resulting in a large underestimation of them and bringing to an important decreasing of the IC/CG ratio. Moreover, the maximum detection efficiency has been measured in Central Europe, where there is the highest density of LINET sensors, as can be seen by the LINET sensors (represented by purple squares) map in Figure 56 (from Betz et al., (2009)). Indeed, Fig. 56 clearly shows that these sensors mainly cover european areas going from Eastern Spain to Poland and from Denmark to Central Italy. However, our study area corresponds to the Campania Region in Southern Italy from 2012 to 2015. Consequently, if we compare the localization of LINET sensors with the study area examined, probably only the sensor located in Rome (purple square in Central Italy) was able to measure great part of lightning activity occurring in these areas. Despite that, in hailstorms lightning activity abruptly increases (especially in some timeslots, see Fig. 52) and the presence of only one or few instruments prevents them from detecting the correct number of flashes because, during the recording time in which the stroke has been detected, the sensor is inactive and not able to measure other pulses. As a consequence, considering both that CG strokes are easier to detect and there are not other available sensors in the nearby areas, the IC/CG ratio could be strongly underestimated during these storms, since much more IC flashes are produced and missed by the instrumentation. Another important topic regards the potential misclassification of pulses type: for example, Montanyà et al., (2009) found a very large amount of negative CG flashes which showed peak current in absolute value much lower than 10 kA: these features usually belong to negative IC flashes trends during the evolution of the hailstorms. Furthermore, Cummins et al. (2006) and Johnson and Mansell (2006) described similar misclassification effects discovered in supercells. So, according to these studies, Montanyà et al., (2009) decided to reject negative CG strokes having a peak current in absolute value lower than 10 kA, finally reaching an IC/CG ratio close to 400. Despite that the misclassification of strikes has been widely studied and confirmed by many works, the application of this filter contributes removing the most of CG flashes from the lightning dataset and it is a crucial point that can explain the reasons why in this work different results regarding the IC/CG ratio in thunderstorms have been found.

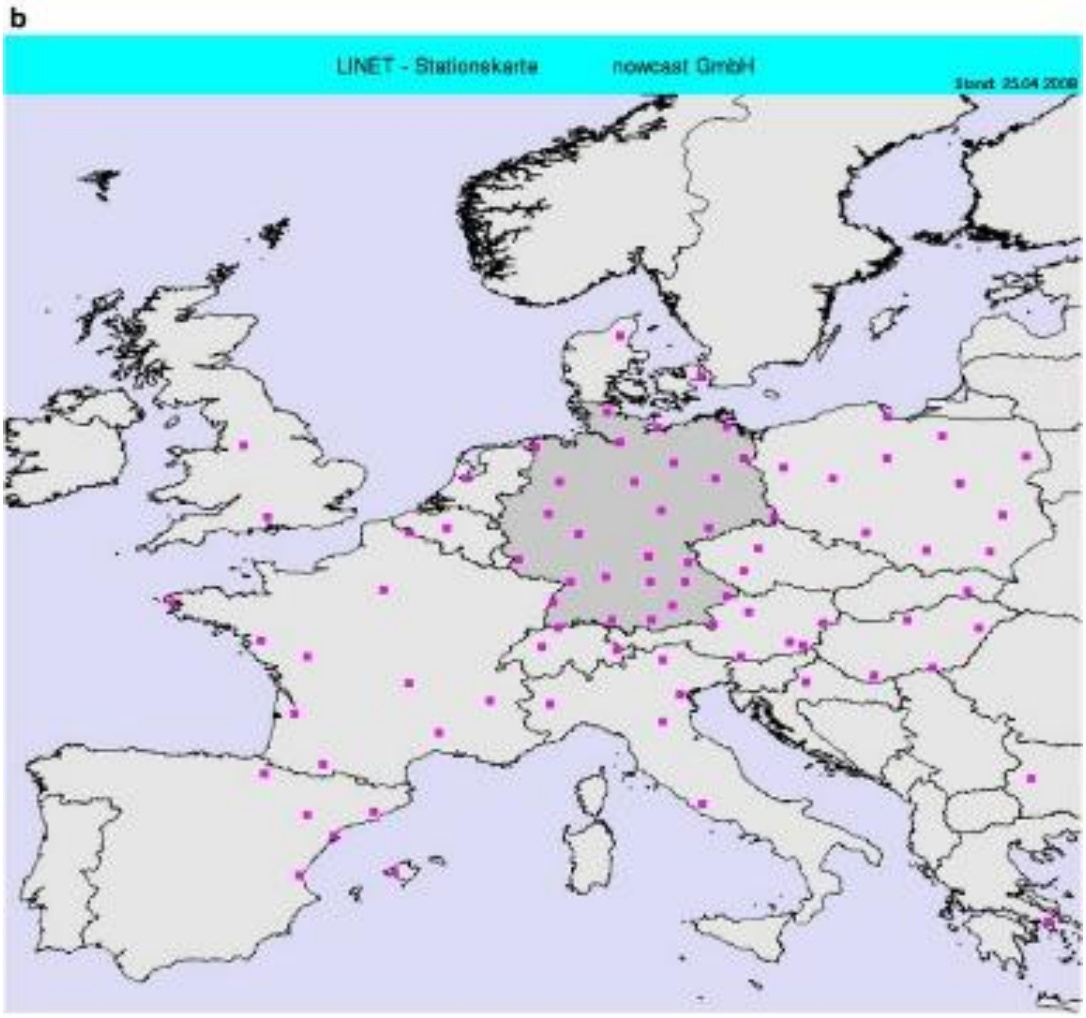

Figure 56. LINET sensors (purple squares) located in European territory (adapted from Betz et al. (2009)).

4.2.4 Conclusions

In this work, an analysis on the relationship between hail occurrence and lightning activity has been performed on 16 storm systems that happened in Campania Region from 2012 to 2015, exploiting lightning data provided by the Lightning Network LINET. These cases have been classified in 11 positive (HAIL YES) and 5 negative (HAIL NO) hail events, thanks to the observations made by volunteers and collected in a database: so, for each case study, the information is given at a fixed point in terms of latitude, longitude and time in which hail has been detected or not, but other details like the maximum hail size are not available. However, we exploited the case study that occurred on the 05 September 2015 in the Gulf of Naples, that was also analyzed in Vermi et al., (2025) to compare lightning data measured from LAMPINET and LINET networks. From this first elaboration, it emerged that LINET network systematically detects a number of strikes that generally moves from 5 to 10 times higher with respect to LAMPINET. However, even if total lightning (TL) measured is strongly different, both lightning networks identify a very similar TL trend studying consecutive 10-minute timeslots, with TL growing and decreasing stages that appear in the same time windows. It follows that these

gaps are likely due to the different sensitivity of LINET and LAMPINET antennas that allows LINET ones to systematically measure many more flashes highlighting that, even for future studies, lightning data coming from these two networks can't be exploited in an interchangeable way. This first outcome is crucial to understand that TL can widely differ only by changing the type of lightning detection network: for this reason, the development of a method for recognizing the hailstorms also involving lightning jumps (LJ) or the type of flashes (IC% and CG%) could be more robust even when applied for other settings (e.g. different lightning detection networks, lightning data from satellites and so on).

After elaborating LJ series for 16 storms, LJ_{30} and LJ_{40} series detected the highest maximum (LJ) in 14/16 case studies, suggesting that usually the rise of lightning activity needs some tens of minutes to fully develop (similar results were already found by Vermi et al., (2025)). For 7/11 HAIL YES case studies, LJ ranges from 9.5 to 20.6, indicating a strong increase in TL. On the oher hand, 4/11 HAIL YES cases were characterized by a very low TL and weak jumps: the latter happened during the winter season (January and February), when lightning activity is often much lower (see Section 3.5 and Petracca et al., 2024) and it can also affect the LJ computation. Moving to the remaining five HAIL NO events, here LJ values are between 1.4 and 8.6: it means that, on average, these jumps are weaker than those observed in HAIL YES class but, at the same time, winter hail cases would be easily misclassified as no hail-bearing thunderstorms. This is the main reason why, at this stage of the work, the only detection of the highest maximum cannot be used to univocally distinguish between hailstorms and ordinary thunderstorms. However, the highest maximum identification also allows to compute lead time: considering 11 HAIL YES cases, 9 of them were in advance with respect to the time of hail report, one was coincident in time and one was in late by 30 minutes. Consequently, the highest maximum detection could also have a beneficial impact on nowcasting tools, letting weather forecasters to infer the potential development of hailstones in storms flagged by a LJ detection.

The last topic investigated is the type of flashes detected during the evolution of 16 thunderstorms. The CG% average is generally higher for positive events, even considering the winter hail case studies, confirming that the information related to the type of strikes is independent from TL. The gap between HAIL YES and HAIL NO case studies further enhances when the ±5/10 minute-CG% average round the hail signal is calculated. For positive hail events, the CG% average goes from 19% to 65% (IC/CG ratio between 0.54 and 4.3), suggesting that this value progressively increases as the hailstorms become stronger and more severe. For the negative ones, in three events the CG% average is below 10% (IC/CG ratio between 9 and 32.5) while in the other two it oscillates between 20% and 22%. These results are completely in contrast with findings published in previous studies which state that, starting from a clear prevalence of IC flashes in ordinary thunderstorms, the IC/CG ratio abruptly increases when severe hailstorms are studied (Carey and Rutledge, 1998; Montanyà et al., 2007; Montanyà et al., 2009). For explaining these outcomes in our work, we also considered some basic features of sensors making up the LINET network: indeed, the DE is about 90% for CG strikes but it considerably decreases for IC flashes, having the effect of reducing the IC/CG ratio. The second important element is the sensors distribution throughout the European territory: indeed, many of them are located in Central Europe

whereas Central and Southern Italy suffer by a poorer coverage (Fig. 56 from Betz et al., 2009): it causes a general decreasing of DE, especially when a few sensors have to deal with many flashes per second. Combining the latter with the preferred CG detection operated by sensors, it follows that IC/CG ratio can be strongly underestimated. In addition, some studies (e.g. Cummins et al., 2006; Johnson and Mansell, 2006; Montanyà et al., 2009) state that, mainly during the evolution of supercells and hailstorms, lightning networks can misclassificate IC flashes as CG ones. To overcome this problem, these above-mentioned studies applied a filter rejecting a large part of negative IC strikes falsely detected as negative CG strikes. This procedure, which has been adopted in many works, causes the remotion of great part of CG strokes from the dataset, heavily changing the final result in favour of a higher IC/CG ratio detected during the hailstorms.

Chapter 5 Total lightning as a support for MASHA Method

This Chapter focuses on the integration of lightning activity in the MASHA Method to increase the performance of the HP computation, especially for severe thunderstorms having OT, whose signal coming from the stratosphere causes the rise of $TB_{10.8}$ and the consequent depression of HP (for further details see Section 2.3.2). In the following paragraphs, the potential improvements into the MASHA Method final output will be evaluated by exploiting lightning data coming from LAMPINET network. The main idea was to calculate a "new hail probability", which takes into account not only the $TB_{10.8}$ but also the lightning activity pattern. Indeed, Jurković et al. (2015) state that the spatial distribution of lightning generally coincides with the spatial distribution of the detected OT. In addition, lightning activity shows a similar temporal distribution, with an increase in lightning activity evident at or close to the time of the OT detections.

5.1 The geolocation of hail reports and lightning activity

The MASHA Method provides a result in terms of HP every five minutes covering all the Mediterranean Basin, but it suffers from a general HP underestimation when the algorithm is dealing with deep convective storm systems characterized by OT. Thus, the integration of lightning activity may represent an important opportunity to improve the MASHA Method performance. For exploring the potential links between the HP depression in OT regions, hail reports from ESWD and TL pattern, we decided to compare them using a 6×6 km^2 regular grid, starting to evaluate their spatial distribution. The latter is represented in Figure 57, in which two OT hailstorms occurred on 24 July 2023 at 19:10 UTC in Northwestern Italy (Fig. 57a-b) and at 19:15 UTC in Northeastern Italy (Fig. 57c-d) are shown (see Fig. 23b in Section 2.3.2 for further details about OT development). In Fig. 57a-c and in Fig. 57b-d, we propose the overlapping between HP and hail reports (red dots) and between TL pattern and hail reports (red dots), respectively. These three variables have been treated in the following way: for instance, considering Fig. 57a-b, the HP map refers to 19:10 UTC as well as hail reports (with a maximum temporal tolerance of ± 5 minutes around 19:10 UTC) while the TL pattern has been obtained counting lightning strikes from 19:07:30 UTC and 19:12:30 UTC to center the 5-minute lightning strikes time window around 19:10 UTC. As can be noticed in both events, sometimes the hail reports distribution is not coincident with HP maxima (Fig. 57a-c), due to the OT structure development. When it happens, a central ring having very low HP (white pattern with HP below 0.20 corresponding to OT area), rounded by much higher HP values, is typically observed. So, even if on one hand the HP range assigned to the hailstorm is updated to the last calibration performed by the MWCC-H method, on the other, the distribution of the HP range is forced on the outside edge of the hailstorm (where $TB_{10.8}$ are lower) by the OT structure, affecting the final HP spatial distribution. Consequently, in Fig. 57a-c, many hail reports (with maximum hail size between 4.5 and 12 cm) are geolocated in No Hail or Hail Potential areas. Moving to Fig. 57b-d, it is interesting to highlight that, for both events, lightning strikes are located easterly or northeasterly with respect to HP maxima, partially overlapping the OT region, as suggested by Jurković et al. (2015). In

addition, for both cases, the lightning pattern is geolocated in correspondence of the hail reports, even if TL maxima not always match with the exact location of ground hail observations. This final statement is very important because, if it was confirmed, it could allow us to partially overcoming the HP depression problem in OT regions, exploiting the TL as a new proxy for the HP computation. For this reason, we decided to analyze the lightning activity occurred in correspondence of 288 hail reports contained in the ESWD database related to hailstorms happened on the Italian Peninsula on three different summer days:

- 26 July 2021: 51 hail reports;
- 18 August 2022: 27 hail reports;
- 24 July 2023: 210 hail reports.

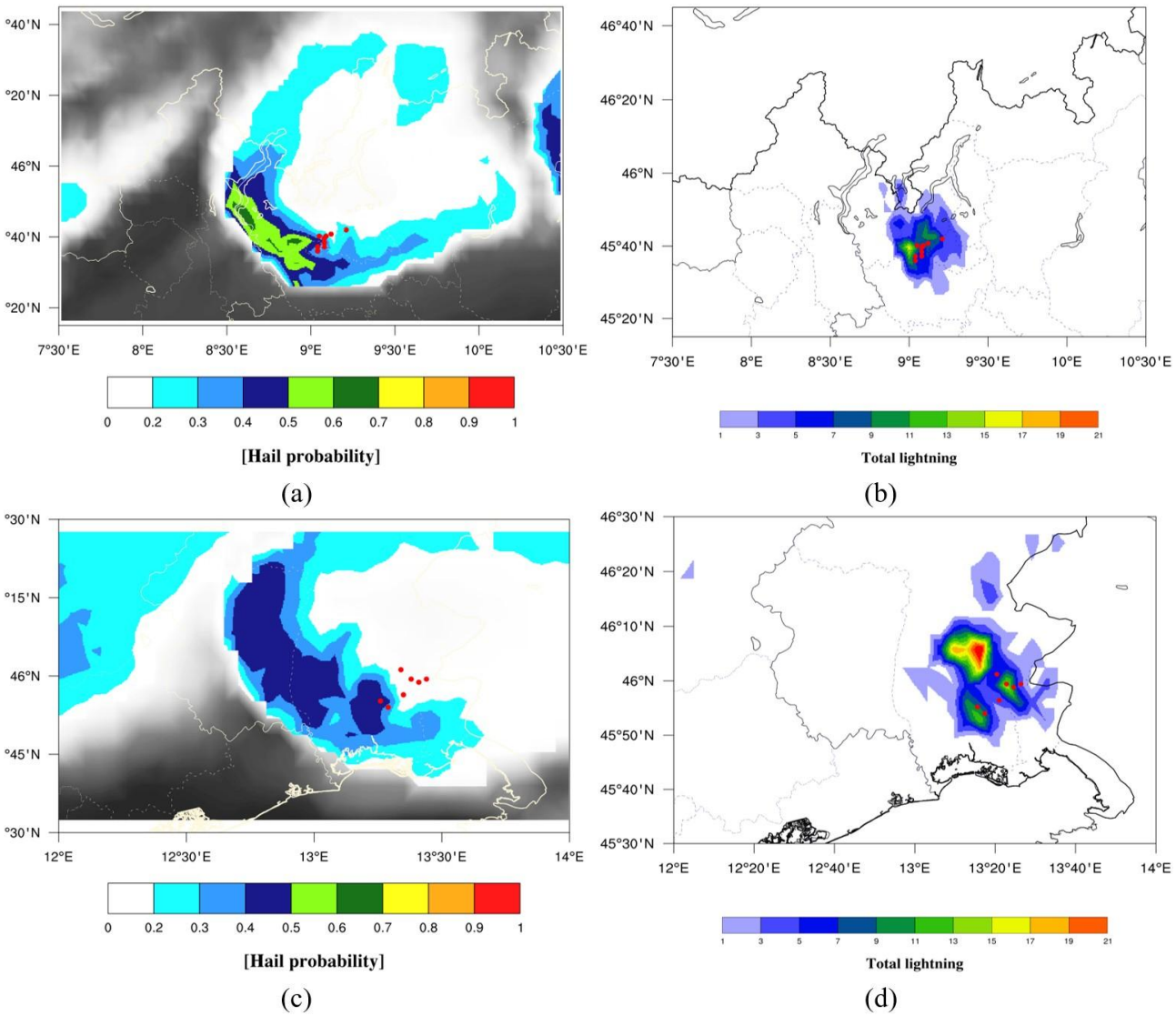

Figure 57. OT hailstorms occurred on 24 July 2023 at 19:10 UTC (a-b) and at 19:15 UTC (c-d). For both events, the overlapping between HP and hail reports (a-c) and between TL and hail reports (b-d) is proposed. Hail reports (red dots) have been obtained by ESWD.

In this way, each hail observation was assigned to the nearest TL data obtaining 288 matchings: after that, we computed the frequency with which hail reports are associated with a certain number of lightning strikes, which has been reported in Figure 58. For each column, TL is split into 5-strike steps, except for the first two bars on the left in which it has been made explicit the condition TL = 0 (and consequently the second bar represents the $1 \leq TL \leq 4$ interval) and for the last one in which the $TL \geq 45$ column includes all the cases in the tail of the distribution. From this preliminary investigation, it emerged that:

- only 6.3% of hail reports are detected when TL = 0;
- 64.3% of hail observations are in 6×6 km^2 grid cells showing the $1 \leq TL \leq 9$ interval;
- the gradual decreasing of frequency observed when $TL \geq 10$ is not due to a reduction in the probability of finding hail reports when lightning activity is higher but is more related to the approach of the TL distribution tail. Indeed, especially 6×6 km^2 grid cells having $TL \geq 20$, are a priori rarely detected.

Therefore, the most important result of this investigation is the onset of the spatial relationship between hail reports and lightning activity because, in 93.7% of events, ground hail observations are geolocated in grid cells where at least one strike ($TL \geq 1$) was detected in the corresponding 5-minute temporal window. In addition, no trends appear related to the maximum hail size as a function of TL.

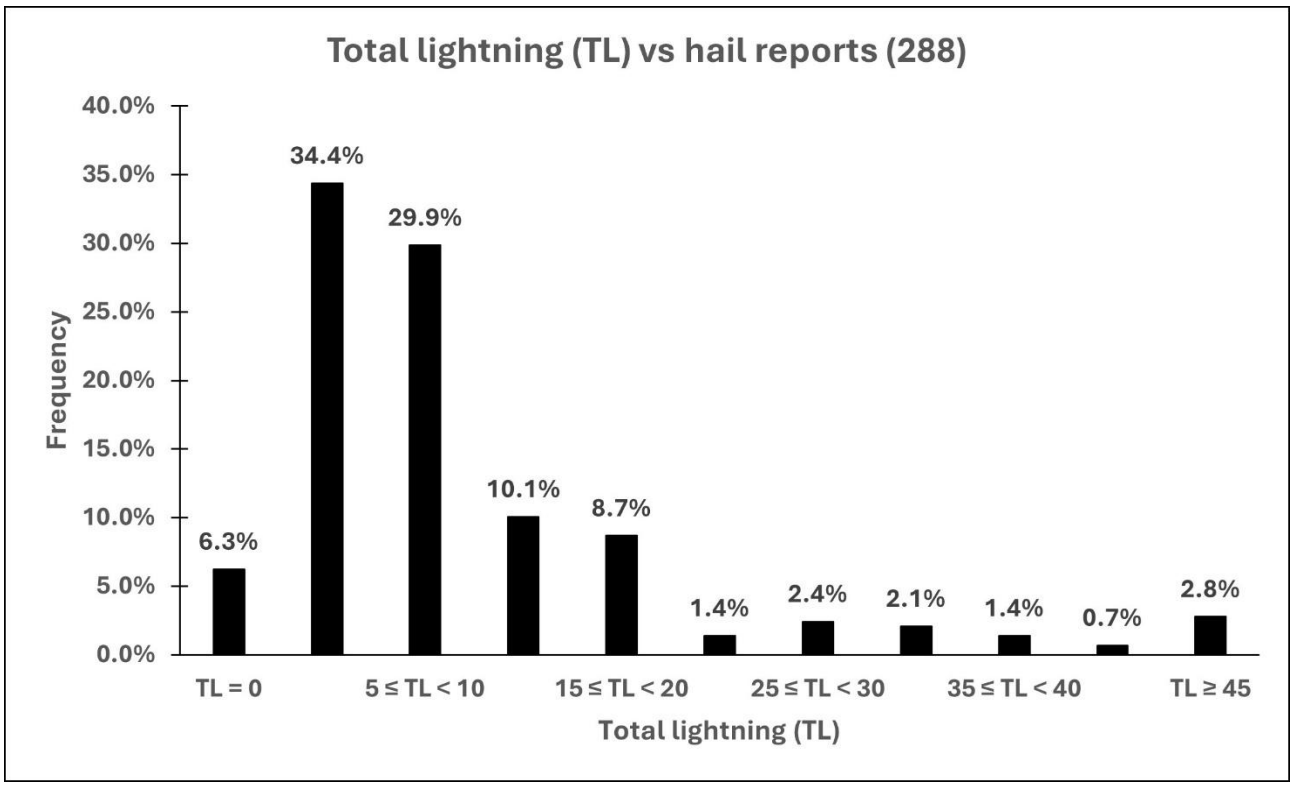

Figure 58. Frequency of hail reports spatial distribution as a function of TL pattern.

5.2 Using TL to compute a new hail probability: a preliminary test

Results shown in Fig. 58 open the way to compute an experimental "new hail probability" (hereafter, NHP), that is also based on the intensity and spatial distribution of TL, to correct the systematic HP underestimation appearing in OT region. Before doing that, it is important to remember that the HP provided by MWCC-H method as well as that calculated by the MASHA Method represents the probability of finding ice in clouds, resulting from the interaction of the latter with high frequency microwave radiation. Even if introducing hail reports can change the point of view on hail phenomenon (hailstones are collected on the ground and not detected from space), the information provided by the MASHA Method remains crucial to describe the complex physical process that ice crystals take before becoming hailstones. For this reason, even for NHP, we decided to maintain the contribution given by the MASHA Method HP (hereafter, HP_{MASHA}) for 50% of the total. The remaining 50% of NHP was based on the TL detected in each grid cell (hereafter, HP_{TL}) and it was computed as follows:

$$1) \text{ when } TL = 0 \quad \rightarrow \quad HP_{TL} = 0 \tag{9}$$

$$2) \text{ when } 1 \leq TL \leq 9 \quad \rightarrow \quad HP_{TL} = \log_{10} TL \tag{10}$$

$$3) \text{ when } TL \geq 10 \quad \rightarrow \quad HP_{TL} = 1 \tag{11}$$

Equations (9), (10) and (11) and corresponding TL ranges are based on results reported in Fig. 58. Indeed, it is reasonable to approximate $HP_{TL} = 0$ when TL = 0, since only in 6.3% of cases hail reports are detected in absence of lightning activity in the same grid cell. On the other hand, for the same principle, HP_{TL} is maximum ($HP_{TL} = 1$), when lightning activity is stronger ($TL \geq 10$). The most frequent matchings are observed in $1 \leq TL \leq 4$ (34.4%) and in $5 \leq TL < 10$ (29.9%) ranges, in which TL doesn't show strong peaks but hail reports, even with hailstones belonging to Super Hail category, have been recorded. The possibility of having large hailstones even with few strikes is the main reason why it is necessary to rapidly increase HP_{TL}, according to lightning activity. Thus, to achieve this purpose, the $\log_{10}$TL function was chosen for computing HP_{TL} in the $1 \leq TL < 10$ interval, as shown in Figure 59. Being aware of the approximations made in the HP_{TL} computation, it is important to remind that the main goal of this preliminary test is to understand if the TL pattern can partially improve the HP_{MASHA}, whose intensity and geolocation is affected by the OT structure. Using this approach, NHP is expressed in the following Equation (12) as the average between HP_{MASHA} and HP_{TL}:

$$NHP = \frac{(HP_{MASHA} + HP_{TL})}{2} \tag{12}$$

As it was for HP_{MASHA}, NHP moves from 0 to 1, being obtained thanks to an equal (50%) contribution provided by both HP_{MASHA} and HP_{TL}. The whole logical flow and the key-steps for the NHP computation are schematized in Figure 60. If we reconsider the two OT hailstorms and hail reports (red dots) introduced in Section 5.1, now we can compare the previous HP_{MASHA} output (Figure 61a-c) with the NHP one (Fig. 61b-d), taking into account that these severe storms produced hailstones with maximum size of 12 cm in Northwestern Italy (Fig. 61a-b) and of 9.5 cm in Northeastern Italy (Fig. 61c-d).

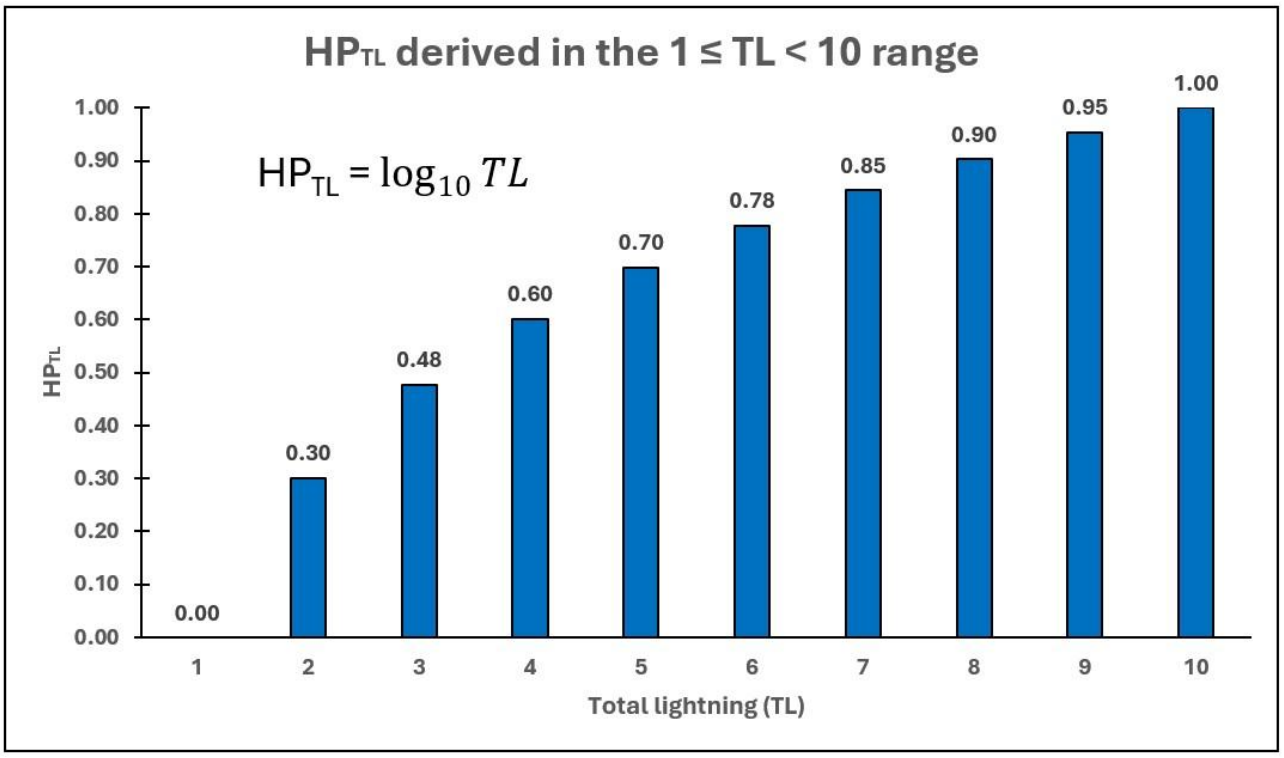

Figure 59. HP_{TL} computed as a function of $\log_{10}TL$ when TL ranges from 1 to 9 in the grid cell.

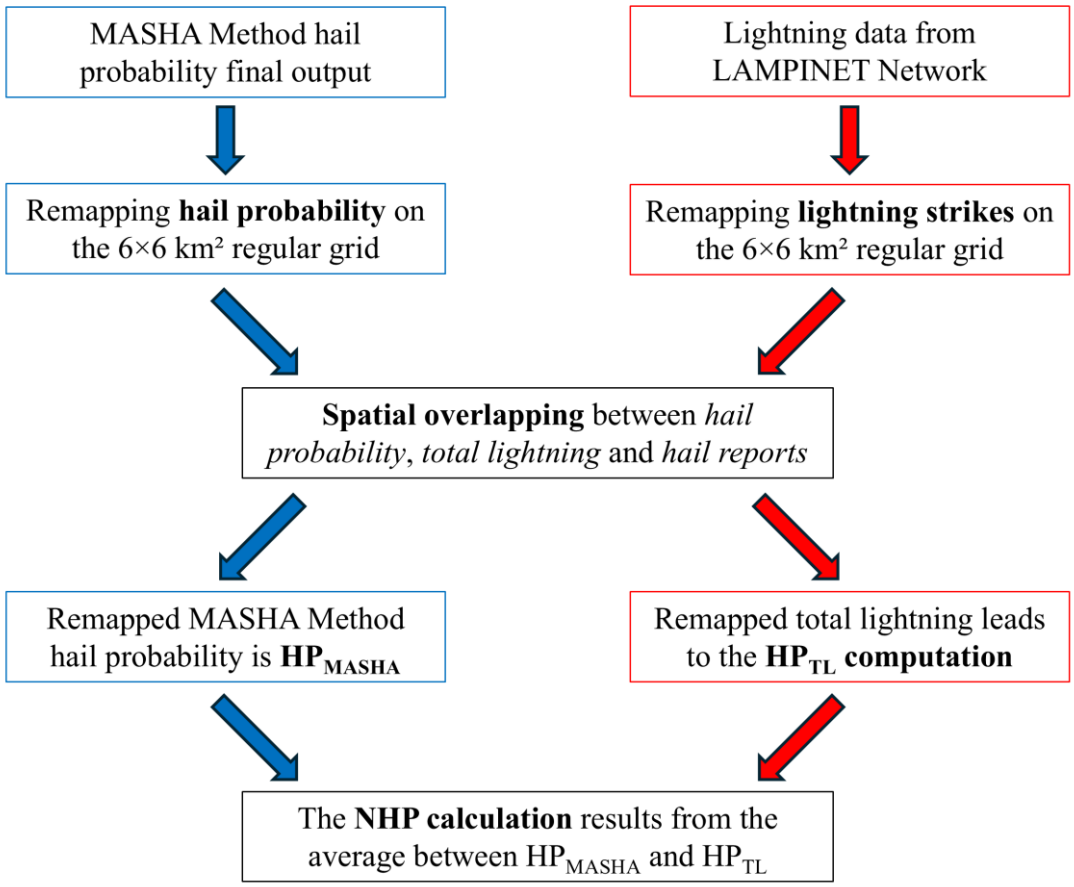

Figure 60. The data flow architecture for calculating the NHP.

As can be noticed in both events, the major change in Fig. 61b-d is related to the increase of NHP in an area partially overlapping the OT region, that also corresponds to the location of most hail ground observations. In the Northwestern case study (Fig. 61a-b), the main effect is to change the NHP geolocation, with a weak increase of NHP maxima of about one tenth (from dark green to yellow pattern). In Northeastern Italy hail event (Fig. 61c-d), both effects are more evident: here, the most of hail reports moves from No Hail to Large Hail class, with some NHP maxima belonging to the Super Hail category. On the other hand, HP_{TL} leads to a partial decreasing of NHP in other areas affected by the two hailstorms, according to the low lightning activity detected.

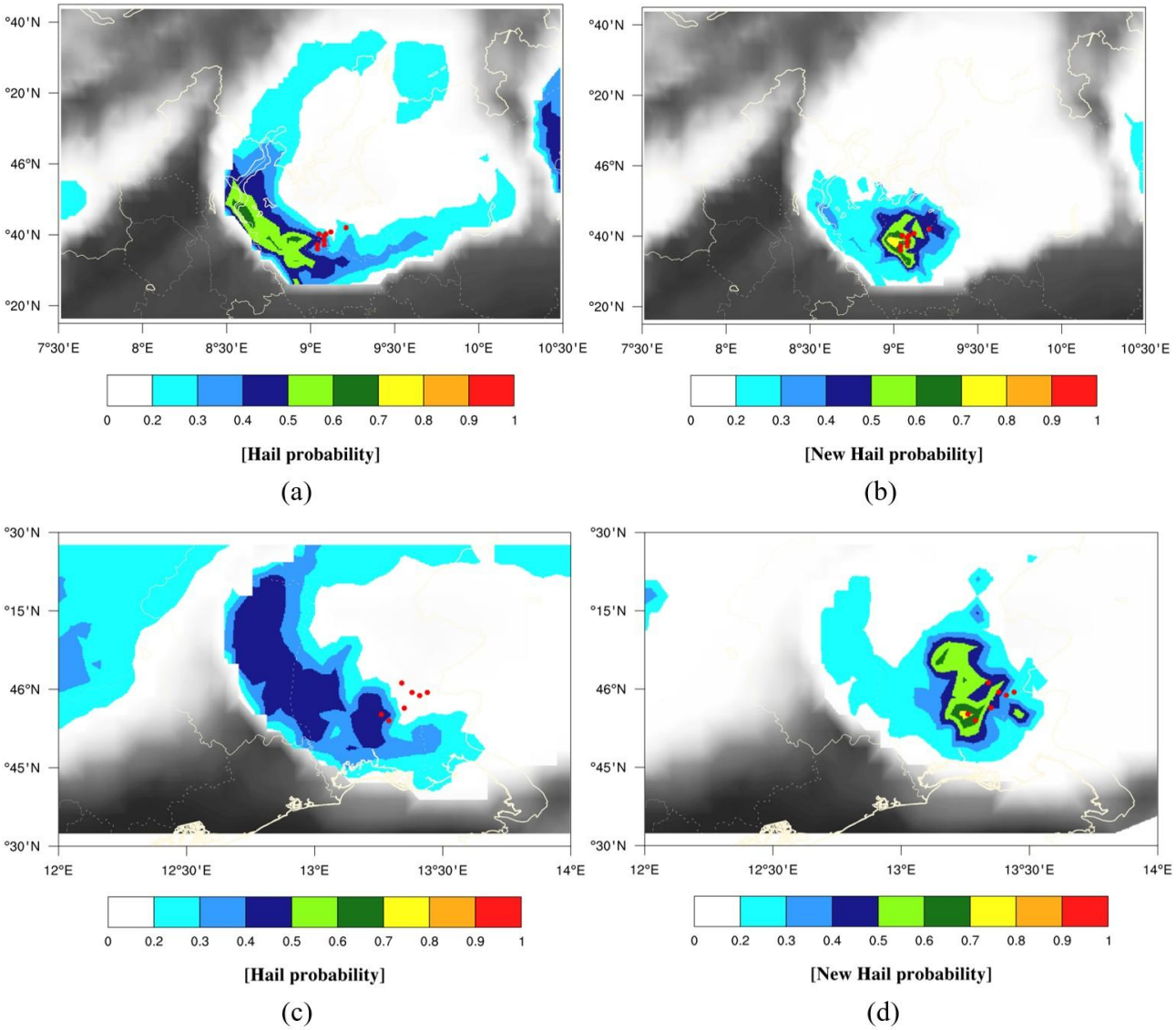

Figure 61. HP_{MASHA} on the left (a-c) and NHP on the right (b-d) for hailstorms occurred on 24 July 2023 at 19:10 UTC (a-b) and at 19:15 UTC (c-d). ESWD hail reports are represented with red filled dots.

5.3 NHP validation: is it a good proxy for the growth and falling of the hailstones?

Hailstorms introduced in Fig. 61a-b and Fig. 61c-d seem to confirm that including lightning activity in the NHP computation could represent an opportunity to better identify the OT region and, consequently, the falling

of the hailstones in specific areas, which were systematically underestimated by the HP_{MASHA}. Starting from these hypotheses, we applied the MASHA and NHP Methods to a new and independent hail reports dataset obtained by the ESWD database, in which we selected 92 hail ground observations recorded for 14 summer days of 2021, 2022 and 2023 on the Italian Peninsula, having a temporal uncertainty not higher than ± 5 minutes. This analysis was crucial to objectively quantify the different performance of MASHA and NHP Methods with respect to the hail ground observations. Thus, for each of them, the geolocation and hail diameter were compared with HP_{MASHA} and NHP outputs, to assess the different performance of the hail probability pattern. According to Table 1 (see Section 2.1), the hail size and hail probability (valid both for HP_{MASHA} and NHP) were split into four (2-2.5 cm; 3-6.5 cm; 7-9.5 cm; ≥ 10 cm) and nine (having an HP interval of one tenth from 0.20 to 1.00) categories, respectively. Subsequently, considering the information provided by hail reports in terms of time, geolocation and hail size, HP_{MASHA} and NHP have been classified in conditions of underestimation (orange boxes), correct estimation (green boxes) or overestimation (light blue boxes), as represented in Table 11. The type of classification proposed for each box derives from Table 1: borderline conditions moving from correct estimation to a slight underestimation or overestimation have been maintained flagged as "correct" for highlighting only hail phenomena clearly underestimated or overestimated. As can be noticed from Table 11, the two hail size minor categories (i.e. 2-2.5 cm and 3-6.5) evolve in a symmetrical way with the hail diameter while, for very large or super hail classes (i.e. 7-9.5 cm and ≥ 10 cm), overestimation is no longer considered. After applying the comparison between HP_{MASHA} and NHP on 92 independent hail reports, in Figure 62a-c, results about the validation dataset have been reported.

Table 11. Underestimation (orange), correct estimation (green) and overestimation (light blue) conditions have been assigned as a function of the hail diameter reported with respect to the HP computed.

Hail probability categories: rating assigned based on hail size (cm)									
	HP < 0.20	0.20 ≤ HP < 0.30	0.30 ≤ HP < 0.40	0.40 ≤ HP < 0.50	0.50 ≤ HP < 0.60	0.60 ≤ HP < 0.70	0.70 ≤ HP < 0.80	0.80 ≤ HP < 0.90	HP ≥ 0.90
2-2.5 cm	Underestimation	Correct	Correct	Correct	Correct	Overestimation	Overestimation	Overestimation	Overestimation
3-6.5 cm	Underestimation	Underestimation	Correct	Correct	Correct	Correct	Overestimation	Overestimation	Overestimation
7-9.5 cm	Underestimation	Underestimation	Underestimation	Correct	Correct	Correct	Correct	Correct	Correct
≥ 10 cm	Underestimation	Underestimation	Underestimation	Underestimation	Correct	Correct	Correct	Correct	Correct

Red bars represent the MASHA Method while purple ones indicate NHP performance. Outcomes about MASHA Method (Fig. 62a) show that hail observations perfectly divide into case studies underestimated (50.0%) and correctly classified (50%), whereas overestimation cases don't appear. Given these results, NHP correctly classified events increase passing from 50.0% to 67.4%. Almost all the remaining part (32.6% of events) falls into underestimation category (29.3%) and more rarely into the overestimation one (3.3%). Before discussing these findings, we computed the same frequencies as a function of the hail size for checking possible

asymmetries hidden in the general result. For doing that, the validation dataset was split into the two lower (i.e. 2-2.5 cm and 3-6.5 cm; Fig. 62b) and two larger (i.e. 7-9.5 cm and ≥ 10 cm; Fig. 62c) hail diameter classes which count 75 and 17 hail reports, respectively. Results of this second analysis can be summarized as follows:

1) when the hail diameter is between 2 and 6.5 cm (Fig. 62b), the underestimation is equal to 45.3% for MASHA Method while drops to 26.7% for the NHP Method. The correct estimation contains the remaining 54.7% for the MASHA Method (for which no overestimation cases have been detected) and the 69.3% for the NHP Method which finally shows a 4% of case studies overestimated;
2) when the hail size is equal or higher than 7 cm (Fig. 62c), the overestimation is no longer considered. In very large and super hail conditions, the difference of performance is amplified: indeed, the MASHA Method underestimates 70.6% of events, while for NHP Method it decreases to 41.2%. On the other hand, more than half of reports (58.8%) has been correctly classified by NHP, whereas only 29.4% of events are flagged as "correctly estimated" using the HP_{MASHA}.

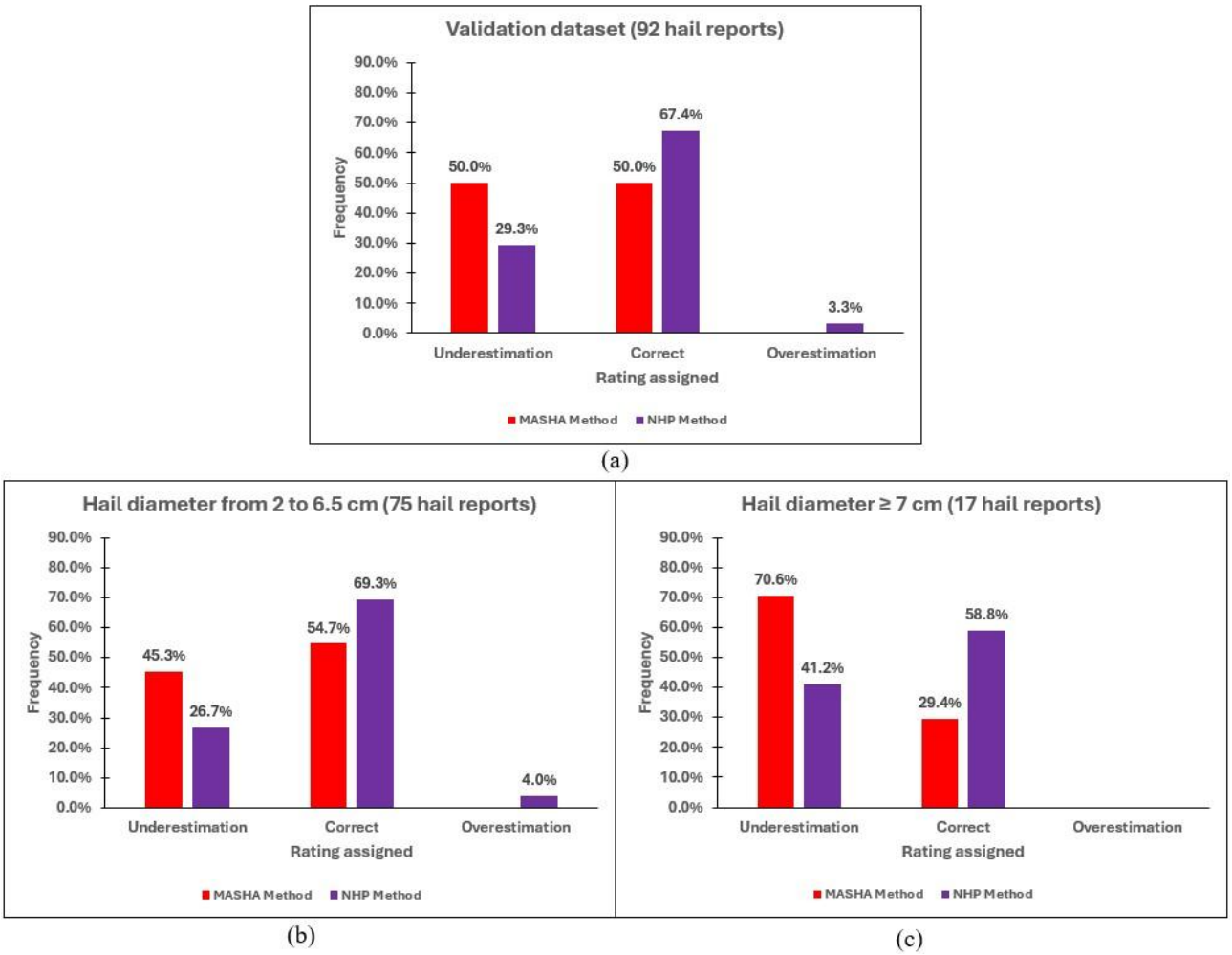

Figure 62. Hail diameter underestimation, correct estimation and overestimation obtained by applying MASHA (red bars) and NHP (purple bars) methods on the validation dataset. Results about the whole dataset (a) or as a function of the hail size (b-c) are provided.

Looking at Fig. 62a, the first interesting result regards the equal subdivision (50% vs 50%) of the underestimation and correct estimation involving the size of the hailstones recorded. At the same time, overestimation cases are never detected. These trends can be explained by considering the two most important MASHA Method limitations which were treated in Section 2.3: the space-time limited calibration provided by the MWCC-H Method and the modified HP_{MASHA} pattern in OT regions. These problems derive from different sources but cause the same effect to generally decrease the HP_{MASHA}, in a way that especially depends on the time of the polar satellite overpass and on the stage of development reached by the OT structure, respectively. The latter are also the reasons why it is likely that the HP_{MASHA} may underestimate the size of the hailstones collected on the ground. Nevertheless, it is important to remind that the MASHA Method has been conceived to observe the hailstorms from space providing the probability of ice in clouds. If from one side changing the point of view is surely penalizing, on the other, the HP_{MASHA} demonstrates itself to be decisive even for computing the 50% of NHP, providing the crucial information related to ice and clouds physical processes. Considering NHP, from Fig. 62a, it can be noticed that underestimated case studies significantly decrease going from 50.0% to 29.3%: consequently, most of them pass to the correct estimation category (rising from 50.0% to 67.4%), whereas only a few events are flagged as overestimated (3.3%). These results highlight the useful contribution of HP_{TL} to the NHP output, improving the correct classified events by 17.4%. The latter also confirms the good impact of the new method for computing the HP_{TL} based on the Equations (9), (10), (11) proposed in Section 5.2 as well as the good balance between HP_{MASHA} and HP_{TL} introduced in Equation (12). Indeed, it is easy to understand that a higher contribution coming from the HP_{MASHA} would gradually lead to the starting situation characterized by much more underestimation. On the other hand, further increasing the HP_{TL} contribution would more strongly decrease the frequency of underestimated cases, but probably the improving effect of moving other cases to the correct estimation could be equated or even worsened by the same effect leading many hail events to the overestimation class. The latter is especially valid for the two minor hail size classes, for which overestimation is considered. However, other tests will be carried out in the future, with the final perspective to further improve results presented with this NHP configuration.

Passing Fig. 62b-c, the same frequencies have been computed as a function of the diameter of the hailstones collected, dividing them into 75 hail reports ranging from 2 and 6.5 cm (Fig. 62b) and 17 hail observations having size equal or greater than 7 cm. The imbalance in the number of hail reports belonging to the two groups depends on the occurring frequency of hail phenomena, which is clearly much higher for hailstones having a lower diameter. Focusing on correctly classified events in Fig. 62b, we can note that the frequency difference between HP_{MASHA} and NHP slightly reduces (from 17.4% to 14.6%) with respect to the whole validation dataset and, at the same time, both HP_{MASHA} and NHP enhance their performance going from 50.0% to 54.7% and from 67.4% to 69.3%, respectively. The results sketched in Fig. 62c are based on 17 hail reports, having a size $\geq$ 7 cm. If compared with Fig. 62b, NHP Method undergoes a limited reduction by 10.5% (from 69.3% to 58.8%), whereas the MASHA Method strongly drops by 25.3% (from 54.7% to 29.4%). Thus, results involving the largest hailstones show that both HP_{MASHA} and NHP worse their performance but, in the latter, HP_{TL} partially balances the strong lowering of the HP_{MASHA}. This behavior can be explained considering how the

MASHA Method limitations affect the final HP_{MASHA} pattern: indeed, if from one side the space-time limited calibration provided by MWCC-H Method is random and not directly related to the hailstorm severity, on the other, it is reasonable to think that the development of OT structure is linked to the size reached by the hailstones. In addition, wider OT regions will force the HP pattern to the edges of the hailstorm as explained in Section 5.1, losing much of the physical information provided by HP_{MASHA} in this specific area of the hailstorm. Given all the above, the NHP Method obtained by the combination of MASHA satellite products with LAMPINET lightning activity has demonstrated to generally improve the detection of the hailstones in terms of size and geolocation. Indeed, on average, the NHP Method enhances the performance for the whole considered diameter range (hailstones going from 2 to more than 10 cm), but it becomes particularly useful for deep OT hailstorms producing hailstones with size equal or higher than 7 cm. Many of these findings and trends are graphically shown in Figure 63a-h. The latter highlights the NHP Method potential through the comparison of four case studies obtained from the validation dataset, in which the NHP decisively contributed to a correct classification of the hailstones affecting different areas of the Italian Peninsula. In Fig. 63a-h, hail reports (red filled dots) have been added to HP_{MASHA} (Fig. 63a-c-e-g) and to NHP (Fig. 63b-d-f-h) patterns. The four hail events and linked hail reports depicted in Fig. 63a-h happened on:

- 12 July 2023 at 19:55 UTC (Northern Italy, Lombardia region): two hail reports with maximum size of 3 and 5 cm (Fig. 63a-b);
- 21 July 2023 at 12:45 UTC (Central Italy, Marche region): two ground hail observations ranging from 5 to 6.5 cm (Fig. 63c-d);
- 08 July 2021 at 17:50 UTC (Northern Italy, Veneto region): one hail report having maximum diameter of 6 cm (Fig. 63e-f);
- 21 July 2023 at 10:15 UTC (Northern Italy, Veneto region): two hail observations having maximum size of 7 and 8 cm (Fig. 63g-h).

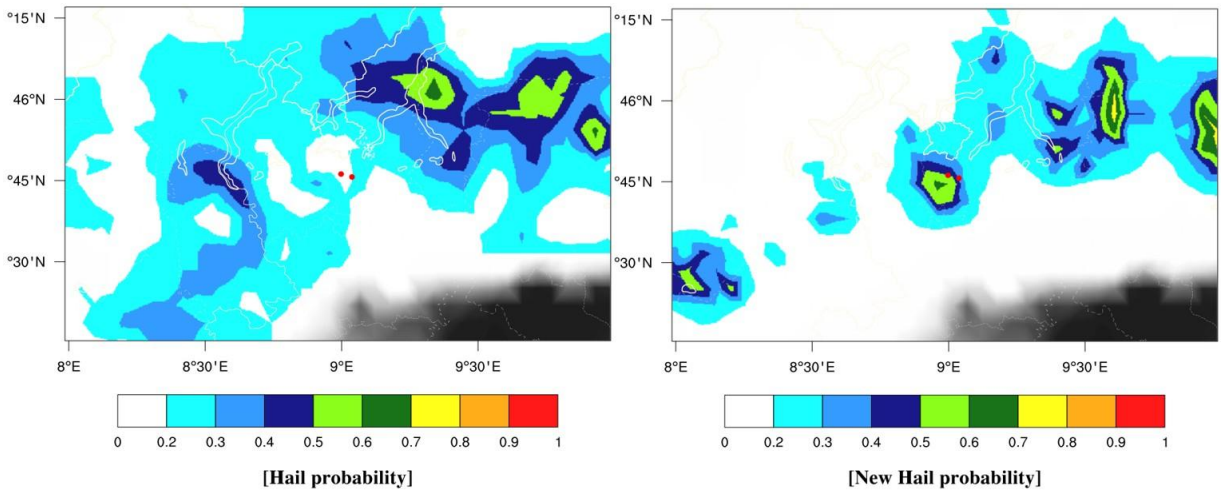

(a) (b)

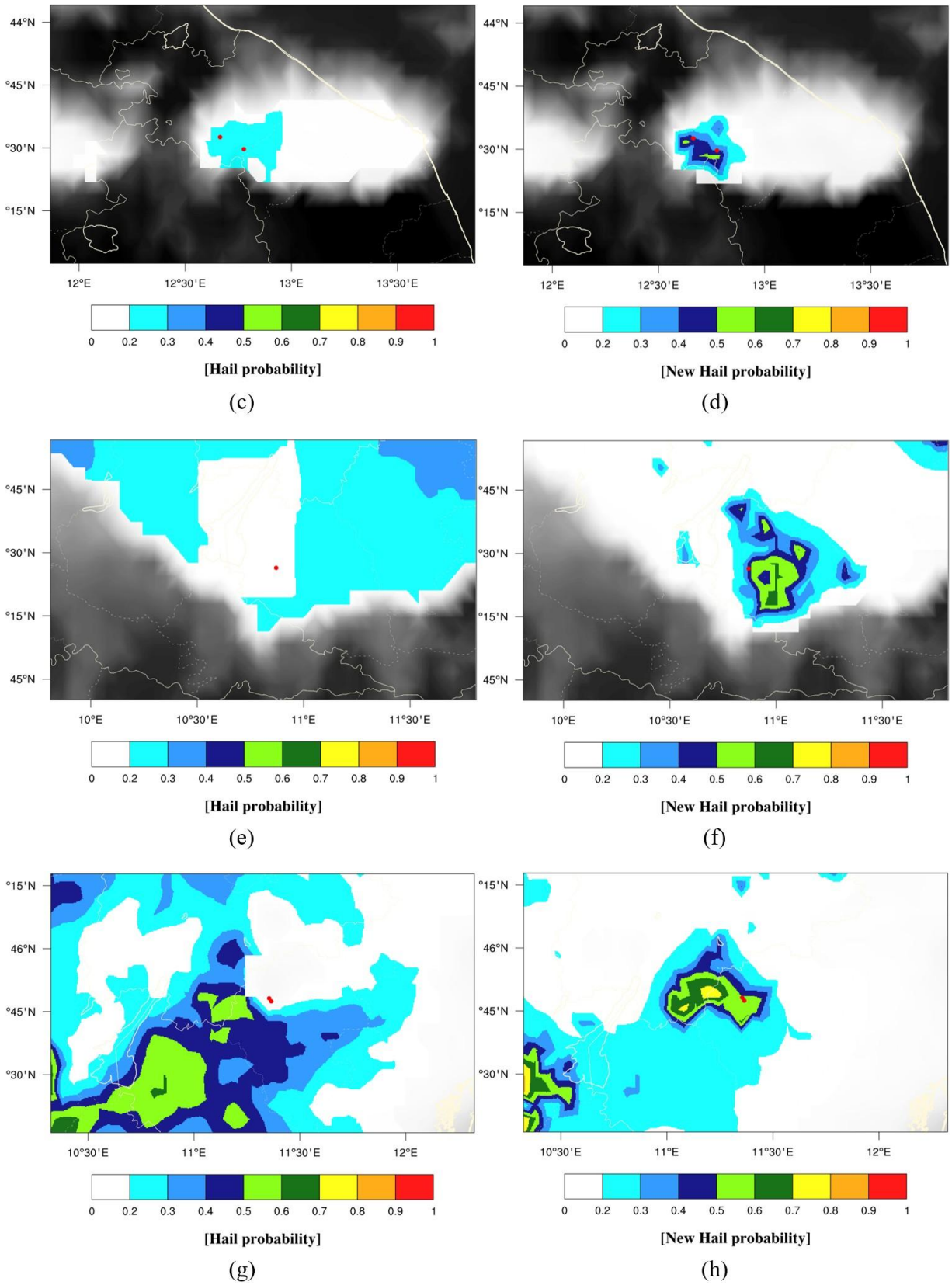

Figure 63. HP_{MASHA} (a-c-e-g; on the left) and NHP (b-d-f-h; on the right) maps shown for four hailstorms occurred on 12 July 2023 at 19:55 UTC (a-b), 21 July 2023 at 12:45 UTC (c-d), 08 July 2023 at 17:50 UTC (e-f) and on 21 July 2023 at 10:15 UTC (g-h). In (a-h), red filled dots refer to hail reports from ESWD.

Considering future perspectives, the NHP Method could be exploited in synergy with the MASHA Method for supporting control rooms and early warning systems which try to track the hailstorms and to identify areas possibly affected by the falling of the hailstones.

Chapter 6 Exploring the use of lightning characteristics to improve the radar-based detection of hailstorm severity

The two exploratory studies proposed in Chapter 4 have revealed new preliminary but interesting results about how lightning activity develops in thunderstorms on the Italian Peninsula. The key points are related to a new mathematical approach, introduced by Vermi et al. (2025), for the LJ detection. In turn, the latter may depend on the increase of lightning rate, which can take a linear or exponential trend in the first stages of the hailstorms. In addition, the LJ approach can be exploited using different lightning detection networks (e.g. LAMPINET and LINET), whereas TL strongly depends on the characteristics of sensors that make up the network. LT shows good performances usually anticipating ground hail observations, while IC and CG trends are more complex to interpret. Indeed, the correct classification of the stroke type seems more related to the DE, the density of antennas and to their ability to avoid flashes misclassification.

In the following work, an evolved version of the LJ method introduced by Vermi et al. (2025) has been used to examine 31 hailstorms occurred in Campania Region from 2015 to 2023. For the first time, the LJ algorithm performance has been compared with the radar-based hail detection algorithm developed by Capozzi et al. (2022) in the framework of "Campania Region Meteorological Radar Network".

6.1 Introduction

Weather radars appear to be invaluable instruments for the detection and the estimation of hail, thanks to their ability to provide key-information to infer the severity of convective clouds. In many studies, radar data have been reprocessed together with hail ground observations giving light to new hail distribution maps and new hail climatologies (e.g. Saltikoff et al., 2010; Cintineo et al., 2012; Burcea et al., 2016; Nisi et al., 2016; Fluck et al., 2021; Murillo et al., 2021; Brook et al., 2024). Nowadays, the most-innovative approaches developed to distinguish between raindrops and hailstones take advantage of dual-polarization weather radar features, which allow to detect hail precipitation and to better explore features and morphological characteristics of hail clouds through the differential reflectivity and other polarimetric parameters (e.g. Bechini and Chandrasekar, 2015; Zhao et al., 2020; Li et al., 2023). Several techniques based on single-polarization systems have been also proposed. Such methods rely on some features in horizontally-polarized reflectivity measurements that can be used as proxies of the physical processes connected to the hail growth (Holleman, 2001; Kunz and Kugel, 2015; Vulpiani et al., 2015; Capozzi et al., 2016; Puskeiler et al., 2016; Capozzi et al., 2018; Capozzi et al., 2022). Moreover, hail and damage reports can be used to link radar variables to the effects of hailstorms at the ground, showing average values of the radar parameters increasing accordingly with the rise of the hail diameter (Cică et al., 2015). However, the radar-based hail detection can be affected by some common range-dependent and systematic errors that may locally introduce relevant uncertainties in the estimation of hail risk.

Also, Murillo et al. (2021) state that hail climatologies based on radar observations alone are insufficient for reproducing the broad characteristics of hail report distributions. For these reasons, algorithms based on a proper merge between radar data and other meteorological measurements, such as in situ and atmospheric sounding data, could help to overcome these limitations.

In this study, we exploit the potentiality in severe hail identification of a new combined method that incoporates radar data and several lightning characteristics. Recently, in fact, the relationship between lightning activity and large hail has been explored in the Italian territory obtaining very interesting results (Vermi et al., 2025). Some previous works stated that the hailstorm's severity is well correlated to the rate of flashing during the hailfall (e.g. Changnon, 1992) and that most of thunderstorms have peaks in lightning flash rate that occur at or near the plowable hail report times (Kalina et al., 2016). From the physical point of view, lightning strikes can be considered a proxy for hail formation, since graupel particles play a crucial role during the electrification process in hailstorms (e.g. Williams et al., 1991; Saunders, 1993). Previous investigations about lightning activity during the life cycle of the hailstorms revealed that the total lightning is the best information to recognize the intensification of storms (Schultz et al., 2011). Indeed, total lightning and lightning densities are several times more active in the hailstorms than ordinary thunderstorms (Jurković et al., 2015; Wapler, 2017) and the probability of lightning occurrence is much higher in convective rain regions than in the stratiform ones (Feng et al., 2007). In addition, large and rapid increases in lightning flash rates, termed "lightning jumps" by Williams et al. (1999), indicate the growth of a storm but, on the other hand, it should be noted that level or decreasing strokes don't necessarily imply that thunderstorms are in steady state or weakening (Emersic et al., 2011). Since lightning jumps have been observed to occur as severe weather manifests within the storm, these outcomes lead to the development of several lightning jump algorithms (Schultz et al., 2009; Gatlin and Goodman, 2010; Schultz et al., 2011; Metzger and Nuss, 2013; Yao et al., 2013; Chronis et al., 2015; Farnell et al., 2017; Wapler, 2017; Farnell et al., 2018; Tian et al., 2019; Farnell and Rigo, 2020; Tian et al., 2022) used to diagnose possible severe weather manifestations such as large hail, strong wind gusts, heavy rainfall, tornadoes and flash floods. Farnell et al. (2017) introduced a modified lightning jump algorithm, in which the identification of storm cells was solely based on total lightning data, without radar data. This innovative concept has been also implemented in Vermi et al. (2025). Links between lightning jumps and updraft intensification have been confirmed by Gatlin and Goodman (2010) and Schultz et al. (2017) while Chronis et al. (2015) reported that, when at least one LJ is detected, storms last longer and are better related to maximum hail size expected, vertical integrated liquid and lightning flash rates. Also, the authors determined that stronger jumps imply more time until storm decay but a clear relationship between the maximum hail diameter and the number of lightning jumps has never been observed (Farnell et al., 2018). Consequently, the algorithms related to the total lightning and lightning jumps may be used as hailfall nowcasting predictors, especially considering lead times obtained between lightning jump detection and severe weather occurrence. Indeed, almost all above-mentioned studies state that the average lead times range typically from 10 to 40 minutes (e. g. Schultz et al., 2009; Gatlin and Goodman, 2010; Metzger and Nuss, 2013; Wapler, 2017; Tian et al., 2019) but lightning jumps can be detected until 120 minutes before and 30 minutes after severe weather observations (e. g. Farnell

et al., 2017; Farnell et al., 2018; Rigo and Farnell, 2022). Moreover, lightning jump algorithms based on total lightning outperform the corresponding cloud-to-ground algorithms, showing lead times furtherly improved (e. g. Schultz et al., 2011; Yao et al., 2013).

In this work, we introduce a combined method for integrating lightning data into into the radar-based hail detection algorithm developed by Capozzi et al. (2022) in the framework of "Campania Region Meteorological Radar Network" (hereafter, CARMEN). Starting from results obtained by Capozzi et al. (2022), the main goal of this study is to support the radar hail detection tool adding the information provided by lightning activity, in order to better discriminate the evolving hailstorms. For achieving this purpose, we investigated 31 case studies occurred in the Campania Region (Southern Italy) and surrounding areas in which large hail or very large hail (maximum diameter of the hailstones ≥ 2 cm or ≥ 5 cm, respectively) has been detected. In the second part of this work, we will discuss some features of lightning activity that could help to infer the potential maximum diameter of the hailstones. Since these trends are based on lightning activity and are found during the initial development of the hailstorms, these preliminary findings may represent an important outcome for hailfall nowcasting predictors.

The organization of this work is the following: Section 6.2 presents the study area and describes types of data analyzed (hail reports, radar and lightning strikes) and the corresponding methodologies applied. In Section 6.3, comparing two methods derived by radar and lightning data, we will show how lightning features can support the CARMEN project in identifying and tracking the hailstorms. After that, the potential relationship between some lightning variables and the maximum hail diameter will be discussed. Finally, main conclusions of this work will be provided in Section 6.4.

6.2 Data and Methodology

6.2.1 Study area

In this work, the combined method involving hail reports, radar and lightning data has been tested on the Campania Region (Southern Italy) and adjacent areas within a geographical domain starting from 40.10°N to 41.50°N in latitude and from 13.60°E to 15.60°E in longitude, as shown in the red box in Figure 64. This territory is characterized by a diversified morphology that rapidly changes: the coastline and main inland sectors in the western side of the region are opposed to the Appennine ridge, that is located into the eastern one. The latter occupies a large part of the region and stands out for a complex orography in which the Mount Miletto reaches the highest top, i.e., 2050 meters above the sea level (hereafter, m asl) in the northern sector but many other mountain chains exceed 1400-1500 m asl. These morphological features impede radar data measurements, reducing their quality in terms of reliability and spatial coverage. For these reasons, the introduction of lightning activity may support the radar hail detection tool without being affected by lack of measurements due to the complex orography.

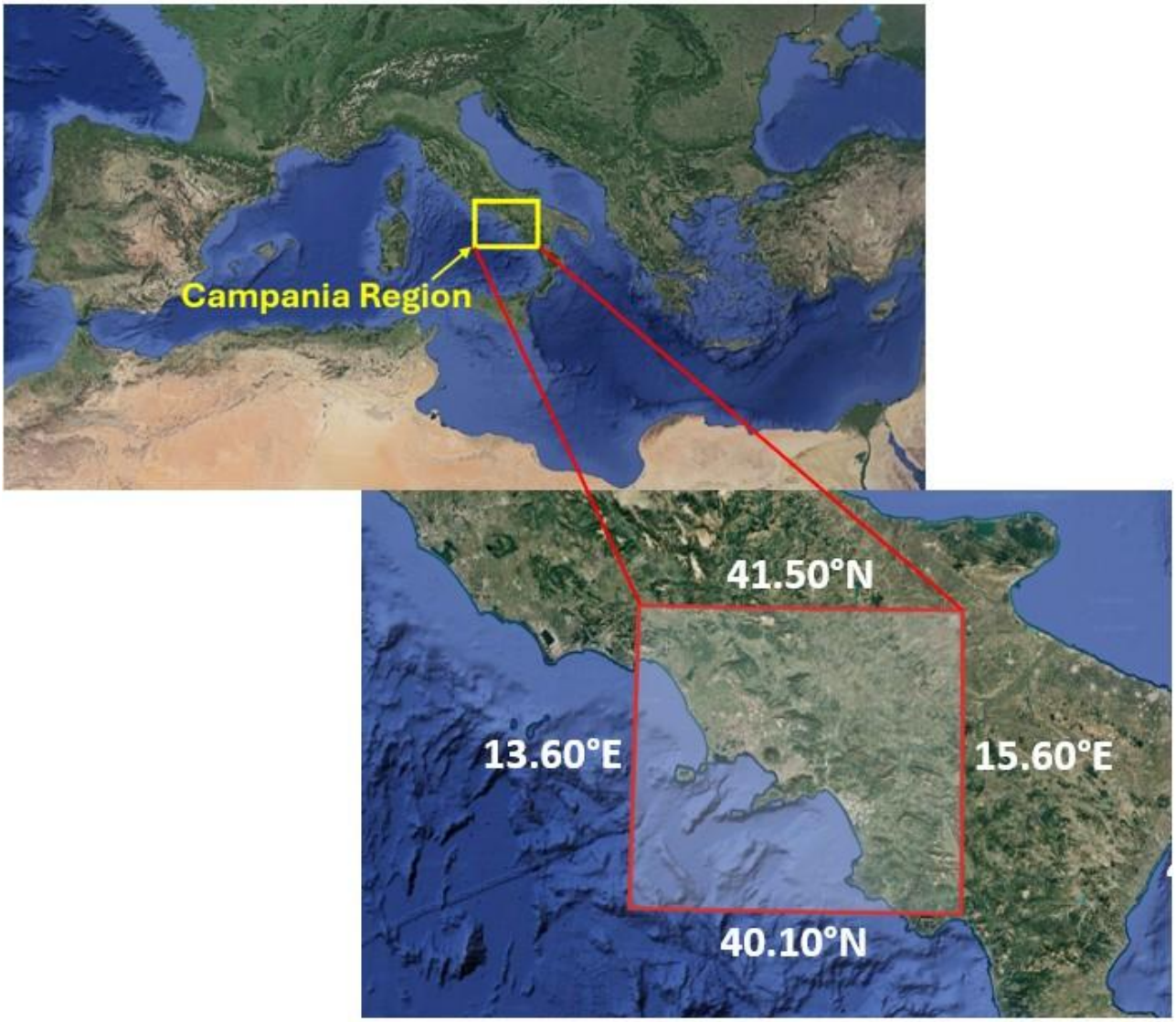

Figure 64. In the top map, the Campania Region and surrounding areas are emphasized by the yellow box in the Mediterranean basin. Below, the inner part of the red box describes the study area defined in this work in terms of latitude and longitude (Images credit: © Google Earth, Data Sio, NOAA, U.S. Navy, NGA, GEBCO).

6.2.2 Hail reports

Hail reports are fundamental to testify the falling of the hailstones at a given location. Indeed, thanks to this information it is possible to classify the hailstorms and to understand how they are born and develop, considering the entire lifecycle of these systems. On the other hand, we must take into account that ground hail observations are strongly dependent on population density and sometimes hail phenomena can be greatly underestimated or totally missed. In this work, we exploited two networks to select hail reports in Campania Region from 2015 to 2023 (a detailed table about hail observations used in this study is provided in Appendix B). Most of them belong to the European Severe Storm Laboratory's European Severe Weather Database (Dotzek et al., 2009) which is the first european database containing many different severe weather observations, including large hail reports (maximum hail diameter ≥ 2.0 cm). In the European Severe Weather

Database (https://eswd.eu/; hereafter, ESWD), for each hail observation, date, time, latitude, longitude, maximum hail size (cm), pictures, newspaper articles or post by social media are provided. All reports are classified using four quality-control levels:

- QC0 ("as received");
- QC0+ ("plausibility check passed");
- QC1 ("report confirmed by reliable source");
- QC2 ("scientific case study").

As in previous works (e.g. Púčik et al., 2019), only QC1 and QC2 data were used, also discarding data with temporal uncertainties more than ± 30 minutes, but most of them are contained within ± 5 minutes. Thanks to this dataset, many studies about hailstorm characteristics, hail frequency and large hail climatology in Europe (Punge et al., 2014; Pilorz, 2015; Punge and Kunz, 2016; Istrate et al., 2017; Kunz et al., 2020; Fluck et al., 2021; Wilhelm et al., 2021; Battaglioli et al., 2023a-b; Hulton and Schultz, 2024; Kahraman et al., 2024) were developed. Secondly, few hail events were identified through the monitoring network "Campanialive" (http://www.campanialive.it/), that is a regional network in which users can upload pictures, comments or news about weather phenomena occurred in this territory. Considering the high variability of the popoulation density in Campania Region, this local network is particularly useful to provide information on hailstorms in remote areas.

6.2.3 Radar data and CARMEN project

Radar data used in this study are provided by two single-polarization X-band weather radars (Figure 65) located in Naples urban area, at the top of Castel Sant'Elmo (40.8433°N, 14.2385°E; 280 m asl, approaching the coastline) and in Trevico (41.0522°N, 15.2357°E; 1050 m asl, eastern sector of the Campania Region) that together make up the CARMEN project hail detection tool. These systems, named WR-10X and manufactered by ELDES srl, ensure some advantadges such as low power consumption (< 300 W on average), low weight (about 100 kg) and minor costs of installation and maintenance. Radars are sinchronized in time, producing a scan every 10 minutes characterized by a spatial resolution of 450 m, an azimuth resolution equal to 1.0° and a maximum available range of 108 km. The only difference is the elevation scanning mode, since Trevico radar performs the scan exploiting nine different elevations (1, 2, 3, 4, 5, 7.5, 10, 12.5 and 15°) while for Naples radar it has been also added the 20° elevation. In some areas, especially between Naples and Trevico, the radar beams may overlap (as visible by the light circles in Fig. 65): in this case, we will use the highest reflectivity measurement coming from the two instruments. Further technical details and about the development of a radar composite product are provided by Capozzi et al. (2022). In the framework of the CARMEN project, the probability of hail results from the Vertically Integrated Liquid Density (VILD) algorithm that was proposed by Amburn and Wolf (1997) and subsequently it was applied for the hailstorms detection in many works (e.g.

Belk and Wilson, 1998; Blaes et al., 1998; Lahiff, 2005; Cică et al., 2015; Wapler et al., 2016; Capozzi et al., 2018; Ortega, 2018; Nisi et al., 2020).

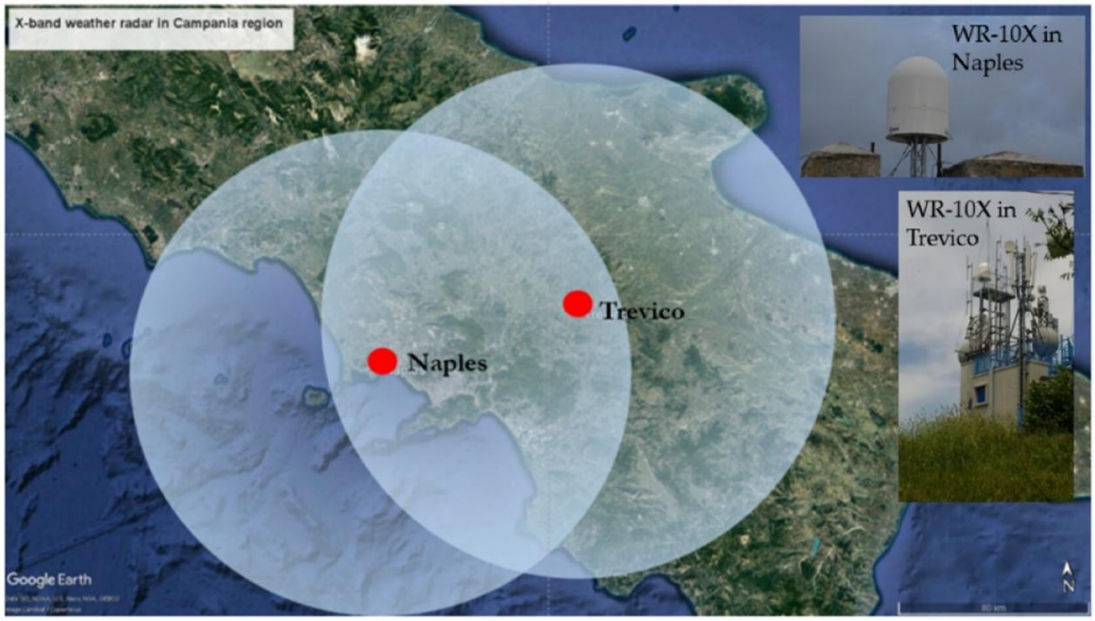

Figure 65. Red dots indicate the X-band weather radars location throughout the Campania Region. The light circle surrounding red dots shows what is the maximum spatial coverage of the two instruments. In the upper right, pictures of the two instruments are provided (adapted from Capozzi et al., 2022).

The VILD parameter, expressed in g · m^{-3}, can be defined as the ratio between the Vertical Integrated Liquid (VIL; Greene and Clark, 1972) and the EchoTop in Equation (13):

$$VILD = 1000 \cdot \frac{VIL}{EchoTop} \tag{13}$$

where VIL (expressed in kg · m^{-2}) is computed through the vertical integral of the horizontal reflectivity (Z_h) within the atmospheric column, while the EchoTop (expressed in m) is the maximum altitude at which a significative radar reflectivity has been detected. According to these previous studies, VILD can be considered as a more homogeneous parameter for the identification of the hailstorms, thanks to the normalization with respect to the vertical extension of the thunderstorms. For evaluating the performance of the VILD method, it was tested on 53 case studies occurred in the Campania Region from April 2012 to June 2015 (more details about this dataset can be found in Capozzi et al., (2018)). After investigating this dataset, the authors described final results in Figure 66 (Capozzi et al., 2022), using a scatterplot of VIL values versus the EchoTop. These outcomes lead to an evaluation about three possible VILD threshold values (each black line in Fig. 66 represents one of them: 2.0, 2.4 and 3.0 g · m^{-3}) for discriminating between hail (blue dots) and non-hail producing (orange dots) events (further methdological details are explained in Capozzi et al. (2018) and in Capozzi et al. (2022)). After making these assessments, the authors established that VILD equal to 2.4 g · m^{-3} was the best value obtaining the following results:

- 33/34 hail cases were correctly classified as hailstorms;
- 11/19 convective events (only heavy rainfall) were falsely detected as hail-producing.

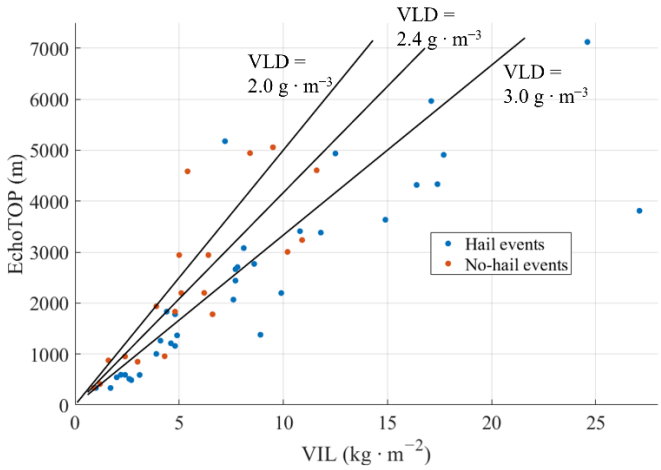

Figure 66. Scatter diagram reporting VIL values versus EchoTop. Hailstorms are represented using blue dots while no hail events are marked with orange ones. The black lines in the graph indicate three possible optimal VILD thresholds for recognizing the hailstorms (adapted from Capozzi et al., 2022).

Using these threesholds, the VILD method correctly identified almost all hail case studies but, on the other hand, more than half of non-hail producing events were misclassified. For this reason, in this work it was decided to support the hail detection tool with an additional information (i.e. lightning activity and related variables), in order to improve the identification and tracking of the hailstorms. In the same way, the VILD threshold value equal to 2.4 g · m^{-3} was used to classify 31 hailstorms occurred in the Campania Region from 2015 to 2023. Using one or more hail ground observations available for each hail event, the VILD pattern (that directly depends on the horizontal reflectivity Zh) has been analyzed. Starting from the hail report, we can recognize the hail-producing storm cell that is affecting the corresponding area and go back in time until the first scan having VILD values higher than 0 g · m^{-3}. Once the hailstorm has been identified, for every scan we surround it with a box of variable size, depending on the dimensions reached by the evolving storm system. After that, it is possible to investigate the entire hailstorm lifecycle, collecting all 10-minute scans moving from the formation to the dissipative stage and computing the VILD maximum value that characterizes the hailstorm. An example of this procedure is provided in Figure 67a-h, which depicts the VILD pattern for the 09 August 2022 from 13:00 UTC to 14:10 UTC. In this case, the ESWD database gives out an hail report (represented by the pink dot in the red box in Fig. 67g) in “San Giorgio del Sannio” (41.06°N, 14.89°E) at 14:00 UTC (± 5 minutes), indicating hailstones having a maximum diameter of 2 cm. Starting from this information, we reconstructed the whole lifecycle of the hailstorm, which gave the first VILD signal at 13:00 UTC (i.e. radar scan and lightning data have been synchronized in time and processed from 12:57:30 UTC to 13:07:30 UTC; the same synchronization is valid for other timeslots) and the last one at 14:50 UTC (for brevity, in Fig 65a-h last four scans are not shown).

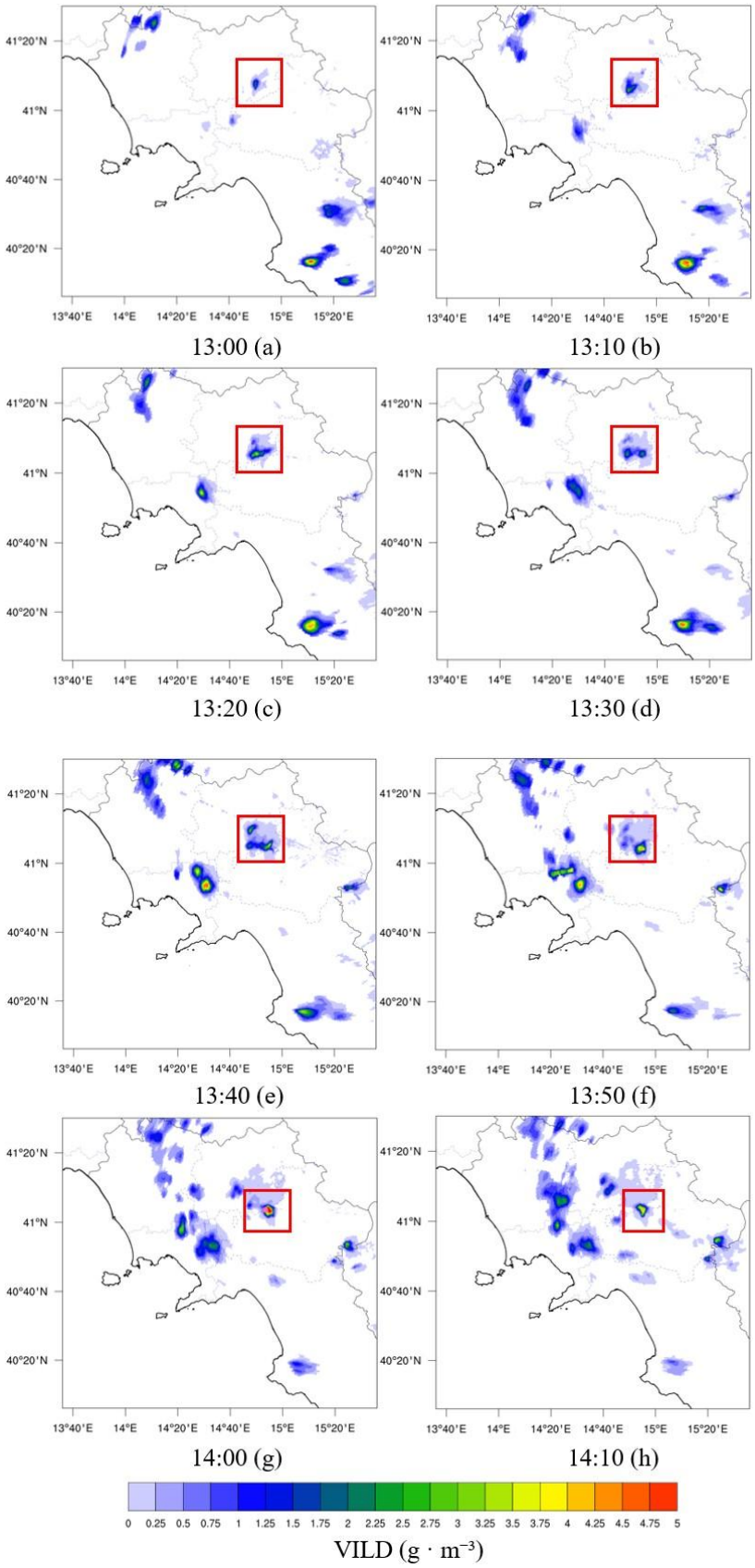

Figure 67. VILD maps (a-h) for the 09 August 2022 from 13:00 UTC to 14:10 UTC. The inner part of the red box shows the area in which the hailstorm developed and where the VILD maximum value has been computed. The pink dot in (g) shows the hail report detected in "San Giorgio del Sannio" (41.06° N, 14.89° E) at 14:00 UTC (± 5 minutes) referring of a maximum hail size of 2 cm (ESWD source, https://eswd.eu/).

Then, a red box like in Fig. 67a-h is applied to define the hailstorm area, which allows to calculate the VILD maximum value without affecting this data with other storm cells not belonging to this system. Finally, we compare the VILD threshold value equal to 2.4 $g \cdot m^{-3}$ proposed by Capozzi et al. (2022) with the VILD maximum value found: if the latter is higher, the thunderstorm will be classified as hail-bearing storm by the hail detection tool. For instance, in this case study, Table 12 shows that the VILD maximum value exceeds the VILD threshold in most of the reconstruction (yellow lines), having a maximum of 6.7 $g \cdot m^{-3}$ that was reached in correspondence of the ESWD hail report, at 14:00 UTC (orange line).

Table 5. VILD maximum values for the case study of 09 August 2022. Yellow lines highlight when the VILD threshold has been exceeded while the orange one indicates the VILD maximum value found at the same time of the hail report.

09 August 2022 case study		
Date	Time (UTC)	VILD maximum value ($g \cdot m^{-3}$)
09/08/2022	13:00	2.2
09/08/2022	13:10	2.8
09/08/2022	13:20	3.3
09/08/2022	13:30	2.6
09/08/2022	13:40	3.5
09/08/2022	13:50	4.3
09/08/2022	14:00	6.7
09/08/2022	14:10	4.5
09/08/2022	14:20	3.8
09/08/2022	14:30	3.4
09/08/2022	14:40	1.1
09/08/2022	14:50	0.7

6.2.4 Lightning data

The Meteorological Service of the National Air Force manages the Italian lightning detection network LAMPINET, which consists of 15 sensors that provide lightning data in the Italian territory both on the sea and on the inlands. LAMPINET antennas bandwidth is 1 – 350 kHz (containing Low and Very Low Frequency emissions), an optimal frequency range especially to measure cloud-to-ground (CG) strokes. Consequently, the detection efficiency for CG lightning strikes reaches 90% while it decreases to about 30% for intra-cloud (IC) flashes (Biron, 2009; Rosati, 2023). For each stroke time, latitude, longitude, type (IC or CG), polarity and electric field values are reported, with a spatial resolution of about 500 m and a temporal resolution of 1 second. These features make lightning data very useful for supporting the CARMEN project hail detection tool. Firstly, we must sinchronize radar and lightning data in time, aggregating strokes in 10-minute files in order to have an output comparable with scans performed by X-band weather radars. Subsequently, we remap lightning data using a regular grid to ease the strokes count and, employing the same methodology proposed for computing the VILD maximum value, we apply a box surrounding the distribution of lightning strikes related to the hailstorm we are investigating. The box size and location are the same used to analyze the VILD pattern, even if sometimes it can happen there are small differences linked to the different distribution of the

two variables. In the framework of lightning strikes, we define the box to count the total number of strokes produced by the hailstorm in the last 10 minutes (hereafter, total lightning) for the whole duration of the storm. In Figure 68a-h we revive the 09 August 2022 case study, but considering lightning data. As for the VILD pattern, first strokes related to the hail report in "San Giorgio del Sannio" (41.06°N, 14.89°E; pink dot in Fig. 68g) appear at 13:00 UTC going on until 14:20 UTC. In Table 13, total lightning is reported, showing that the peak of lightning activity occurs between 13:30 UTC and 13:50 UTC.

Using the total lightning data, we can introduce the lightning jump computation. As explained in Section 6.1, lightning jump (hereafter, LJ) detection has been widely used in many previous works for the determination of severe weather manifestations (e.g. heavy rain, large hail, severe wind gusts, tornadoes, flash floods etc.) and many algorithms have been proposed on this topic. In this work, we adapted the method introduced by Vermi et al. (2025), which exclusively focuses on the identification of the hailstorms, through the Equations (7a-7b-7c):

$$LJ_{20} = \frac{TL_t}{TL_{t-20}} \quad (7a) \qquad LJ_{30} = \frac{TL_t}{TL_{t-30}} \quad (7b) \qquad LJ_{40} = \frac{TL_t}{TL_{t-40}} \quad (7c)$$

where LJ is defined as the ratio between the TL measured at time t (TL_t) and the TL recorded 20, 30 or 40 minutes before (TL_{t-20}, TL_{t-30} and TL_{t-40}), respectively. These formulations are applied when the TL_t is equal or higher than 20 flashes: it means that, on average, the minimum lightning rate considered to calculate LJ is equal to 2 per minute. This threshold is quite low, especially if compared with previous studies (e.g. Schultz et al., 2009), but it should be noted that LAMPINET network detection efficiency reaches only 30% for IC strokes.

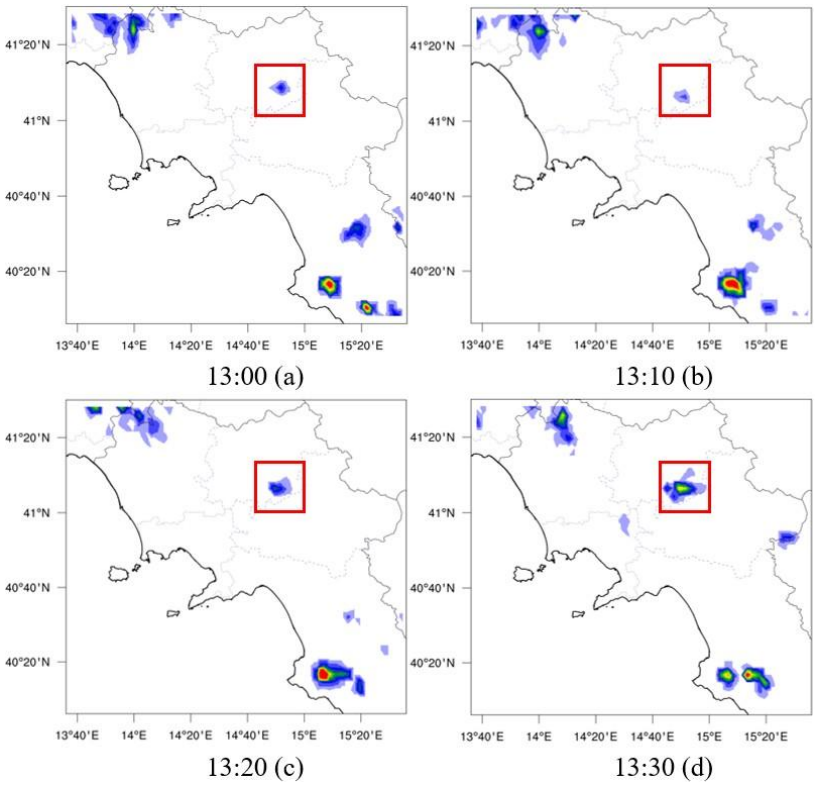

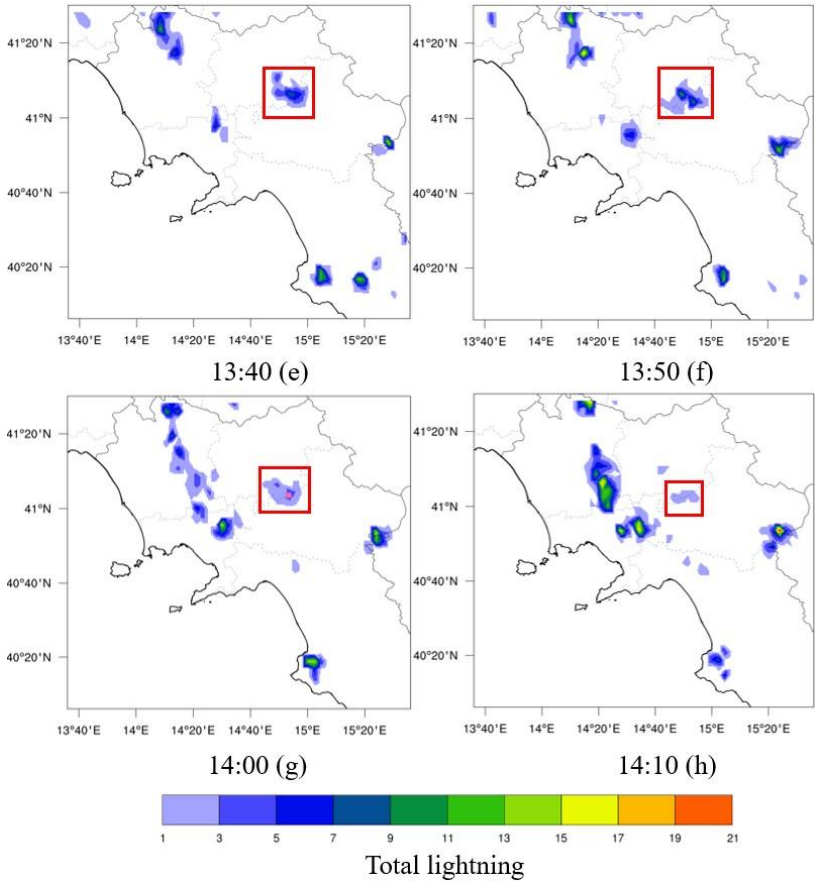

Figure 68. Total lightning maps (a-h) for the 09 August 2022 from 13:00 UTC to 14:10 UTC. The inner part of the red box shows the area in which the hailstorm developed and where lightning strikes have been counted, like in Fig. 67 for VILD maximum value. The pink dot in (g) shows the hail report detected in "San Giorgio del Sannio" (41.06° N, 14.89° E) at 14:00 UTC (± 5 minutes) referring to a maximum hail size of 2 cm (ESWD source, https://eswd.eu/).

Table 6. TL measured every 10 minutes for the hail event of the 09 August 2022 related to the ground hail observation in "San Giorgio del Sannio" (41.06° N, 14.89° E), at 14:00 UTC (± 5 minutes).

09 August 2022 case study		
Date	Time (UTC)	Total Lightning (TL)
09/08/2022	13:00	14
09/08/2022	13:10	10
09/08/2022	13:20	27
09/08/2022	13:30	72
09/08/2022	13:40	55
09/08/2022	13:50	58
09/08/2022	14:00	35
09/08/2022	14:10	13
09/08/2022	14:20	10

This justifies the use of such a threshold, since IC flashes are predominant in thunderstorms (Montanyà et al., 2007): indeed, especially during the development of the hailstorms, the IC/CG ratio can reach values even close to 400 (Montanyà et al., 2009). In addition, the operative frequency range of LAMPINET sensors (1-350

kHz) is lower than that of other lightning strikes detection networks, leading to a smaller TL measured, in the same conditions. The second important threshold concerns the denominator (i.e. TL_{t-20}; TL_{t-30}; TL_{t-40}) of Eq. 7a, Eq. 7b and Eq. 7c: indeed, when TL is above 20 but the denominator is very low or even equal to 0, it can result in a very high but insignificant LJ. To overcome this problem we decided to put the denominator equal to 10, even when its value is between 0 and 9. This normalization is valid throughout the whole duration of the hailstorm but it's particularly useful to highlight potential jumps occurring in the initial stage of the storm that, otherwise, would be lost. Consequently, the minimum LJ value that is possible to calculate is $LJ_i = 20/10 = 2.0$.

In view of the above, reconsidering the TL recorded in Table 13 for the case study of the 09 August 2022, we can compute the three LJ temporal series (LJ_{20} – LJ_{30} – LJ_{40}) depicted in Figure 69a-c. LJ series computation allows us to introduce two new variables related to lightning activity:

- *Number of lightning jumps* (NLJ): number of times that, in each LJ series, LJ value is equal or higher than 2.0 (e.g. in Fig. 69a, NLJ = 2; in Fig. 69b, NLJ = 4; in Fig. 69c, NLJ = 4);
- *Intensity of the strongest lightning jump* (ISLJ): the LJ that reaches the maximum value in each LJ series (e.g. in Fig. 69a, ISLJ = 7.2; in Fig. 69b, ISLJ = 5.5; in Fig. 69c, ISLJ = 7.2).

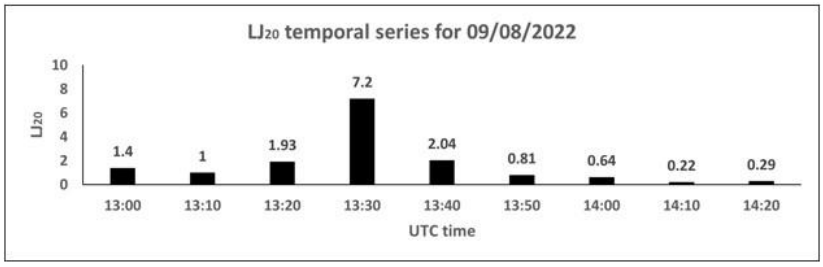

(a)

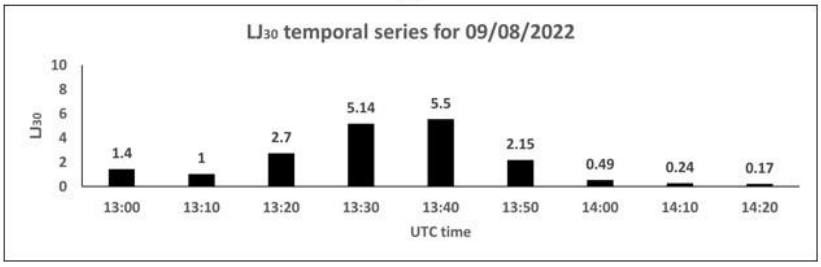

(b)

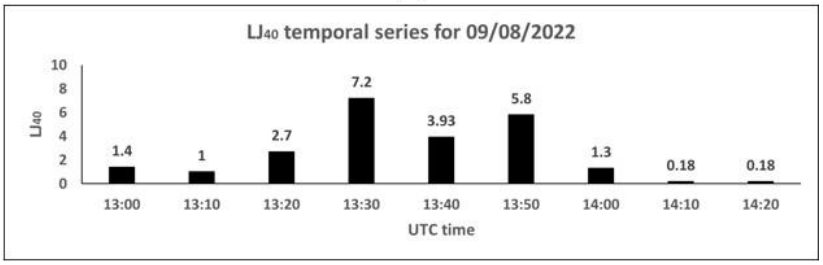

(c)

Figure 69. LJ temporal series at 20 (a), 30 (b) and 40 (c) minutes (LJ_{20}, LJ_{30} and LJ_{40}) for the hail event occurred in "San Giorgio del Sannio" (41.06° N, 14.89° E) on 09 August 2022 at 14:00 UTC (± 5 minutes).

After calculating the three LJ series, we must choose which LJ series will represent lighning activity and linked variables (NLJ and ISLJ) for this case study. Since we are very interested in studying abrupt increases in TL (i.e. lightning jumps) potentially related with develping hailstorms, we decided to use the LJ series that reaches the highest ISLJ. In some hail events (like in the above-mentioned one), it is possible that in more than one LJ series the ISLJ is equal (in this case study LJ_{20} and LJ_{40} produce an ISLJ = 7.2). In this situation, the LJ series choice is based on the second highest ISLJ measured in the corresponding series that, from Fig. 69a-c, is equal to 2.04 and 5.80 for LJ_{20} and LJ_{40}, respectively. Therefore, the LJ series used to describe lightning activity for this case study is LJ_{40} whereas LJ_{20} and LJ_{30} are rejected. At the same time, lightning activity could be analyzed even calculating other LJ series, for instance considering a time difference of 10 or 50 minutes (i.e. LJ_{10} or LJ_{50}) or even larger. However, Vermi et al. (2025) found that the ISLJ found in LJ_{10} series is constantly lower when compared to Eq. 7a, Eq. 7b and Eq. 7c representing only partially jumps produced by lightning activity. On the other hand, enlarging too much the temporal window (LJ_{50} or more) doesn't take into account the dynamic evolution of strokes: in this way, a large part of LJ values is simply obtained normalizing the TL by 10, without adding anything to the information already provided by TL itself.

Lead time (hereafter, LT) is the last variable we decided to investigate in order to understand if hailstorms can be detected in advance exploiting lightning activity. LT is defined as the time difference (in minutes) between the first hail report measured and the first LJ detected (i.e. LJ $\geq$ 2.0) in the LJ series. It follows that LT will be:

- positive, when LJ advances the hail report;
- equal to 0, when LJ and the hail observation are coincident;
- negative, when LJ is in late compared to the time of hail detection.

Indeed, considering the hail event occurred on 09 August 2022 in "San Giorgio del Sannio", the time of hail report is 14:00 UTC (± 5 minutes), while the first LJ detected in LJ_{40} temporal series is equal to 2.7 at 13:20 UTC. Following our definition, for this case study, the first LJ is 40 minutes in advance of the hail report.

6.2.5 Very large hail dataset

In the second part of the next Section, we will discuss the behaviour and possible trends of lightning activity found for large hail and very large hail classes, analyzing them with the methodology proposed in the previous paragraph. Very large hail events cause a strong increase in the probability of people injuries, damage to cars and buildings and, even if their frequency is much lower (Pilorz, 2015; Púčik et al., 2019; Laviola et al., 2022), understanding their dynamics can be crucial to prevent people, economic and social negative impacts. As expected, considering the 31 case studies dataset in which radar and lightning data have been analyzed on the Campania Region and surrounding areas from 2015 to 2023, only two of them include very large hail (maximum diameter of the hailstones $\geq$ 5 cm) observations. Consequently, the split of hail events in two categories (large hail and very large hail) would lead to two very unbalanced datasets (29 case studies for large

hail class and only 2 for the very large hail one) that would make statistically not significant any trend found themselves. To overcome this problem, we decided to enlarge the very large hail dataset including other 10 case studies happened on the Italian Peninsula from 2015 to 2023, exploiting the hail reports provided by ESWD (for further details about this dataset see Table 5 in Vermi et al. (2025) in Section 4.1.2). In this way, we will examine and compare lightning features, variables and potential trends that characterize large hail (29 case studies) and very large hail (12 case studies) categories.

6.3 Results and Discussion

6.3.1 LJ algorithm to support the CARMEN project

In the framework of CARMEN project, we examined the hailstorms dataset applying both VILD and LJ algorithms until the final evaluation of results, in which each method can contribute for recognizing the main features of the hailstorms. A schematization of this data flow architecture is provided in Figure 70.

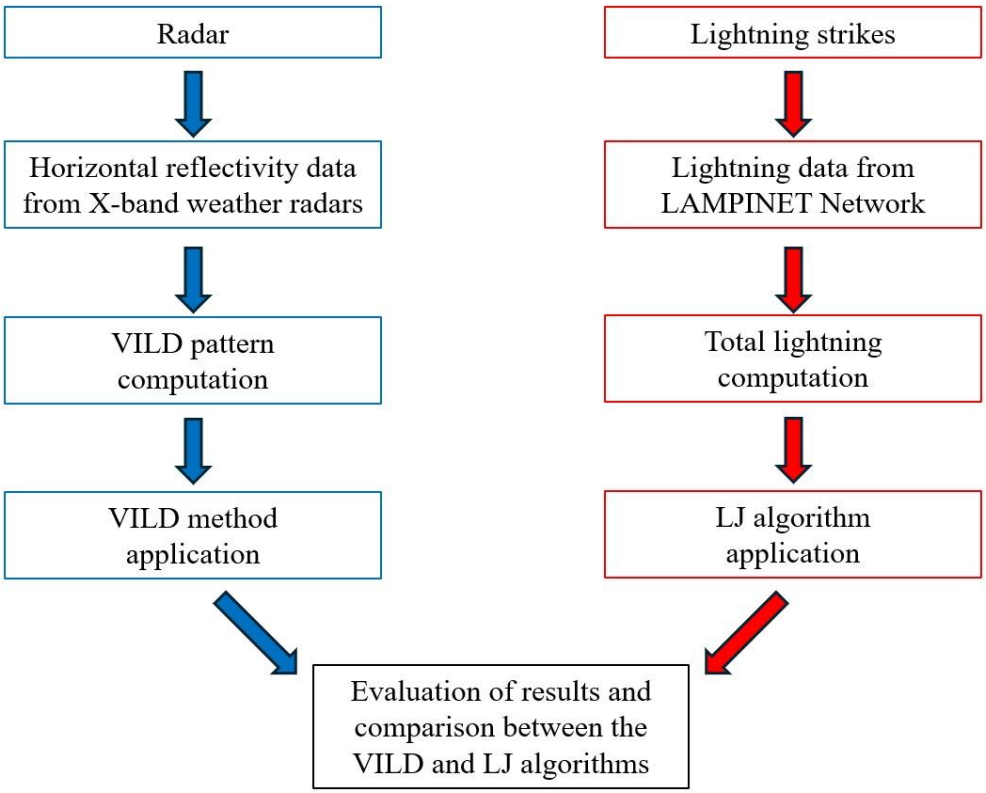

Figure 70. The data flow architecture converging into the VILD and LJ algorithms.

Considering the 31 case studies occurred in the study area in the 2015-2023 period, if we focus on the number of hail events identified by each method, we can simply compute the probability of detection (hereafter, POD) indicator which can be expressed as the ratio between the number of positive tests and the total number of

tests. The latter results from the sum of positive (named “hits”; hereafter, H) and negative (denominated “missed”; hereafter, M) tests, as shown in Equation (14):

$$POD = \frac{number\ of\ positive\ tests}{total\ number\ of\ tests} = \frac{H}{H+M} \quad (14)$$

From Table 14, we can notice a very similar outcome for both VILD and LJ methods: indeed, the VILD threshold value has been reached in 25/31 (POD = 80.6%) hailstorms while the lightning algorithm found at least one LJ in 24/31 (POD = 77.4%) case studies. Table 14 highlights that VILD and LJ algorithms identify most of the hailstorms and sometimes the two methods give out the same result.

Table 7. Results derived from the application of VILD and LJ algorithms. The "YES" column reports the number of case studies (%) in which the threshold value has been overcome. In contrast, the “NO” column counts the hail events that weren’t recognized by these methods.

VILD and LJ algorithms applied on 31 case studies		
	YES	NO
VILD ≥ 2.4 g · m^{-3}	25 (80.6%)	6 (19.4%)
LJ ≥ 2.0	24 (77.4%)	7 (22.6%)

To better understand how they perform, we divided these findings into a contingency table (Table 15) in which all available information is taken into account. From Table 15, it emerges that in 20/31 (POD = 64.5%) case studies both methods correctly classify the developing hailstorm but their agreement rises until 71% if we consider 2/31 (6.5%) hail events completely misclassified. The latter is probably related to isolated and fast decaying storm cells, for which both methods didn’t reach the thresholds established. Moving to the remaining 9 case studies, it’s interesting to note that these events are almost symmetrically split in the last two categories: 5/31 (16.1%) are recognized only by the VILD method while, in the same way, solely the LJ algorithm identifies 4/31 (12.9%) hailstorms.

Table 8. The contingency table shows how results can be split after the application of VILD and LJ algorithms.

Contingency table			
		VILD ≥ 2.4 g · m^{-3}	
		YES	NO
LJ ≥ 2.0	YES	20 (65%)	4 (13%)
	NO	5 (16%)	2 (6%)

Thus, considering four different configurations, results provided in Table 14 and in Table 15 can be summarized as follows:

- VILD method-only (VILD ≥ 2.4 g · m^{-3}): H = 25, M = 6, POD = 80.6%;
- LJ method-only (LJ ≥ 2.0): H = 24, M = 7, POD = 77.4%;
- Combined method-AND (VILD ≥ 2.4 g · m^{-3} AND LJ ≥ 2.0): H = 20, M = 11, POD = 64.5%;

- Combined method-OR (VILD ≥ 2.4 g · m^{-3} OR LJ ≥ 2.0): H = 29, M = 2, POD = 93.5%.

Unfortunately, the lack of a dataset including ordinary thunderstorms without hail production, doesn't allow us to calculate other indicators such as the false alarm rate (hereafter, FAR). However, looking at the combined methods, we can state that the "AND" configuration needs the overcoming of both thresholds to confirm the hail event detection and it is probably more useful to minimize FAR. On the other hand, the "OR" configuration is able to correctly classify almost all hailstorms analyzed (29/31 case studies; POD = 93.5%) but we can reasonably hypothesize that is associated with a higher FAR. These findings highlight that the LJ algorithm can represent a good support to monitor and track the hailstorms and also that in some situations the lightning method is the only one able to identify these storm systems.

In the following part, we will describe two hail events showing how the CARMEN project benefits from the LJ algorithm addition. The first instance is related to the hailstorm occurred in Caivano (40.95°N, 14.30°E) on 09 August 2022, when hailstones having a maximum size of 2 cm were collected at 14:45 UTC (± 30 minutes; https://eswd.eu/). This is one of the 20 cases in which both algorithms identified a potential developing hailstorm, thanks to the overcoming of the two algorithm threshold values. VILD maximum values and LJ_{40} series values are reported, every 10 minutes, in Table 16. Starting from 13:40 UTC, we can notice that the VILD maximum value costantly exceeds the VILD threshold value equal to 2.4 g · m^{-3} and, at the same time, the LJ method confirms the presence of strong lightning activity detecting four consecutive jumps from 14:10 UTC to 14:40 UTC, having an ISLJ = 10.30 measured at 14:20 UTC. Moreover, both methods reach threshold values well before the hail report recorded in Caivano at 14:45 UTC (± 30 minutes), leading to a LT = 35 minutes considering the first jump detected at 14:10 UTC.

Table 9. VILD maximum values and LJ values (using the LJ_{40} series) are shown for the case study of Caivano on the 09 August 2022 from 13:30 UTC to 15:20 UTC.

Caivano case study			
Date	Time (UTC)	VILD maximum value (g · m^{-3})	LJ_{40}
09/08/2022	13:30	0.578	-
09/08/2022	13:40	4.004	0.2
09/08/2022	13:50	5.653	0.3
09/08/2022	14:00	6.573	1.70
09/08/2022	14:10	6.898	4.60
09/08/2022	14:20	5.993	10.30
09/08/2022	14:30	5.237	7.70
09/08/2022	14:40	4.057	2.53
09/08/2022	14:50	4.476	1.80
09/08/2022	15:00	4.479	1.43
09/08/2022	15:10	3.755	1.77
09/08/2022	15:20	3.520	1.28

In Figure 71a-c, on the left a map of Campania Region (https://cartinadatieuropa.it/) is provided (Fig. 71a): here, the red circle rounds the hail report geolocation while the two red arrows indicate from where the Naples

and Trevico X-radar beams are coming. Caivano is located in the napolitan plain and, as visible in Fig. 71a, the Naples radar is in a favourable position to carry out reflectivity measurements whereas the Trevico radar beam is blocked by the presence of the Partenio mountain chain. Consequently, for this case study we used data from Naples radar which reported the highest reflectivity values. Considering that the hail report time was at 14:45 UTC (± 30 minutes), in Fig. 71b-c we show VILD and TL maps produced at 14:50 UTC, respectively. The pink dot in Fig. 71b-c represents the hail observation close to Caivano.

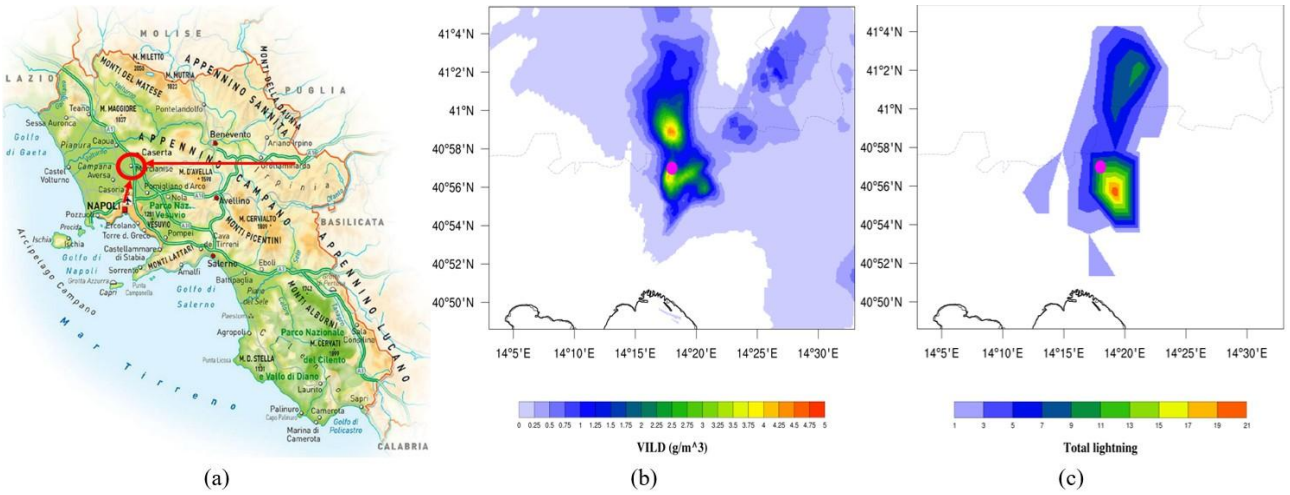

Figure 71. On the left (a), a Campania Region map is provided (https://cartinadatieuropa.it/) where the red circle rounds the city of Caivano while the red arrows represent the radar beams coming from Naples and Trevico. In the middle (b) and on the right (c), VILD and TL maps at 14:50 UTC are depicted, respectively. The pink dot in b-c indicates the geolocation of the hail report at 14:45 UTC (± 30 minutes; https://eswd.eu/).

As it can be noticed, VILD and TL maxima are arranged near the hail report, indicating an elevated hail risk for that area, keeping in consideration that both algorithm threshold values were exceeded. This hail event shows how lightning activity and LJ algorithm can be a good support for the CARMEN project hail detection tool, confirming results obtained by VILD method.

However, the potentiality of LJ algorithm can be furtherly investigated analyzing the hailstorm that affected the cities of Battipaglia and Eboli on 23 September 2023: here, two different hail observations of maximum hail diameter equal to 4 cm were detected in both locations at 11:00 UTC (40.62°N, 14.97°E; ± 5 minutes) and 11:10 UTC (40.63°N, 15.05°E; ± 5 minutes), respectively (https://eswd.eu/). This case study is particularly interesting because only the LJ method was able to detect a potential hailstorm, largely exceeding the threshold value established. Indeed, if we focus on the VILD maximum value column in Table 17, we can observe that only one temporal window (at 11:10 UTC) exceeds the threshold of 2.4 $g \cdot m^{-3}$ but these values have been measured at a distance greater than 10 km with respect to the geolaction of the hail reports. Consequently, for this case study, there are not valid VILD values useful to classify the storm system as a potential hailstorm. On the other hand, enhanced lightning activity has been observed: from the right column in Table 17, it can be noted that the LJ_{40} series is characterized by five consecutive jumps from 10:10 UTC to 10:50 UTC, showing

an ISLJ = 54.80 at 10:30 UTC. In addition, the LJ method shows a very good performance in prediciting in advance the occurrence of the hailstorm, with a LT = 50 minutes (first jump detected at 10:10 UTC and first hail report recorded at 11:00 UTC). As in Fig. 71a-c, in Figure 72a-c we provide the Campania Region map (https://cartinadatieuropa.it/; Fig. 72a), VILD (Fig. 72b) and TL (Fig. 72c) maps processed on 23 September 2023 at 11:00 UTC. The pink dot refers to the hail observation recorded in Battipaglia at 11:00 UTC (± 5 minutes).

Table 10. VILD maximum values and LJ values (using the LJ_{40} series) are shown for the case study of Battipaglia and Eboli on 23 September 2023 from 09:50 UTC to 11:30 UTC.

Battipaglia and Eboli case study			
Date	Time (UTC)	VILD maximum value ($g \cdot m^{-3}$)	LJ_{40}
23/09/2023	09:50	0.303	0.7
23/09/2023	10:00	1.095	1.8
23/09/2023	10:10	1.492	12.50
23/09/2023	10:20	1.666	35.40
23/09/2023	10:30	1.470	54.80
23/09/2023	10:40	1.272	23.94
23/09/2023	10:50	1.312	4.24
23/09/2023	11:00	1.961	0.84
23/09/2023	11:10	3.050	0.33
23/09/2023	11:20	1.391	0.32
23/09/2023	11:30	2.331	0.13

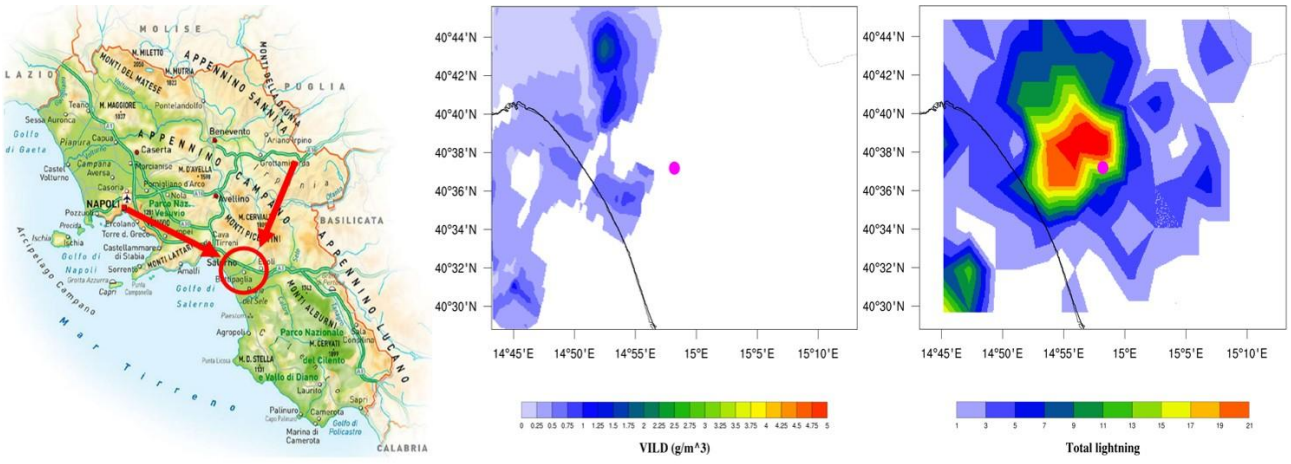

(a) (b) (c)

Figure 72. On the left (a), the red circle rounds the cities of Battipaglia and Eboli (https://cartinadatieuropa.it/) while the red arrows indicate where the radar beams of Naples and Trevico come from. In the middle (b) and on the right (c), VILD and TL maps at 11:00 UTC are depicted, respectively. The pink dot in b-c indicates the geolocation of the hail report in Battipaglia at 11:00 UTC (± 5 minutes) having a maximum size of 4 cm (https://eswd.eu/).

Probably, the main reason of low reflectivity measurements is linked to the presence of the Vesuvius volcano, the Monti Lattari and the Monti Picentini mountain chains which block both radar beams coming from Naples and Trevico (red arrows in Fig. 72a): considering that the cities of Battipaglia and Eboli (contained in the red

circle in Fig. 72a) are placed in the Piana del Sele, that is located on the other side of the above mentioned ridges, the VILD pattern is totally compromised (Fig. 72b). In these situations, TL demonstrates to be a reliable variable, being able to monitor in real-time what is happening even in regions characterized by a complex orography, as can be noticed by the strong lightning activity (red and orange colours in Fig. 72c) detected around the hail report location. In addition, the LJ algorithm points out an abrupt increase in lightning activity from 10:10 UTC to 10:50 UTC, indicating the possible formation of hailstones in the storm system analyzed.

6.3.2 Lightning activity as a proxy for the hailstorms

In this Section, we will focus on the analysis of lightning activity in hailstorms, distinguishing between large hail (maximum hail size ≥ 2 cm) and very large hail (maximum hail size ≥ 5 cm) case studies. The dataset used in the previous paragraph is too unbalanced, so we decided to enrich the number of very large hail events, even considering cases occurred outside the study area defined in Section 6.2.1, but measured in the same way by the LAMPINET network on the Italian Peninsula (further details in Vermi et al. (2025)). Depending on the two hail categories, here we will examine:

- 29 large hail events;
- 12 very large hail case studies.

Starting from the LJ series which make up the LJ algorithm, in Table 18 we reported how many hailstorms have been studied using each LJ series for large hail and very large hail categories. In the latter, the LJ_{40} series is totally predominant, describing the most of the hailstorms (11/12 hail events). On the other hand, in the large hail class, results are more distribuited: 7 case studies are missed because lightning activity is not strong enough to be detected by LJ algorithm while for other three hailstorms LJ method returns the same outcomes using different LJ series. In about half of the events (52%), the LJ_{40} is preferred to find the ISLJ but also LJ_{20} and LJ_{30} series show a not negligible contribution (4/29 case studies).

Table 11. Number of hailstorms described by each LJ series: the LJ_{40} series prevails in both categories. For the large hail class, some cases are missed or equally catched by more than one LJ series.

	Large hail (29 case studies)	Very large hail (12 case studies)
	Hailstorms (%)	Hailstorms (%)
LJ_{20}	2 (7%)	0 (0%)
LJ_{30}	2 (7%)	1 (8%)
LJ_{40}	15 (52%)	11 (92%)
Equivalent	3 (10%)	0 (0%)
Missed	7 (24%)	0 (0%)

According to Table 18, it is particularly interesting noting that, moving from large to very large hail category, missed hailstorms disappear indicating that lightning activity generally increases in storms producing very

large hailstones. In addition, LJ_{40} series dominates (92%) the very large hail class meaning that, on average, these hailstorms need more time to reach the peak of lightning activity and also that the growth of the hailstones is longer, allowing them to become larger in size.

After that, we examined both datasets calculating NLJ, ISLJ and LT. Main results are summarized in Figure 73a-c, where the average and median of NLJ (Fig. 73a), ISLJ (Fig. 73b) and LT (Fig. 73c) have been computed for large hail (blue columns) and very large hail (orange columns) categories. If we focus on the median (similar results are given by the average), it emerges that NLJ (Fig. 73a) is equal to 3 in hailstorms producing large hail but it rises to 7.5 for very large hail events. For the latter, considering that lightning data are counted every 10 minutes, the number of jumps found by the LJ method is 2.5 times higher. It means that these hailstorms have a longer period of time in which the TL is increasing with respect to the previous 10-minute temporal steps, being definitely more active from the lightning activity point of view. However, the most marked difference between the two datasets was found for the ISLJ (Fig. 73b): indeed, for large hail events ISLJ = 3.8 whereas for hailstorms producing very large hail ISLJ = 27.75. This strong difference between the two categories indicates that very large hail cases are characterized not only by a larger number of jumps, but also by jumps much more intense. In Fig. 73c, we introduce lead times calculated as the difference between the first jump detected and the first hail report recorded. Globally, LT distribution is very wide going from two hours in advance to ten minutes in late, showing a median equal to 35 minutes in advance for large hail, rising until 47.5 minutes for very large hail events. So, even in this case, LT increases for hailstorms producing very large hailstones: probably, the main reason is related to stronger updrafts characterizing these storms, which maintain hailstones more time in clouds, allowing them becoming larger and heavier.

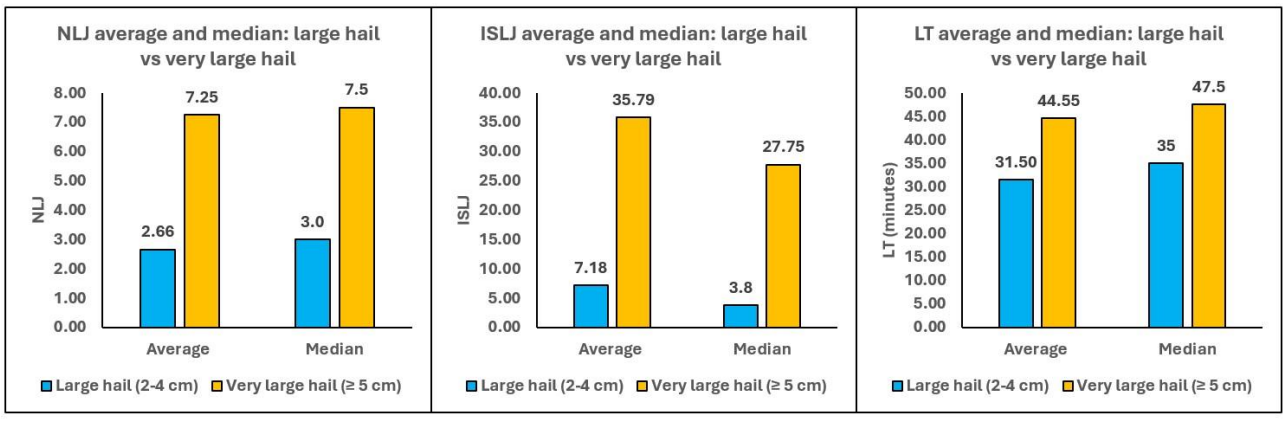

(a) (b) (c)

Figure 73. The average and median of NLJ (a), ISLJ (b) and LT (c) are provided for large hail (blue columns) and very large hail (orange columns) categories.

These findings confirm that very large hailstones are most likely to form when lightning activity is stronger, more persistent and when the intensity of the strongest jump increases by several tens of times. These aspects are particularly interesting also from the operative point of view for identifying hailstorms and supporting

other hail detection tools in real-time. Indeed, NLJ and ISLJ can be calculated only from lightning data, making easier to obtain these variables even in real-time. Considered the big gap found for the ISLJ between large and very large hail (Fig. 73b), we decided to deep the analysis on this topic. Figure 74 skecthes, for each case study, the ISLJ as a function of the maximum hail diameter (cm) recorded in the ESWD (https://eswd.eu/) and in the monitoring network "Campanialive" (http://www.campanialive.it/). The vertical purple dashed line splits the large hail category (on the left) from the very large hail one (on the right) while blue and red dots represent 29 large hail and 12 very large hail events, respectively. From this graph, it is clear that most of large hail events are found at the bottom left: indeed, 27/29 large hail events have an ISLJ lower than 12.0 (green horizontal dashed line in Fig. 74), having only two cases characterized by stronger jumps. On the other hand, 10/12 very large hail case studies overcome this value, showing a TL and an ISLJ much more intense. Given this distribution, we computed the Pearson's correlation coefficient (r) which resulted r = 0.70, indicating a good correlation between these two variables. Being aware of the limitations of taking the maximum hail diameter (e.g. some larger hailstones could be not collected and recorded) and only lightning data (e.g. the detection efficiency of the lightning network is far from 100%), we think that any upgrade of these datasets could furtherly improve these results.

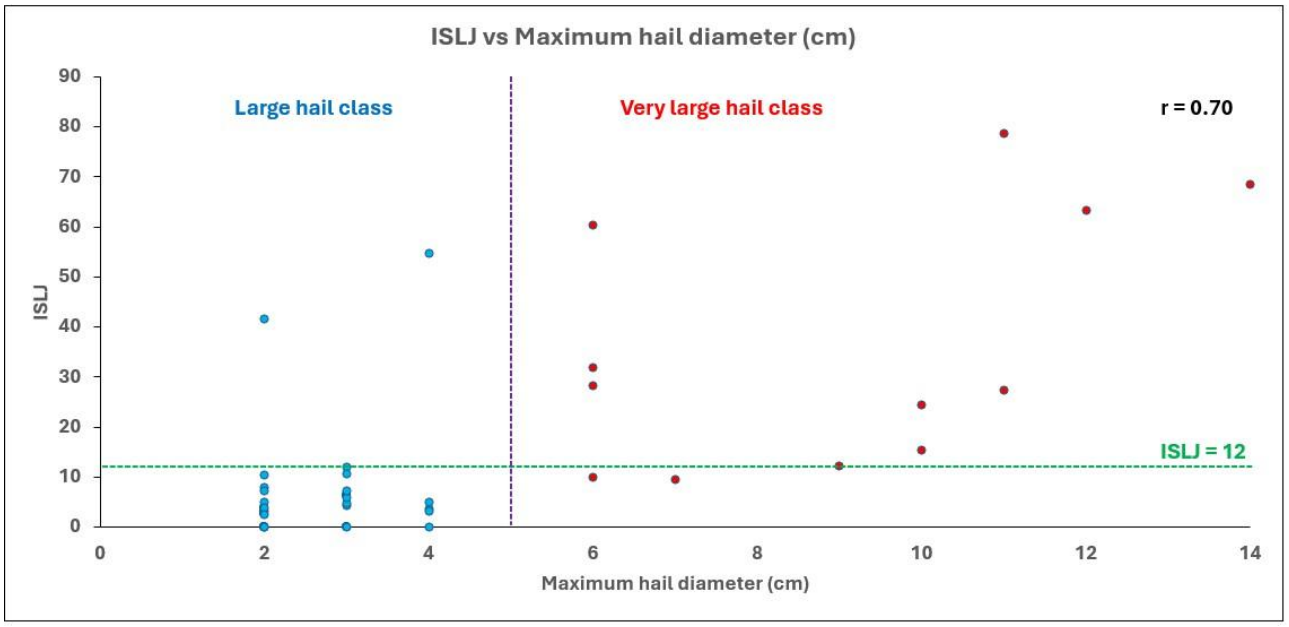

Figure 74. For each case study, ISLJ and maximum hail diameter (cm) are reported. Blue dots represent large hail events while red dots indicate very large hail cases. The horizontal green dashed line shows ISLJ = 12, while the vertical purple dashed line separates large hail and very large hail classes.

6.3.3 Lightning support for large and very large hail events: two case studies in Campania Region

In the next two subsections, we propose the analysis of two indipendent hail events (one producing large hail and one very large hail) occurred in Campania Region, not belonging to the 31 case studies examined in Section

6.3.1. Since, in those days, the X-band weather radars of the CARMEN project were not working due to planned maintenance work, we studied these two hailstorms only applying the LJ algorithm. The latter will show that analyzing lightning data with the new method introduced can be very effective to identify and monitor these phenomena, even in absence of other hail detection tools.

6.3.3.1 Large hail event on 7 July 2022

The first case study we examine is a large hail event which affected the southern part of the Molise Region and the northern sector of the Campania Region on 7 July 2022. In the areas stated above, two hail observations were recorded in Longano (41.52°N, 14.24°E) at 13:10 UTC (± 5 minutes) and in Piedimonte Matese (41.36°N, 14.38°E) at 13:45 UTC (± 5 minutes), reporting both a maximum hail diameter of 3 cm (Figure 75a-c, https://eswd.eu/). The analysis of this large hail event starts preparing TL maps every 10 minutes for the areas marked by the hail reports. In Figure 76a-h, the most active part of the hailstorm is depicted in TL maps provided from 12:50 UTC (Fig. 76a) to 14:00 UTC (Fig. 76h).

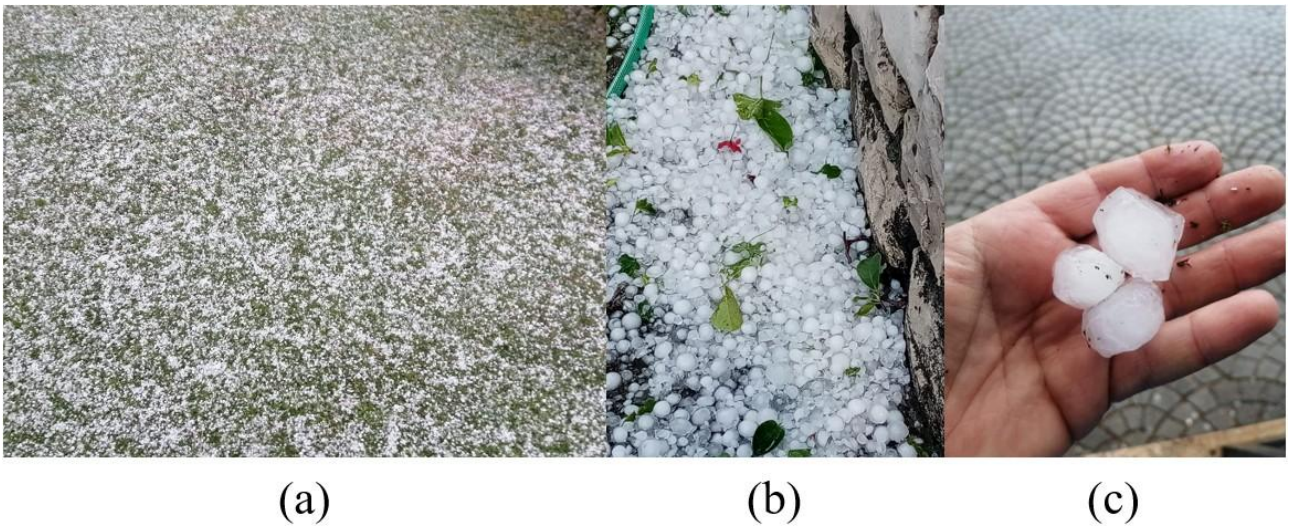

Figure 75. Hailstones detected in Longano (a, Molise Region) at 13:10 UTC (± 5 minutes) and in Piedimonte Matese (b-c, Campania Region) at 13:45 UTC (± 5 minutes) having a maximum size of 3 cm (https://eswd.eu/).

The hail observations in Longano at 13:10 UTC (Fig. 76c) and in Piedimonte Matese at 13:45 UTC (Fig. 76f) are indicated by two pink dots while the red box surrounds strokes that are produced by the storm system, showing that the hailstorm moves from the Molise Region (Fig. 76a-d) to the northern sector of the Campania Region (Fig. 76e-h), consistently with the hail reports provided by the ESWD.

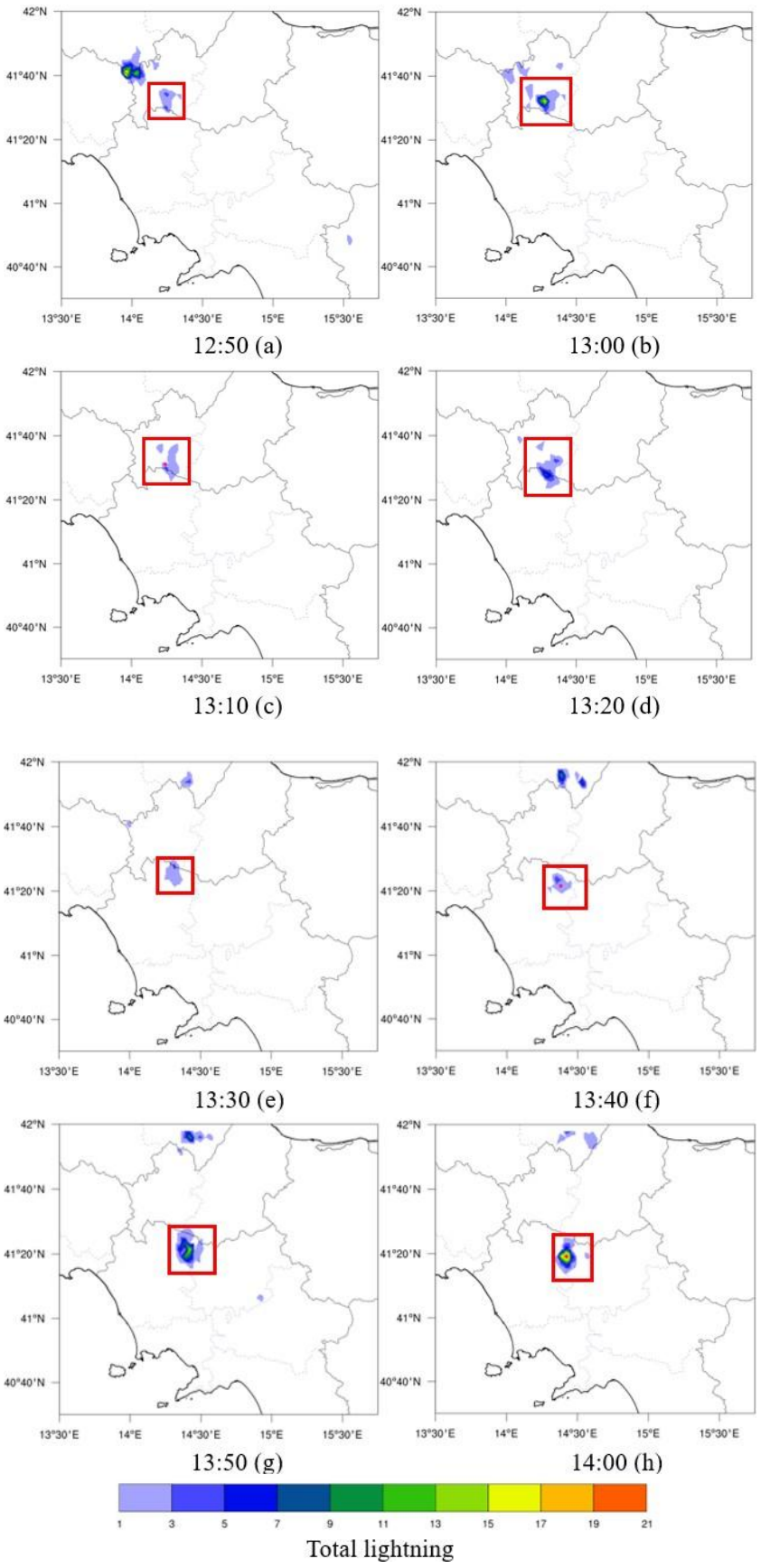

Figure 76. Total lightning maps (a-h) for the hailstorm occurred on the 07 July 2022 from 12:50 UTC to 14:00 UTC among Molise and Campania Region. The inner part of the red box shows the area in which the hailstorm developed and where lightning strikes have been counted. The pink dots in (c-f) refer to the two hail observations reported in Longano and in Piedimonte Matese, respectively (https://eswd.eu/).

The lightning activity of this hailstorm had a duration of 100 minutes, from 12:40 UTC to 14:20 UTC, as described by black columns representing TL in Figure 77a. In this case, using the ISLJ criteria proposed in Section 6.2.4, it was chosen the LJ_{40} series that is represented by the graph in Fig. 77b. The latter shows that NLJ = 6, having four consecutive jumps detected from 12:50 UTC to 13:20 UTC and, subsequently, other two jumps at 13:50 UTC and 14:00 UTC, when a new temporary increase in TL was measured. In addition, considering that the first jump was found at 12:50 UTC and the first hail report was in Longano at 13:10 UTC, it follows that LT is in advance of 20 minutes with respect to the first hailstones collected. Given this information, if we compare NLJ and LT found for this case study with results shown in Fig. 73a-c, we can observe that lightning activity seems to confirm the development of hail phenomena (Fig. 73a), having intermediate characteristics (NLJ = 6) between large and very large hail categories, whereas LT (20 minutes) appears to be closer to values more typical of large hail class (Fig. 73c). However, the comparison between the ISLJ equal to 6.1 at 13:10 UTC and the distribution provided in Fig. 74 probably gives out a more crucial result. Indeed, if we look at Fig. 74, we can observe that the ISLJ of the hailstorm examined is placed in the bottom left of the panel, that is the area commonly popoulated by large hail events analyzed in Section 6.3.2. It confirms that this large hail case study was characterized by a quite high number of jumps (NLJ) but, even considering the most intense one, the ISLJ value is more in accordance with the large hail events distribution.

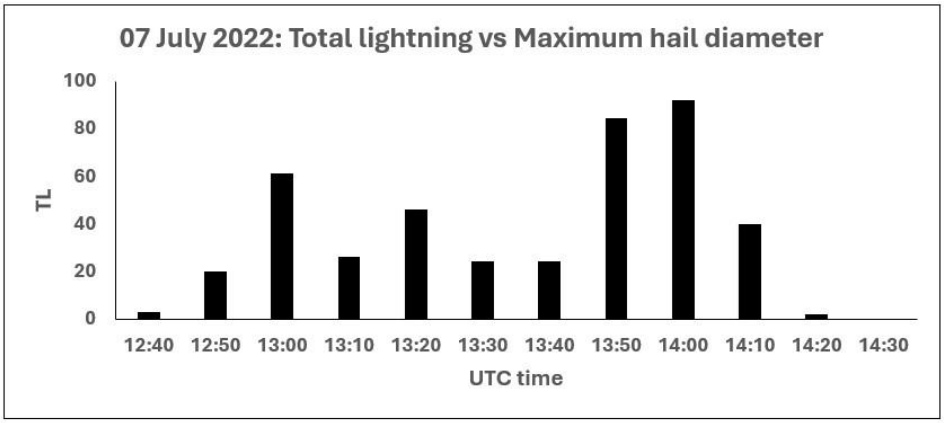

(a)

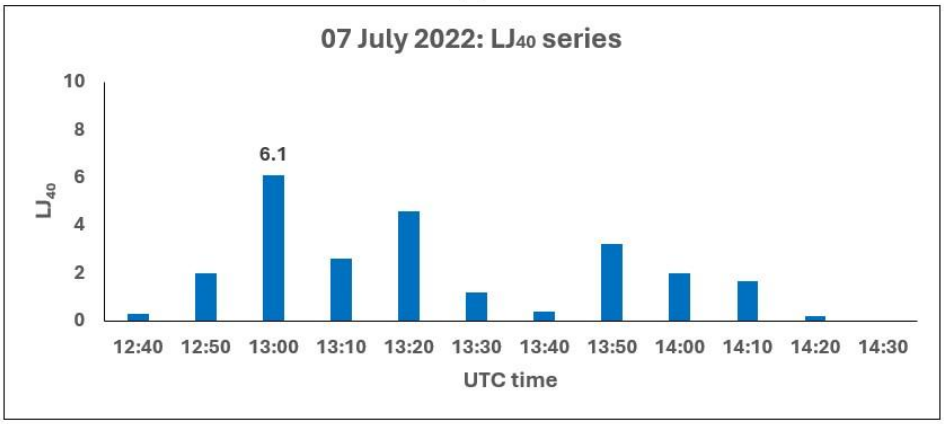

(b)

Figure 77. TL evolution of the hailstorm (a) and LJ algorithm application using the LJ_{40} series (b). In (b), the ISLJ is equal to 6.1 and it is identified with the label above the corresponding time window.

6.3.3.2 Very large hail event on 16 June 2025

The second case study proposed is a very large hail event happened on 16 June 2025. The development of this hailstorm was similar to the previous one, with a storm system that evolved from the Molise to northeastern sector of the Campania Region. The first two hail reports are located in the Molise Region in the city of Campobasso (41.56°N, 14.66°E) at 15:55 UTC (± 5 minutes) and in Ferrazzano (41.53°N, 14.67°E) at 16:05 UTC (± 5 minutes), having both a maximum hail size of 6 cm (Figure 78a-b). Later, the hailstorm moved from Molise to Campania Region and, at 16:30 UTC (± 5 minutes), other hailstones were collected in Castelvetere in Val Fortore (41.44°N, 14.94°E; Figure 78c) and in Colle Sannita (41.37°N, 14.84°E) with a maximum hail diameter of 5 and 4.5 cm, respectively. Finally, at 16:35 UTC (± 5 minutes), the last hail report was measured in San Bartolomeo in Galdo (41.40°N, 15.01°E), with hailstones reaching again a maximum diameter of 5 cm (https://eswd.eu/).

Figure 78. Pictures of hailstones collected in Campobasso (a, Molise Region) at 15:55 UTC (± 5 minutes), in Ferrazzano (b, Molise Region) at 16:05 UTC (± 5 minutes) and in Castelvetere in Val Fortore (c, Campania Region) at 16:30 UTC (± 5 minutes). The hailstones picked had a maximum size of 6 cm in (a-b) and of 5 cm in (c) (https://eswd.eu/).

In Figure 79a-h, we propose eight timeslots from 15:20 UTC to 16:30 UTC in which lightning activity was very intense: in Fig. 79a-f, the storm system is moving southeasterly in the Molise Region while in Fig. 79g-h most of strokes was counted in the north-eastern sector of the Campania Region. During this period, the hail observations in Campobasso and Ferrazzano have been indicated using pink dots in Fig. 79d and Fig. 79e, respectively, while the three pink dots in the last TL map (Fig. 79h) refer to the hail reports in Castelvetere in Fortore, Colle Sannita and San Bartolomeo in Galdo.

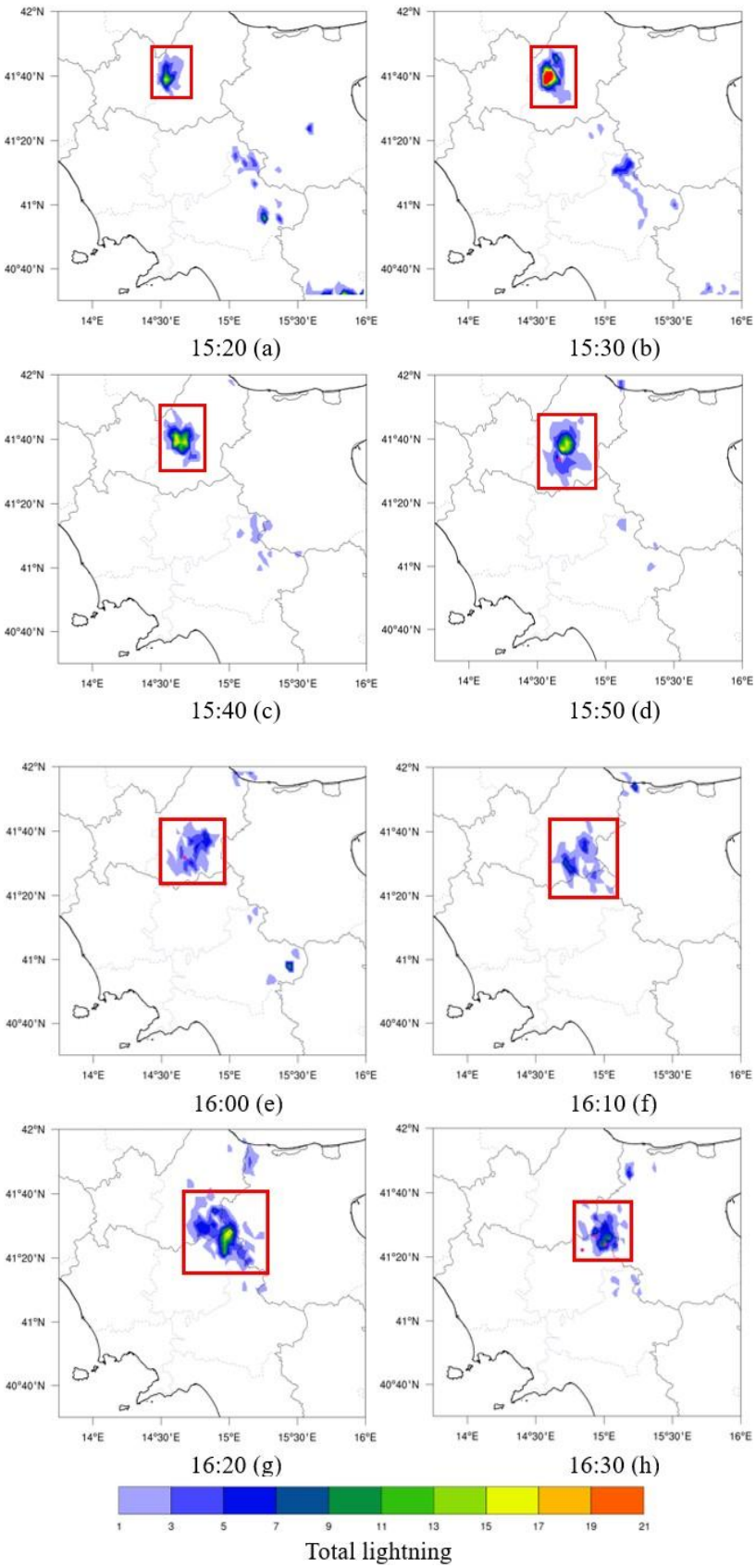

Figure 79. Like in Fig. 76, TL maps (a-h) for the hailstorm occurred on the 16 June 2025 from 15:20 UTC to 16:30 UTC among Molise and Campania Region. The inner part of the red box shows the area in which the hailstorm developed and where lightning strikes have been counted. The pink dots in (d-e-h) refer to the five hail reports contained in the ESWD (https://eswd.eu/).

From Figure 80a, it can be noted that lightning activity had a total duration of four hours, from 14:50 UTC to 18:50 UTC, in which the hailstorm produced even more than 300 strokes in 10 minutes at 16:20 UTC (Fig. 79g and Fig. 80a) and an overall of almost 2500 strokes during the whole period of development. The LJ algorithm determined again that the best temporal series to highlight the ISLJ was the LJ_{40} series: in Fig. 80b, the latter shows five consecutive jumps from 15:10 UTC to 15:50 UTC and, after more than two hours, a final jump at 18:20 UTC resulting in a NLJ = 6. Being the first jump at 15:10 UTC and the first hail report in Campobasso at 15:55 UTC, it follows that LT is equal to 45 minutes. Comparing these results with average and median values of large and very large hail datasets analyzed in Fig. 73a-c, we can state that six jumps are an intermediate value not decisive for discriminating among the two categories while an advance of 45 minutes is more typical of the very large hail class.

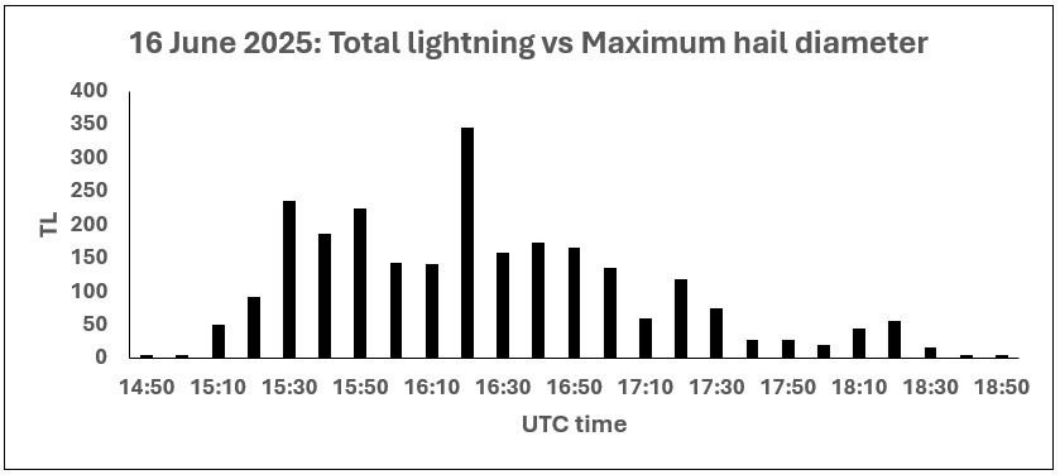

(a)

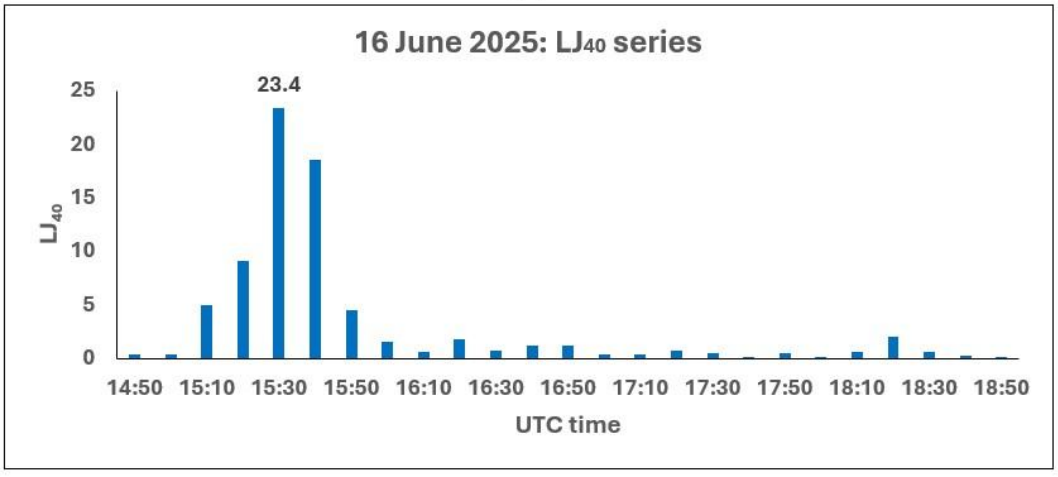

(b)

Figure 80. As in Fig. 77, for the case study of 16 June 2025, TL (a) and LJ_{40} series (b) have been reported. In (b), the ISLJ equal to 23.4 and it is identified with the label above the corresponding time window.

In Fig. 80b, the ISLJ is equal to 23.4 and it has been detected at 15:30 UTC. The LJ_{40} series shows that the TL has increased at least by 23 times in the last 40 minutes, definitely exhibiting a very intense lightning activity

happening in the hailstorm. If we reconsider the distribution of ISLJ provided in Fig. 74, the highest maximum diameter reported for this case study is associated to a much more intense jump that differs from values typically measured for large hail events ranging almost always between 2.0 and 12.0. This is a very important outcome because, only exploiting lightning data, the combination of TL with the information derived from LJ algorithm in terms of ISLJ, NLJ and LT can help characterizing the developing hailstorms, even with the final aim to distinguish in real-time between large hail and very large hail storms.

6.4 Conclusions and Future Perspectives

In this work, we proposed a new lightning data based method (derived from Vermi et al., 2025), for identifying and tracking the hailstorms in real-time on the Italian Peninsula. The main goal of this study was supporting the CARMEN project hail detection tool (Capozzi et al., 2022), which computes the hail probability through the Vertically Integrated Liquid Density (VILD) Method (Amburn and Wolf, 1997), exploiting data coming from two X-band weather radars located in Campania Region (Southern Italy). Considering a dataset of 31 hailstorms occurred in Campania Region from 2015 to 2023, the VILD and LJ algorithms had a very similar performance classifying as hail-bearing storms the 80.6% and 77.4% of the case studies, respectively. More in detail, the two methods were in accordance in the 71% of case studies whereas the remaining 29% was split in 16% correctly classified only by VILD Method and 13% only by LJ algorithm. If both methods are combined together, the "OR" configuration maximizes the POD indicator (93.5%) but is reasonably associated with a larger FAR. On the other hand, using the "AND" configuration we can make the hypothesis that false alarms are minimized, at the expenses of a lower POD (64.5%). Results about the LJ algorithm highlight that lightning strikes can follow the evolution of the hailstorms even in complex orography, where the beam blockage plays a crucial role in worsening the quality of radar measurements, or in areas very far from the radar leading to a better monitoring of the hailstorms even at the edges of the Campania Region, being valid in the same way on land and sea surface. For these reasons, the synchronization in time between radar measurements and the strokes counting, both carried out every ten minutes, can add important information on lightning activity that characterizes the storm systems, especially in the above-mentioned areas not accurately observed by X-band weather radars.

In the second part of this study, we analyzed the same dataset but adding some very large hail events occurred on the Italian Peninsula from 2015 to 2023 in order to examine all of them only from lightning activity point of view, exploiting results obtained by the application of the LJ algorithm. In this case, we dealt with 29 large hail (maximum hail size ≥ 2 cm) phenomena and 12 very large hail (maximum hail size ≥ 5 cm) events. The LJ method misses the 24% of large hail case studies, while it always detects jumps produced in very large hail class, meaning that total lightning (TL) generally increases in the latter. The LJ_{40} temporal series is particularly preferred in the very large hail category, emphasizing that in these hailstorms the increase of TL is stronger and needs more time to reach the peak, allowing hailstones to develop and become larger in size. After computing some strokes-related variables like the number of jumps (NLJ), the intensity of the strongest jump

(ISLJ) and lead time (LT) characterizing each hailstorm, we found that, on average, all these indicators reach higher values when very large hail storms are examined: this is particularly true for ISLJ, for which an intensity difference oscillating from five to seven times was observed moving from large hail to very large hail category. In addition, to strenghten this trend, a positive correlation (r = 0.70) was found between the maximum hail size reported (https://eswd.eu/ and http://www.campanialive.it/) and the ISLJ computed. In the last part of this work, these outcomes have been confirmed to be very useful to describe new indipendent large hail and very large hail case studies, especially when the CARMEN project hail detection tool was switched off due to planned maintenance work and the LJ algorithm was the only method operating in real-time. Indeed, the potential relationship between lightning features and the severity of the hailstorms could let to recognize storm systems belonging to different categories (e.g. large or very large hail) simply by using lightning data and applying the LJ algorithm. However, in future studies, these findings will have to be confirmed by deeper analyses and larger datasets, as weel as it will become crucial the comparison with a dataset only including no-hail producing thunderstorms.

Chapter 7 Conclusions and Future Perspectives

Hailstorms are dangerous and impactful phenomena in people's lives and can cause important damage to agriculture, buildings, cars and at socio-economic level. For these reasons, in this PhD research project, a multi-sensor analysis of hailstorms in the Mediterranean Basin based on satellite, lightning and radar data has been presented. In the first part of this work, we introduced the "Multi-sensor Approach for Satellite Hail Advection" (MASHA) Method, a new satellite technique that exploits the interaction between ice crystals, graupel and hailstones in clouds and microwave and infrared electromagnetic waves. The key point of this technique regards the physical interaction among ice particles and microwaves, which leads to the depression of microwave brightness temperature (MW-TB) signal arriving to the satellite. Subsequently, the latter is exploited by the "MicroWave Convective Cloud method for Hail Detection" (MWCC-H) algorithm to calibrate the infrared radiation in terms of hail probability (HP), being available on the whole Mediterranean Basin every 5 minutes, thanks to the Meteosat Second Generation Rapid Scan Service (MSG-RSS) mode. In this way, the MASHA Method allows us to determine the severity of the hailstorms and to track them on a very wide domain, which in this work ranges in latitude from 27.50°N to 50.00°N and in longitude from –20.00° to 31.00°E, covering a spatial area even larger than the Mediterranean Basin. In addition, this technique allows us to monitor the development of the hailstorms even in the Mediterranean Sea and in general on the sea surface, where usually other instruments such as weather radars cannot provide any useful information. On the other hand, the two main limitations of the MASHA Method are linked to the calibration of the MWCC-H Method, which is not continuous depending on the frequency of polar satellite overpasses and to the onset of the overshooting top (OT) structure in severe hailstorms, which causes a systematic reduction of HP pattern in the central area of the hailstorm.

The first one is random but when the calibration of the MWCC-H Method is not correctly updated in a specific region, the final result is a typical HP underestimation occurring in this area. To overcome this problem, we tried a new neural network approach based on a ResNet-50 (Residual Network family), a 50-layer model which belongs to the Convolutionary Neural Networks (CNNs), which are primarily used to solve difficult image-driven pattern recognition tasks. Therefore, it was decided to exploit their ability to recognize potential developing hailstorms by IR-images. After training the ResNet-50 model with about 10 000 IR-images, the best result was obtained through a 50-epoch configuration, in which 81.6% of hailstorms were correctly identified and, on the other hand, 90.7% of ordinary thunderstorms were classified as true negatives, with only 9.3% of storms resulting as false alarms. These preliminary findings open the way to new interesting perspectives which involve testing the dataset with alternative models to compare their performance, exploiting the higher spatial and temporal resolution provided by Meteosat Third Generation (MTG) satellite and evaluating IR-images with new variables such as lightning activity. At the same time, in the future it seems to be crucial to increase the training and test datasets with more IR-images, to improve the training of the model.

The second limitation is linked to the development of the OT structure in thunder clouds, which is misinterpreted by the MASHA Method and forces the highest HP values at the edge of the hailstorm, losing the information about the physical process happening in the hailstorm. In Chapter 3 and Chapter 5, to improve the MASHA Method HP result, it was considered lightning activity that usually hailstorms produce during their development. In particular, exploiting the concept that often the spatial distribution of lightning discharges overlaps with OT region, lightning strikes were leveraged as a proxy to correct the HP pattern. In Chapter 3, after discussing the main mechanisms and physical processes of clouds electrification, it was studied the lightning activity occurred on the Italian Peninsula from 2015 to 2023 through lightning data provided by the Italian Air Force Lightning Detection Network "LAMPINET". From this general analysis, it emerged that lightning activity is strongly related to the thunderstorms climatologies proposed and that the peak of the lightning rate follows the seasonality, being measured in months of May, June and July in Northern Italy, during August and September in Central Italy and finally in October and November in Southern Italy. This introductive section was useful to deal with the main topic of Chapter 5, in which the HP pattern improved using lightning data. Starting from the spatial combination of hail reports provided by the European Severe Storm Laboratory's European Severe Weather Database (ESWD) and the total lightning (TL) counted in each 6×6 km^2 grid cell, a "new hail probability" (NHP) was computed. The latter is given by the average between the MASHA Method HP (HP_{MASHA}) and the total lightning hail probability (HP_{TL}; derived by the relationship found between ground hail observations and TL), for assigning to both HP_{MASHA} and HP_{TL} the 50% of the final contribution. Comparing HP_{MASHA} with NHP, the main outcomes revealed that the correct classification of hail reports increases from 50.0% (HP_{MASHA}) to 67.4% (NHP) and, at the same time, underestimation conditions significantly decrease from 50.0% (HP_{MASHA}) to 29.3% (NHP) of hail events, even if in 3.3% of cases, NHP overestimates hail phenomena. The improvement resulting from NHP computation is even more evident for deep OT hailstorms producing hailstones with maximum size equal or higher 7 cm, for which the OT structure is more impactful on the distribution of the HP pattern. In these cases, the difference of performance between HP_{MASHA} and NHP is more emphasized, with correctly classified hail reports decreasing from 67.4% to 58.8% for NHP whereas a stronger reduction is observed for HP_{MASHA}, passing from 50.0% to 29.4%. Given these results, the NHP Method showed an improved performance for the detection of the hailstones falling to the ground and, in the future, both MASHA and NHP Methods could work together for identifying and following the evolution of the hailstorms on the Italian Peninsula. In addition, new tests about the computation of NHP could be carried out to further enhance the NHP performance.

In Section 4, two first exploratory studies were proposed to better investigate the relationship between the formation and evolution of the hailstorms and lightning activity occurring in these storm systems. In the first one, studying 10 hailstorms producing very large hail (maximum size ≥ 5 cm) on the Italian Peninsula through the LAMPINET network, it was introduced a new mathematical approach for the lightning jump (LJ) detection, for investigating potential links between lightning activity and hailstorms. The LJ computation depends on three temporal windows at 20, 30 or 40 minutes, named LJ_{20}, LJ_{30} and LJ_{40}. Using this approach, it emerged that LJ_{30} and LJ_{40} are more effective in catching the strongest LJ characterizing the hailstorms, even if the

highest LJ detection can be partially affected by the initial lightning rate which can take a linear or exponential trend in the first stages of the hailstorms. Even if, at this step, LJ values didn't show a clear relationship with the maximum hail diameter detected, good results came from lead time (LT) computation, defined as the difference (in minutes) between the LJ detection and the first hail report recorded. After calculating LT, it came out that in 7/10 hail events, LT was in advance (5/10 case studies) or coincident with hail reports (2/10 case studies) whereas for the remaining 3/10 cases LJ was observed at least 10 minutes after the first hailstones reached the ground. In the second exploratory work, 16 case studies (11 hailstorms and 5 ordinary thunderstorms) occurred in the Campania Region from 2012 to 2015, were studied to assess the relationship between hailstorms and strokes by using lightning data provided by the European Lightning Network "LINET". In particular, considering the case study happened on 5 September 2015, both lightning data from LAMPINET and LINET were compared. Results about TL showed that LINET network systematically detects a number of strikes that generally moves from 5 to 10 times higher with respect to LAMPINET (probably due to a higher sensitivity of LINET antennas), highlighting that lightning data coming from these two networks can't be exploited in an interchangeable way. As in the previous study, LJ_{30} and LJ_{40} series detected the highest LJ in 14/16 case studies, suggesting that usually the rise of lightning activity needs some tens of minutes to fully develop. For 7/11 hailstorms, LJ ranged from 9.5 to 20.6, indicating a strong increase in TL. On the oher hand, the remaining 4/11 hail cases were characterized by a very low TL and weak jumps comparable to those measured for the other 5 ordinary thunderstorms analyzed. However, it must be considered that the 4/11 hailstorms having low jumps, happened during the winter season when lightning activity is often much lower. In turn, it also affects the LJ computation, definitely making more complex the detection of these hail phenomena. Considering the LT computation for 11 hailstorms, 9 of them were in advance with respect to the time of hail report, one was coincident in time and one was in late by 30 minutes. Taking into account the intra-cloud (IC) and cloud-to-ground (CG) trends, for the hailstorms the CG% average went from 19% to 65% (IC/CG ratio between 0.54 and 4.3), whereas for ordinary thunderstorms in 3/5 events the CG% average was below 10% (IC/CG ratio between 9 and 32.5) and in the other 2/5 it oscillated between 20% and 22%. These results were against findings published in previous studies which state that IC discharges prevail much more in hailstorms with respect to no-hail producing storm systems. Possible explanations to this anomalous trend involve the low DE for IC flashes, the poorer density of sensors in Southern Italy (depressing more the IC detection) and the misclassification of IC flashes as CG strokes, especially occurring during the development of severe hailstorms.

From these preliminary findings, in Chapter 6, it was proposed an evolved version of the mathematical approach introduced in Section 4, to examine 31 hailstorms occurred in Campania Region from 2015 to 2023. For the first time, the performance of LJ method was compared with the radar-based hail detection algorithm developed in the framework of "Campania Region Meteorological Radar Network" (CARMEN). From this first analysis, we computed the "probability of detection" (POD) indicator for both algorithms, showing that VILD and LJ methods had very similar results (POD = 80.6% and POD = 77.4%, respectively). Nevertheless, best results were obtained when algorithms were combined together: in this way, according to the main goal

of the hail detection tool, the OR-configuration seems to maximize the POD (93.5%) but it is reasonable to hypothesize that it is associated with an increasing FAR. On the other hand, it is very likely that the minimization of FAR can be obtained exploiting the AND-configuration, at the expenses of a lower POD (64.5%). In the second part of this study, 29 large hail and 12 very large hail case studies were analyzed only from the lightning activity point of view. The LJ method missed the 24% of large hail case studies, while it always detected jumps produced in very large hail class. In addition, the LJ_{40} temporal series was particularly preferred in the very large hail category, emphasizing that in these hailstorms the increase of TL is stronger and needs more time to reach the peak. After computing some lightning-related variables such as the number of jumps detected (NLJ), the intensity of the strongest jump measured (ISLJ) and LT, it was found that all these indicators reached greater values when very large hail thunderstorms were considered. The most important difference appeared for ISLJ, which increased from five to seven times moving from large hail to very large hail category. This outcome was also supported by a positive correlation ($r = 0.70$) which came out between the maximum hail size reported and the ISLJ computed. Finally, the LJ Method was tested on two indipendent case studies occurred in Campania Region, showing that LJ algorithm is able to monitor the evolution of the hailstorms as well as to infer the potential maximum size of the hailstones produced, especially thanks to the ISLJ and NLJ computation. One of the LJ method key-points is that it can easily work in real-time, using only lightning data. The latter is very important, allowing the LJ algorithm to work in synergy with other hail detection tools (e.g. CARMEN Project) for maximizing results about the identification and monitoring of the hailstorms in real-time. In addition, using this mathematical approach, the LJ detection may lead to predict the falling of the hailstones in advance and to infer the potential maximum size of the hailstones produced (i.e. if they belong to large hail or very large hail category). Talking about future perspectives, it will be fundamental to analyze a new dataset including no-hail producing thunderstorms using the LJ method, in order to confirm these results and the hypothesis of a gradual escalation of lightning indicators as they approach the very large hail category.

Acknowledgments

Firstly, I am very grateful to my tutors Professor Giorgio Budillon and Dr. Vincenzo Capozzi at the University of Study of Naples Parthenope and to Dr. Sante Laviola at the Institute of Atmospheric Sciences and Climate of the National Research Council (ISAC-CNR) for supporting me during the studies carried out in these three years. Their experience and knowledge of these topics were crucial to develop and complete this research project, as well as their precious advice and constant availability to discuss the choices to be made, always with courtesy and kindness. A special mention goes to Dott. Giulio Monte of ISAC-CNR, who gave me fundamental support and many valuable tips.

I would also like to extend my thanks to the people who welcomed me at the Institute for Geophysics and Meteorology of the University of Cologne, during my three-month abroad period in Germany. In particular, my gratitude goes to my tutor Dr. Claudia Acquistapace for introducing me into the framework of her research project involved in the study of machine learning methods applied to atmospheric phenomena. In addition, my thanks go to Dott. Daniele Corradini and Dott. Paula Bigalke for supporting me during the development of this work and to the other members of the Institute, who contributed to increase my cultural and human background and helped my acclimatization in Germany.

Furthermore, I would like to thank the Meteorological Service of the Italian Air Force for providing lightning data on the Italian Peninsula from 2015 to 2025 and ELDES srl for taking care X-weather radars used in this thesis work with periodical planned maintenance work.

My gratitude also goes to all my colleagues with which I have worked and cooperated in the Laboratory of Meteorology and Oceanograpghy at the University of Study of Naples Parthenope and the people met at ISAC-CNR. The friendship established as well as the mutual respect and esteem were fundamental to best conduct this three-year period and I sincerely wish to all of them the best for their future.

Last but not least, I really thank all the people making part of my life who sustained me during this journey, which posed complex challenges but was also full of profound rewards.

References

Allen, J. T., Giammanco, I. M., Kumjian, M. R., Jurgen Punge, H., Zhang, Q., Groenemeijer, P., Kunz, M. and Ortega, K. (2020). Understanding hail in the earth system. *Reviews of Geophysics, 58*(1), e2019RG000665. doi:https://doi.org/10.1029/2019RG000665

Amburn, S. A. and Wolf, P. L. (1997). VIL Density as a Hail Indicator. *Weather and Forecasting, 12*(3), 473-478. doi:https://doi.org/10.1175/1520-0434(1997)012%3C0473:VDAAHI%3E2.0.CO;2

Battaglioli, F., Groenemeijer, P., Púčik, T., Taszarek, M., Ulbrich, U. and Rust, H. (2023a). Modeled multidecadal trends of lightning and (very) large hail in europe and north america (1950–2021). *Journal of Applied Meteorology and Climatology, 62*(11), 1627-1653. doi:https://doi.org/10.1175/JAMC-D-22-0195.1

Battaglioli, F., Groenemeijer, P., Tsonevsky, I. and Púčik, T. (2023b). Forecasting large hail and lightning using additive logistic regression models and the ECMWF reforecasts. *Natural Hazards and Earth System Sciences, 23*(12), 3651-3669. doi:https://doi.org/10.5194/nhess-23-3651-2023

Bechini, R. and Chandrasekar, V. (2015). A Semisupervised Robust Hydrometeor Classification Method for Dual-Polarization Radar Applications. *Journal of Atmospheric and Oceanic Technology, 32*(1), 22-47. doi:https://doi.org/10.1175/JTECH-D-14-00097.1

Bedka, K., Brunner, J., Dworak, R., Feltz, W., Otkin, J. and Greenwald, T. (2010). Objective Satellite-Based Detection of Overshooting Tops Using Infrared Window Channel Brightness Temperature Gradients. *Journal of Applied Meteorology and Climatology, 49*, 181-202.

Bedka, K. M. (2011). Overshooting cloud top detections using MSG SEVIRI Infrared brightness temperatures and their relationship to severe weather over Europe. *Atmospheric Research, 99*(2), 175-189. doi:https://doi.org/10.1016/j.atmosres.2010.10.001

Belk, N. M. and Wilson, L. D. (1998). *Using cell-based VIL density to identify severe-hail thunderstorms in the central Appalachians and middle Ohio Valley.*

Bering III, E. A., Few, A. A. and Benbrook, J. R. (1998). The global electric circuit. *Physics today, 51*(10), 24-30. doi:https://doi.org/10.1063/1.882422

Bernal Ayala, A. C., Rowe, A. K., Arena, L. E. and Nachlas, W. O. (2025). Physical–chemical properties of particles in hailstones from central Argentina. *Atmospheric Chemistry and Physics, 25*(14), 7597-7617. doi:https://doi.org/10.5194/acp-25-7597-2025

Berthet, C., Dessens, J. and Sánchez, J. L. (2011). Regional and yearly variations of hail frequency and intensity in France. *Atmospheric Research, 100*(4), 391-400. doi:https://doi.org/10.1016/j.atmosres.2010.10.008

Betz, H. D., Schmidt, K., Laroche, P., Blanchet, P., Oettinger, W. P., Defer, E., Dziewit, Z. and Konarski, J. (2009). LINET—An international lightning detection network in Europe. *Atmospheric Research, 91*(2-4), 564-573. doi:https://doi.org/10.1016/j.atmosres.2008.06.012.

Biron, D. (2009). LAMPINET - Lightning Detection in Italy. In H. Betz, U. Schumann and P. Laroche, *Lightning: Principles, Instruments and Applications.* (p. 141-159). Dordrecht: Springer. doi:https://doi.org/10.1007/978-1-4020-9079-0_6

Blaes, J. L., Cerniglia, C. S. and Caropolo, M. A. (1998). *VIL density as an indicator of hail across eastern New York and western New England.*

Boccippio, D. J., Cummins, K. L., Christian, H. J. and Goodman, S. J. (2001). Combined satellite-and surface-based estimation of the intracloud–cloud-to-ground lightning ratio over the continental United States. *Monthly Weather Review, 129*(1), 108-122. doi:https://doi.org/10.1175/1520-0493(2001)129%3C0108:CSASBE%3E2.0.CO;2

Brook, J. P., Soderholm, J. S., Protat, A., McGowan, H. and Warren, R. A. (2024). A Radar-Based Hail Climatology of Australia. *Monthly Weather Review, 152*(2), 607-628. doi:https://doi.org/10.1175/MWR-D-23-0130.1

Brooks, C. E. (1925). The distribution of thunderstorms over the globe. *Geophys. Memo., 3*(24), 147–164.

Browning, K. A., Ludlam, F. H. and Macklin, W. C. (1963). The density and structure of hailstones. *Quarterly Journal of the Royal Meteorological Society, 89*(379), 75-84. doi:https://doi.org/10.1002/qj.49708937905

Burcea, S., Cică, R. and Bojariu, R. (2016). Hail climatology and trends in Romania: 1961–2014. *Monthly Weather Review, 144*(11), 4289-4299. doi:https://doi.org/10.1175/MWR-D-16-0126.1

Capozzi, V., Picciotti, E., Mazzarella, V., Budillon, G. and Marzano, F. S. (2016). Hail storm hazard in urban areas: Identification and probability of occurrence by using a single-polarization X-band weather radar. *Hydrology and Earth System Sciences Discussions*, 1-22. doi:https://doi.org/10.5194/hess-2016-177

Capozzi, V., Picciotti, E., Mazzarella, V. and Marzano, F. S. (2018). Fuzzy-logic detection and probability of hail exploiting short-range X-band. *Atmospheric Research, 201*, 17-33. doi:https://doi.org/10.1016/j.atmosres.2017.10.006.

Capozzi, V., Mazzarella, V., De Vivo, C., Annella, C., Greco, A., Fusco, G. and Budillon, G. (2022). A Network of X-Band Meteorological Radars to Support the Motorway System (Campania Region Meteorological Radar Network Project). *Remote Sensing, 14*(9), 2221. doi:https://doi.org/10.3390/rs14092221

Carey, L. D. and Rutledge, S. A. (1998). Electrical and multiparameter radar observations of a severe hailstorm. *Journal of Geophysical Research: Atmospheres, 103*(D12), 13979-14000. doi:https://doi.org/10.1029/97JD02626

Cavicchia, L., von Storch, H. and Gualdi, S. (2014). A long-term climatology of medicanes. *Climate dynamics, 43*(5), 1183-1195. doi:https://doi.org/10.1007/s00382-013-1893-7

Cecil, D. J. (2009). Passive microwave brightness temperatures as proxies for hailstorms. *Journal of applied meteorology and climatology, 48*(6), 1281-1286. doi:https://doi.org/10.1175/2009JAMC2125.1

Cecil, D. J. and Blankenship, C. B. (2012). Toward a global climatology of severe hailstorms as estimated by satellite passive microwave imagers. *Journal of Climate, 25*(2), 687-703. doi:https://doi.org/10.1175/JCLI-D-11-00130.1

Changnon, S. A. (1992). Temporal and Spatial Relations between Hail and Lightning. *Journal of Applied Meteorology and Climatology, 31*, 587-604. doi:https://doi.org/10.1175/1520-0450(1992)031%3C0587:TASRBH%3E2.0.CO;2

Christian, H. J., Blakeslee, R. J., Boccippio, D. J., Boeck, W. L., Buechler, D. E., Driscoll, K. T., Goodman, S. J., Hall, J. M., Koshak, W. J., Mach, D. M. and Stewart, M. F. (2003). Global frequency and distribution of lightning as observed from space by the Optical Transient Detector. *Journal of Geophysical Research: Atmospheres, 108*(D1), ACL-4. doi:https://doi.org/10.1029/2002JD002347

Chronis, T., Carey, L. D., Schultz, C. J., Schultz, E. V., Calhoun, K. M. and Goodman, S. J. (2015). Exploring Lightning Jump Characteristics. *Weather and Forecasting, 30*(1), 23-37. doi:https://doi.org/10.1175/WAF-D-14-00064.1

Cică, R., Burcea, S. and Bojariu, R. (2015). Assessment of severe hailstorms and hail risk using weather radar data. *Meteorological Applications, 22*(4), 746-753.

Cintineo, J. L., Smith, T. M., Lakshmanan, V., Brooks, H. E. and Ortega, K. L. (2012). An objective high-resolution hail climatology of the contiguous United States. *Weather and Forecasting, 27*(5), 1235-1248.

Cooray, V., Cooray, C. and Andrews, C. J. (2007). Lightning caused injuries in humans. *Journal of electrostatics, 65*(5-6), 386-394. doi:https://doi.org/10.1016/j.elstat.2006.09.016

Cooray, V. (2015). *An introduction to lightning.* Dordrecht: Springer.

Cummins, K. L., Murphy, M. J., Bardo, E. A., Hiscox, W. L., Pyle, R. B. and Pifer, A. E. (1998). A combined TOA/MDF technology upgrade of the US National Lightning Detection Network. *Journal of Geophysical Research: Atmospheres, 103*(D8), 9035-9044. doi:https://doi.org/10.1029%2F98JD00153

Cummins, K. L., Murphy, M. J. and Tuel, J. V. (2000). Lightning detection methods and meteorological applications. *IV International Symposium on Military Meteorology*, (p. 26-28).

Cummins, K. L., Cramer, J. A., Biagi, C. J., Krider, E. P., Jerauld, J., U. M. and Rakov, V. A. (2006). 6.1. the us national lightning detection network: post-upgrade status. *Second Conference on Meteorological Applications of Lightning Data.*

Dotzek, N., Groenemeijer, P., Feuerstein, B. and and Holzer, A. M. (2009). Overview of ESSL's severe convective storms research using the European Severe Weather Database ESWD. *Atmospheric research, 93*(1-3), 575-586. doi:https://doi.org/10.1016/j.atmosres.2008.10.020

Emersic, C., Heinselman, P. L., MacGorman, R., D. and Bruning, E. C. (2011). Lightning activity in a hail-producing storm observed with phased-array radar. *Monthly Weather Review, 139*(6), 1809-1825. doi:https://doi.org/10.1175/2010MWR3574.1

Farnell, C., Rigo, T. and Pineda, N. (2017). Lightning jump as a nowcast predictor: Application to severe weather events in Catalonia. *Atmospheric Research, 183*(1), 130-141. doi:https://doi.org/10.1016/j.atmosres.2016.08.021.

Farnell, C., Rigo, T. and Pineda, N. (2018). Exploring radar and lightning variables associated with the Lightning Jump. Can we predict the size of the hail? *Atmospheric Research, 202*, 175-186. doi:https://doi.org/10.1016/j.atmosres.2017.11.019

Farnell, C. and Rigo, T. (2020). The Lightning Jump Algorithm for Nowcasting Convective Rainfall in Catalonia. *Atmosphere, 11*(4), 397. doi:https://doi.org/10.3390/atmos11040397

Farnell, C., Batalla, E., Rigo, T., Pineda, N., Sole, X., Mercader, J. and Martin-Vide, J. (2023). Reanalysis of giant hail event in Catalonia (NE of the Iberian Peninsula). *Atmospheric Research, 296*, 107051. doi:https://doi.org/10.1016/j.atmosres.2023.107051

Feng, G., Qie, X., Yuan, T. and Niu, S. (2007). Lightning activity and precipitation structure of hailstorms. *Science in China Series D: Earth Sciences, 50*(4), 629-639. doi:https://doi.org/10.1007/s11430-007-2063-8

Ferraro, R., Beauchamp, J., Cecil, D. and Heymsfield, G. (2015). A prototype hail detection algorithm and hail climatology developed with the Advanced Microwave Sounding Unit (AMSU). *Atmospheric Research, 163*, 24-35. doi:https://doi.org/10.1016/j.atmosres.2014.08.010

Ferraro, R. R., Cecil, D. and Laviola, S. (2020). Hailfall Detection. In *Satellite Precipitation Measurement: Volume 2* (p. 861-879).

Fluck, E., Kunz, M., Geissbuehler, P. and Ritz, S. P. (2021). Radar-based assessment of hail frequency in Europe. *Natural Hazards and Earth System Sciences, 21*(2), 683-701. doi:https://doi.org/10.5194/nhess-21-683-2021

Foote, G. B. (1984). A study of hail growth utilizing observed storm conditions. *Journal of Applied Meteorology and Climatology, 23*(1), 84-101. doi:https://doi.org/10.1175/1520-0450(1984)023%3C0084:ASOHGU%3E2.0.CO;2

Galanaki, E., Lagouvardos, K., Kotroni, V., Flaounas, E. and Argiriou, A. (2018). Thunderstorm climatology in the Mediterranean using cloud-to-ground lightning observations. *Atmospheric Research, 207*, 136-144. doi:https://doi.org/10.1016/j.atmosres.2018.03.004

García-Ortega, E., Fita, L., Romero, R., López, L., Ramis, C. and Sánchez, J. L. (2007). Numerical simulation and sensitivity study of a severe hailstorm in northeast Spain. *Atmospheric Research, 83*(2-4), 225-241. doi:https://doi.org/10.1016/j.atmosres.2005.08.004

Gatlin, P. N. and Goodman, S. J. (2010). A Total Lightning Trending Algorithm to Identify Severe Thunderstorms. *Journal of Atmospheric and Oceanographic Technology, 27*(1), 3-22. doi:https://doi.org/10.1175/2009JTECHA1286.1

Giordani, A., Kunz, M., Bedka, K. M., Punge, H. J., Paccagnella, T., Pavan, V., Cerenzia, I. M. L. and Di Sabatino, S. (2024). Characterizing hail-prone environments using convection-permitting reanalysis and overshooting top detections over south-central Europe. *Natural Hazards and Earth System Sciences, 24*(7), 2331-2357. doi:https://doi.org/10.5194/nhess-24-2331-2024

Gish, O. H. and Wait, G. R. (1950). Thunderstorms and the earth's general electrification. *Journal of Geophysical Research, 55*(4), 473-484. doi:https://doi.org/10.1029/JZ055i004p00473

Glickman, T. S. (2000). *Glossary of meteorology.* American Meteorological Soc.

Greene, D. R. and Clark, R. A. (1972). Vertically integrated liquid water - A new analysis tool. *Monthly Weather Review, 100*, 548-552. doi:https://doi.org/10.1175/1520-0493(1972)100%3C0548:VILWNA%3E2.3.CO;2

He, K., Zhang, X., Ren, S. and Sun, J. (2016). Deep Residual Learning for Image Recognition. *Proceedings of the IEEE Conference on Computer Vision and Pattern Recognition (CVPR)*, (p. 770-778).

Hewson, T., Ashoor, A., Boussetta, S., Emanuel, K., Lagouvardos, K., Lavers, D., Magnusson, L., Pillosu, F. and Zsoter, E. (2024). Medicane Daniel: An extraordinary cyclone with devastating impacts. *ECMWF newsletters, 179*, 33-47.

Heymsfield, A., Szakáll, M., Jost, A., Giammanco, I. and Wright, R. (2018). A comprehensive observational study of graupel and hail terminal velocity, mass flux, and kinetic energy. *Journal of the Atmospheric Sciences, 75*(11), 3861-3885. doi:https://doi.org/10.1175/JAS-D-18-0035.1

Holleman, I. (2001). *Hail detection using single-polarization radar.* De Bilt: The Nederlands: Ministerie van Verkeer en Waterstaat, Koninklijk Nederlands Meteorologisch Instituut.

Hou, A. Y., Kakar, R. K., Neeck, S., Azarbarzin, A. A., Kummerow, C. D., Kojima, M., Oki, R., Nakamura, K. and Iguchi, T. (2014). The Global Precipitation Measurement Mission. *Bulletin of the American Meteorological Society, 95*, 701-722.

Hulton, F. and Schultz, D. M. (2024). Climatology of large hail in Europe: characteristics of the European Severe Weather Database. *Natural Hazards and Earth System Sciences, 24*(4), 1079-1098. doi:https://doi.org/10.5194/nhess-24-1079-2024, 2024.

Istrate, V., Dobri, R. V., Bărcăcianu, F., Ciobanu, R. A. and Apostol, L. (2017). A ten years hail climatology based on ESWD hail reports in Romania. *Geographia Technica, 12*(2), 110-118. doi:http://dx.doi.org/10.21163/GT_2017.122.10

Johnson, E. V. and Mansell, E. R. (2006). 6.5 THREE-DIMENSIONAL LIGHTNING MAPPING OF THE CENTRAL OKLAHOMA SUPERCELL ON 26 MAY 2004.

Jurković, P. M., Mahović, N. S. and Počakal, D. (2015). Lightning, overshooting top and hail characteristics for strong convective storms in Central Europe. *Atmospheric Research, 161*, 153-168. doi:https://doi.org/10.1016/j.atmosres.2015.03.020

Kahraman, A., Kendon, E. J. and Fowler, H. J. (2024). Climatology of severe hail potential in Europe based on a convection-permitting simulation. *Climate Dynamics, 62*(7), 6625-6642. doi:https://doi.org/10.1007/s00382-024-07227-w

Kalina, E. A., Friedrich, K., Motta, B. C., Deierling, W., Stano, G. T. and Rydell, N. N. (2016). Colorado plowable hailstorms: Synoptic weather, radar, and lightning characteristics. *Weather and Forecasting, 31*(2), 663-693. doi:https://doi.org/10.1175/WAF-D-15-0037.1

Knight, C. A. and Knight, N. C. (2001). Hailstorms. In *Severe convective storms* (p. 223-254). Boston: American Meteorological Society.

Kunz, M., Sander, J. and Kottmeier, C. (2009). Recent trends of thunderstorm and hailstorm frequency and their relationship to atmospheric characteristics in southwest Germany. *International journal of climatology, 29*, 2283-2297. doi:https://doi.org/10.1002/joc.1865

Kunz, M. and Kugel, P. I. (2015). Detection of hail signatures from single-polarization C-band radar reflectivity. *Atmospheric Research, 153*, 565-577. doi:https://doi.org/10.1016/j.atmosres.2014.09.010

Kunz, M., Wandel, J., Fluck, E., Baumstark, S., Mohr, S. and Schemm, S. (2020). Ambient conditions prevailing during hail events in central Europe. *Natural Hazards and Earth System Sciences, 20*(6), 1867-1887. doi:https://doi.org/10.5194/nhess-20-1867-2020

Lahiff, C. T. (2005). Vertically Integrated Liquid Density and its associated hail size range across the Burlington, Vermont County warning area. *Eastern Region Technical Attachment*(05-01).

Laviola, S., Levizzani, V., Ferraro, R. and Beauchamp, J. (2020a). Hailstorm Detection by Satellite Microwave Radiometers. *Remote Sensing, 12*(4), 621. doi:https://doi.org/10.3390/rs12040621

Laviola, S., Monte, G., Levizzani, L., Ferraro, R. and Beauchamp, J. (2020b). A New Method for Hail Detection from the GPM Constellation: A Prospect for a Global Hailstorm Climatology. *Remote Sensing, 12*(21), 3553. doi:https://doi.org/10.3390/rs12213553

Laviola, S., Monte, G., Cattani, E. and Levizzani, V. (2022a). Hail climatology in the Mediterranean basin using the GPM constellation (1999–2021). *Remote Sensing, 14*(17), 4320. doi:https://doi.org/10.3390/rs14174320

Laviola, S., Vermi, F., Guarascio, M., Monte, G., Folino, G. and Levizzani, V. (2022b). The Multi-sensor Approach for Satellite Hail Advection (MASHA): a new technique for nowcasting applications. *EMS Annual Meeting 2022*, (p. EMS2022-571). Bonn, Germany. doi:https://doi.org/10.5194/ems2022-571

LeCun, Y., Bengio, Y. and Hinton, G. (2015). Deep Learning. *Nature, 521*, 436-444. doi:https://doi.org/10.1038/nature14539

Levizzani, V., Schmetz, J., Lutz, H. J., Kerkmann, J., Alberoni, P. P. and Cervino, M. (2001). Precipitation estimations from geostationary orbit and prospects for METEOSAT Second Generation. *Meteorological Applications, 8*, 23-41.

Li, N., Zhang, J., Wang, D. and Wang, P. (2023). Research on Hail Mechanism Features Based on Dual-Polarization Radar Data. *Atmosphere, 14*(12), 1827. doi:https://doi.org/10.3390/atmos14121827

Liu, D., Feng, G. and Wu, S. (2009). The characteristics of cloud-to-ground lightning activity in hailstorms over northern China. *Atmospheric Research, 91*, 459-465. doi:https://doi.org/10.1016/j.atmosres.2008.06.016

Luo, Y. (2007). Terrestrial carbon–cycle feedback to climate warming. *Annual Review of Ecology, Evolution, and Systematics, 38*(1), 683-712. doi:https://doi.org/10.1146/annurev.ecolsys.38.091206.095808

Magurno, D. and Levizzani, V. (2012). *IDENTIFICAZIONE E LOCALIZZAZIONE DEI FULMINI TRAMITE SISTEMI AUTOMATICI.*

Malan, D. J. (1963). *Physics of Lightning.* London: The English Universities Press, Ltd.

Marra, A. C., Porcù, F., Baldini, L., Petracca, M., Casella, D., Dietrich, S., Mugnai, A., Sanò, P., Vulpiani, G. and Panegrossi, G. (2017). Observational analysis of an exceptionally intense hailstorm over the Mediterranean area: Role of the GPM Core Observatory. *Atmospheric Research, 192*, 72-90. doi:https://doi.org/10.1016/j.atmosres.2017.03.019

Martín, M. L., Calvo-Sancho, C., Taszarek, M., González-Alemán, J. J., Montoro-Mendoza, A., Díaz-Fernández, J., Bolgiani, P., Sastre, M., and Martín, Y. (2024). Major role of marine heatwave and anthropogenic climate change on a Giant hail Event in Spain. *Geophysical Research Letters, 51*(6), e2023GL107632. doi:https://doi.org/10.1029/2023GL107632

Merino, A., G.-O. E., L. L., Sánchez, J. L. and Guerrero-Higueras, A. M. (2013). Synoptic environment, mesoscale configurations and forecast parameters for hailstorms in Southwestern Europe. *Atmospheric Research, 122*, 183-198. doi:https://doi.org/10.1016/j.atmosres.2012.10.021

Merino, A., Wu, X., Gascón, E., Berthet, C., García-Ortega, E. and Dessens, J. (2014). Hailstorms in southwestern France: Incidence and atmospheric characterization. *Atmospheric research, 140*, 61-75. doi:https://doi.org/10.1016/j.atmosres.2014.01.015

Metzger, E. and Nuss, W. A. (2013). The relationship between total cloud lightning behavior and radar-derived thunderstorm structure. *Weather and Forecasting, 28*(1), 237-253. doi:https://doi.org/10.1175/WAF-D-11-00157.1

Meyer, P. S. and Ausubel, J. H. (1999). Carrying Capacity: A Model with Logistically Varying Limits. *Technological Forecasting and Social Change, 61*(3), 209-214. doi:https://doi.org/10.1016/S0040-1625(99)00022-0

Michaud, A. B., Dore, J. E., Leslie, D., Lyons, W. B., Sands, D. C. and Priscu, J. C. (2014). Biological ice nucleation initiates hailstone formation. *Journal of Geophysical Research: Atmospheres, 119*(21), 12-186. doi:https://doi.org/10.1002/2014JD022004

Miglietta, M. M., Flaounas, E., González-Alemán, J. J., Panegrossi, G., Gaertner, M. A., Pantillon, F., Pasquero, C., Schultz, D. M., D'Adderio, L. P., Dafis, S., Husson, R., Ricchi, A., Carrió Carrió, D. S., Davolio, S., Fita, L., Picornell, M. Á., Pytharoulis, I., Raveh-Rubin, S., Scoccimarro, E., Bernini, L., Cavicchia, L., Conte, D., Ferretti, R., Flocas, H., Gutiérrez-Fernández, J., Hatzaki, M., Homar Santaner, V., Jansà, A. and Patlakas, P. (2025). Defining Medicanes: Bridging the Knowledge Gap between Tropical and Extratropical Cyclones in the Mediterranean. *Bulletin of the American Meteorological Society, 106*(9), E1955-E1971. doi:https://doi.org/10.1175/BAMS-D-24-0289.1

Mikuš, P. and Strelec Mahović, N. (2013). Satellite-based overshooting top detection methods and an analysis of correlated weather conditions. *Atmospheric research, 123*, 268-280. doi:https://doi.org/10.1016/j.atmosres.2012.09.001

Mikuš, P. and Strelec Mahović, N. (2013). Lightning distribution during the hailstorms with the overshooting tops. *Proceedings - 2013 EUMETSAT Meteorological Satellite Conference*.

Montanyà, J., Soula, S. and Pineda, N. (2007). A study of the total lightning activity in two hailstorms. *Journal of Geophysical Research: Atmospheres, 112*(D13118). doi:https://doi.org/10.1029/2006JD007203

Montanyà, J., Soula, S., Pineda, N., van Der Velde, O., Clapers, P., Solà, G., Bech, J. and Romero, D. (2009). Study of the total lightning activity in a hailstorm. *Atmospheric research, 91*(2-4), 430-437. doi:https://doi.org/10.1016/j.atmosres.2008.06.008

Murillo, E. M., Homeyer, C. R. and Allen, J. T. (2021). A 23-year severe hail climatology using GridRad MESH observations. *Monthly weather review, 149*(4), 945-958.

Nisi, L., Martius, O., Hering, A., Kunz, M. and Germann, U. (2016). Spatial and temporal distribution of hailstorms in the Alpine region: a long-term, high resolution, radar-based analysis. *Quarterly Journal of the Royal Meteorological Society, 142*(697), 1590-1604.

Nisi, L., Hering, A., Germann, U., Schroeer, K., Barras, H., Kunz, M. and Martius, O. (2020). Hailstorms in the Alpine region: Diurnal cycle, 4D-characteristics, and the nowcasting potential of lightning properties. *Quarterly Journal of the Royal Meteorological Society, 146*(733), 4170-4194. doi:https://doi.org/10.1002/qj.3897

Noppel, H., Blahak, U., Seifert, A. and Beheng, K. D. (2010). Simulations of a hailstorm and the impact of CCN using an advanced two-moment cloud microphysical scheme. *Atmospheric Research, 96*(2-3), 286-301. doi:https://doi.org/10.1016/j.atmosres.2009.09.008

Ortega, K. L. (2018). Evaluating multi-radar, multi-sensor products for surface hailfall diagnosis. *E-Journal of Severe Storms Meteorology, 13*(1), 1-36. doi:https://doi.org/10.55599/ejssm.v13i1.69

O'Shea, K. and Nash, R. (2015). An Introduction to Convolutional Neural Networks. *Neural and Evolutionary Computing*.

Papavasileiou, G., Kotroni, V., Lagouvardos, K. and Giannaros, T. M. (2022). Observational and numerical study of a giant hailstorm in Attica, Greece, on 4 October 2019. *Atmospheric Research, 278*, 106341. doi:https://doi.org/10.1016/j.atmosres.2022.106341

Petracca, M., Federico, S., Roberto, N., Puca, S., D'Adderio, L. P., Torcasio, R. C. and Dietrich, S. (2024). A 13-year long strokes statistical analysis over the Central Mediterranean area. *Atmospheric Research, 304*, 107368. doi:https://doi.org/10.1016/j.atmosres.2024.107368

Piani, F., Crisci, A., De Chiara, G., Maracchi, G. and Meneguzzo, F. (2005). Recent trends and climatic perspectives of hailstorms frequency and intensity in Tuscany and Central Italy. *Natural Hazards and Earth System Sciences, 5*(2), 217-224. doi:https://doi.org/10.5194/nhess-5-217-2005, 2005.

Pilorz, W. (2015). Very large hail occurrence in Poland from 2007 to 2015. *Contemporary Trends in Geoscience, 4*(1), 45-55. doi:10.1515/ctg-2015-0005

Price, C. (2006). Global thunderstorm activity. In *Sprites, elves and intense lightning discharges* (p. 85-99). Dordrecht: Springer Netherlands.

Price, C. G. (2013). Lightning applications in weather and climate research. *Surveys in Geophysics, 34*(6), 755-767. doi:https://doi.org/10.1007/s10712-012-9218-7

Púčik, T., Castellano, C., Groenemeijer, P., Kühne, T., Rädler, A. T., Antonescu, B. and Faust, E. (2019). Large hail incidence and its economic and societal impacts across Europe. *Monthly Weather Review, 147*(11), 3901-3916. doi:https://doi.org/10.1175/MWR-D-19-0204.1

Punge, H. J., Bedka, K. M., Kunz, M. and Werner, A. (2014). A new physically based stochastic event catalog for hail in Europe. *Natural Hazards, 73*, 1625-1645. doi:https://doi.org/10.1007/s11069-014-1161-0

Punge, H. J. and Kunz, M. (2016). Hail observations and hailstorm characteristics in Europe: A review. *Atmospheric Research, 176*, 159-184. doi:https://doi.org/10.1016/j.atmosres.2016.02.012

Punge, H. J., Bedka, K. M., Kunz, M. and Reinbold, A. (2017). Hail frequency estimation across Europe based on a combination of overshooting top detections and the ERA-INTERIM reanalysis. *Atmospheric Research, 198*, 34-43. doi:https://doi.org/10.1016/j.atmosres.2017.07.025

Puskeiler, M., Kunz, M. and Schmidberger, M. (2016). Hail statistics for Germany derived from single-polarization radar data. *Atmospheric Research, 178*, 459-470. doi:https://doi.org/10.1016/j.atmosres.2016.04.014

Rädler, A. T., Groenemeijer, P. H., Faust, E., Sausen, R. and Púčik, T. (2019). Frequency of severe thunderstorms across Europe expected to increase in the 21st century due to rising instability. *npj Climate and Atmospheric Science, 2*(1), 30. doi:https://doi.org/10.1038/s41612-019-0083-7

Rakov, V. A. (2013a). The physics of lightning. *Surveys in Geophysics, 34*(6), 701-729. doi:https://doi.org/10.1007/s10712-013-9230-6

Rakov, V. A. (2013b). Electromagnetic methods of lightning detection. *Surveys in Geophysics, 34*(6), 731-753. doi:https://doi.org/10.1007/s10712-013-9251-1

Rakov, V. A. (2021). Lightning, the science. In *Lightning: Science, Engineering, and Economic Implications for Developing Countries* (p. 1-36). Singapore: Springer Singapore. doi:https://doi.org/10.1007/978-981-16-3440-6_1

Rasmussen, R. M. and Heymsfield, A. J. (1987). Melting and shedding of graupel and hail. Part I: Model physics. *Journal of Atmospheric Sciences, 44*(19), 2754-2763. doi:https://doi.org/10.1175/1520-0469(1987)044%3C2754:MASOGA%3E2.0.CO;2

Raupach, T. H., Martius, O., Allen, J. T., Kunz, M., Lasher-Trapp, S., Mohr, S., Rasmussen, K. L., Trapp, R. and Zhang, Q. (2021). The effects of climate change on hailstorms. *Nature reviews earth & environment, 2*(3), 213-226. doi:https://doi.org/10.1038/s43017-020-00133-9

Reynolds, S. E. (1953). Thunderstorm-precipitation growth and electrical-charge generation. *Bulletin of the American Meteorological Society, 34*(3), 117-123. doi:https://doi.org/10.1175/1520-0477-34.3.117

Ricchi, A., Rotunno, R., Miglietta, M. M., Picciotti, E., Montopoli, M., Marzano, F. S., Baldini, L., Vulpiani, G., Tiesi, A. and Ferretti, R. (2023). Analysis of the development mechanisms of a large-hail storm event on the Adriatic Sea. *Atmospheric Research, 296*, 107079. doi:https://doi.org/10.1016/j.atmosres.2023.107079

Rigo, T. and Farnell, C. (2022). Characterisation of thunderstorms with multiple lightning jumps. *Atmosphere, 13*(2), 171. doi:https://doi.org/10.3390/atmos13020171

Romero, R. and Emanuel, K. (2013). Medicane risk in a changing climate. *Journal of Geophysical Research: Atmospheres, 118*(12), 5992-6001. doi:https://doi.org/10.1002/jgrd.50475

Rosati, V. (2023). I principi della lightning detection: la rete LAMPINET dell'Aeronautica Militare. *Rivista di Meteorologia Aeronautica*(3), p. 6-23. doi:https://www.aeronautica.difesa.it/wp-content/uploads/2023/10/RM_032023_5_LIGHTNING_DETECT_AFF.pdf

Rosinski, J. and Kerrigan, T. C. (1969). The role of aerosol particles in the formation of raindrops and hailstones in severe thunderstorms. *Journal of Atmospheric Sciences, 26*(4), 695-715. doi:https://doi.org/10.1175/1520-0469(1969)26%3C695:TROAPI%3E2.0.CO;2

Saha, S., Moorthi, S., Pan, H., Wu, X., Wang, J., Nadiga, S., Tripp, P., Kistler, R., Woollen, J., Behringer, D., Liu, H., Stokes, D., Grumbine, R., Gayno, G., Wang, J., Hou, Y., Chuang, H., Juang, H. H., Sela, J., Iredell, M., Treadon, R., Kleist, D., Van Delst, P., Keyser, D., Derber, J., Ek, M., Meng, J., Wei, H., Yang, R., Lord, S., van den Dool, H., Kumar, A., Wang, W., Long, C., Chelliah, M., Xue, Y., Huang, B., Schemm, J., Ebisuzaki, W., Lin, R., Xie, P., Chen, M., Zhou, S., Higgins, W., Zou, C., Liu, Q., Chen, Y., Han, Y., Cucurull, L., Reynolds, R. W., Rutledge, G. and Goldberg, M. (2010). The NCEP Climate Forecast System Reanalysis. *Bulletin of the American Meteorological Society, 91*(8), 1015-1058. doi:https://doi.org/10.1175/2010BAMS3001.1

Saltikoff, E., Tuovinen, J. P., Kotro, J., Kuitunen, T. and Hohti, H. (2010). A climatological comparison of radar and ground observations of hail in Finland. *Journal of applied meteorology and climatology, 49*(1), 101-114. doi:https://doi.org/10.1175/2009JAMC2116.1

Santurette, P. and Georgiev, C. G. (2005). *Weather Analysis and Forecasting: Applying Satellite Water Vapor Imagery and Potential Vorticity Analysis. .* Academic Press.

Saunders, C. P., Keith, W. D. and Mitzeva, R. P. (1991). The effect of liquid water on thunderstorm charging. *Journal of Geophysical Research: Atmospheres, 96*(D6), 11007-11017. doi:https://doi.org/10.1029/91JD00970

Saunders, C. P. (1993). A review of thunderstorm electrification processes. *Journal of Applied Meteorology and Climatology, 32*(4), 642-655.

Saunders, C. P., Bax-Norman, H., Emersic, C., Avila, E. E. and Castellano, N. E. (2006). Laboratory studies of the effect of cloud conditions on graupel/crystal charge transfer in thunderstorm electrification. *Quarterly Journal of the Royal Meteorological Society: A journal of the atmospheric sciences, applied meteorology and physical oceanography, 132*(621), 2653-2673. doi:https://doi.org/10.1256/qj.05.218

Schultz, C. J., Petersen, W. A. and Carey, L. D. (2009). Preliminary Development and Evaluation of Lightning Jump Algorithms for the Real-Time Detection of Severe Weather. *Journal of Applied Meteorology and Climatology, 48*(12), 2543-2563. doi:https://doi.org/10.1175/2009JAMC2237.1

Schultz, C. J., Petersen, W. A. and Carey, L. D. (2011). Lightning and Severe Weather: A Comparison between Total and Cloud-to-Ground Lightning Trends. *Weather and Forecasting, 26*(5), 744-755. doi:https://doi.org/10.1175/WAF-D-10-05026.1

Schultz, C. J., Carey, L. D., Schultz, E. V. and Blakeslee, R. J. (2017). Kinematic and microphysical significance of lightning jumps versus nonjump increases in total flash rate. *Weather and forecasting, 32*(1), 275-288. doi:https://doi.org/10.1175/WAF-D-15-0175.1

Takahashi, T. (1978). Riming electrification as a charge generation mechanism in thunderstorms. *Journal of Atmospheric Sciences, 35*(8), 1536-1548. doi:https://doi.org/10.1175/1520-0469(1978)035%3C1536:REAACG%3E2.0.CO;2

Taszarek, M., Allen, J., Púčik, T., Groenemeijer, P., Czernecki, B., Kolendowicz, L., Lagouvardos, K., Kotroni, V. and Schulz, W. (2019). A climatology of thunderstorms across Europe from a synthesis of multiple data sources. *Journal of Climate, 32*(6), 1813-1837. doi:https://doi.org/10.1175/JCLI-D-18-0372.1

Tian, Y., Qie, X., Sun, Y., Wang, D., Yuan, S., Sun, Z., Lu, G., Yu, L., Sun, H., Li, L. and Du, C. (2019). Total lightning signatures of thunderstorms and lightning jumps in hailfall nowcasting in the Beijing area. *Atmospheric Research, 230*, 104646. doi:https://doi.org/10.1016/j.atmosres.2019.104646

Tian, Y., Yao, W., Sun, Y., Wang, Y., Liu, X., Jiang, T., Zhang, L., Meng, L., Wang, L., Sun, X. and Wang, H. (2022). A method for improving the performance of the 2σ lightning jump algorithm for nowcasting hail. *Atmospheric Research, 280*, 106404. doi:https://doi.org/10.1016/j.atmosres.2022.106404.

Tiesi, A., Mazzà, S., Conte, D., Ricchi, A., Baldini, L., Montopoli, M., Picciotti, E., Vulpiani, G., Ferretti, R. and Miglietta, M. M. (2022). Numerical simulation of a Giant-hail-bearing Mediterranean supercell in the Adriatic Sea. *Atmosphere, 13*(8), 1219. doi:https://doi.org/10.3390/atmos13081219

Torricella, F., Levizzani, V. and Turk, F. J. (2007). Application of a blended MW-IR rainfall algorithm to the Mediterranean. . In *Measuring precipitation from space: EURAINSAT and the future* (p. 497-507). Dordrecht: Springer Netherlands.

Tous, M. and Romero, R. (2013). Meteorological environments associated with medicane development. *International Journal of Climatology, 33*(1), 1-14. doi:10.1002/joc.3428

Uman, M. A. (2001). *The lightning discharge.* Courier Corporation.

Uman, M. A. (2012). *Lightning.* Courier Corporation.

van Delden, A. (2001). The synoptic setting of thunderstorms in western Europe. *Atmospheric research, 56*(1-4), 89-110. doi:https://doi.org/10.1016/S0169-8095(00)00092-2

Vermi, F. (2022). *Analisi ad alta risoluzione spazio-temporale di eventi grandinigeni nel bacino del Mediterraneo mediante una nuova tecnica satellitare ibrida multisensore.* [Tesi di laurea magistrale, Alma Mater Studiorum – Università di Bologna]. https://amslaurea.unibo.it/id/eprint/26527/1/Tesi_Federico_Vermi.pdf

Vermi, F., Capozzi, V., Monte, G., Budillon, S. and Laviola, S. (2025). Lightning jump as precursor of very large hail occurrence: first evidence in the Italian territory. *Bulletin of Atmospheric Science and Technology, 6*, 21. doi:https://doi.org/10.1007/s42865-025-00104-2

Vulpiani, G., Baldini, L. and Roberto, N. (2015). Characterization of Mediterranean hail-bearing storms using an operational polarimetric X-band radar. *Atmospheric Measurement Techniques, 8*(11), 4681-4698. doi:https://doi.org/10.5194/amt-8-4681-2015

Waldvogel, A., Federer, B. and Grimm, P. (1979). Criteria for the Detection of Hail Cells. *Journal of Applied Meteorology and Climatology, 18*(12), 1521-1525. doi:https://doi.org/10.1175/1520-0450(1979)018%3C1521:CFTDOH%3E2.0.CO;2

Wapler, K., Hengstebeck, T. and Groenemeijer, P. (2016). Mesocyclones in Central Europe as seen by radar. *Atmospheric Research, 168*, 112-120. doi:https://doi.org/10.1016/j.atmosres.2015.08.023

Wapler, K. (2017). The life-cycle of hailstorms: Lightning, radar reflectivity and rotation characteristics. *Atmospheric Research, 193*, 60-72. doi:https://doi.org/10.1016/j.atmosres.2017.04.009

Wapler, K. (2018). TEMPORAL AND SPATIAL DISTRIBUTION OF TOTAL LIGHTNING DENSITIES IN THUNDERSTORMS IN CONJUNCTION WITH OVERSHOOTING TOPS . *Proceedings for the 2018 EUMETSAT Meteorological Satellite Conference.* Tallinn.

Wilhelm, J., Mohr, S., Punge, H. J., Mühr, B., Schmidberger, M., Daniell, J. E., Bedka, K. M. and Kunz, M. (2021). Severe thunderstorms with large hail across Germany in June 2019. *Weather, 76*(7), 228-237. doi:https://doi.org/10.1002/wea.3886

Williams, E. R. (1988). The electrification of thunderstorms. *Scientific American, 259*(5), 88-99. doi:https://www.jstor.org/stable/24989265

Williams, E. R. (1989). The tripole structure of thunderstorms. *Journal of Geophysical Research: Atmospheres, 94*(D11), 13151-13167. doi:https://doi.org/10.1029/JD094iD11p13151

Williams, E. R., Weber, M. E. and Orville, R. E. (1989). The relationship between lightning type and convective state of thunderclouds. *Journal of Geophysical Research: Atmospheres, 94*(D11), 13213-13220. doi:https://doi.org/10.1029/JD094iD11p13213

Williams, E. R., Zhang, R. and Rydock, J. (1991). Mixed-phase microphysics and cloud electrification. *Journal of Atmospheric Sciences, 48*(19), 2195-2203. doi:https://doi.org/10.1175/1520-0469(1991)048%3C2195:MPMACE%3E2.0.CO;2

Williams, E. R., Boldi, B., Matlin, A., Weber, M., Hodanish, S., Sharp, D., Goodman, S., Raghavan, R. and Buechler, D. (1999). The behavior of total lightning activity in severe Florida thunderstorms. *Atmospheric Research, 51*, 245-265. doi:https://doi.org/10.1016/S0169-8095(99)00011-3.

Williams, E. R. (2009). The global electrical circuit: A review. *Atmospheric Research, 91*(2-4), 140-152. doi:https://doi.org/10.1016/j.atmosres.2008.05.018

Yang, H. L., Xiao, H. and Hong, Y. C. (2011). A numerical study of aerosol effects on cloud microphysical processes of hailstorm clouds. *Atmospheric Research, 102*(4), 432-443. doi:https://doi.org/10.1016/j.atmosres.2011.09.007

Yao, W., Zhang, Y., Meng, Q., Wang, F. and Lu, W. (2013). A comparison of the characteristics of total and cloud-to-ground lightning activities in hailstorms. *Acta Meteorologica Sinica, 27*(2), 282-293. doi:https://doi.org/10.1007/s13351-013-0212-x

Zhao, C., Zhang, Y., Zheng, D., Zhou, Y., Xiao, H. and Zhang, X. (2020). An improved hydrometeor identification method for X-band dual-polarization radar and its application for one summer Hailstorm over Northern China. *Atmospheric Research, 245*, 105075. doi:https://doi.org/10.1016/j.atmosres.2020.105075

Ancillary Activities

- Oral presentation: “Osservazione delle grandinate in Emilia-Romagna combinando misure dallo spazio e da sistemi radar”. Laviola S., Fornasiero A., Celano M., Monte G., Vermi F., Tonnini M., Alberoni P. P. and Levizzani V. V Convegno Nazionale di Radarmeteorologia, Bologna, 07 July 2023.
- Oral presentation: “A multi-sensor technique in support to the nowcasting of severe weather and hailstorms”. Laviola S., Monte G., Vermi F. and Cattani E. 5° Congresso Nazionale AISAM, Lecce, 08 February 2024.
- Oral presentation: “Lightning jump as precursor signature of hail occurrence: first evidence in the Italian territory”. Vermi F., Capozzi V., Monte G., Budillon G. and Laviola S. 5° Congresso Nazionale AISAM, Lecce, 08 February 2024.
- Summer School: “International School on Satellite Meteorology” (ISSM) held by CNR-ISAC, in collaboration with the University of Naples “Parthenope”. Naples, 02-06 September 2024.
- Oral presentation: “Exploring the use of lightning characteristics to improve the radar-based detection of hailstorm severity”. Vermi F., Capozzi V., Monte G., Budillon G. and Laviola S. 12th European Conference on RADar in meteorology and hydrology (ERAD 2024), Rome, 09 September 2024.
- Poster session: “Hailstorm characterization with a synergistic active and passive, GEO and LEO observation strategy”. Cattani E., Vermi F., Monte G., Galfione A., Battaglia A. and Laviola S. European Geoscience Union, General Assembly, Vienna, Austria, 27 April – 02 May 2025.
- Oral presentation: “Multi-sensor Approach for Satellite Hail Advection (MASHA): a new technique to support the nowcasting of hailstorms”. Laviola S., Vermi F., Monte G. and Cattani E. European Geoscience Union, General Assembly, Vienna, Austria, 27 April – 02 May 2025.
- Scientific article publication: “Lightning jump as precursor of very large hail occurrence: first evidence in the Italian territory”. Vermi F., Capozzi V., Monte G., Budillon G. and Laviola S. (2025). Bulletin of Atmospheric Science and Technology. DOI: https://doi.org/10.1007/s42865-025-00104-2 (published on 28 May 2025).
- Summer School: “2nd International School on Satellite Meteorology” (ISSM) held by CNR-ISAC, in collaboration with the University of Naples “Parthenope”. Bologna, 01-05 September 2025.
- Oral presentation: “Monitoraggio dei temporali grandinigeni attraverso la combinazione di tecniche radar e dati di fulminazione”. Vermi F., Capozzi V., Monte G., Budillon G. and Laviola S. VI Convegno Nazionale di Radarmeteorologia (RadMet2025.IT), Milan, 01 October 2025.
- Drafting and publishing: “Weather forecast reports for the Campania Region” on the official website of the University of Naples “Parthenope” (https://meteo.uniparthenope.it/) as a weather forecaster (from January 2023 to October 2025).

Appendix A

This Appendix contains 42 Figures related to the study entitled **"Lightning jump as precursor of very large hail occurrence: first evidence in the Italian territory"** and published on the "Bulletin of Atmospheric Science and Technology" on the 28 May 2025 (Section 4.1). Figures are organized as follows:

1) 40 Figures replicating Fig. 50 in Section 4.1.3 for every case study examined in the paper: for each hail event, four plots about the total lightning vs maximum hail diameter and the LJ timeseries at 20, 30 and 40 minutes are provided.

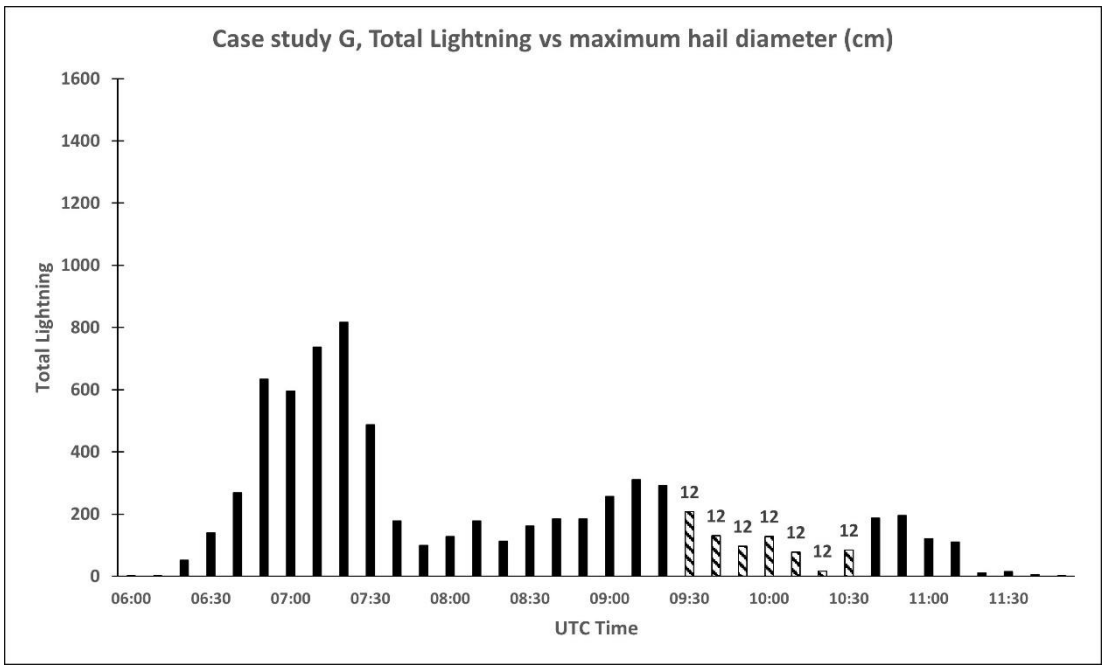

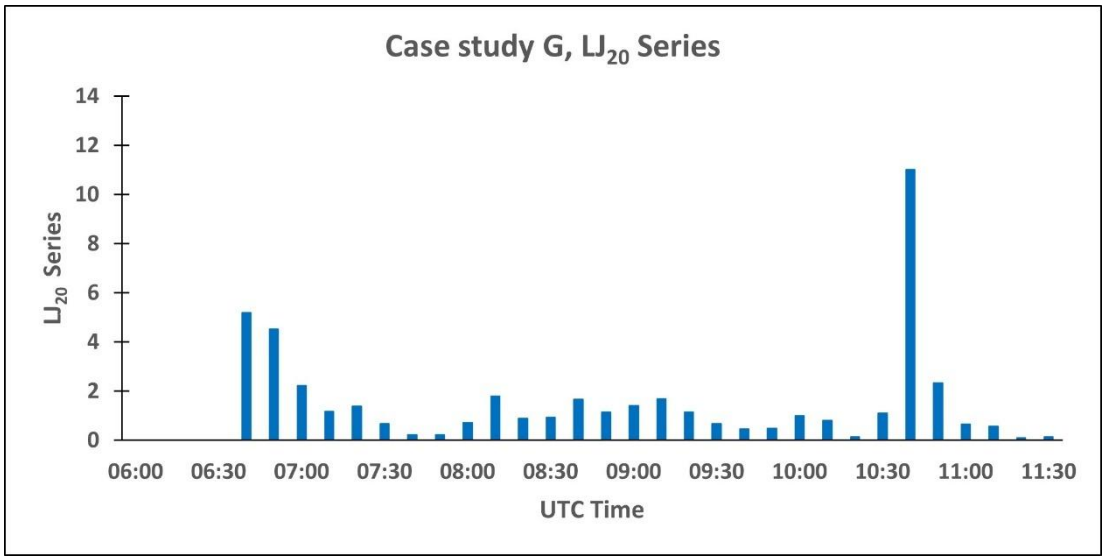

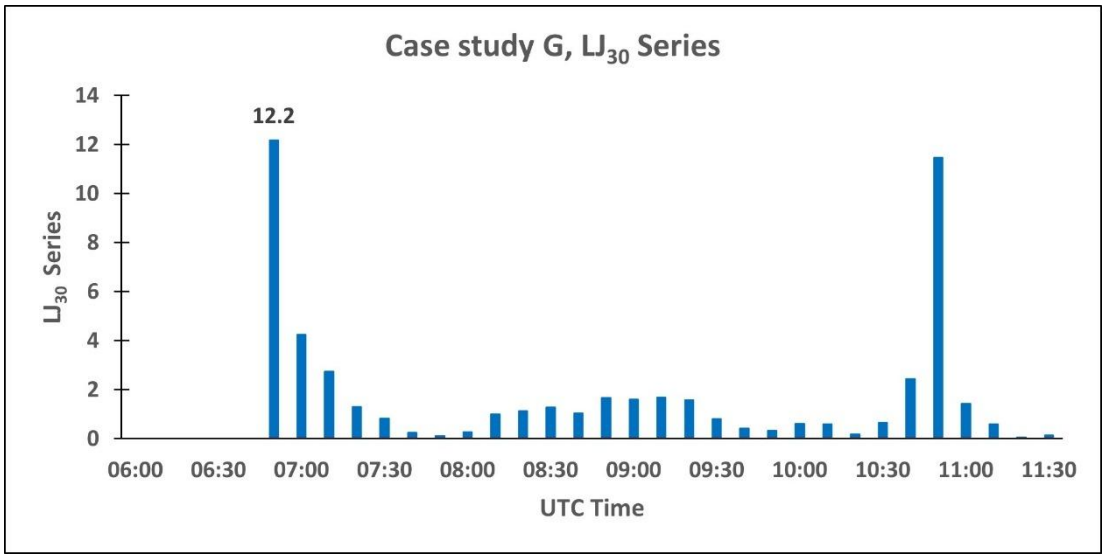
Case study G, LJ30 Series
12.2
LJ30 Series
0
2
4
6
8
10
12
14
06:00
06:30
07:00
07:30
08:00
08:30
09:00
09:30
10:00
10:30
11:00
11:30
UTC Time

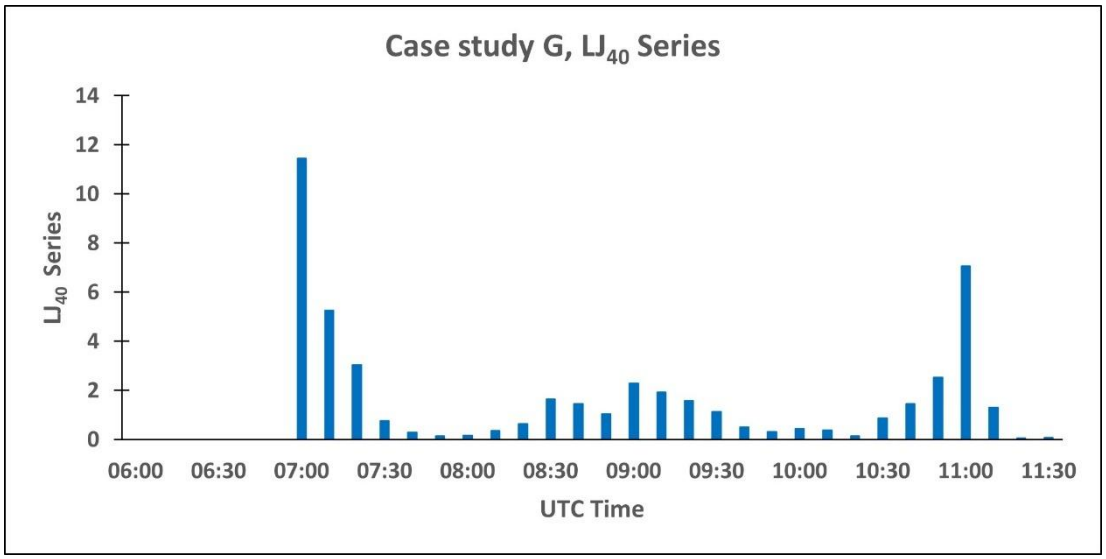
Case study G, LJ40 Series
LJ40 Series
0
2
4
6
8
10
12
14
06:00
06:30
07:00
07:30
08:00
08:30
09:00
09:30
10:00
10:30
11:00
11:30
UTC Time

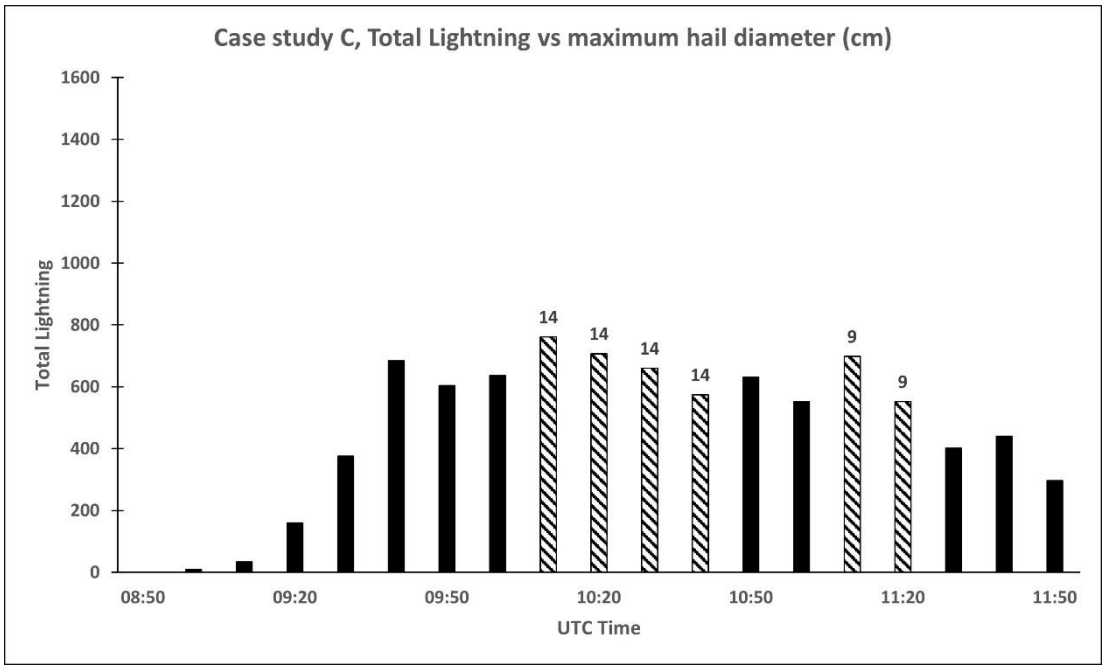
Case study C, Total Lightning vs maximum hail diameter (cm)
Total Lightning
0
200
400
600
800
1000
1200
1400
1600
14
14
14
14
9
9
08:50
09:20
09:50
10:20
10:50
11:20
11:50
UTC Time

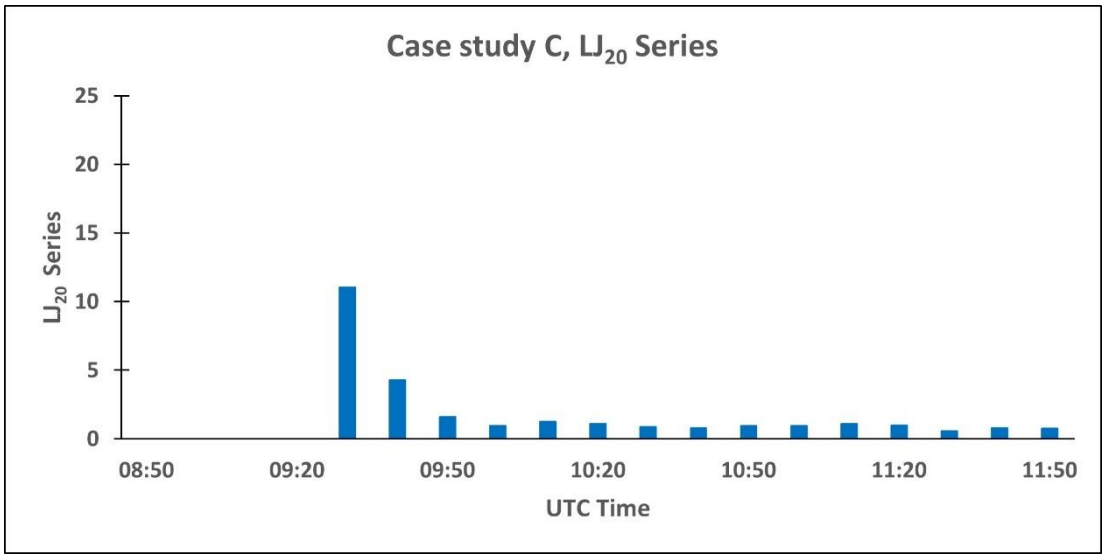
Case study C, LJ20 Series
LJ20 Series
25
20
15
10
5
0
08:50
09:20
09:50
10:20
10:50
11:20
11:50
UTC Time

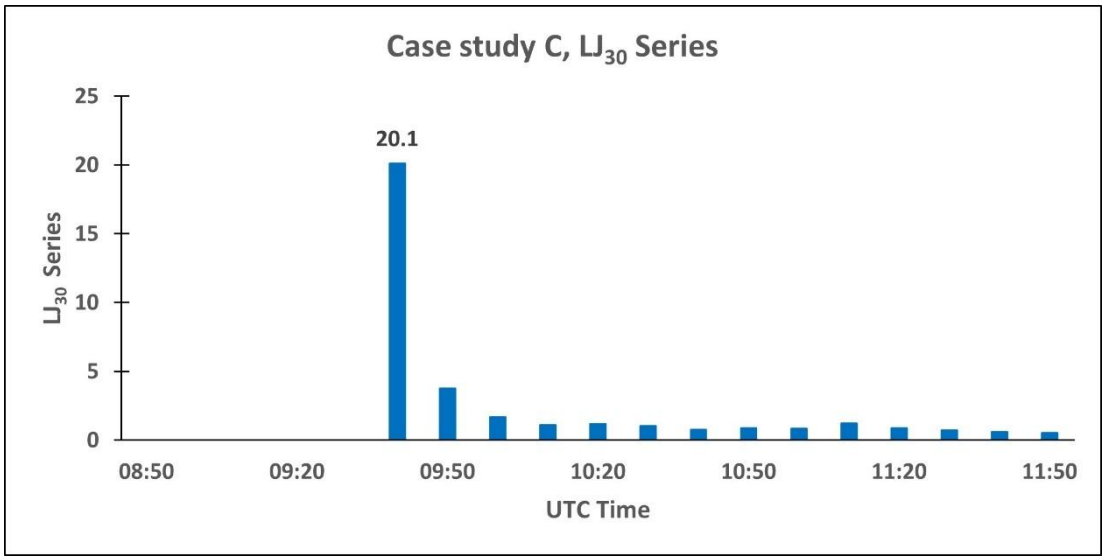
Case study C, LJ30 Series
LJ30 Series
20.1
25
20
15
10
5
0
08:50
09:20
09:50
10:20
10:50
11:20
11:50
UTC Time

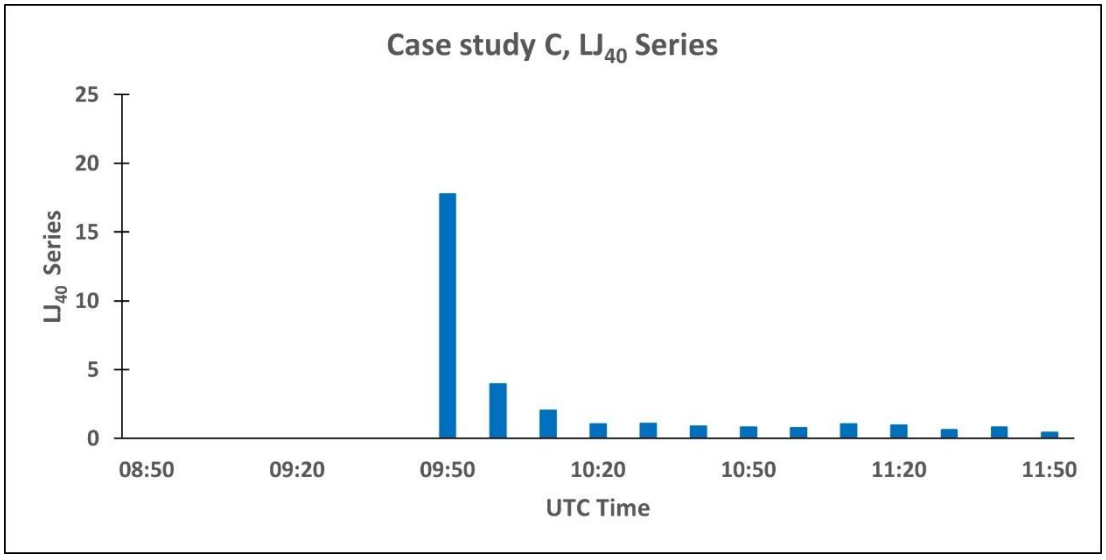
Case study C, LJ40 Series
LJ40 Series
25
20
15
10
5
0
08:50
09:20
09:50
10:20
10:50
11:20
11:50
UTC Time

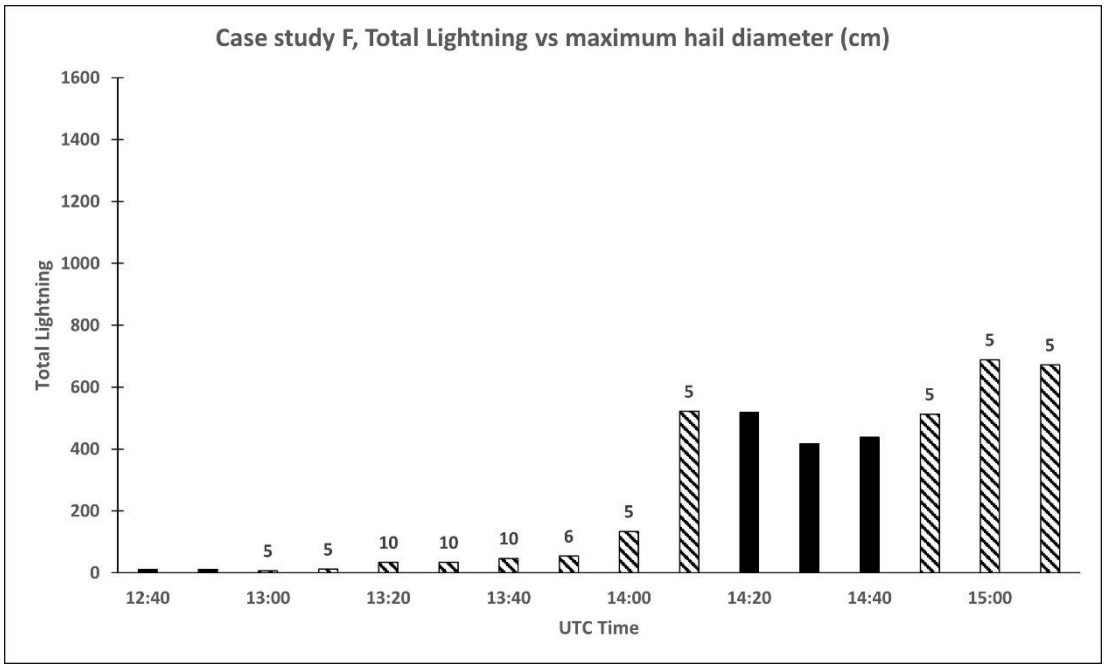
Case study F, Total Lightning vs maximum hail diameter (cm)
Total Lightning
1600
1400
1200
1000
800
600
400
200
0
5
5
10
10
10
6
5
5
5
5
5
12:40
13:00
13:20
13:40
14:00
14:20
14:40
15:00
UTC Time

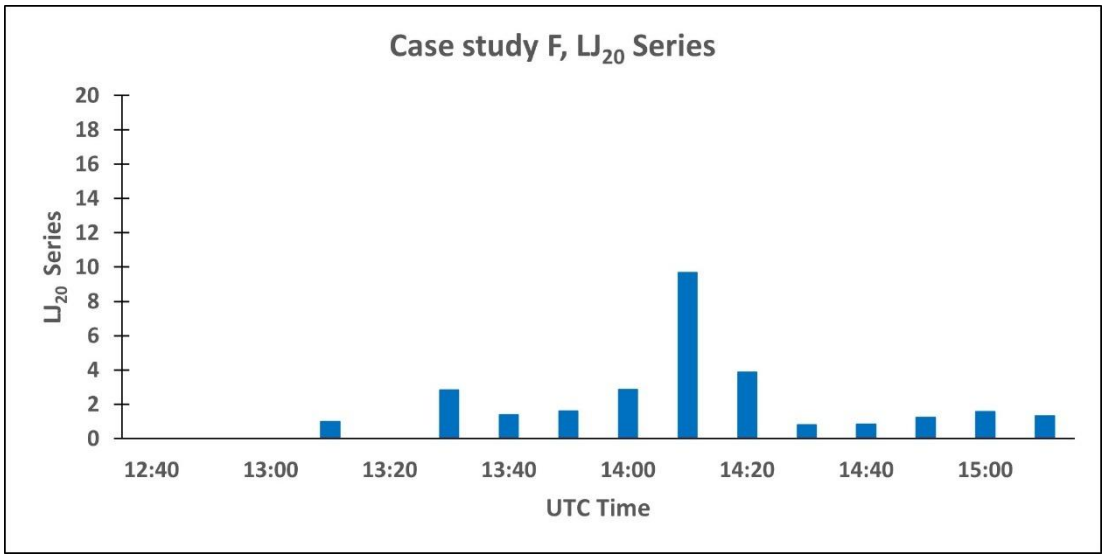
Case study F, LJ20 Series
LJ20 Series
20
18
16
14
12
10
8
6
4
2
0
12:40
13:00
13:20
13:40
14:00
14:20
14:40
15:00
UTC Time

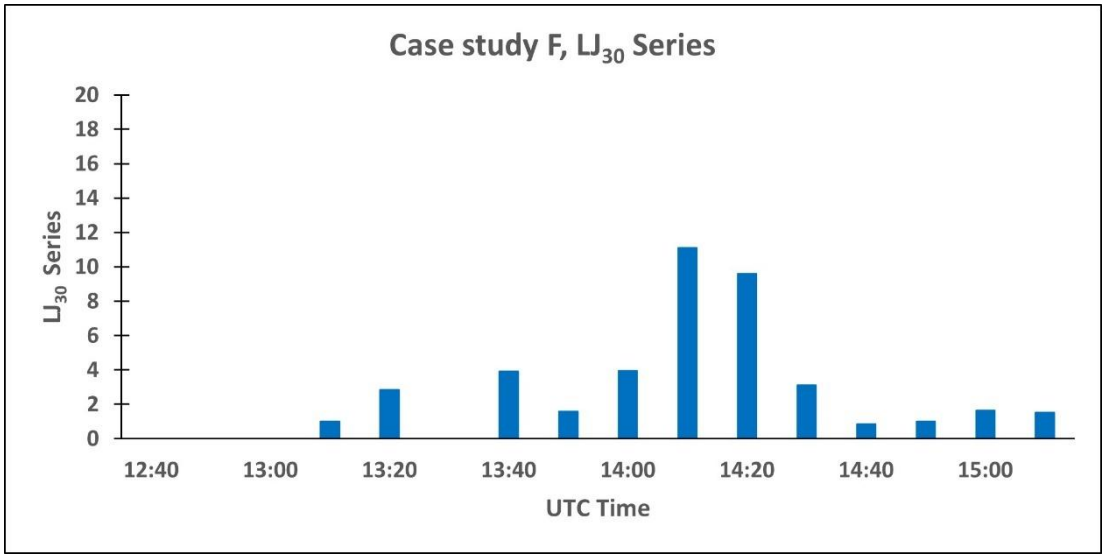
Case study F, LJ30 Series
LJ30 Series
20
18
16
14
12
10
8
6
4
2
0
12:40
13:00
13:20
13:40
14:00
14:20
14:40
15:00
UTC Time

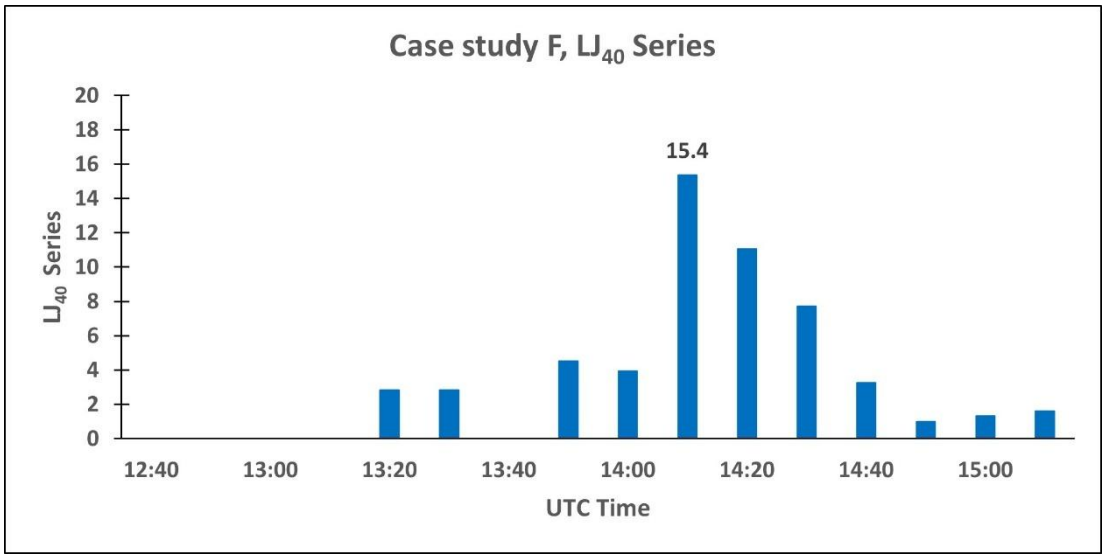
Case study F, LJ40 Series
LJ40 Series
20
18
16
14
12
10
8
6
4
2
0
15.4
12:40
13:00
13:20
13:40
14:00
14:20
14:40
15:00
UTC Time

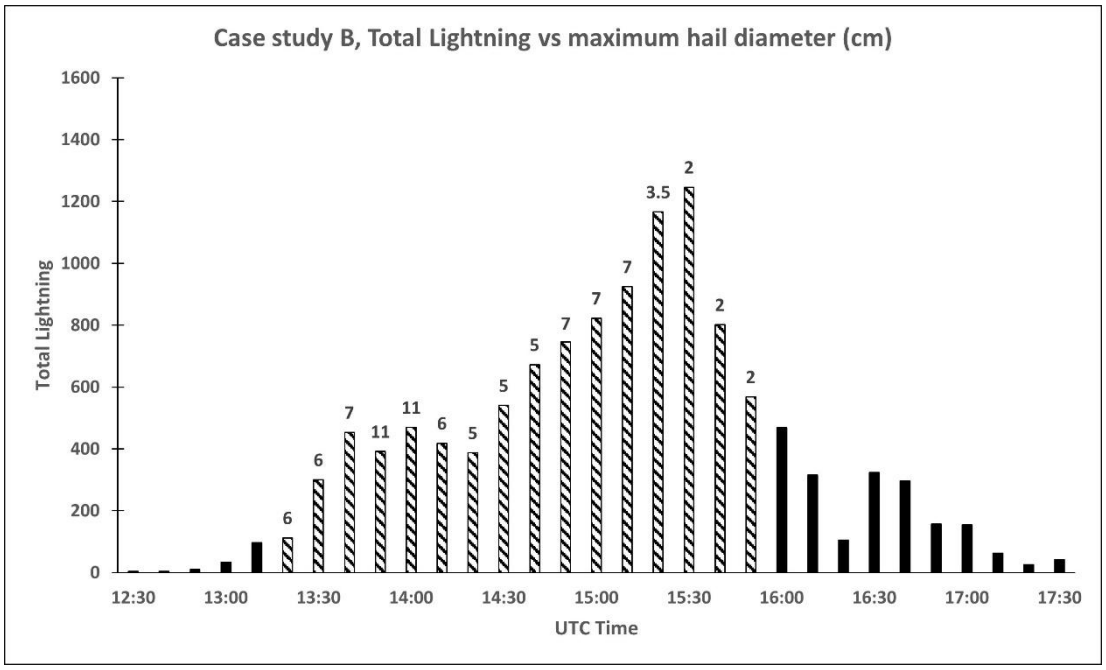
Case study B, Total Lightning vs maximum hail diameter (cm)
Total Lightning
1600
1400
1200
1000
800
600
400
200
0
6
6
7
11
11
6
5
5
7
7
7
3.5
2
2
2
12:30
13:00
13:30
14:00
14:30
15:00
15:30
16:00
16:30
17:00
17:30
UTC Time

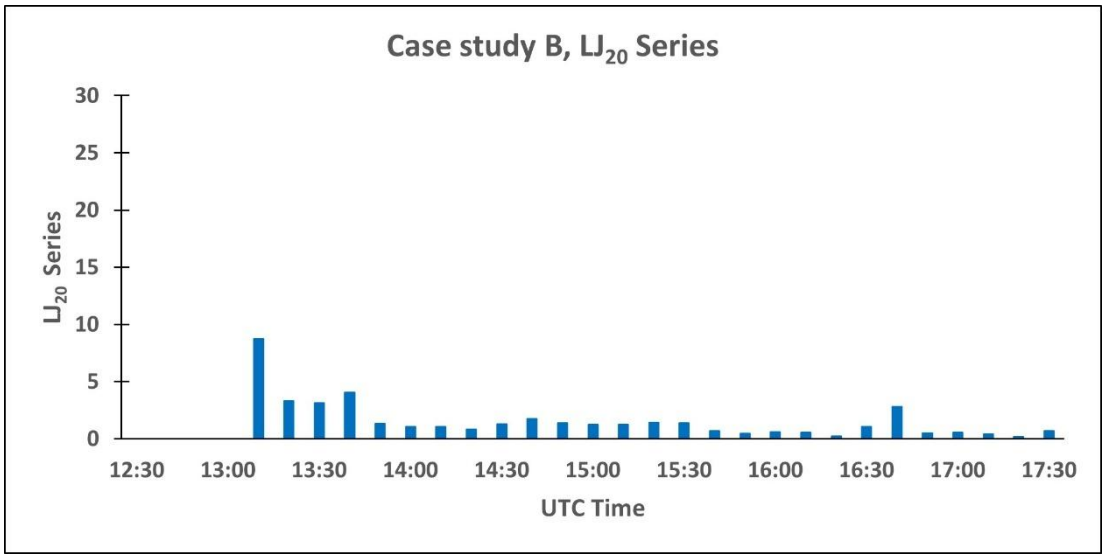
Case study B, LJ20 Series
LJ20 Series
30
25
20
15
10
5
0
12:30
13:00
13:30
14:00
14:30
15:00
15:30
16:00
16:30
17:00
17:30
UTC Time

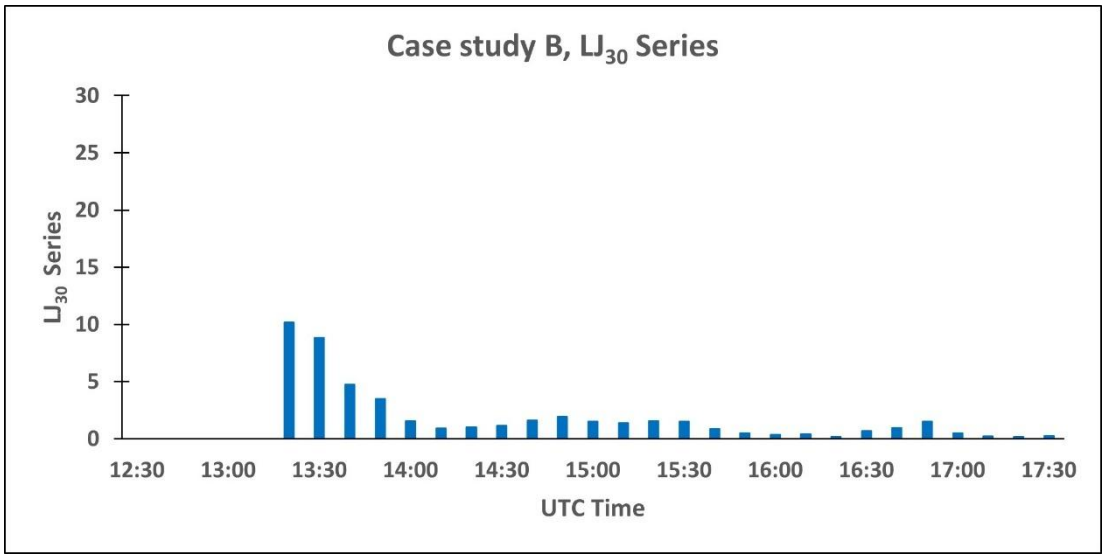
Case study B, LJ30 Series
LJ30 Series
30
25
20
15
10
5
0
12:30
13:00
13:30
14:00
14:30
15:00
15:30
16:00
16:30
17:00
17:30
UTC Time

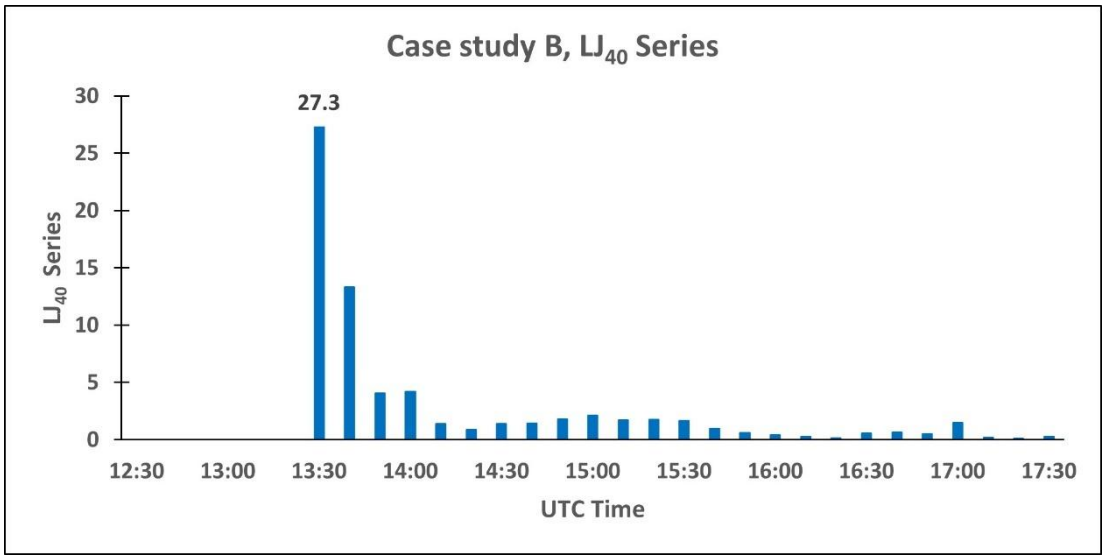
Case study B, LJ40 Series
LJ40 Series
27.3
30
25
20
15
10
5
0
12:30
13:00
13:30
14:00
14:30
15:00
15:30
16:00
16:30
17:00
17:30
UTC Time

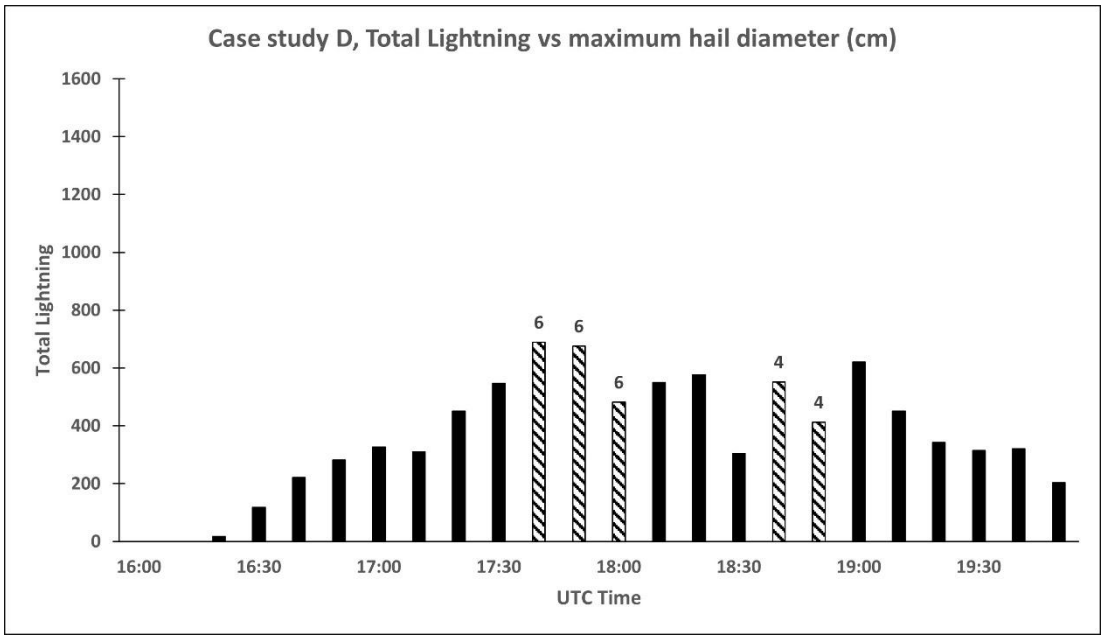
Case study D, Total Lightning vs maximum hail diameter (cm)
Total Lightning
1600
1400
1200
1000
800
600
400
200
0
6
6
6
4
4
16:00
16:30
17:00
17:30
18:00
18:30
19:00
19:30
UTC Time

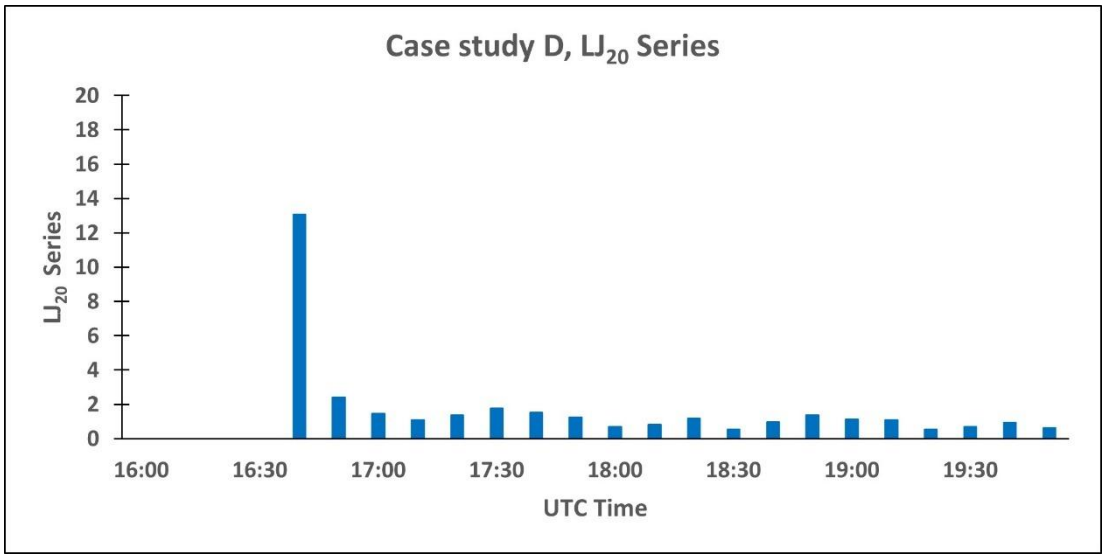
Case study D, LJ20 Series
LJ20 Series
20
18
16
14
12
10
8
6
4
2
0
16:00
16:30
17:00
17:30
18:00
18:30
19:00
19:30
UTC Time

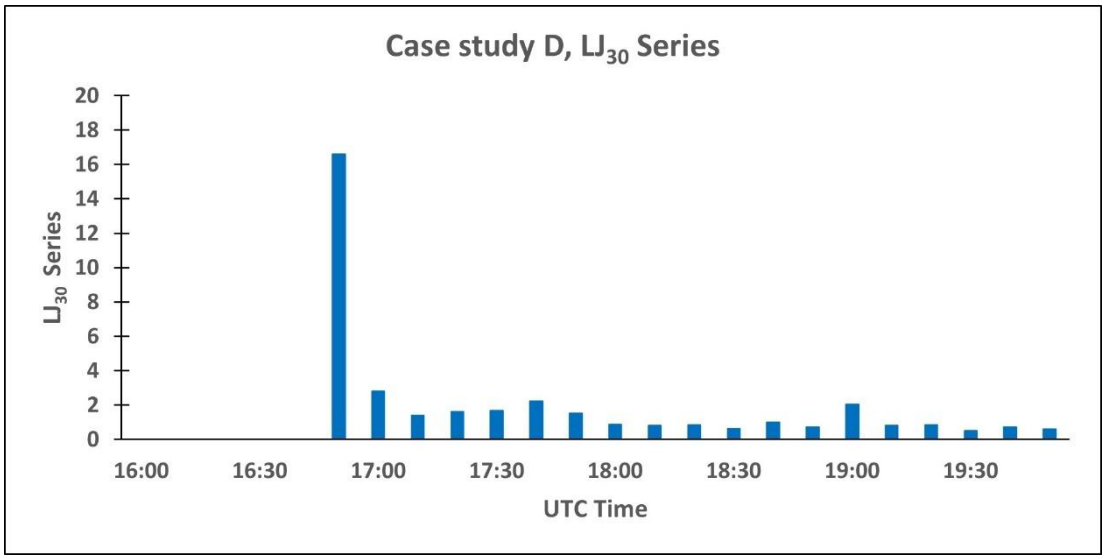
Case study D, LJ30 Series
LJ30 Series
20
18
16
14
12
10
8
6
4
2
0
16:00
16:30
17:00
17:30
18:00
18:30
19:00
19:30
UTC Time

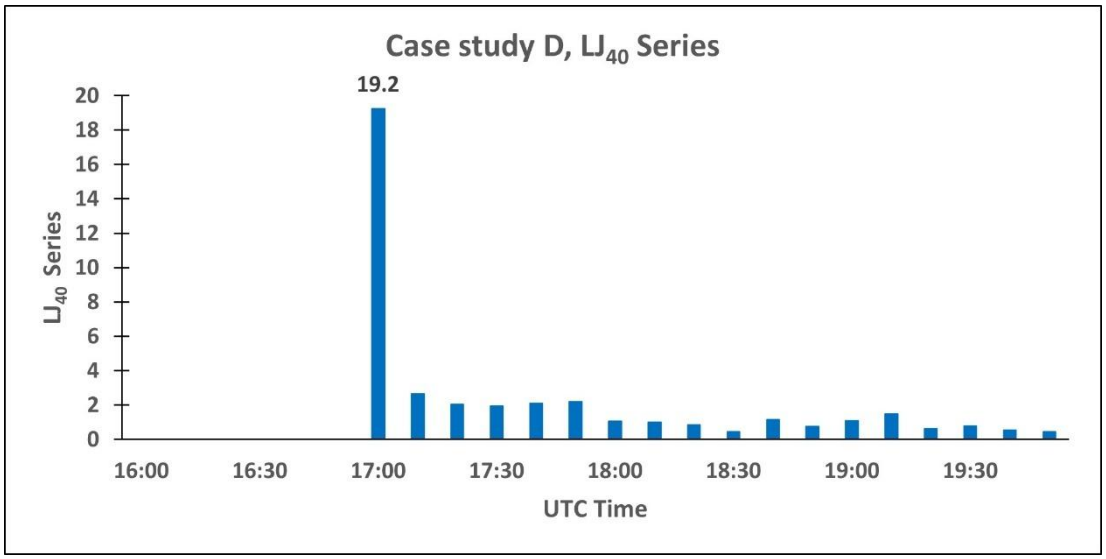
Case study D, LJ40 Series
19.2
LJ40 Series
20
18
16
14
12
10
8
6
4
2
0
16:00
16:30
17:00
17:30
18:00
18:30
19:00
19:30
UTC Time

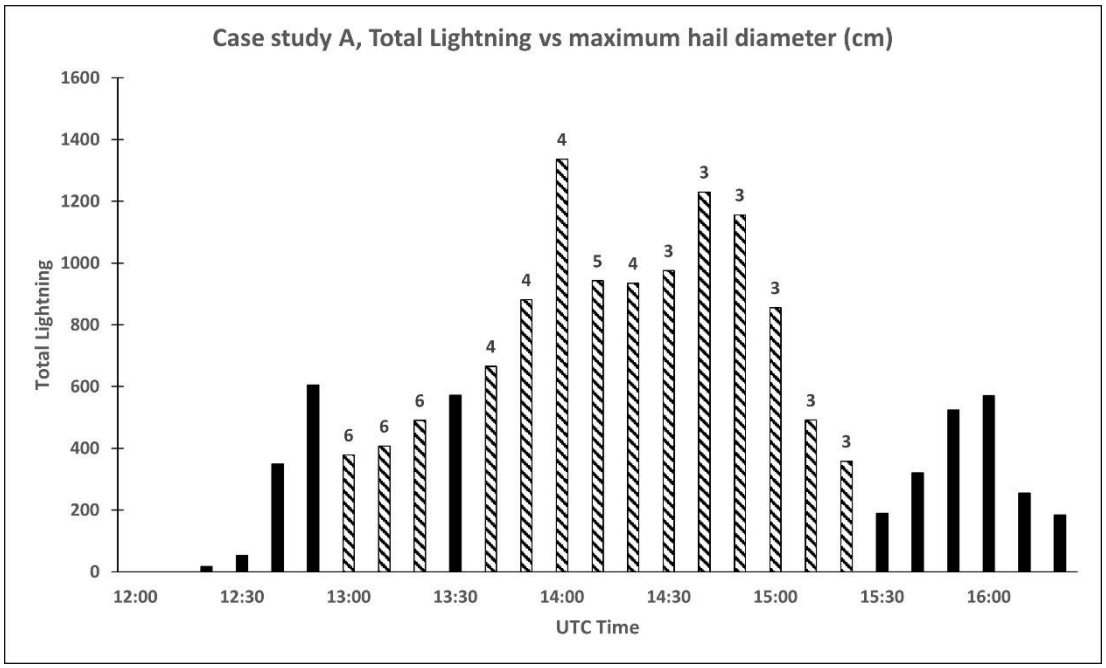
Case study A, Total Lightning vs maximum hail diameter (cm)
Total Lightning
1600
1400
1200
1000
800
600
400
200
0
6
6
6
4
4
4
5
4
3
3
3
3
3
12:00
12:30
13:00
13:30
14:00
14:30
15:00
15:30
16:00
UTC Time

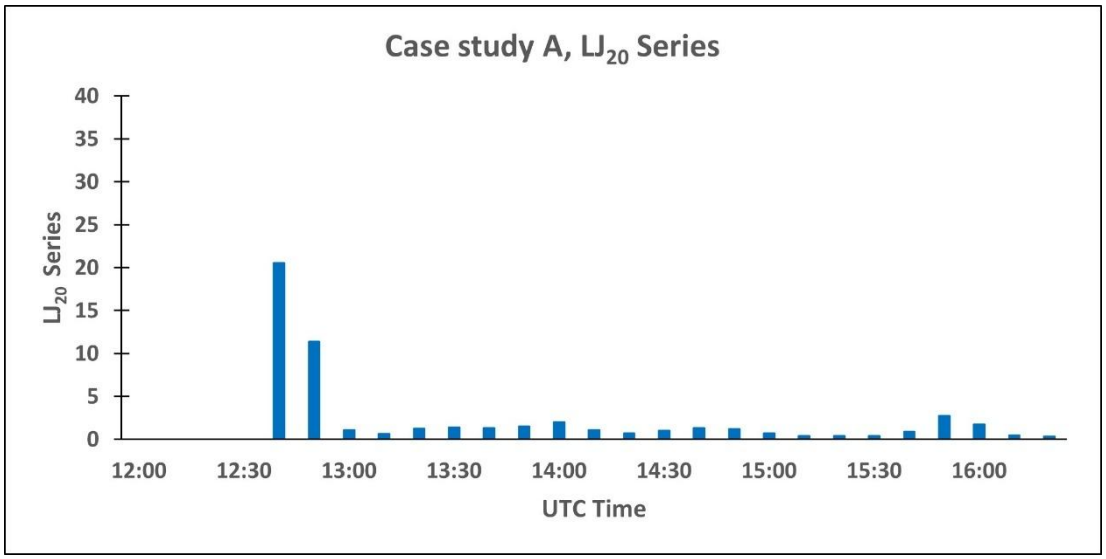
Case study A, LJ20 Series
LJ20 Series
40
35
30
25
20
15
10
5
0
12:00
12:30
13:00
13:30
14:00
14:30
15:00
15:30
16:00
UTC Time

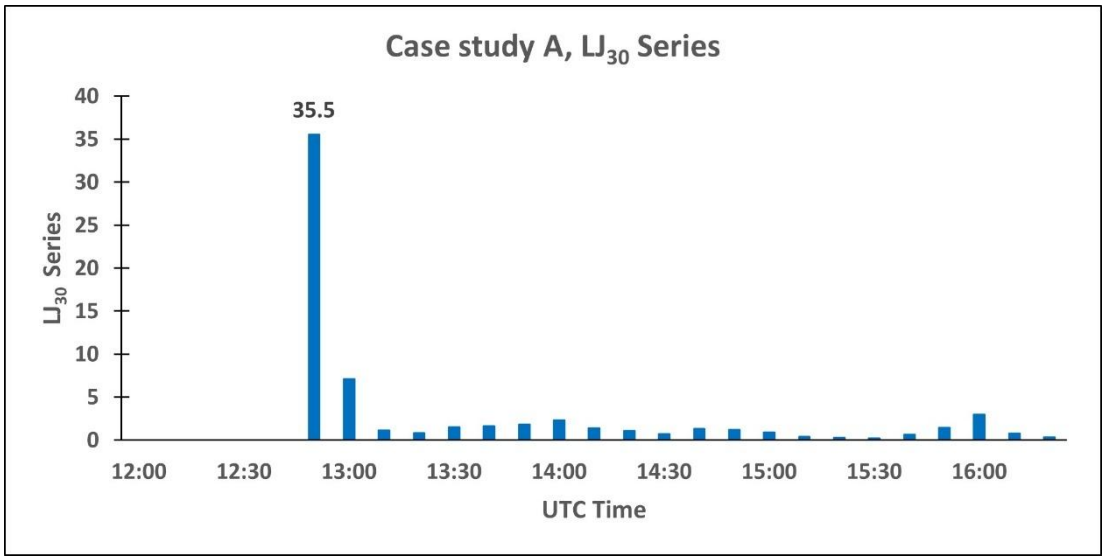
Case study A, LJ30 Series
LJ30 Series
35.5
40
35
30
25
20
15
10
5
0
12:00
12:30
13:00
13:30
14:00
14:30
15:00
15:30
16:00
UTC Time

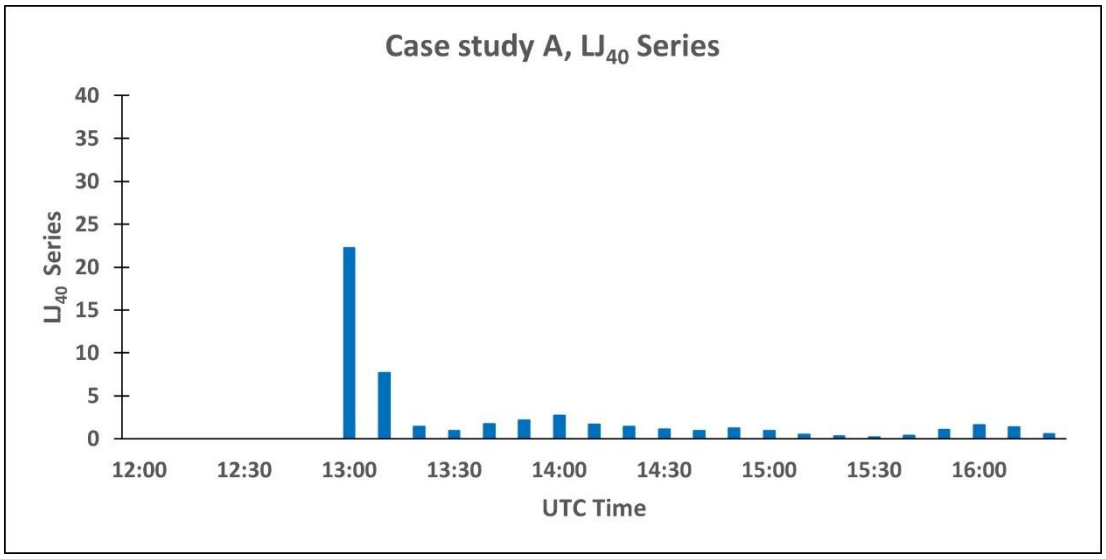
Case study A, LJ40 Series
LJ40 Series
40
35
30
25
20
15
10
5
0
12:00
12:30
13:00
13:30
14:00
14:30
15:00
15:30
16:00
UTC Time

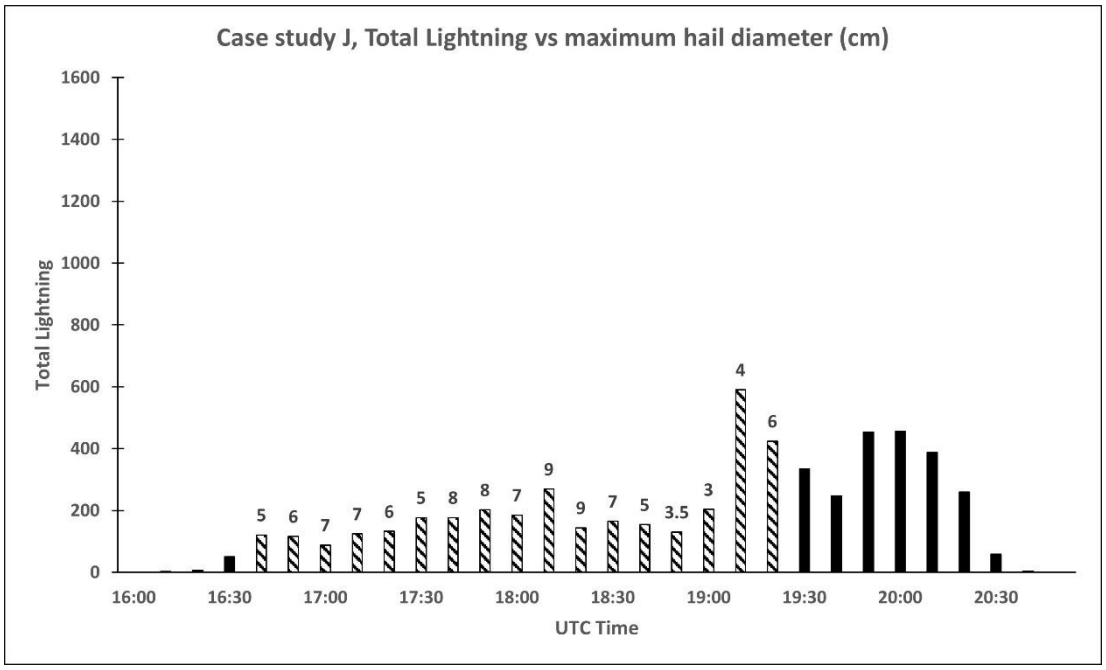
Case study J, Total Lightning vs maximum hail diameter (cm)
Total Lightning
1600
1400
1200
1000
800
600
400
200
0
5
6
7
7
6
5
8
8
7
9
9
7
5
3.5
3
4
6
16:00
16:30
17:00
17:30
18:00
18:30
19:00
19:30
20:00
20:30
UTC Time

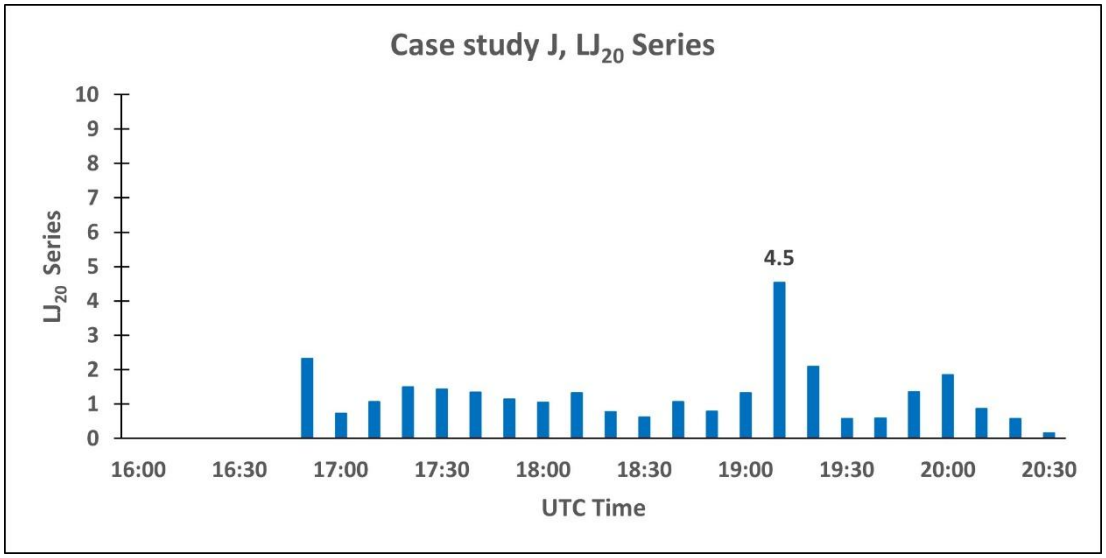
Case study J, LJ20 Series
LJ20 Series
10
9
8
7
6
5
4
3
2
1
0
4.5
16:00
16:30
17:00
17:30
18:00
18:30
19:00
19:30
20:00
20:30
UTC Time

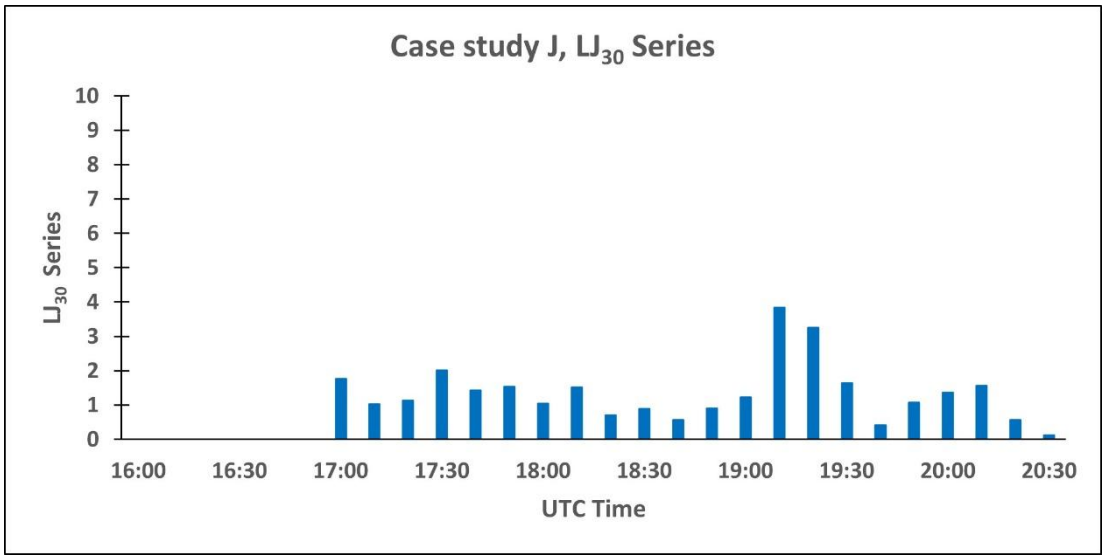
Case study J, LJ30 Series
LJ30 Series
10
9
8
7
6
5
4
3
2
1
0
16:00
16:30
17:00
17:30
18:00
18:30
19:00
19:30
20:00
20:30
UTC Time

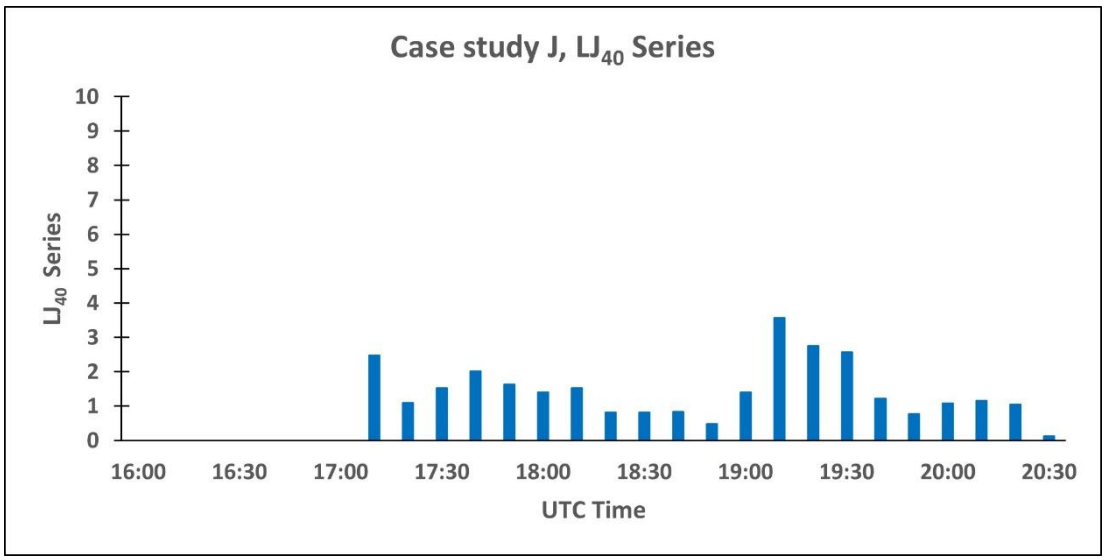
Case study J, LJ40 Series
LJ40 Series
10
9
8
7
6
5
4
3
2
1
0
16:00
16:30
17:00
17:30
18:00
18:30
19:00
19:30
20:00
20:30
UTC Time

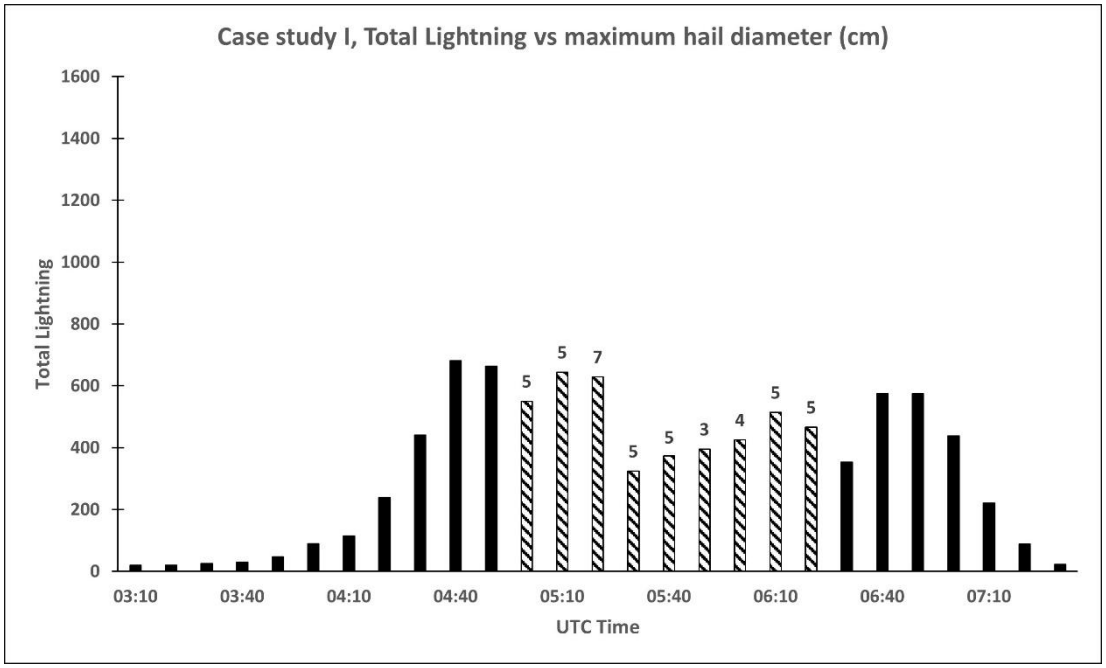
Case study I, Total Lightning vs maximum hail diameter (cm)
Total Lightning
1600
1400
1200
1000
800
600
400
200
0
5
5
7
5
5
3
4
5
5
03:10
03:40
04:10
04:40
05:10
05:40
06:10
06:40
07:10
UTC Time

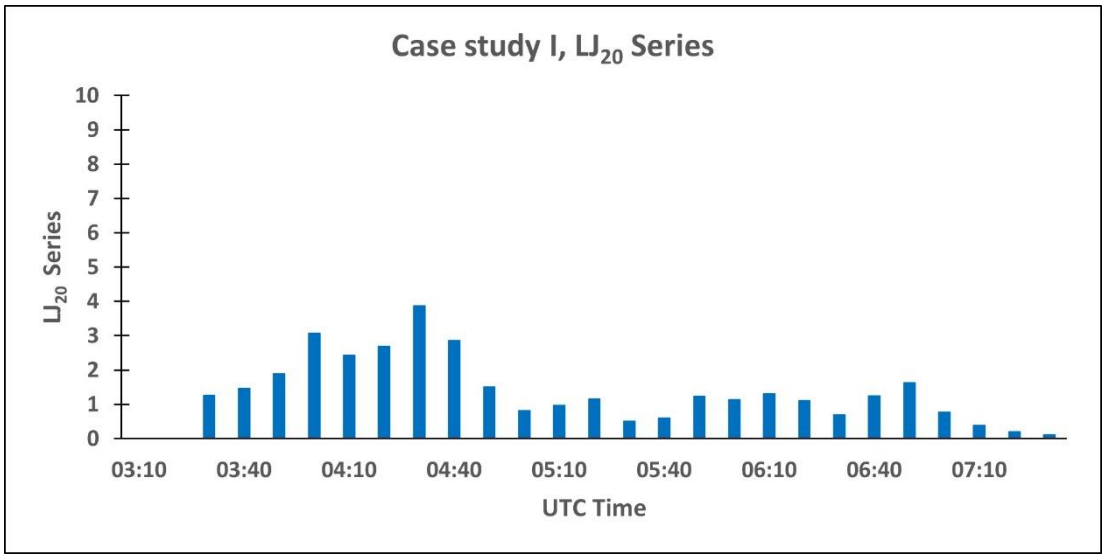
Case study I, LJ20 Series
LJ20 Series
10
9
8
7
6
5
4
3
2
1
0
03:10
03:40
04:10
04:40
05:10
05:40
06:10
06:40
07:10
UTC Time

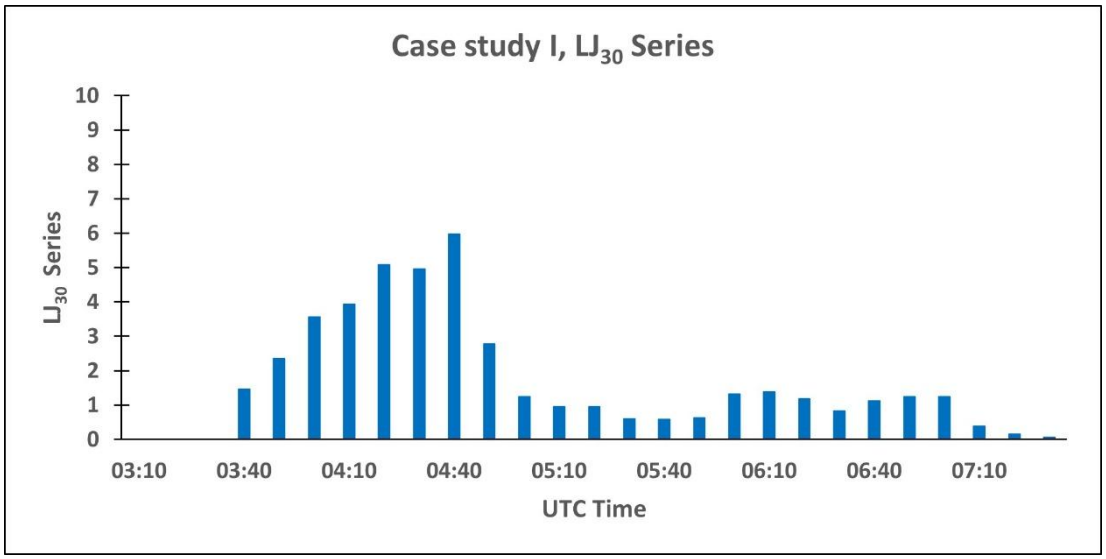
Case study I, LJ30 Series
LJ30 Series
10
9
8
7
6
5
4
3
2
1
0
03:10
03:40
04:10
04:40
05:10
05:40
06:10
06:40
07:10
UTC Time

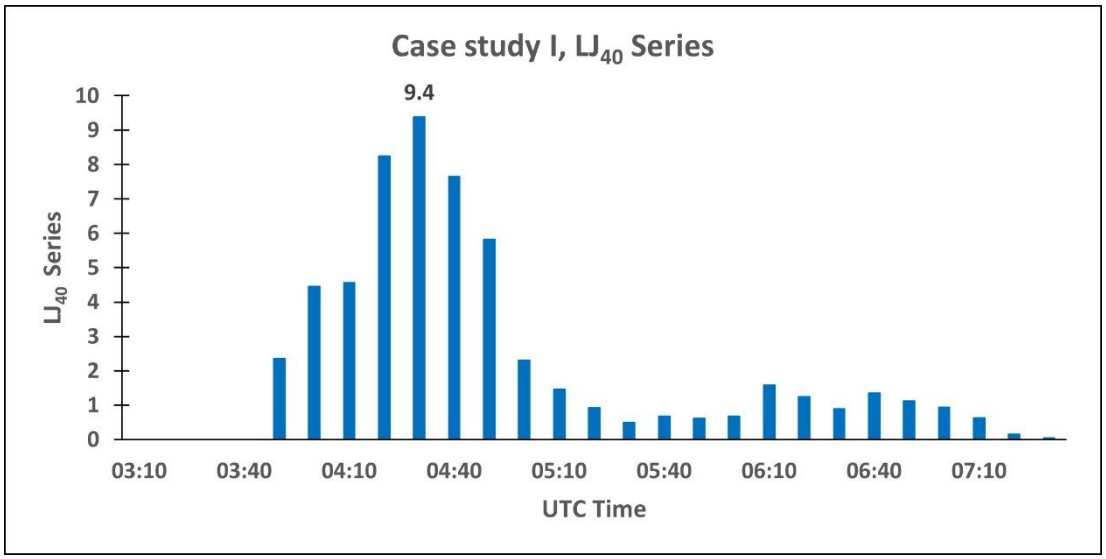
Case study I, LJ40 Series
9.4
LJ40 Series
10
9
8
7
6
5
4
3
2
1
0
03:10
03:40
04:10
04:40
05:10
05:40
06:10
06:40
07:10
UTC Time

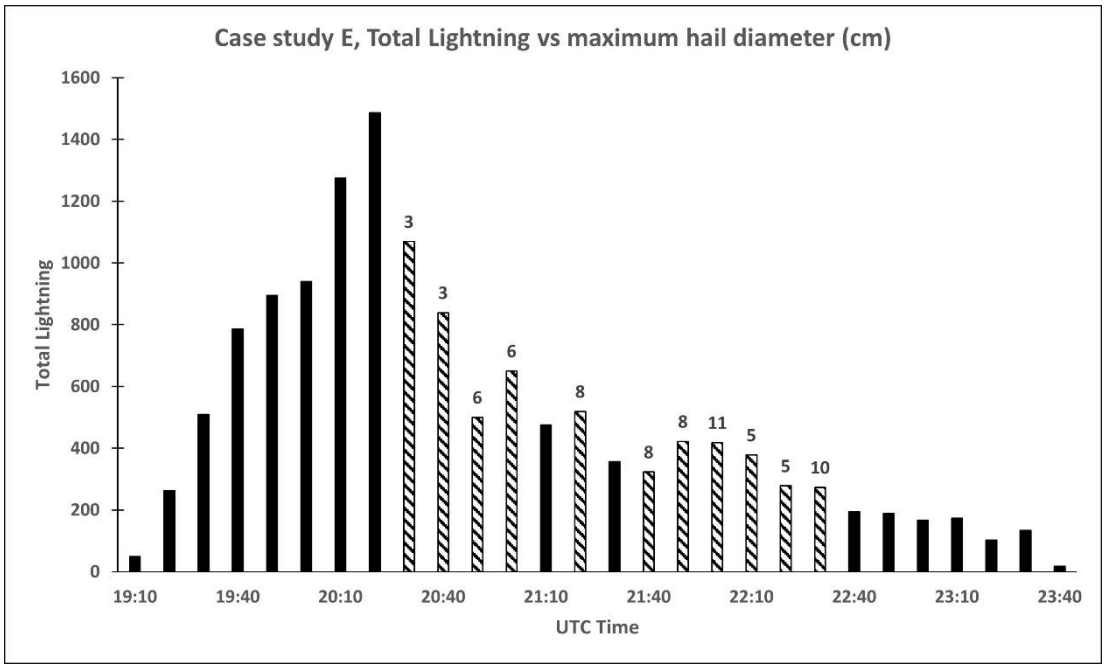
Case study E, Total Lightning vs maximum hail diameter (cm)
Total Lightning
1600
1400
1200
1000
800
600
400
200
0
3
3
6
6
8
8
8
11
5
5
10
19:10
19:40
20:10
20:40
21:10
21:40
22:10
22:40
23:10
23:40
UTC Time

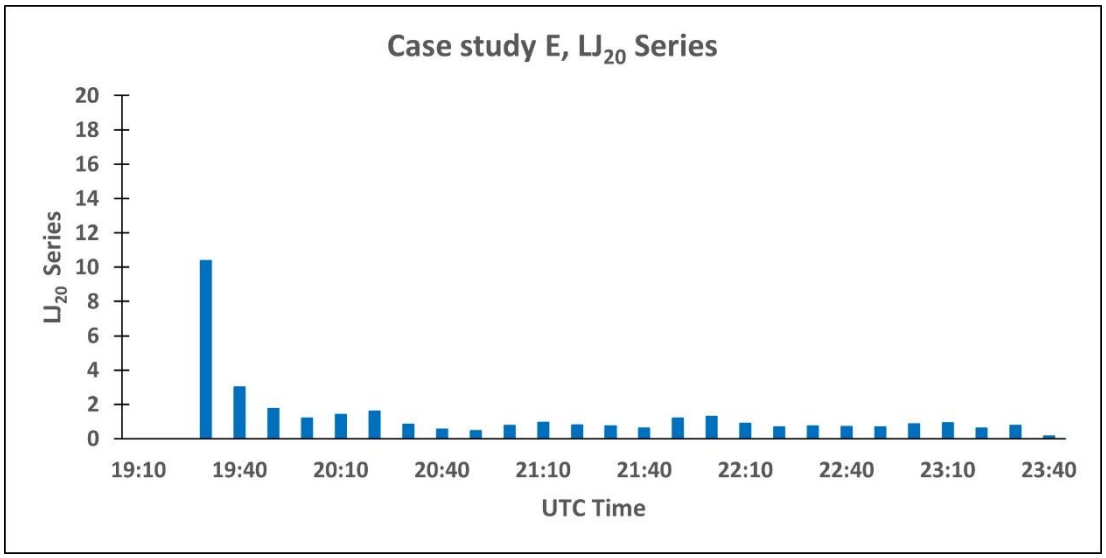
Case study E, LJ20 Series
LJ20 Series
20
18
16
14
12
10
8
6
4
2
0
19:10
19:40
20:10
20:40
21:10
21:40
22:10
22:40
23:10
23:40
UTC Time

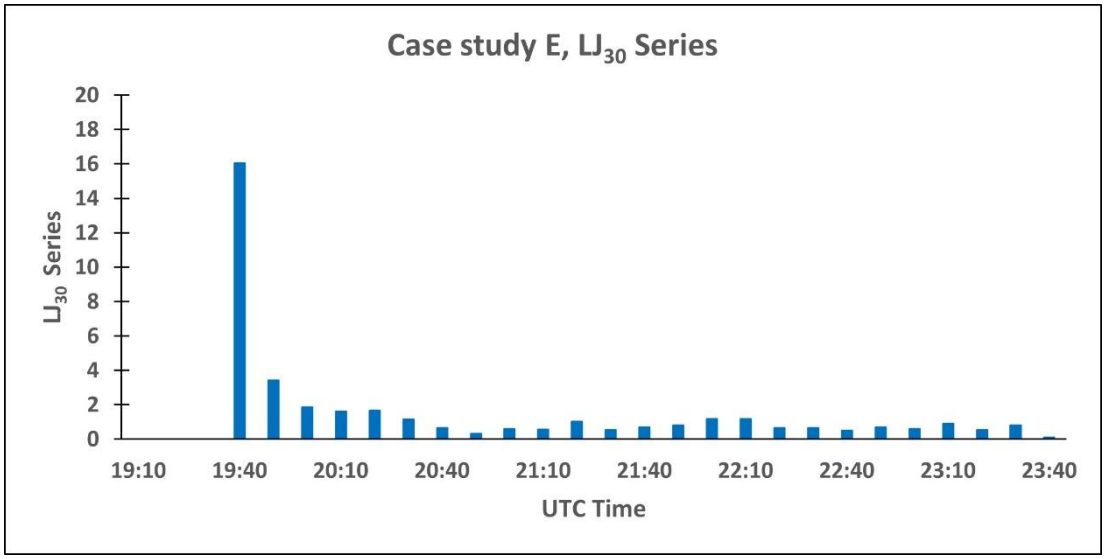
Case study E, LJ30 Series
LJ30 Series
20
18
16
14
12
10
8
6
4
2
0
19:10
19:40
20:10
20:40
21:10
21:40
22:10
22:40
23:10
23:40
UTC Time

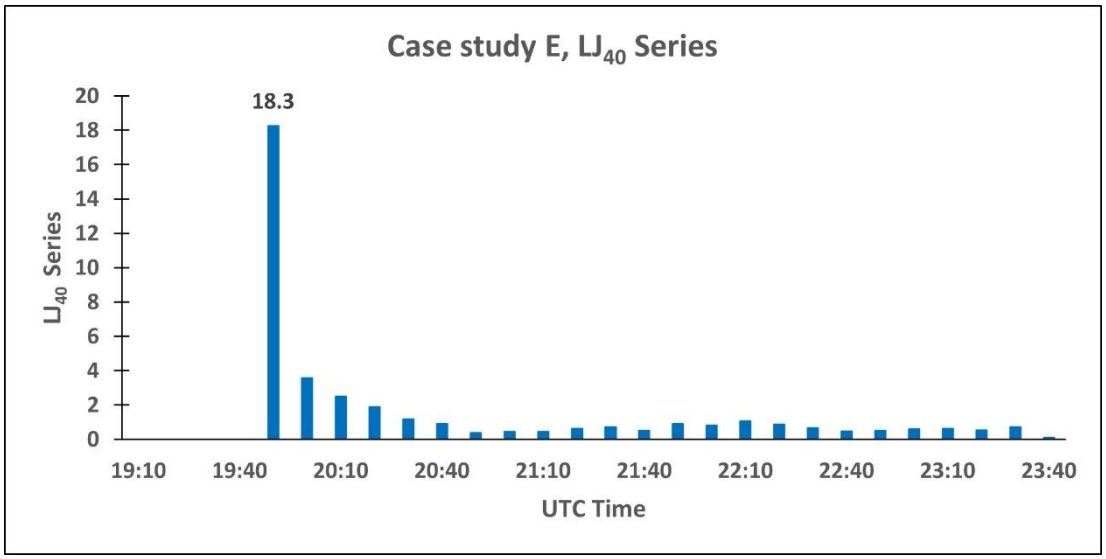
Case study E, LJ40 Series
18.3
LJ40 Series
20
18
16
14
12
10
8
6
4
2
0
19:10
19:40
20:10
20:40
21:10
21:40
22:10
22:40
23:10
23:40
UTC Time

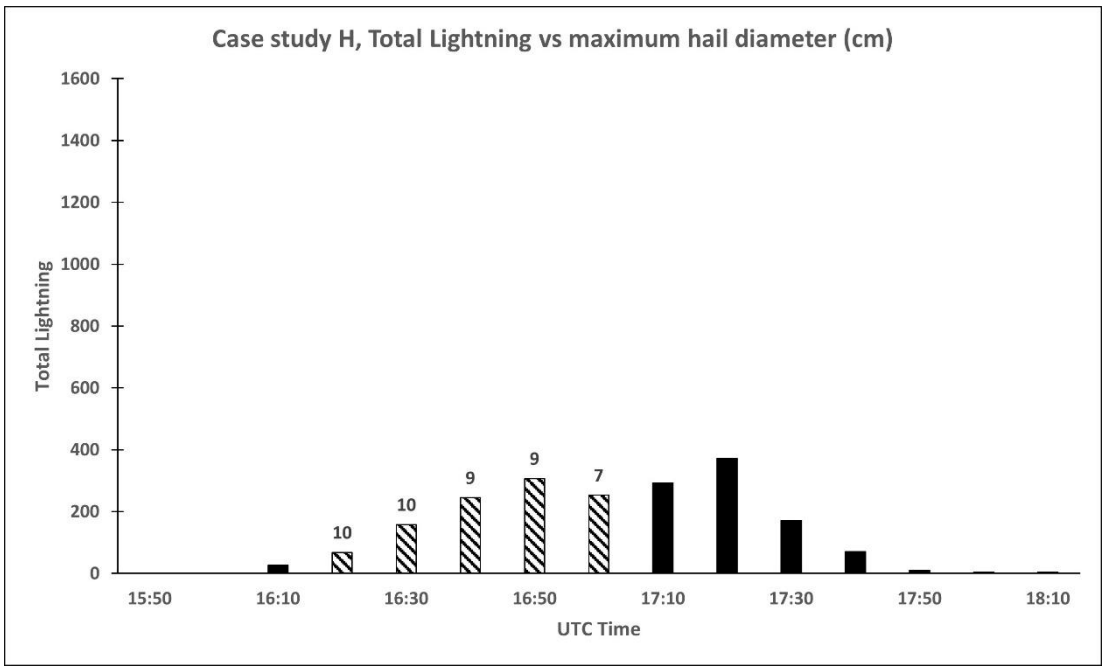
Case study H, Total Lightning vs maximum hail diameter (cm)
Total Lightning
1600
1400
1200
1000
800
600
400
200
0
10
10
9
9
7
15:50
16:10
16:30
16:50
17:10
17:30
17:50
18:10
UTC Time

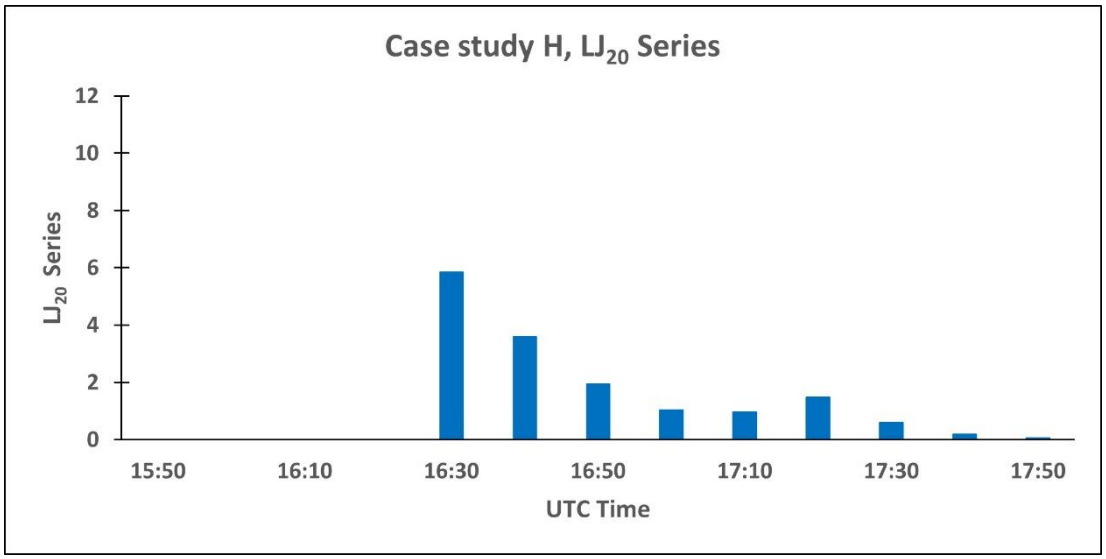
Case study H, LJ20 Series
LJ20 Series
12
10
8
6
4
2
0
15:50
16:10
16:30
16:50
17:10
17:30
17:50
UTC Time

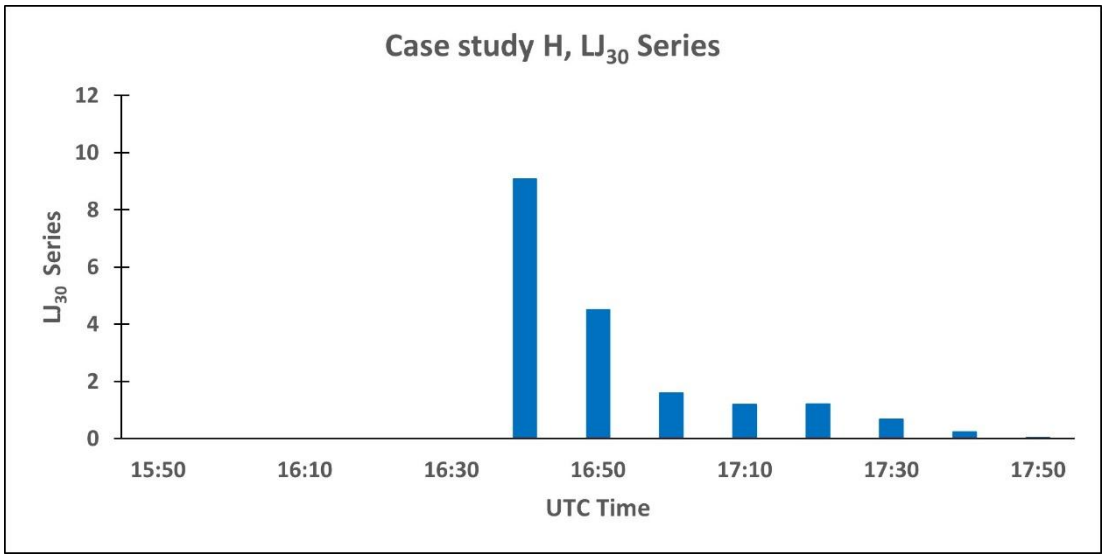
Case study H, LJ30 Series
12
10
8
6
4
2
0
LJ30 Series
15:50
16:10
16:30
16:50
17:10
17:30
17:50
UTC Time

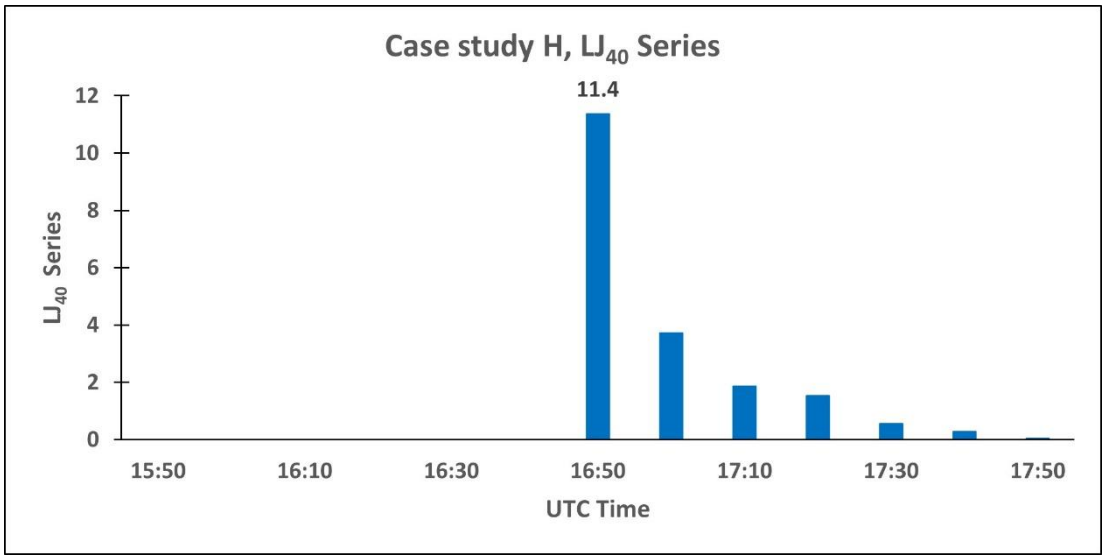
Case study H, LJ40 Series
11.4
12
10
8
6
4
2
0
LJ40 Series
15:50
16:10
16:30
16:50
17:10
17:30
17:50
UTC Time

2) 2 Figures showing the analysis performed to establish if the growth rate of strokes, in case studies D and I, can be approximated with a linear or an exponential trend.

Coefficient of determination R^2: 0.96106

Results of the hypothesis test:

Estimated slope (beta1): 7.1976
Standard error (SE_beta1): 0.51221
t-statistic: 14.0519
p-value: 6.3859e-07
Conclusion: The slope is significantly different from zero.

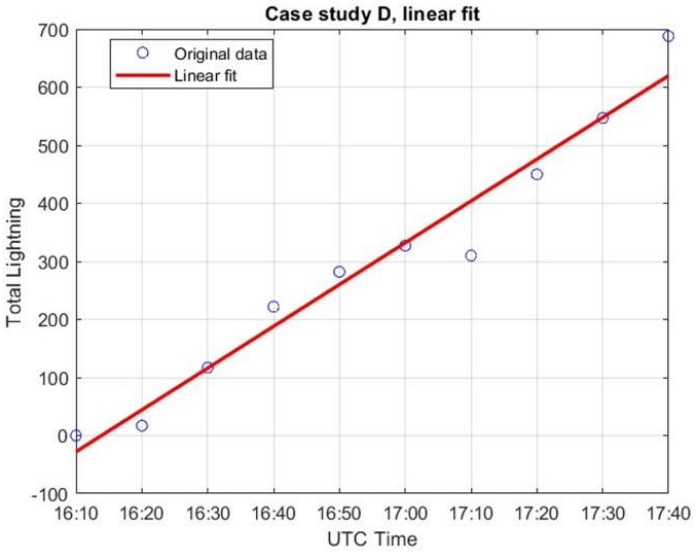

Coefficient of determination R^2: 0.92313

Results of the hypothesis test:

Estimated Growth/Decay Rate (b): 0.042083
Standard error of b (SE_b): 0.0033318
t-statistic: 12.6306
p-value: 1.4498e-06
Conclusion: The growth/decay rate is significantly different from zero.

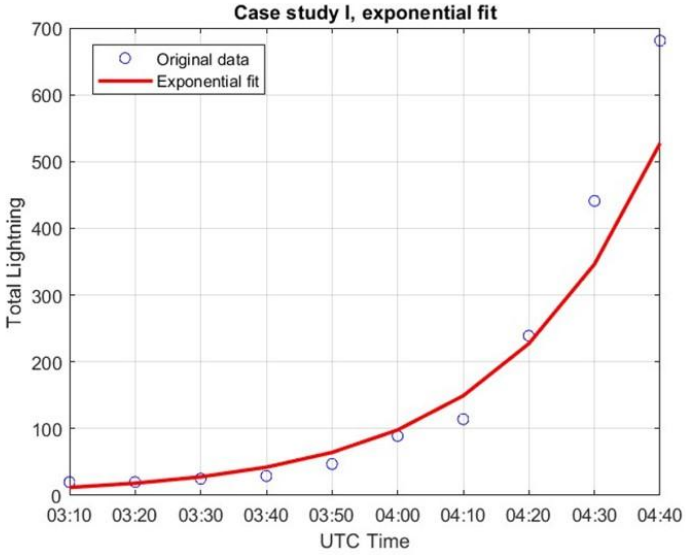

Appendix B

In this Appendix, we provide the following table containing the hail reports used in the study entitled: "**Exploring the use of lightning characteristics to improve the radar-based detection of hailstorm severity**" for the comparison between the VILD and the LJ methods (Section 6.2.2).

Date	UTC Time	Temporal uncertainty (min)	Latitude (°)	Longitude (°)	Location (District)	Maximum hail diameter (cm)
20-11-2018	12:30	± 30.0	40.65	14.64	Maiori (SA)	4
04-07-2019	14:00	± 15.0	41.21	15.56	Ascoli Satriano (FG)	4
04-07-2019	13:30	± 15.0	41.01	15.38	Bisaccia (AV)	2
10-07-2019	11:00	± 5.0	41.47	14.04	Venafro (IS)	6
19-05-2020	19:50	± 5.0	40.91	15.72	Ripacandida (PZ)	3
01-08-2020	14:00	± 5.0	41.02	14.84	Montefusco (AV)	3
01-08-2020	14:15	± 30.0	41.02	15.02	Fontanarosa (AV)	2
01-08-2020	14:30	± 15.0	41.04	15.00	Mirabella Eclano (AV)	2
15-08-2020	15:00	± 15.0	41.32	15.16	Faeto (FG)	2
15-10-2020	09:00	± 5.0	40.84	14.05	Bacoli (NA)	4
15-10-2020	09:06	± 1.0	40.84	14.09	Pozzuoli (NA)	4
15-10-2020	10:00	± 15.0	41.08	14.54	Moiano (BN)	2
15-10-2020	13:00	± 15.0	41.06	14.27	Macerata Campania (CE)	4
15-10-2020	13:00	± 15.0	41.08	14.32	Caserta (CE)	2
10-01-2021	12:55	± 5.0	40.87	14.44	Somma Vesuviana (NA)	2
10-01-2021	13:20	± 5.0	40.92	14.74	Mercogliano (AV)	2
09-06-2021	12:00	± 5.0	41.33	15.71	Orta Nova (FG)	2
17-09-2021	06:00	± 15.0	41.13	14.34	Castel Morrone (CE)	3
17-09-2021	12:15	± 5.0	41.28	14.48	Faicchio (BN)	3
09-12-2021	16:00	± 30.0	40.84	14.23	Napoli Vomero (NA)	2
07-02-2022	18:00	± 30.0	40.93	15.24	Morra de Sanctis (AV)	2
17-06-2022	14:50	± 5.0	40.81	15.71	Filiano (PZ)	2
07-07-2022	16:20	± 5.0	41.48	13.90	Cervaro (FR)	3
05-08-2022	14:25	± 5.0	40.93	15.04	Castelfranci (AV)	3
08-08-2022	17:15	± 5.0	40.81	14.62	Sarno (SA)	2
09-08-2022	14:00	± 5.0	41.06	14.89	San Giorgio del Sannio (BN)	2
09-08-2022	14:45	± 30.0	40.95	14.30	Caivano (NA)	2
11-08-2022	16:00	± 5.0	40.81	14.62	Sarno (SA)	2
13-08-2022	17:50	± 5.0	41.27	14.30	Dragoni (CE)	2
27-03-2023	15:05	± 5.0	41.48	14.05	Venafro (IS)	3
27-03-2023	16:50	± 5.0	40.77	14.79	Fisciano (SA)	3
27-03-2023	17:20	± 5.0	40.62	14.95	Bellizzi (SA)	2
08-04-2023	12:40	± 5.0	40.95	14.29	Crispano (NA)	2
25-05-2023	12:40	± 30.0	40.82	14.70	Bracigliano (SA)	2
23-09-2023	08:20	± 5.0	41.26	14.70	Casalduni (BN)	6
23-09-2023	07:30	± 5.0	41.17	14.66	Foglianise (BN)	3
23-09-2023	10:35	± 5.0	40.84	15.03	Montella (AV)	2
23-09-2023	11:00	± 5.0	40.62	14.97	Battipaglia (SA)	4
23-09-2023	11:10	± 5.0	40.63	15.05	Eboli (SA)	4